UNIVERSIDAD DE SALAMANCA

DOCTORAL THESIS

Beam and plasma diagnostics for high-repetition rate laser-driven particle accelerators

Author:
Carlos Salgado López

Directors:
Dr. Giancarlo Gatti
Prof. Robert Fedosejevs
Tutor:
Prof. Luca Volpe

A thesis submitted in fulfilment of the requirements for the degree of International Doctor in Physics

VNiVERSiDAD D SALAMANCA

CAMPUS DE EXCELENCIA INTERNACIONAL

August 29, 2023

Declaration of Authorship

I, Carlos Salgado López, declare that this thesis titled, "Beam and plasma diagnostics for high-repetition rate laser-driven particle accelerators" and the work presented in it are my own. I confirm that:

- This work was done wholly or mainly while in candidature for a research degree at this University.
- Where I have consulted the published work of others, this is always clearly attributed.
- Where I have referenced the work of others, the source is always given. With the exception of such mentions, this thesis is entirely my own work.
- I have acknowledged all main sources of help.
- Where the thesis is based on work done by myself jointly with others, I have made clear exactly what was done by others and what I have contributed myself.

Signed: SALGADO LOPEZ CARLOS - 70889729A Firmado digitalmente por SALGADO LOPEZ CARLOS - 70889729A Fecha: 2023.08.29 16:05:47 +02'00'

Date: 29/08/2023

UNIVERSIDAD DE SALAMANCA

Abstract

Escuela de doctorado
Programa de doctorado de Física Aplicada y Tecnología

Doctor in Physics

Beam and plasma diagnostics for high-repetition rate laser-driven particle accelerators

by Carlos Salgado López

This thesis focuses on the Physics of intense laser-driven particle accelerators, which has proven as a valuable alternative to conventional accelerator technology in several aspects, presenting improved bunch duration and transversal beam quality. The advent of a new generation of compact particle accelerators based on laser-plasma interaction and the interest of its potential applications has implied the consequent development of novel diagnostics techniques, capable to resolve the fine temporal and spatial scales of these experiments. In addition, these dedicated diagnostics are required to operate at the high repetition rate of the new class of fs-long table-top petawatt laser systems. This manuscript presents the development and the experimental application of several diagnostics designed for the three different main laser-plasma interaction regimes.

- An extensive study of several characterization techniques of gaseous targets for laser-matter interaction experiments is presented, including interferometry, wavefront measurement and Schlieren imaging. A parametric study of different classes of gaseous targets with diverse geometries, compositions and operation principles is elaborated. The application of underdense gas targets for laser wakefield electron acceleration and high harmonics generation experiments in the sub-petawatt level is shown.

- An international collaborative research project in laser-driven ion acceleration in near-critical plasmas generated by high-density gas jets is presented. A summary of the campaigns carried out in petawatt laser facilities is given, as well as the corresponding experimental outcomes. A detailed description of the targetry and ultra-fast plasma diagnostics elaborated for such campaigns is provided, yielding relevant findings for the experimental optimization.

- The angular-resolved tomography of a laser-driven ion source has been achieved in a overdense plasma experiment with a concept modification of a Thomson Parabola spectrometer. The same instrument has also been successfully adapted into a novel approach for pepper-pot spectrally-resolved measurements of the proton beam lateral trace-space. This newly developed method have demonstrated to be capable to perform a thorough characterization of the spatial features and laminarity regime of the very complex ion beams generated by laser-plasma interaction, recognizing several operational and resolution improvements when comparing with previous techniques.

Resumen de la tesis

Diagnósticos de alta tasa de repetición de haces y plasmas para aceleradores de partículas por láser

El trabajo descrito en esta tesis se centra en la Física de los aceleradores de partículas basados en la interacción de láseres intensos y plasmas, los cuales han demostrado ser una alternativa considerable a los aceleradores de partículas convencionales en muchos aspectos, presentando mejor duración y calidad transveral de los haces. La aparición de una nueva generación de aceleradores de partículas compactos basados en la interacción láser-plasma y el interés en sus potenciales aplicaciones ha supuesto el desarrollo de nuevas técnicas de diagnóstico, capaces de resolver las pequeñas escalas espaciales y temporales de dichos experimentos. Además, estos diagnósticos deben ser capaces de operar a la alta tasa de repetición de los nuevos sistemas láser compactos de petavatio de duración de femtosegundo. Esta tesis presenta el desarrollo y la aplicación experimental de una serie de diagnósticos diseñados para los tres principales regímenes de la interacción laser-plasma.

- Se presenta un extenso estudio de varias técnicas de caracterización de blancos gaseosos para experimentos de interacción láser-materia, incluyendo interferometría, medida de frente de onda y estrioscopía. La investigación paramétrica de distintos tipos de blancos gaseosos, con diversos princpios de funcionamiento, geometrías y composiciones es elaborada. Así mismo, se muestra el uso de estos blancos subdensos para la aceleración de electrones en estela láser y para la generación de altos armónicos con potencias láser por debajo de petavatio.

- Se presenta un proyecto de investigación colaborativo internacional centrado en la aceleración de iones basada en láser en plasma de densidad crítica creados a partir de un sistema de gas de alta presión. Se elabora un resumen de las campañas experimentales llevadas acabo en instalaciones láser de potencia de petavatio y de los resultados experimentales correspondientes. Los diagnósticos elaborados para la inspección del blanco y del plasma son detallados, habiendo arrojado resultados relevantes para la optimización experimental.

- Se ha realizado la tomografía resuelta en ángulo de una fuente de iones generada por láser en un plasma sobre-denso gracias a la modificación de un espectrómetro tipo Thomson Parabola. El mismo instrumento también ha sido exitosamente adaptado en un diagnóstico tipo "pepper-pot" para medidas del espacio de fases de un haz de protones resuelto en energía. Este nuevo método ha demostrado ser capaz de realizar una detallada caracterización de las propiedades espaciales y del régimen de laminaridad de los complejos haces de iones generados por interacción láser-plasma, reconociendo además diversas mejoras operacionales y de resolución de medida frente a técnicas anteriores.

Contents

A mi familia.

Scientific publications and conference contributions

The participation of the candidate at different research lines has led to his authorship in several scientific publication at peer reviewed journal, as well as to different contributions to international conferences:

Articles:

- A. Curcio, J. I. Apiñaniz Aginako, T. Cebriano Ramírez, M. Ehret, B. Kebladj, A. Morabito, A. Pérez Delgado, C. Salgado López, L. Volpe and G. Gatti *Liouville Theory for Fully Analytic Studies of Transverse Beam Dynamics in Laser-Plasma Ion Accelerators*, Symmetry 2022, 14, 1875. DOI: 10.3390/sym14091875. Participation: experimental support.
- C. Salgado-López, J. I. Apiñaniz, J. L. Henares, J. A. Pérez-Hernández, D. de Luis, L. Volpe and G. Gatti, *Angular-Resolved Thomson Parabola Spectrometer for Laser-Driven Ion Accelerators*, Sensors 2022, **22**(9), 3239. DOI: 10.3390/s22093239. Participation: concept, design, experiment, formal analysis, article writing.
- M. Ehret, C. Salgado-López, V. Ospina-Bohorquez, J. A. Pérez-Hernández, M. Huault, M. de Marco, J. I. Apiñaniz, F. Hannachi, D. de Luis, J. Hernández Toro, D. Arana, C. Méndez, O. Varela, A. Debayle, L. Gremillet, T.-H. Nguyen-Bui, E. Olivier, G. Revet, N. D. Bukharskii, H. Larreur, J. Caron, C. Vlachos, T. Ceccotti, D. Raffestin, P. Nicolai, J. L. Feugeas, M. Roth, X. Vaisseau, G. Gatti, L. Volpe and J. J. Santos, *Ion acceleration by an ultrashort laser pulse interacting with a near-critical-density gas jet*, ArXiV preprint. DOI: arXiv.2012.09455. Participation: concept, design, experiment, formal analysis, article writing.
- J. Pasley, G. Andrianaki, A. Baroutsos, D. Batani, E. P. Benis, A. Ciardi, D. Cook, V. Dimitriou, B. Dromey, I. Fitilis, G. Gatti, A. Grigoriadis, M. Huault, J. A. Pérez Herández, E. Kaselouris, O. Klimo, M. Koenig, G. Koundourakis, M. Kucharik, J. Limpouch, R. Liska, C. Salgado López, S. Malko, S. Olmos-Migueláñez, Y. Orphanos, V. Ospina, N. A. Papadogiannis, S. Petrakis, J. Psikal, M. S. Rivetta, M. J. Rodríguez-Conde, J. J. Santos, M. Sinor, A. Skoulakis, I. Tazes, L. Tejada Pascual, C. Tsitou, P. Vacha, L. Volpe, J. Vyskocil, S. White, M. Yeung, G. Zerouli, and M. Tatarakis, *Innovative education and training in high power laser plasmas (PowerLaPs) for plasma physics, high power laser matter interactions and high energy density physics: experimental diagnostics and simulations*, High Power Laser Science and Engineering, (2020), Vol. **8**, e5, 7 pages. DOI: 10.1017/hpl.2020.4. Participation: teaching at school, lecture "Under-critical and near-critical dense plasmas: laser-driven particle acceleration and diagnostics".
- A. Longman, C. Salgado, G. Zeraouli, J. I. Apiñaniz, J. A. Pérez-Hernández, M. Eltahlawy, G. Gatti, L. Volpe and R. Fedosejevs, *Off-Axis Spiral Phase Mirrors for Generating High Intensity Optical Vortices*, Optics Letters **45**-8, 2187-2190 (2020). DOI: 10.1364/OL.387363. Participation: setup preparation, experiment.
- C. Z. He, A. Longman, J. A. Pérez-Hernández, M. de Marco, C. Salgado, G. Zeraouli, G. Gatti, L. Roso, R. Fedosejevs and W. T. Hill, *Towards an in situ, full-power gauge of the focal-volume intensity of petawatt-class lasers*, Optics Express **27**, 30020-30030 (2019). DOI: 10.1364/OE.27.030020. Participation: setup preparation, formal analysis.
- L. Volpe, R. Fedosejevs, G. Gatti, J. A. Pérez-Hernández, C. Méndez, J. I. Apiñaniz, X. Vaisseau, C. Salgado, M. Huault, S. Malko, G. Zeraouli, V. Ospina, A. Longman, D. de Luis, K. Li, O. Varela, E. García, I. Hernández, J. D. Pisonero, J. G. Ajates, J. M. Álvarez, C. García, M. Rico, D. Arana, J. Hernández-Toro and L. Roso, *Generation of high energy laser-driven electron and proton sources with the 200 TW system VEGA 2 at the Centro de Láseres Pulsados*, High Power Laser Science and Engineering, (2019), Vol. 7, e25, 6 pages. DOI: 10.1017/hpl.2019.10. Participation: methodology, setup preparation, experiment, formal analysis, draft writing.
- F. Valle Brozas, C. Salgado, J. I. Apiñaniz, A. V. Carpentier, M. Sánchez Albaneda, L. Roso, C. Raposo, C. Padilla and A. Peralta Conde, *Determination of the species generated in atmospheric-pressure laser-induced plasmas by mass spectrometry techniques*, Laser Phys. **26** (2016) 055602. DOI: 10.1088/1054-660X/26/5/055602. Participation: methodology, setup preparation, experiment, formal analysis, draft writing.

Conference proceedings:

- C. Salgado-López, J. I. Apiñaniz, A. Curcio, D. de Luis, J. L. Henares, J. A. Pérez-Hernández, L. Volpe and G. Gatti, *Angular-Resolved Thomson Parabola Spectrometer For Laser-Driven Ion Acceleration*, published at the proceedings of the 11th the International Beam Instrumentation Conference 2002, at Kraków, Poland. DOI: 10.18429/JACoW-IBIC2022. Participation: concept, design, experiment, formal analysis, article writing.
- M. Huault, G. Zeraouli, J. G. Ajates, J. Apiñaniz, E. García, I. Hernández, S. Malko, C. Méndez, J. A. Pérez-Hernández, J. D. Pisonero, C. Salgado, X. Vaisseau, O. Varela, G. Gatti, L. Volpe, L. Roso, R. Fedosejevs, A. Longman, R. Shepherd and W. T. Hill, *Commissioning experiments of VEGA-2 at Centro de Láseres Pulsados (CLPU)*, in Frontiers in Optics 2017, OSA Technical Digest (Optical Society of America, 2017), paper FM2B.4. DOI: 10.1364/FIO.2017.FM2B.4 Participation: methodology, setup preparation, experiment.

Conference oral contributions:

- Oral presentation by C. Salgado: C. Salgado-López, J. I. Apiñaniz, A. Curcio, D. de Luis, J. L. Henares, J. A. Pérez-Hernández, L. Volpe and G. Gatti, *Angular-resolved Thomson Parabola Spectrometer for Laser-Plasma Ion Accelerators*, at 5th European Conference on Plasma Diagnostics (ECPD 2023), in Rethymno, Greece. Participation: conceptualization, methodology, setup preparation, experiment, formal analysis, presentation.
- Oral presentation by C. Salgado: C. Salgado-López, J. I. Apiñaniz, A. Curcio, D. de Luis, J. L. Henares, J. A. Pérez-Hernández, L. Volpe and G. Gatti, *Angular-Resolved Thomson Parabola Spectrometer For Laser-Driven Ion Acceleration*, at 11th the International Beam Instrumentation Conference 2002, in Kraków, Poland. Participation: conceptualization, methodology, setup preparation, experiment, formal analysis, presentation.
- Oral presentation by J. M. Gjevre: J. M. Gjevre, J. A. Pérez-Hernández, R. Lera, C. Salgado-López, M. Ehret, G. Zeraouli, L. Roso and R. Fedosejevs, *Focal Cone High Harmonic Generation* at the Canadian Association of Physicists Congress 2022, at Hamilton, Canada. Participation: experiment, formal analysis.
- Oral presentation by V. Ospina: V. Ospina, C.Salgado *et al.*, *Experimental and numerical investigations of ion acceleration by ultraintense laser pulses in near-critical transparent gas jets*, at EPS conference on Plasma Physics 2022, in Maastricht, the Netherlands. Participation: conceptualization, methodology, setup preparation, experiment, formal analysis.
- Lecture by C. Salgado: *Laser driven particle acceleration and optical diagnostics* at the LaPlaSS 2021 Summer School, at CLPU, Salamanca, Spain.
- Oral presentation by V. Ospina: V. Ospina, C.Salgado *et al.*, *Numerical and experimental investigations of ion acceleration by ultraintense laser pulses in high-density gas jets*, at 63rd Annual Meeting of the APS Division of Plasma Physics 2021, in Pittsburgh, USA. Participation: conceptualization, methodology, setup preparation, experiment, formal analysis.
- Oral presentation by R. Fedosejevs: R. Fedosejevs, A. Longman, M. Huault, C. Salgado, G. Zeraouli, S. Malko, M. de Marco, J. A. Pérez-Hernández, G. Gatti and L. Volpe, *MeV electron and proton generation using OAM laser modes*, at 47th European Physical Society Conference on Plasma Physics (EPS 2021), in Barcelona, Spain. Participation: setup preparation, experiment, formal analysis.
- Lecture by C. Salgado: *Under-critical and near-critical dense plasmas: laser-driven particle acceleration and diagnostics* at the LaPlaSS 2020 Summer School, at CLPU, Salamanca, Spain.
- Lecture by C. Salgado: *Under-critical and near-critical dense plasmas: laser-driven particle acceleration and diagnostics* at the LaPlaSS 2019 Summer School, at CLPU, Salamanca, Spain.
- Lecture by C. Salgado: *Under-critical and near critical dense plasmas: laser-driven particle acceleration and diagnostics* at the PowerLaPs Intensive Training 2019: Laser-Plasma Diagnostics, at University of Salamanca, Spain.

- Oral presentation by J. J. Santos: C. Salgado, M. Ehret, V. Ospina, J. A. Pérez-Hernández, M. Huault, M. de Marco, J. I. Apiñaniz, F. Hannachi, D. de Luis, J. Hernández Toro, C. Méndez, J. D. Pisonero, O. Varela, A. Debayle, E. d'Humieres, L. Gremillet, T.-H. Nguyen-Bui, E. Olivier, G. Revet, C. Brabetz, J. Caron. T. Ceccotti, R. Nuter, D. Raffestin, M. Roth, G. Schaumann, X. Vaisseau, G. Gatti, L. Volpe and J. Santos, *Near-critical density plasmas from supersonic gas jets for enhanced ion acceleration by ultra-intense laser interaction*, at IFSA 2019 in Osaka, Japan. Participation: conceptualization, methodology, setup preparation, experiment, formal analysis.
- Oral presentation by O. Lundh: O. Lundh, I. Gallardo González, H. Ekerfelt, J. Bjorklund Svensson, G. Gatti, D. Guenot, A. Gonoskov, M. Hansson, J. A. Pérez-Hernández, M. Marklund, C. Salgado, E. Wallin and G. Zeraouli, *Electron acceleration in merging laser wakefields*, at 4th European Advanced Accelerator Concepts Workshop 2019, in Isola d'Elba, Italy. Participation: setup preparation, experiment, formal analysis.
- Oral presentation by C. Salgado: C. Salgado *et al.*, *Near-critical plasmas from supersonic gas jets for enhanced ion acceleration by ultra-intense laser interaction*, at the 4th Targetry for High Repetition Rate Laser-Driven Sources 2019 (TARG4), in Milan, Italy. Participation: conceptualization, methodology, setup preparation, experiment, formal analysis, presentation.
- Oral presentation by M. Ehret: V. Ospina, M. Ehret, C. Salgado *et al.*, *Near-critical plasmas from supersonic gas jets for enhanced ion acceleration by ultra-intense laser interaction*, at 25th Congrès Général de la Société Française de Physique (CGSFP) 2019, in Nantes, France. Participation: setup preparation, experiment, formal analysis.
- Oral presentation by R. Fedosejevs: R. Fedosejevs, A. Longman, C. Salgado, G. Zeraouli, J. I. Apiñaniz, J. A. Pérez-Hernández, M. de Marco, G. Gatti, L. Volpe, C. Z. R. He and W. T. Hill III, *MeV electron and Betatron production from Wakefield interactions using Orbital Angular Momentum Laser Pulses*, at Frontiers of Plasma Physics and Technology Conference 2019, in Colombo arae, Sri Lanka. Participation: setup preparation, experiment, formal analysis.
- Practical lecture by C. Salgado: *Characterization of gas jet by interferometry* at the Laser Plasma Summer School (LAPLASS) 2018: Diagnostic techniques for laser-plasma experiments at HRR, at CLPU, Salamanca, Spain.
- Oral presentation by A. Longman: A. Longman, C. Salgado, G. Zeraouli, J. I. Apiñaniz, J. A. Pérez-Hernández, M. de Marco, C. Z. He, G. Gatti, L. Volpe, W. T. Hill III and R. Fedosejevs, *Wakefield acceleration and betatron radiation driven by linearly polarizer Laguerre-Gaussian orbital angular momentum laser pulses*, at Super-Intense Laser-Atom Physics international workshop 2018, Toronto, Canada. Participation: setup preparation, experiment, formal analysis.
- Oral presentation by A. Longman: A. Longman, R. Fedosejevs, C. Salgado, G. Zeraouli, J. I. Apiñaniz, J. A. Pérez-Hernández, M. de Marco, G. Gatti, L. Volpe, C. Z. R. He and W. T. Hill III, *Wakefield acceleration and betatron radiation driven by linearly polarized Laguerre-Gaussian orbital angular momentum modes*, at 60th APS Plasma Physics Annual Meeting 2018, Portland, USA. Participation: setup preparation, experiment, formal analysis.
- Oral presentation by R. Fedosejevs: R. Fedosejevs, A. Longman, C. Salgado, G. Zeraouli, J. I. Apiñaniz, J. A. Pérez-Hernández, M. de Marco, G. Gatti, L. Volpe, C. Z. R. He and W. T. Hill III, *Wakefield Electrons and Betatron Radiation Driven by Laguerre-Gaussian Orbital Angular Momentum Laser Pulses*, at 35th European Conference on Laser Interaction with Matter 2018, Rethymno, Greece. Participation: setup preparation, experiment, formal analysis.
- Oral presentation by W. T. Hill: M. Huault, G. Zeraouli, J. G. Ajates, J. Apiñaniz, E. García, I. Hernández, S. Malko, C. Méndez, J. A. Pérez-Hernández, J. D. Pisonero, C. Salgado, X. Vaisseau, O. Varela, G. Gatti, L. Volpe, L. Roso, R. Fedosejevs, A. Longman, R. Shepherd and W. T. Hill, *Commissioning experiments of VEGA-2 at Centro de Láseres Pulsados (CLPU)*, at Frontiers in Optics/Laser Science Conference 2017, Washington D.C., USA. Participation: setup preparation, formal analysis.

- Oral presentation by C. Salgado: C. Salgado, A. Longman, S. Malko, G. Zeraouli, M. Huault, X. Vaisseau, J. I. Apiñaniz, J. A. Pérez-Hernández, J. D. Pisonero, J. Ajates, I. Hernández, E. García, O. Varela, C. Méndez, J. Hernández-Toro, G. Gatti, L. Volpe, L. Roso and R. Fedosejevs, *VEGA-2 commissioning experiment: WDM study by using X-ray betatron radiation*, at 3rd Targetry for High Repetition Rate Laser-Driven Sources 2017 (TARG3), Salamanca, Spain. Participation: methodology, setup preparation, experiment, formal analysis, presentation.

Conference poster contributions:

- Poster presented by C. Salgado: M. de Marco, G. Gatti, C. Salgado, J. Hernández-Toro, D. de Luis and L. Volpe, *Liquid target characterization for laser-plasma interaction experiment*, presented at 4th Targetry for High Repetition Rate Laser-Driven Sources 2019 (TARG4), Milan, Italy. Participation: setup preparation, presentation.
- Poster presented by L. Volpe: L. Volpe, G. Gatti, J. A. Pérez-Hernández, C. Méndez, J. I. Apiñaniz, M. de Marco, C. Salgado, M. Huault, S. Malko, G. Zeraouli, V. Ospina, D. de Luis, R. Fedosejevs, M. Ehret, J. J. Santos, F. Hannachi, O. Varela, E. García, I, Hernández, J. D. Pisonero, J. García Ajates, J. M. Álvarez, C. García, M. Rico, D. Arana, J. Hernández-Toro and L. Roso, *Targetry for High Power high repetitions rate experiments: The CLPU strategy*, at 4th Targetry for High Repetition Rate Laser-Driven Sources 2019 (TARG4), Milan, Italy. Participation: conceptualization, formal analysis.
- Poster presented by S. Malko: S. Malko, C. Salgado, R. Fedosejevs, J. I. Apiñaniz, G. Gatti, D. de Luis, J. A. Pérez-Hernández and L. Volpe, *Characterization of the pre-plasma formation for high intensity laser-solid target experiment*, at 3rd European Conference on Plasma Diagnostics 2019, Lisbon, Portugal. Participation: conceptualization, methodology, setup preparation, experiment, formal analysis.
- Poster by V. Ospina: V. Ospina *et al.*, *Near-critical plasmas from supersonic gas jets for laser-driven ion acceleration*, at Forum Interaction Laser Plasma 2019 (FORUM-ILP 2019), Fréjus, France. Participation: setup preparation, experiment, formal analysis.
- Poster presented by G. Revet: G. Revet, M. Erhet, J. J. Santos, C. Salgado, F. Hannachi, A. Casner, D. Raffestin, *Particle energy deposition in CR-39 detectors: track's diameter/length couple analysis method*, at 3rd European Conference on Plasma Diagnostics 2019, Lisbon, Portugal. Participation: setup preparation, experiment, formal analysis.
- Poster presented by I. Gallardo: I. Gallardo González, H. Ekerfelt, J. Björklund Svensson, G. Gatti, A. Gonoskov, D. Guenot, M. Hansson, M. Marklund, J. A. Pérez-Hernández, C. Salgado, E. Wallin, G. Zeraouli and O. Lundh, *Electron acceleration and X-ray emission from interacting wakefields*, presented at IONS Scandinavia 2018, Lyngby, Denmark. Participation: setup preparation, experiment, formal analysis.
- Poster presented by S. Malko: S. Malko, A. Longman, C. Salgado, J. I. Apiñaniz, G. Gatti, I. Hernández, J. A. Pérez-Hernández, J. D. Pisonero, L. Roso, X. Vaisseau, L. Volpe, G. Zeraouli and R. Fedosejevs, *Study of ionization states dynamics of Warm Dense Aluminum*, at Direct Drive and Fast Ignition Wokshop 2017 (DDFIW2017), Salamanca, Spain. Participation: setup preparation, experiment, formal analysis.
- Poster presented by C. Salgado: C. Salgado, A. Longman, S. Malko, G. Zeraouli, M. Huault, X. Vaisseau, J. A. Pérez-Hernández, J. I. Apiñaniz, E. García, O. Varela, C. Méndez, J. Hernández-Toro, G. Gatti, L. Volpe and R. Fedosejevs, *Laser driven electrons and X-ray Betatron radiation generation at VEGA*, presented at DDFIW 2017, Salamanca, Spain. Participation: setup preparation, experiment, formal analysis, presentation.
- Poster presented by C. Salgado: C. Salgado, F. Valle-Brozas, A. San Blas, J. Cortina, A. V. Carpentier, A. Peralta Conde and L. Roso, *Characterization of gas jets with and interferometric system*, presented at the Spanish Meeting of Optoelectronics (OPTOEL 2015), Salamanca, Spain.

Experimental experience

- **Development of Tape Targets in VEGA for high repetition rate experiments and optimization of related HRR diagnostics**
  July/2023 (2 weeks of beam-time) at VEGA 3 (1 PW), CLPU, Salamanca, Spain. PI: J. L. Henares (CLPU, Spain).
  Participation: conception, construction and analysis of high-repetition-rate proton divergence diagnostic, general experimental support.
- **Efficient Proton Acceleration via Double Pulse Laser Approach using a Fresnel lens as a main diagnostic**
  June/2023 (2 weeks of beam-time) at VEGA 3 (1 PW), CLPU, Salamanca, Spain. PI: J. A. Pérez-Hernández (CLPU, Spain).
  Participation: conception, construction and analysis of high-repetition-rate proton divergence diagnostic.
- **Efficient Proton Acceleration via Double Pulse Laser Approach**
  May/2023 (4 weeks beam-time) at VEGA 3 (1 PW), CLPU, Salamanca, Spain. PI: L. Volpe (Universidad Politécnica de Madrid, Spain). Participation: conception, construction and analysis of high-repetition-rate proton divergence and emittance diagnostic of proton beam.
- **Commissioning Experiment of the high pressure system at CLPU**
  Jul/2022 (2 weeks beam-time) at VEGA 3 (1 PW), CLPU, Salamanca, Spain. PI: J.L. Henares (CLPU, Spain).
  Participation: ion spectrometer operation and gas characterization bench construction.
- **Protons' Characterization, Transport and Applications, towards experimental stations**
  Jun/2022 (4 weeks beam-time) at VEGA 3 (1 PW), CLPU, Salamanca, Spain. PI: G. Gatti (CLPU, Spain).
  Participation: ion spectrometer operation, proton emittance measurement and data analysis.
  Publications: 10.3390/sym14091875 and 10.18429/JACoW-IBIC2022.
- **High Harmonic Hot Spot**
  Feb/2022 (3 weeks beam-time) at VEGA 3 (1 PW), CLPU, Salamanca, Spain. PI: R. Fedosejevs (University of Alberta, Canada).
  Participation: gas jet target handling and characterization and experiment support.
- **Ion acceleration by ultra-intense laser interaction with high density gas jet -towards PW regime**
  Jun/2021 (4 weeks beam-time) at VEGA 3 (1 PW), CLPU, Salamanca, Spain. PI: J. J. Santos (CELIA, France).
  Participation: local coordination, experiment conceptualization, beamline control, probe beam construction and particle spectrometer diagnostic design and construction.
- **VEGA 3 commissioning: characterization of ion acceleration**
  Dec/2020 (8 weeks beam-time) at VEGA 3 (1 PW), CLPU, Salamanca, Spain. PI: A. Morace (ILE Osaka, Japan).
  Participation: responsible of the streak interferometry diagnostic and ion spectrometer.
  Publication: 10.3390/s22093239.
- **High Harmonic Hot Spot Generation**
  Oct/2020 (2 weeks beam-time) at VEGA 2 (200 TW), CLPU, Salamanca, Spain. PI: R. Fedosejevs (University of Alberta, Canada).
  Participation: gas target handling and harmonics diagnostics setup.
- **Proton/Electron Beams' Space/Time Characterization**
  Mar/2020 (4 weeks beam-time) at VEGA 2 (200 TW), CLPU, Salamanca, Spain. PI: G. Gatti (CLPU, Spain).
  Participation: setup construction, including gas target, probe and mid-infrared beamline for transition radiation diagnostics.

- **Test and characterization of the special flat liquid target at CLPU**
  Dec/2019 (2 weeks beam-time) at VEGA 3 (1 PW), CLPU, Salamanca, Spain. PI: L. Volpe (CLPU, Spain).
  Participation: target and beamline setup and general experimental support.
- **Enhancement of electron guiding and proton generation using orbital angular momentum modes**
  Jun/2019 (2 weeks beam-time) at VEGA 2 (200 TW), CLPU, Salamanca, Spain. PI: R. Fedosejevs (University of Alberta, Canada).
  Participation: probe beam construction and implementation of ultrafast preplasma diagnostic.
- **Ion acceleration by ultra-intense laser interaction with high density gas jet.**
  Oct/2018 (3 weeks beam-time) at VEGA 2 (200 TW), CLPU, Salamanca, Spain. PI: J. J. Santos (CELIA, France).
  Participation: local coordinator, probe setup, interferometry diagnostic.
  Publication: arXiv.2012.09455.
- **Relativistic Thompson Scattering based vacuum gauge**
  Jul/2018 (2 weeks beam-time) at VEGA 2 (200 TW), CLPU, Salamanca, Spain. PI: W. T. Hill (University of Maryland, USA).
  Participation: gas target setup.
  Publication: 10.1364/OE.27.030020.
- **Betatron enhancement with orbital angular momentum laser beams**
  Jun/2018 (3 weeks beam-time) at VEGA 2 (200 TW), CLPU, Salamanca, Spain. PI: R. Fedosejevs (University of Alberta, Canada).
  Participation: gas target handling, implementation of orbital momentum beamline and probe beam construction.
  Publication: 10.1364/OL.387363.
- **Braided electron beams and X-ray radiation emission from interacting wake-fields.**
  Apr/2018 (3 weeks beam-time) at VEGA 2 (200 TW), CLPU, Salamanca, Spain. PI: O. Lundh (Lund University, Sweden).
  Participation: beamline and gas target handling.
- **VEGA 2 TNSA proton acceleration commissioning experiment**
  2017-2018 (>10 weeks beam-time) at VEGA 2 (200 TW), CLPU, Salamanca, Spain. PI: L. Volpe (CLPU, Salamanca).
  Participation: probe beam handling and responsible of a ultrafast pre-plasma diagnostic.
  Publications: 10.1364/FIO.2017.FM2B.4 and 10.1017/hpl.2019.10.
- **Electron acceleration from near critical density targets produced by supersonic shock nozzles**
  Jul/2017 (3 weeks beam-time) at ECLIPSE 3 (30 TW), CELIA, Bordeaux, France. PI: J. J. Santos (CELIA, France).
  Participation: setup preparation, implementation of optical diagnostics.
- **Betatron measurement of the ionization state of Warm Dense Matter**
  2016-2017 (>10 weeks beam-time) at VEGA 2 (200 TW), CLPU, Salamanca, Spain. PI: R. Fedosejevs (University of Alberta, Canada).
  Participation: WDM heater beam handling, and probe beam construction and gas jet target handling and characterization.
  Publications: 10.1364/FIO.2017.FM2B.4 and 10.1017/hpl.2019.10.
- **High density gas jet characterization for laser-near critical plasma experiments.**
  Oct/2016 and Apr/2017 (4 weeks beam-time) at ECLIPSE 3 (30 TW), CELIA, Bordeaux, France. PI: J. J. Santos (CELIA, France).
  Participation: target system commissioning, setup preparation, diagnostic setup and data analysis.
- **Liquid target laser-driven hard x-ray source development.**
  Oct/2015 (2 weeks beam-time) at CEP laser (<1 TW), CLPU, Salamanca, Spain. PI: D. Papp (ELI-ALPS, Hungary).
  Participation: beam and target handling.

- **Commissioning of a atmospheric-pressure laser-induced plasmas mass spectrometer**
  2014 (2 weeks beam-time) at VEGA 2 (200 TW), CLPU, Salamanca, Spain. PI: A. Peralta-Conde (CLPU, Spain).
  Participation: experimental spectrometer commissioning, data analysis.
  Publications: 10.1088/1054-660X/26/5/055602.

List of Abbreviations

1D	**1**-**D**imensional
2D	**2**-**D**imensional
3D	**3**-**D**imensional
6D	**6**-**D**imensional
Al	**Al**uminium
Ar	**Ar**gon
ATI	**A**bove **Threshold I**onization
BBO	**B**eta **B**arium **B**oriate
BOA	**B**reak-**O**ut **A**fterburner
BPP	**B**eam **P**roduct **P**arameter
BPR	**B**ragg **P**eak **R**ange
C	**C**arbon
CCD	**C**harge-**C**oupled **D**evice
CEA	**C**ommissariat a l'**É**nergie **A**tomique
CENBG	**C**entre d'**E**tudes **N**ucléaires de **B**ordeaux-**G**radignan
CERN	**C**onseil **E**uropéen por la **R**echerche **N**ucléaire
CLPU	**C**entro de **L**áseres **Pu**lsados
CMOS	**C**omplementary **M**etal-**O**xide-**S**emiconductor
CO_2	**C**arbon **Dio**xide
CPA	**C**hirped **P**ulse **A**mplification
CR39	**C**olumbia **R**esin #**39**
CSA	**C**ollisionless **S**hock **A**cceleration
Cu	**C**opper
CW	**C**ontinuous **W**ave
e.g.	for example (**e**xempli **g**ratia)
EM	**E**lectro-**M**agnetic
EMP	**E**lectro**m**agnetic **P**ulse
ES	**E**lectro**s**tatic
ESV	**E**mergency **S**ecurity **V**alve
et al.	and others (**et al**ia)
EUV	**E**xtreme **U**ltra-**V**iolet
FCHHG	**F**ocal **C**one **H**igh **H**armonic **G**eneration
FEL	**F**ree-**E**lectron-**L**aser
FT	**F**ourier **T**ransform
FFT	**F**ast **F**ourier **T**ransform
FWHM	**F**ull **W**idth at **H**alf **M**aximum
GRM	**G**raded **R**eflectivity **M**irror
GVD	**G**roup **V**elocity **D**ispersion
H	**H**ydrogen
HB	**H**ole **B**oring
He	**He**lium
HHG	**H**igh **H**armonic **G**eneration

HRR	**H**igh-**R**epetition-**R**ate
ICF	**I**nertical **C**onfinement **F**usion
IDEA	**I**nterferometric **D**ata **E**valuation **A**lgorithms
i.e.	that is (**i**d **e**st)
IP	**I**maging **P**late
IPPLM	**I**nstitute of **P**lasma **P**hysics and **L**aser **M**icrofusion
IR	**I**nfra**r**ed
Laser	**L**ight **A**mplification by **S**timulated **E**mission of **R**adiation
Linac	**Lin**ear **Ac**celerator
LPA	**L**aser-**p**lasma based **a**ccelerators
LS	**L**ight **S**ail
LWFA	**L**aser **W**ake**f**ield **A**cceleration
MCNP	**M**onte **C**arlo **N**-**P**article
MCP	**M**icro**c**hannel **P**late
MPI	**M**ulti **P**hoton **I**onization
Mylar	Biaxially-oriented polyethylene terephthalate
MZI	**M**ach-**Z**ehnder **I**nterferometer
N	**N**itrogen
NCP	**N**ear-**C**ritical **P**lasma
Nd:Glass	**N**eo**d**ymium doped **Glass**
Nd:YAG	**N**eo**d**yimium doped **Y**ttrium **A**luminum **G**arnet
Ne	**Ne**on
OAP	**O**ff-**A**xis **P**arabola
OPA	**O**ptical **P**arametric **A**mplifier
PALS	**P**rague **A**sterix **L**aser **S**ystem
PIC	**Particle**-**i**n-**C**ell
PiN	Acceptor-Neutral-Donor (semiconductor layers)
PSF	**P**oint **S**pread **F**ucntion
RCF	**R**adio**c**hromic **F**ilms
RF	**R**adio-**f**requency
RMS	**R**oot-**M**ean-**S**quare
RMSD	**R**oot-**M**ean-**S**quare **D**eviation
RPA	**R**adiation **P**ressure **A**cceleration
SEM	**S**canning **E**lectron **M**icroscope
SHG	**S**econd **H**armonic **G**eneration
SXR	**S**oft **X**-**R**ays
TA	**T**arget **A**rea
TCC	**T**arget **C**hamber **C**enter
TEM	**T**ransverse **E**lectro-**M**agnetic
THG	**T**hird **H**armonic **G**eneration
Ti:Sa	**Ti**tanium doped **Sa**pphire
TNSA	**T**arget **N**ormal **S**heath **A**cceleration
TOD	**T**hird **O**rder **D**ispersion
ToF	**T**ime-**o**f-**F**light
TP	**T**homson **P**arabola
UPF	**U**p**p**er **F**requency limit
UV	**U**ltra-**V**iolet
W	Tungsten
WDM	**W**arm **D**ense **M**atter
WKB	**W**entzel-**K**ramers-**B**rillouin
Xe	**Xe**non

Physical Constants

Speed of Light	$c = 2.997\,924\,58 \times 10^{8}\,\mathrm{m\,s^{-1}}$
Vacuum Permittivity	$\epsilon_0 = 8.854\,187 \times 10^{-12}\,\mathrm{F\,m^{-1}}$
Vacuum Permeability	$\mu_0 = 1.256\,637 \times 10^{-6}\,\mathrm{N\,A^{-2}}$
Electron Charge	$e = 1.602 \times 10^{-19}\,\mathrm{C}$
Electron Mass	$m_e = 9.109\,38 \times 10^{-31}\,\mathrm{kg}$
Proton Mass	$m_p = 1.6726 \times 10^{-27}\,\mathrm{kg}$
Plank Constant	$\hbar = 1.054\,57 \times 10^{-34}\,\mathrm{J\,s}$
Boltzmann Constant	$k_B = 1.38 \times 10^{-23}\,\mathrm{J\,K^{-1}}$
Avogadro Number	$N_A = 6.022 \times 10^{23}\,\mathrm{mol^{-1}}$

Chapter 1

Introduction

This chapter introduces the research field of laser-matter interaction and laser-plasma based accelerators (LPA), depicting their challenges and foreseen applications. The most important families of diagnostics tools for LPA are outlined and classified. Finally, the goal of the thesis is introduced.

1.1 General motivation

The invention of the laser technology in 1960 by T. H. Maiman [1] started the development of a new and promising research field. Laser-matter interaction studies have led to interesting applications in different knowledge areas, including cultural heritage conservation [2], medicine [3] and energy production strategies, as in the case of Inertial Confinement Fusion (ICF) [4]. The invention of the Chirped Pulse Amplification (CPA) in 1985 by D. Strickland and G. Mourou [5] (awarded with the Nobel Prize in 2018) was a major breakthrough, as it has resulted in the development of a new class of table-top pulsed lasers, with moderate energy (tens of Joules) but very short duration (< 100 fs) capable of reaching petawatt level and intensities above $10^{21}\,\mathrm{W/cm^{-2}}$. When interacting with matter under specific conditions, this kind of laser has proven their capability to efficiently accelerate particle beams (including ions [6] and electrons [7]) and to generate secondary radiation (as X-rays [8] and extreme ultra-violet [9]), establishing a new class of table-top particle accelerators and ionizing radiation generators.

The laser-driven particle accelerator technology has evolved rapidly in the last twenty years [10]. Particle and radiation beams generated by interaction of ultra-intense lasers and plasmas are nowadays matching, even improving in some cases, several of the beam features from conventional accelerators. Induced mostly by the very transient nature of the interaction process (due to the very short pulse duration of the driver laser), the generation of very steep and confined accelerating fields and the development of controlled particle injection mechanisms, the production of high quality particle and radiation beams by intense lasers has been proven. Very narrow phase-space volumes in the longitudinal beam direction lead to ultrashort particle pulses, meanwhile a small phase-space distribution in the transversal direction is an indicator of a laminar particle flow. These features can be used to concentrate the generated radiation in very small focal volumes achieving very high peak currents, which is fundamental for most the foreseen applications and research fields. Solid-state physics [11], material science [12], plasma physics [13], fusion energy [14] and cancer treatment [15] are just a few of the potential fields where these state-of-the-art compact accelerators might be utilized.

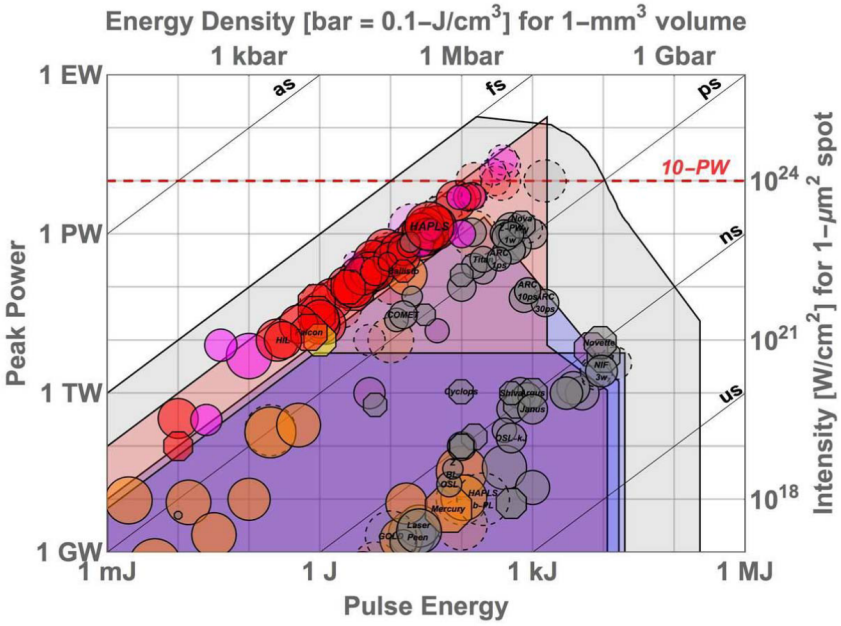

FIGURE 1.1: Global status of the high-power lasers in 2019. Operational systems are represented by circles with continuous borders and lasers under construction by dashed borders. Decommissioned systems are represented with octagons. The colour indicates the amplifier media: Ti:Sapphire (red), Nd:glass (grey), Yb:X (orange), Cr:X (yellow), optical parametric amplifiers (purple-blue) or gas (pink). Diagonal lines represent the corresponding the pulse duration. Image taken from [16].

1.2 Laser plasma interaction

The development of high power pulsed laser technology over the last decades has opened the possibility to reach high irradiance intensities. The interaction of matter with such enormous optical intensities has led to a growing research field worldwide, with several high power laser facilities spread all around the globe, summarized in figure 1.1. The intense laser sources can be divided in three different groups as a function of the delivered energy and pulse duration τ [17]:

- **Long pulsed lasers ($\tau \sim$ ns)**
  High-power nanosecond-long lasers can generate pulses above the kJ energy level, which implies peak power around TW and intensities around $10^{15}\,\mathrm{W/cm^{-2}}$ when focused. Normally based on Nd:glass technology, as is the case of NANO2000 in LULI (France) or the long outputs of PHELIX in GSI (Germany) and VULCAN in RAL (UK), these systems are excellent tools to study High-Energy-Density Physics. Combination of several beamlines on target in dedicated facilities results in the delivery of $\sim$ MJ energy [18], as is the case of NIF (USA) and LMJ (France), facilities dedicated to Inertial Fusion Energy research and limited to $\sim$ 1 shot/day.

- **Short pulsed lasers ($\tau \sim$ ps)**
  By applying the CPA technology to Nd:glass systems, pulse energies below kJ but with pulse duration ranging from 0.5 to 200 ps have been demonstrated in shot-rates around 1 shot/hour. These lasers reach maximum peak power around the PW level and intensities above $10^{21}\,\mathrm{W/cm^{-2}}$ when focused [16]. As is the case of PICO2000 in LULI, TITAN in LNLL (USA) and the short outputs of PHELIX and VULCAN, these

versatile systems are frequently used for proton acceleration, laboratory astrophysics and plasma physics research.

- **Ultra-short pulsed lasers ($\tau \sim 100$ fs)**
  These lasers deliver moderate energy pulses (few to hundreds of J) but in very short times (reaching $\tau < 20$ fs) yielding maximum peak powers above the PW level and intensities above 10^{21} W/cm^{-2} [16]. Their construction architecture allows for high repetition rate (HRR) operation (~ 1 shot/second or higher), as in the case of Ti:Sapphire pulsed laser or the new generation of Optical Parametric Amplifier (OPA) sources, combined with CPA technology. The compactness of these systems (also known as table-top lasers) imply a much cheaper cost when compared to kJ laser facilities. The VEGA laser system at CLPU (Spain) or the 10 PW laser of ELI-NP (Romania) are examples of these ultra-short laser sources. Ultra-short lasers are extensively used in laboratories worldwide, being specially adapted to accelerate electron bunches to relativistic energies, but they can be also applied for proton and ion acceleration. Smaller version of these systems with mJ energy level are widely used for industrial applications as laser micro-machining, as well as for Quantum Physics applied research. In comparison with the nanosecond interaction, where the Physics can be mainly depicted in terms of adiabatic processes and hydrodynamics, ultra-short interaction has to discard steady-state models in favour of fully dynamic non-equilibrium formulations [17]. The work depicted in this manuscript is focused on experiments and applications of this latter kind of sources.

1.2.1 Laser-driven particle accelerators

Since the advent of electrostatic and electromagnetic particle accelerators one century ago, their application for fundamental and applied research and technical, industrial and medical applications has increased steadily. High energy accelerators capable to deliver above 1 GeV energies represent only 1% of the total, and they are built for high energy Physics research, including particle and nuclear physics. Meanwhile, lower energy accelerators are focused on material science, biology and medicine fields. Traditional accelerators are large and expensive facilities with severe radio-protection requirements, which are nowadays extensively exploited not only for research but also for applications as cancer therapy, radio-pharmacy (radio-isotope production), ion implantation, electron cutting and non-destructive inspection (radiography), among others [19].

The main operational limit of conventional accelerators is the electrical breakdown threshold of the device, which limits the accelerating electric field to 100 MV/m. Therefore, kilometre-long facilities are required when very high energies ($>$ 100 GeV) are sought. The recent invention of the CPA technique [5], which paved the way for the development of short and intense pulsed lasers, enabled the development of the concept of laser-plasma accelerators, proposed by Tajima and Dawson [20]. They proposed to use the charge separation driven by intense lasers in plasmas as accelerating structures; in such a regime the threshold for electrical breakdown is not a limitation and fields as large as TV/m can be produced. Consequently the required acceleration length of LPAs reaching conventional beam energies would be several orders of magnitude smaller (around millimetres). Experimental implementation of LPA of electrons [7, 19] and ions [21, 22] is nowadays a common practice in the more than 100 high-intensity laser facilities worldwide [23]. Furthermore, the generation of energetic radiation beams (X-rays and gamma-rays) [24, 25] comparable to synchrotron and free-electron-lasers (FEL) have been achieved, as well as neutron [26] and positron [27, 28] production.

The extensive research on laser-based particle and radiation sources has led to the optimization of its emission in terms of the beam parameters. LPAs are equivalent to conventional accelerator sources in some aspects, and they have even surpassed their predecessors in specific properties. LPA are able to emit extraordinary laminar beams [29] of much shorter duration [30, 31] (meaning high peak current) when compared to conventional sources. Furthermore, the commercial costs of table-top lasers are more affordable than huge accelerator facilities and the radio-protection regulations are less demanding as only the interaction point and its surroundings should be shielded against radiation for safety reasons. However, LPA are quite behind in terms of maximum energy achievable, beam parameters repeatability and average particle flux. The latter is of major importance for industrial and medical applications, which usually require a large time-averaged number of particles for their successful operation. By increasing the number of shots per second in laser facilities, the flux shortage could be addressed. Thus high repetition rate -from 1 to 1000 Hz- laser systems, target assemblies and diagnostics are of considerable interest at the present time.

Proof-of-principle experiments of several beam applications have been carried out, including already well-known applications of conventional accelerated beams and novel ones profiting from the excellent transversal quality and short duration of the LPA beams [10].

- **Ion and proton beams**
  Since the demonstration of collimation and monochromatisation of laser-driven multi-MeV ion beams [32, 33] (specially favoured by the beam laminarity [29] and small source size [34]), their potential applications, such as proton probing of fast phenomena [35–37], isochoric heating of dense plasmas [13], fast ignition scheme of ICF reactions [14], material science [12, 38, 39], cultural heritage [40] and medical purposes (mainly cancer treatment) [15, 41, 42] have been proposed and experimental demonstrations have been carried out.

- **Electron beams**
  Low-divergence, femtosecond-long, stable, tunable and quasi monoenergetic ($\Delta E/E <$ 10%) beams up to several GeV have been measured [43], reaching in some specific cases kHz repetition rate [44]. Thanks to their ultrashort duration, LPA electron beams are the perfect choice for ultrafast probing of transient fields [45, 46], solid state physics studies [11] or even cancer treatment [47]. In addition, due to their compact size and beam parameters, laser-based electron sources are good candidates for staged acceleration schemes, which are required for reaching TeV energy level [48], enough to overcome the threshold for particle physics research. Moreover, these source have proven to be excellent particle seeds for FELs, which emit coherently ultrashort radiation in the soft X-ray (SXR) range [49].

- **X-rays and gamma-rays**
  Several methods have been proposed to generate relatively low divergence X-ray beams from the LPA electron beams, as for instance the so-called Betatron radiation appearing with the electron acceleration [24, 50]. These photons are generated from a virtual source of small size (several micrometres) which makes the radiation spatially coherent, meanwhile their pulse duration has been characterized as short as few femtoseconds. Such conditions, similar to synchrotron and FEL radiation, make these sources ideal for time-resolved probing of matter [51], biological or condensed matter non-invasive inspection with advanced techniques as phase contrast imaging [52, 53], X-ray absorption spectroscopy, X-ray diffraction or triggering of photo-nuclear reactions [50].

- **Extreme Ultraviolet (EUV) and soft X-rays (SXR) from High Harmonic Generation (HHG)**
  Interaction of short lasers with gases or solid in certain special conditions have shown the generation of EUV broadband temporal coherent radiation, known as High Harmonics. Emission at the wavelength range known as the *water window* has been demonstrated (282-533 eV) [9], where the water is transparent to the radiation but carbon is still absorbing, therefore perfectly fitted for X-ray imaging of biological samples. When generated under specific circumstances, attosecond pulse width can be reached [54], thus electron dynamics studies, with typical time-scale of such duration, have become accessible [55].

It important to mention that, besides the short pulse duration of the LPA particle and radiation sources, they have the advantage of being intrinsically synchronized -with femtosecond accuracy- with the driver laser system. This can be beneficial in pump-probe type experiment, where the pump (whose role can be played either by the laser or particle beam) is used for triggering the reaction to study, meanwhile the other is used to study such matter and measure its properties. Thanks to the short duration of the probing beam it is possible to take a snapshot of the reaction with very fine precision (from attosecond to picosecond, depending on the nature of the probing beam), allowing resolution for fast phenomena, as atomic dynamics processes [56], chemical reactions [57], crystallization or melting processes [58], fast-evolving field/plasma probing [36, 59], among others.

Moreover, laser primary sources have the main advantage of being extremely versatile. Modifying the interactions conditions, the same intense laser system can accelerate different species by different mechanisms, such as GeV-level electron beam or MeV-level protons [60]. In addition, multi-species beams can be accelerated (with electrons, ions and high energy photons) which has been proven useful for certain applications [39].

1.2.2 Diagnostics

Diagnostics are indispensable for understanding the laser-plasma experiments and therefore for the proper operation of a laser-driven accelerator [61]. The properties of the generated beams highly depend on the laser pulse parameters and on the accelerating plasma structures, which are transient, fast-evolving and present very short spatial gradients, encompassing normally different interaction regimes in a single event. These experiments result in the generation of unprecedented high accelerating fields in very small spatial ($\sim$ μm) and temporal (fs) dimensions, accelerating very complex particle beams in an environment of extreme conditions. For these reasons, a new generation of experimental techniques (or an improvement of already existing ones) capable to resolve this very extreme features in the required conditions had to be elaborated. The diagnostics involved in a laser-based accelerator can be divided as follow:

- **Primary source metrology**
  Measurements of the driver laser parameters, such as its pulse duration, phase, energy, contrast, wavefront and focal spot (and their repeatability) are crucial for the interaction and their control should be guaranteed by any facility. Special techniques had to be elaborated for the characterization of the duration of ultra-short pulses [62].

- **Plasma diagnostics**
  A wide variety of techniques have been developed to deduce valuable information about the state of the plasma from the practical observation of physical processes and their effects. These diagnostics can be divided by the plasma property that is measured [63], as the magnetic field of the plasma, its refractive index, its electromagnetic

and particle emission and many others. Several measurements techniques are routinely used in laser-plasma interaction experiments to infer such plasma characteristics, including particle stopping power studies [59], optical probing, optical/X-ray spectroscopy [61] and particle deflectometry [36, 64], among others. Some of these strategies are derived from the long-pulse laser community but adapted for the short characteristic time of the fs-class laser driven interaction. Studying these fundamental properties of the plasma (density, magnetization, temperature and so on) is essential for most of the plasma experiments (e.g. in ICF), but also is required for the proper understanding of the interaction mechanisms at play in laser-driven acceleration. Feedback and control of such parameters have stimulated the development of tunable laser-plasma accelerators.

- **Secondary source diagnostics**
  Description of the particle and ionizing radiation beams parameters is the ultimate information needed for applications of the a laser-driven accelerated beam. Several techniques have been recovered from the accelerator scientific community (and adapted to the specific laser-driven beam features) for retrieving beam charge, composition, divergence, spectrum, emittance and dose [61, 65]. It is worth to mention that most of the conventional accelerator diagnostics are not fitted for characterizing LPA beams [61], mainly due to their shorter pulse duration (hence, their high peak current), their extended bandwidth, the particle species diversity, and their higher transversal quality, requiring therefore more accurate, versatile and faster diagnostics.

- **Target diagnostics**
  Off-line target characterization (prior to the interaction event) is an advantageous experimental task, which is feasible with the help of certain techniques, as neutral gas interferometry. Target diagnostics have been proven to be of great utility as they can give a indication of the plasma conditions during the irradiation [66, 67]. In addition, profit can be taken from such measurements for precise target alignment with respect to the laser.

Laser-driven particle accelerators have become a promising research field, specially for their foreseen applications in society. Nevertheless, several challenges still need to be addressed in the near future before their public usage. Repeatable and tunable beams sources with enough average flux are required for several applications. The limitation of average flux could be overcome if HHR operation is achieved. Increasingly repetition rates are recently achieved in the intense laser technology [16], meanwhile typical targets and diagnostics are not compatible with such repetition rate. Enormous effort is being dedicated at laboratories worldwide to reduce such limitations, both for targets [68] and diagnostics [61, 65].

1.3 Goal of the thesis

The work showed in this thesis addresses the necessity for high-repetition-rate compatible diagnostics in the field of laser-plasma driven particle accelerators with enough sensitivity to resolve the fine target, plasma and characteristic beam features in diverse interaction regimes. The aim of this thesis manuscript is to present the design, construction and commissioning of a set of specific measurement techniques and devices that have been developed for tracking the target conditions, the fast-evolving plasma properties and the quality of the resulting particle beams developed for diverse laser-driven particle acceleration (and ionizing radiation generation) experiments.

1.3.1 Gaseous underdense target inspection

The properties of the target (density, shape, thickness, composition and so on) are determining factors for the laser-matter interaction regime and therefore for the expected (if any) particle acceleration mechanisms sought. Actually, the classification of the laser-plasma interaction is normally made as a function of the transparency regime between the laser radiation and the matter, which is a function of the plasma density and photon wavelength [69]. The interaction of high power laser with transparent plasmas is achieved at low densities (known as underdense regime), normally obtained by means of gaseous targets. On the other hand, irradiation of solid or liquid targets (called overdense regime) lead to reflective (and partially absorbent) plasmas. Finally, a third case can be found in the frontier between the two aforementioned regimes, the near-critical plasmas.

In the first part of manuscript, the experimental effort carried out by the candidate for the characterization of the gaseous targets at the Centro de Láseres Pulsados (CLPU), Spain, is shown. Different measurement sets for gas jets with diverse geometries have been performed, determining their density profile, evolution and dependences with the operational parameters. An in-house built optical interferometry station was prepared for such task. Its working principle, main components and analysis routine are described, and the obtained results are benchmarked with analytical fluid models [70]. Furthermore, the successful implementation of these jets as underdense targets for interaction with the high-power laser VEGA at CLPU is presented. More specifically, an experiment on electron acceleration and optimization of betatron generation [60], and another campaign focused on high-harmonic generation in focal cone geometry are shown.

1.3.2 Diagnostics for near-critical plasma (NCP) regime

Study of the interaction of ultra-intense lasers with NCP has remained almost unexplored, mainly due to the difficulty of achieving the required densities in a controlled and repetitive manner in the laboratory. Such plasmas lie between the underdense (gas) and overdense (solid and liquid) regimes. In the recent years special interest has been shown in the interaction of high power lasers with this kind of plasmas due to their enhanced laser energy absorption [71] and its potential to trigger collisionless electrostatics shocks [72, 73]. According to simulations (validated by a few experimental demonstrations), these shocks are capable to accelerate monoenergetic ion beams from the bulk of the plasma up to considerable energies, being well adapted for applications. One of the proposed targetry methods to reach such densities is based on the use of high-pressure gaseous systems, attached to specially designed shock nozzles, which would lead to high-repetition-rate and debris-free operation [74].

In the second part of this manuscript, a research line (with the active participation of the candidate) centered on the interaction ultra-short (< 200 fs) ultra-intense (~ 1 PW) lasers with high density (near critical) gaseous targets is elaborated. A first experiment in the VEGA 2 laser facility (200 TW, 6 J, 30 fs, 10 Hz) for the preliminary study of this special plasma regime was accomplished [75]. This campaign was specially useful as commissioning of the novel target for the exposition to the extreme conditions in an experiment of this kind. A subsequent campaign at the VEGA 3 laser facility (1 PW, 30 J, 30 fs, 1 Hz) was successfully carried out for the extensive study of the interaction and characterization of the corresponding particle yield.

Particular attention is paid to the conceptual and technical progress elaborated by the Ph.D. candidate for supporting this research line. This includes several gas jet system characterization campaigns, including studies of the viability of the operation of the target in

realistic experimental conditions and parametric measurements of the gas density applying improved analysis methodology, as well as the construction of on-line diagnostics for shot-to-shot assessment of the laser induced damage on the nozzle and its effect on the target quality. In addition, the achievement of an ultra-fast interferometry diagnostic for NCP electronic density measurement is shown.

1.3.3 Spectrally-resolved ion source tomography and trace-space measurement

Laser-driven particle beams have been reported to show very interesting spatial and temporal features. Very short duration particle bunches [30, 31] and ultra-low transversal emittance values (i.e. high laminarity degree and linear correlation between emission coordinate and divergence angle) [29, 76] have been measured. Achievement of HRR controlled operation for these particle sources may lead to their efficient application in industry, medicine or energy research. Therefore, the development of instrumentation capable of measuring at high repetition rate the spatial quality indicators of the laser-driven beams is a significant task.

In the third part of this manuscript, a HRR-compatible novel measurement technique for laser-driven proton transversal trace-space (resolved in energy) is described. It is based on a mixed methodology between pepper-pot technique [77] and a magnetic spectrometer [65]. This innovative approach presents several technical and conceptual improvements with respect to previous trace-space measurement methods, including better resolution, single-shot measurement of the complete proton spectrum and lack of requirements of structuring the target, among others. In any case, the experimental commissioning of such a tool (by means of measuring the proton source resulting from the irradiation of thin metallic foils with the VEGA 3 laser) yields emittance results that agree with the previous results. Clear beam features are differentiated, obtaining distinct laminarity regimes for the lower and the higher energy part of the spectrum. Additionally, the use of the same tool as an angular-resolved Thomson Parabola (TP) spectrometer for tomographic analysis of the source (with ion-species differentiation capability) is proven.

Chapter 2

Introducción en castellano

Este capítulo introduce el campo de la interacción láser-materia y de los aceleradores basados en interacción láser-plasma, describiendo los retos a acometer y las aplicaciones propuestas. Los grupos de diagnósticos más relevantes de estos campos de investigación son también presentados y clasificados. Finalmente, el objetivo de la tesis es descrito.

2.1 Motivación general

La invención de la teconología laser en el 1960 por T. H. Maiman [1] dio pie al desarrollo de un nuevo y prometedor campo de investigación. Del estudio de la interacción de láser y materia han surgido aplicaciones muy interesantes en distintas áreas , incluyendo la conservación del patrimonio [2], la medicina [3] y la producción de energía, como en el caso de la Fusión por Confinamiento Inercial [4]. Por su parte, la invención en 1985 de la amplificación de pulsos gorgeados (CPA) por D. Strickland y G. Mourou [5] (premiados con el Nobel de Física en 2018) supuso un importante progreso, ya que resultó en el desarrollo de una nueva clase de láseres pulsados compactos, con energías moderadas (decenas de Julios) pero muy corta duración ($<$ 100 fs), siendo capaces de alcanzar potencias de petavatio e intensidades por encima de $10^{21}\,\mathrm{W/cm^2}$. Al interaccionar con la materia en condiciones específicas estos láseres puden acelerar eficientemente haces de paríclas (de iones [6] y electrones [7]) y generar radiación ionizante secundaria (como rayos X [8] y ultra-violeta extremo [9]), estableciendo así un nuevo tipo de aceleradores de partículas compactos.

La tecnología de los aceleradores de partículas basados en láser ha evolucionado rápidamente en las últimas dos décadas [10]. Los haces de radiación y partículas generadas por la interacción de pulsos láser intensos y plasmas alcanzan e incluso mejoran algunas de las características de los haces acelerados por la tecnología convencional. Gracias a la corta duración del proceso de aceleración láser (debido a la corta duración de los pulsos láser), a la creación de campos de aceleración abruptos y confinados y al desarollo de mecanismos de inyección de partículas, se ha logrado la producción de haces de muy alta calidad. La producción de haces de partículas con espacios de fase reducidos en la dirección longitudinal se traduce en haces de partículas ultra-cortos, mientras que en la dirección transversal indican un alto grado de laminaridad. Estas cualidades se pueden aprovechar para concentar la radiación generada en volúmenes focales muy pequeños (consiguiendo altos picos de corriente), lo cuál es fundamental para la mayoría de aplicaciones y campos de investigación propuestos. La Física de estado sólido [11], la cienca de materiales [12], la Física de plasmas [13], la energía de fusión [14] y el tratamiento del cáncer [15] son algunos de los ejemplos de campos donde potencialmente esta nueva generación de aceleradores podrían ser de utilidad.

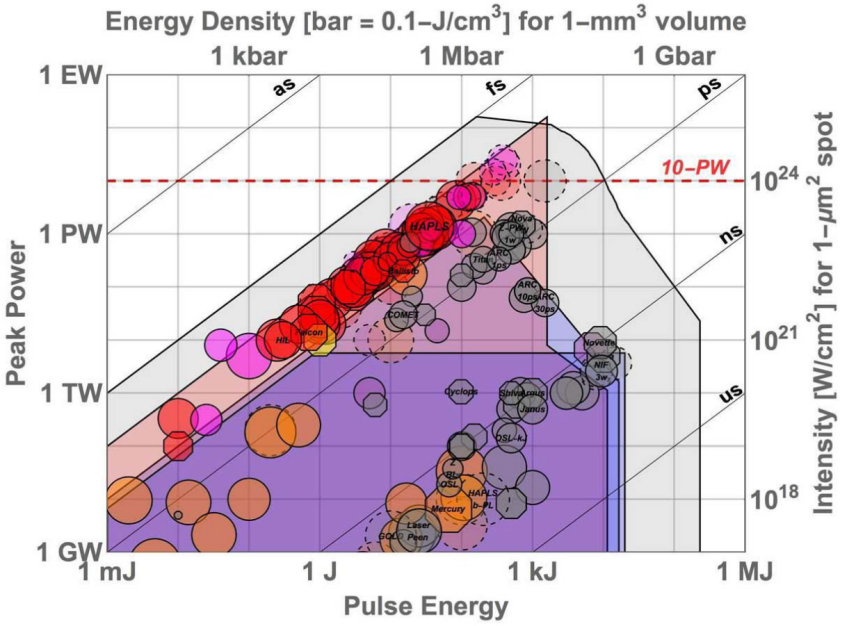

FIGURE 2.1: Estatus global de los láseres de alta potencia en 2019. Los sistemas en funcionamiento son representados por círculos con bordes contínuos mientras que los láseres en construcción por bordes punteados. Los sistemas desmantelados se representan con octágonos. El color indica el medio amplificador: Ti:Zafiro (rojo), Nd:vidrio (gris), Yb:X (naranja), Cr:X (amarillo), amplificación paramétrica (morado) o gas (rosa). Las líneas diagonales representan la duración del pulso. Imagen tomada de [16]

2.2 Interacción láser-plasma

El desarrollo de la tecnología de láseres intensos en las últimas décadas ha ofrecido la posibilidad de alcanzar altas intensidades de irradiación, desde $10^{19}\,\mathrm{W/cm^2}$ hasta $10^{22}\,\mathrm{W/cm^2}$. La interacción de la materia con tales intensidades ópticas (suficiente para ionizar el blanco y crear un plasma) han conducido a un nuevo campo de investigación, siendo muchas las instalaciones de láseres intensos repartidas por todo el mundo, como se resume en la figura 2.1. Los láseres intensos pueden ser divididos en tres principales grupos en función de la energía por pulso que pueden entregrar, así como por la duración temporal de dichos pulsos τ [17].

- **Láseres de pulsos largos ($\tau \sim$ ns)**
  Los láseres de alta potencia de duración de nanosegundos pueden generar pulsos de energía sobre el kilojulio, lo cual implica potencias pico alrededor de teravatio e intensidades de $10^{15}\,\mathrm{W/cm^2}$ al ser enfocados. Normalmente basados en la tecnología de Nd:vidrio, como es el caso del sistema NANO2000 en LULI (Francia) o de las salidas largas de PHELIX en GSI (Alemania) y VULCAN en RAL (Reino Unido), estos sistemas son excelentes herramientas para estudiar la Física de alta energía y densidad. La combinación de varias líneas laser de kJ en instalaciones dedicadas a la investigación de Energía de Fusión Inercial resultan en energías en el blanco de megajulio, como es el caso de NIF (EE.UU.) o LMJ (Francia), con operación limitada a un disparo al día.

- **Láseres de pulsos cortos ($\tau \sim$ ps)**
  Gracias a la aplicación de la tecnología CPA a los sistemas de Nd:vidrio, energías por pulso cercanas al kilojulio pueden ser conseguidas pero en duraciones entre 0.5 y 200

picosegundos, con tasas de repetición de un disparo por hora. Estos láseres alcanzan potencias pico máximas de petavatio e intensidades sobre 10^{21} W/cm^2 al ser enfocados. Como es el caso de los sistemas PICO2000 en LULI, TITAN en LNLL (EE.UU.) y las salidas cortas de PHELIX y VULCAN, estos versátiles sistemas son frecuentemente usados para aceleración de protones, astrofísica de laboratorio e investigación en Física de plasmas.

- **Láseres de pulsos ultra-cortos ($\tau \sim$ 100 fs)**
  Estos láseres generan pulsos de energía moderada (hasta cientos de julios) pero en duraciones de pulso muy cortas (hasta $\tau < 20$ femtosegundos), por lo tanto arrojando potencias pico por encima de petawatio e intensidades por encima de 10^{21} W/cm^2 [16]. Su diseño permite la operación a alta tasa de repetición ($>$ 1 disparo por segundo), como es el caso del láser pulsado de Ti:Zafiro o la nueva clase de láseres por amplifciación paramétrica combinados con la tecnología CPA. El tamaño reducido de estos sistemas implica un coste mucho menor en comparación con los sistemas de kilojulio. El láser VEGA en CLPU (España) o el sistema de 10 PW en ELI-NP (Rumanía) son ejemplos de estas fuentes láser ultra-cortas, los cuales son usados extensivamente en laboratorios de todo el mundo y están especialmente adaptados a la aceleración de electrones a velocidades relativistas, aunque también son utilizados para aceleración de protones. Versiones más pequeñas de estos sistemas (con energía de milijulio) son frecuentemente utilizados para ciertas aplicaciones, como pueden ser la investigación aplicada en Física Cuántica y el micromecanizado láser. En comparación con la interacción de nanosegundos, donde la Física puede ser descrita en térmionos de procesos adiabáticos e hidrodinámica, la interacción con láseres ultra-cortos ha de descartar los modelos estáticos en favor de formulaciones dinámicas fuera de equilibrio. El trabajo descrito en esta tesis se centra en experimentos y aplicaciones de esta clase de láseres.

2.2.1 Aceleradores de partículas basados en láser

Desde la creación de los aceleradores de partículas electrostáticos y electromagnéticos hace un siglo, su aplicacion para investigación aplicada y fundamental, así como para aplicaciones técnicas, industriales y médicas ha aumentado continuamente. Los sistemas capaces de acelerar a energías por encima de 1 GeV representan sólo el 1% del total y son construidos para investigación de Física de altas energías (Física de nuclear y de partículas), mientras que los aceleradores de menor capacidad se centran en ciencia de materiales, biología y medicina. En cualquier caso, los aceleradores convencionales son instalaciones grandes y costosas que además imponen restricciones radiológicas severas en zonas muy extensas, pero que son extensivamente utilizadas para aplicaciones como el tratamiento del cáncer, radio-farmacia (en la generación de radio-isótopos), implantación de iones, corte por electrones o radiografía, entre otros [19].

El principal límite operacional de estos aceleradores es el umbral de ruptura eléctrica, lo que limita los campos eléctricos de aceleración a 100 MV/m. Por lo tanto, para alcanzar altas energías ($>$ 100 GeV) se requiere de instalaciones kilómetricas. La reciente invención de la CPA, que supuso el desarrollo de los láseres cortos e intensos, ha permitido la ejecución del concepto de acelerador láser-plasma, propuesto por Tajima y Dawson [20]. Su propuesta fue utilizar la separación de cargas creada por un láser intenso en un plasma como estructura aceleradora; en este régimen el umbral de ruptura eléctrica no es una limitación y campos de TV/m pueden ser generados. Consecuentemente, la longitud de necesaria en los aceleradores láser-plasma para alcanzar las energías de los convencionales sería reducida varios órdenes de magnitud (llegando a valores alrededor de los milímetros). La

implementación de este esquema experimental para electrones [7, 19] e iones [21, 22] es actualmente una práctica comun en más de cien instalaciones de láseres intensos en todo el mundo [23]. Además, la generación de haces de radiación (rayos X y rayos gamma) [24, 25] comparables a las fuentes de sincrotrón y láseres de electrones libres (FEL) ha sido demostrada, como también la producción secundaria de neutrones [26] y positrones [27, 28].

El enorme esfuerzo en investigación de fuentes de partículas y radiación ionizante por láser ha conllevado la optimización de sus parámetros de emisión. En la actualidad, los aceleradores láser-plasma son equivalentes a los aceleradores convencionales en algunos aspectos, incluso llegando a superarlos en ciertas propiedades. A través de la interacción láser-plasma se ha demostrado la emisión de haces de extraodinaria laminaridad [29] y de menor duración [30, 31] (conllevando una alta corriente pico) en comparación con las fuentes convencionales. Además, los costes de los sistemas láseres compactos son mucho más económicos que las instalaciones de aceleradores, y las demandas de protección radiológicas son mas leves en los primeros ya que sólo el punto de interacción debe ser blindado. Sin embargo, los aceleradores láser-plasma no alcanzan los estándares de energía máxima realizable, de repetitividad de parámetros del haz y de flujo medio de partículas de los aceleradores electrostáticos. Esta última característica es especialmente relevante para aplicaciones médicas e industriales, que suelen requerir un flujo considerable para su operación eficiente. Este problema podría ser solucionado en los aceleradores láser a través de un incremento en la tasa de repetición. Por lo tanto, sistemas láser, blancos y herramientas de medida capaces de operar a alta tasa de repetición son de especial interés.

Una serie de experimentos se han llevado a cabo para la prueba de concepto de la utilización de los haces generado por interacción láser-plasma en las ya conocidas aplicaciones de los aceleradores convencionales, además de en nuevos esquemas que pueden aprovechas la alta calidad transversal y corta duración de los nuevos haces [10].

- **Haces de iones y protones**
  Desde la demostración de colimación y monocromatización de haces de iones de energía de varios MeV acelerados por láser [32, 33] (especialmente favorecida por la alta laminaridad de los haces [29] y el pequeño tamaño de la fuente [34]), su potencial uso en aplicaciones ha sido propuesto (y experimentalmente demostrado) como en radiografía de protones de fenómenos rápidos [35–37], calentamiento isocórico de plasmas [13], ignición rápida en reacciones de fusión nuclear por confinamiento inercial [14], ciencia de materiales [12, 38, 39], conservación de patrimonio [40] y propósitos médicos (principalmente tratamiento del cáncer) [15, 41, 42].

- **Haces de electrones**
  En experimentos de interacción laser-plasma se han llegado a medir haces de electrones de nivel de energía de GeV [43] con características muy interesantes, como baja divergencia, estabilidad y controlabilidad, de espectro mono-energéticos ($\Delta E/E < 10\%$) y de duración de femtosegundo, en algunos casos incluso a tasas de repetición de kHz [44]. Gracias a su corta duración, estos haces de electrones son ideales para el sondeo ultra-rápido de campos transitorios [45, 46], estudio de Física del estado sólido [11] o incluso tratamiento de cáncer [47]. Además son candidatos ideales para esquemas de aceleración por etapas, los cuales proponen alcanzar energías de TeV [48], suficiente para salvar el umbral requerido para la investigación en Física de partículas. Estas fuentes también han demostrado ser excelentes semillas para FELs, los cuales emiten radiación coherente en el rango de los rayos X blandos [49].

- **Rayos X y rayos gamma**
  Muchos métodos han sido propuestos para generar haces de rayos X de baja divergencia a través de los electrones acelerados por láser, como por ejemplo la llamada

radiación de Betatrón que aparece en el propio proceso de aceleración [24, 50]. Dichas fuentes se caracterizan por estar generadas en una fuente virtual de pequeño tamaño (varios micrómetros) lo cual hace a esta radiación coherente espacialmente, y además presentan una duración temporal del orden del femtosegundo. Dichas condiciones, similares a la radiación de un sincrotrón o un FEL, hace que estas fuentes sean ideales para el sondeo de materia con precisión temporal [51], la inspección no invasiva de muestras biológicas o de materia condensada con técnicas avanzadas, como el contraste de fase [52, 53], la espectroscopía por absorción de rayos X o la difracción de rayos X y la producción de reacciones foto-nucleares [50].

- **Ultra-violeta extremo (EUV) y rayos X blandos (SXR) en generación de altos armónicos (HHG)**
  La interacción de láseres ultra-cortos con gases o sólidos en condiciones determinadas puede desencadenar la generación de radiación EUV coherente de banda ancha, en un proceso conocido como genación de altos armónicos. Mediante este proceso se ha demostrado la emisión en el rango de 282-533 eV [9], conocido como la *ventana del agua*, rango en el cual el agua es transparente a la radiación pero el carbono es absorbente, siendo así un candidato ideal para imagen de muestras biológicas. En circusntancias específicas, esta radiación coherente se puede generar en duraciones de attosegundo [54], ideales para estudio experimental de dinámica de electrones, cuya escala de tiempo es de este modo accesible [55].

Merece la pena mencionar que, además de la corta duración de los haces de partículas y fotones generados por láser, éstos tienen la ventaja de estar intrísicamente sincronizados (con precisión de femtosegundo) con el láser que los genera. Esto es de especial utilidad en experimentos tipo bombeo-sonda, donde la bombeo (cuyo rol puede ser llevado a cabo por el láser o por el haz secundario) es usado para desencadenar la reacción a estudiar, mientras que el otro se utiliza para medir las propiedades de la reacción. En cualquier caso, gracias a la corta duración del haz sonda, se puede tomar una *foto* de proceso con buena precisión (de attosegundo a picosegundo, dependiendo de la dinámica del proceso), permitiendo de este modo resolución temporal de fenómenos rápidos, como procesos atómicos [56], reacciones químicas [57], procesos de cristalización o cambio de fase [58] o evolución rapida de campos y plasmas [36, 59].

Además, las fuentes láser intensas tienen la ventaja de ser enormemente versátiles. Modificando las condiciones de la interaccón, el mismo sistema láser puede acelerar distintas especies de partículas a través de una gran variedad de mecanismos, como electrones de GeV y protones de MeV [60]. Por otra parte, haces de varios tipos de partículas (electrones, iones, fotones de alta energía) pueden ser generados simultaneamente, lo cual se ha demostrado útil para ciertas aplicaciones [39].

2.2.2 Diagnósticos

Los diagósticos son indispensables para la comprensión de los experimentos láser-plasma y por lo tanto para la operación adecuada de cualquier acelerador láser-plasma [61]. Las propiedades de los haces generados dependen enormemente de los parámetros del pulso láser, asi como de las estructuras de plasma, las cuáles evolucionan rápidamente y presentan gradientes espaciales muy cortos, abarcando en ocasiones diversos regímenes de interacción en un sólo evento. Estos experimentos resultan en la generación de campos eléctricos y magnéticos de valores máximos sin precedentes (en laboratorios) localizados en escalas espaciales ($\sim$ µm) y temporales ($\sim$ fs) minúsculas, acelerando haces de partículas complejos en un entorno experimental de condiciones extremas. Por estas razones, una nueva generación de técnicas experimentales (o una mejora de las ya existentes) capaces

de resolver estas finas características en las condiciones requeridas ha sido elaborada. Los diagnósticos pueden ser divididos de la siguente forma.

- **Metrología de fuentes primarias**
  Las medidas de los parámetros del pulso láser, como su duración temporal, fase, energía, contraste, frente de onda y punto focal (y su estabilidad) son cruciales para la interacción y su control debe ser garantizado por cualquier instalación de láseres intensos. Se pueden destacar las técnicas de media especiales que fueron elaboradas para la medida de la duración de pulsos ultra-cortos [62].

- **Diagnósticos de plasmas**
  Una amplia variedad de técnicas experimentales ha sido desarollada para investigar el estado del plasma desde la observación indirecta de los procesos físicos en el mismo y sus efectos. Estos diganósticos pueden ser divididos en función de la propiedad del plasma medida [63], como por ejemplo su campo magnético, su índice de refracción y la emisión de partículas o radiación electromagnética, entre otras. Muchas estrategias experimentales han sido concebidas para medir dichas propiedades en experimentos de interacción láser-plasma, incluyendo medidas de poder de parada de partículas [59], sondeo con radiación óptica, espectroscopía de óptica o de rayos X [61] y deflecometría de partículas [36, 64]. Algunas de estas técnicas son derivadas de la comunidad de láseres de pulsos largos, en muchos casos adaptadas a los cortos tiempos característicos de la intercción con láseres de femtosegundo. El estudio de las propiedades fundamentales del plasma (densidad, magnetización, temperatura...) es fundamental en la gran parte de experimentos de plasmas (como por ejemplo en fusión por confinamiento inercial) pero también son requeridos para la adecuada comprensión de los mecanismos de un acelerador basado en interacción láser-plasma. El control de los parámetros del plasma ha conllevado del desarrollo de aceleradores láser-plasma ajustables.

- **Diagnósticos de fuentes secundarias**
  La descripción de los haces de partículas y radiación ionizante es la información esencial necesaria para aplicaciones de los haces generados en experimentos láser-plasma. Muchas técnicas han sido recuperadas de la comunidad científica de aceleradores de partículas (y adaptadas para las especificaciones de los haces por láser) para obtener la carga, composición, divergencia, espectro, emitancia y dosis [61, 65]. Merece la pena mencionar que muchos de los diagnósticos de aceleradores convencionales no están adaptados para los haces generados por láser [61], principalmente debido a la corta duración de los haces (por lo tanto, su alta corriente pico), su extenso ancho de banda, la diversidad de tipos de partículas y su mayor calidad transversal, requiriendo por lo tanto diagnósticos más rapidos, precisos y versátiles.

- **Diagnósticos de blancos**
  La caracterización *off-line* de los blancos de los experimentos (previamente a la propia interacción) es una tarea recomendada, la cual es posible con la ayuda de ciertas técnicas, como la interferometría de gas neutro. Las medidas de blancos han demostrado que son de gran utilidad ya que pueden dar indicios de las condiciones del plasma durante la irradiación láser [66, 67]. Además, se puede sacar provecho de tales mediciones para la alineación de los blancos con respecto al láser.

La aceleración de partículas basada en láser se ha convertido en un prometedor campo de investigación, especialmente por las aplicaciones previstas en la socidedad. Sin embargo, muchos retos deben ser todavía abordados antes de su empleo público. Fuentes repetitivas

y ajustables con sufience flujo medio de partículas son requeridas para la mayoría de aplicaciones. Sin embargo, la limitación en flujo podría ser resuelta gracias a la operación a alta tasa de repetición. El desarrollo tecnológico de los láseres intensos ha hecho aumentar progresivamente la tasa de repetición de los mismos [16], mientras que típicamente los blancos y diagnósticos no son compatibles con dichas tasas. Laboratorios de todo el mundo están dedicando un gran esfuerzo para reducir dichas limitaciones, tanto en blancos [68] como en diagnósticos [61, 65].

2.3 Objetivo de la tesis

El trabajo mostrado en esta tesis está centrado dar en soluciones a la necesidad de diagnósticos de alta tasa de repetición en el campo de la aceleración de partículas láser-plasma, con suficiente precisión y sensibilidad para resolver las características de blancos, plasmas y haces en distintos regímenes de interacción. El objetivo de la tesis es presentar el diseño, construcción y puesta a punto de una serie de ténicas de medida específicas que han sido desarrolladas para registrar las condiciones de los blancos experimentales, las propiedades cambiantes de los plasmas y la calidad de los haces de partículas resultantes en diversos experimentos de aceleración de partículas (y de generación de radiación ionizante) láser-plasma.

2.3.1 Caracterizacióin de blancos gaseosos sub-densos

Las propiedades de los blancos en los experimentos láser-materia (densidad, forma, espesor, composición, etc) son factores determinantes para el régimen de interacción y por lo tanto para el mecanismo de aceleración buscado (si lo hubiese). De hecho la clasificación de la interacción láser-plasma se hace normalmente en función del régimen de transparencia entre la radiación del láser y la materia, el cual es a su vez función de la densidad del plasma y la longitud de onda del láser [69]. La interacción de láseres de alta potencia con plasmas transparentes es conseguida a bajas densidades de plasmas (conocido como el régimen sub-denso), normalmente obtenidas a través de blancos de gas. Por otra parte, la irradiación láser de sólidos o líquidos (conocido como régimen sobre-denso) produce plasmas reflectantes y parcialmente absorbentes. Finalmente, un tercer caso se encuentra en la frontera entre estos dos regímenes, la conocida como densidad crítica.

En la primera parte de la tesis, se muestra el esfuerzo experimental llevado a cabo por el candidato para la caracterización de blancos gaseosos en el Centro de Láseres Pulsados (CLPU), España. Distintos sets de medidas se han realizado con jets de gas de diferentes geometrías, determinando su perfil de densidad, evolución y dependencia con parámetros operacionales. Una estación de interferometría óptica fue preparada para dicha tarea. Su principio de funcionamiento, componentes principales y algoritmos de análisis son descritos, y los resultados obtenidos son comparados con modelos analíticos de fluidos [70]. Por otra parte, se presenta la implementación exitosa de dichos jets de gas como blancos sub-densos para interacción con el láser de alta potencia VEGA en CLPU. Específicamente, se muestra un experimento de aceleración de electrones y optimización de radiación de Betatron [60], y otra campaña experimental centrada en la generación de altos armónicos en geometría de cono focal.

2.3.2 Diagnósticos para plasmas de densidad crítica

El estudio de la interacción de láseres ultra-intensos con plasmas de densidad crítica ha permanecido prácticamente inexplorado, debido en gran parte a la dificultad de conseguir

las densidades requeridas de manera controlada y repetitiva en el laboratorio. Dichos plasmas sitúan su densidad entre los sub-densos (gas) y sobre-densos (sólidos y líquidos). En los últimos años se ha mostrado especial interés en la interacción de láseres intensos con este tipo de plasmas debido a su mejorada absorción de la energía del láser [71] y su pontencial capacidad para desencadenar ondas de choque electrostáticas sin colisiones [72, 73]. De acuerdo con simulaciones (validadas por escasas demostraciones experimentales), estas ondas de choque podrían acelerar haces de iones monoenergéticos del interior del plasma a energías considerables, siendo perfectos para aplicaciones. Uno de los métodos propuestos para alcanzar las densidades requeridas está basado en el uso de sistemas de gas de muy alta presión, ligados a orificios de salida especialmente diseñados conocidos como toberas de *choque*. Dicha combinación podría dar lugar a la operación de un blanco de densidad crítica a alta tasa de repetición y libre de residuos [74].

En la segunda parte de la tesis, se presenta una línea de investigación (en la que el candidato ha participado activamente) centrada en la interacción de pulsos láser ultracortos (< 200 fs) y de alta potencia ($\sim$ 1 PW) con blancos gaseosos de alta densidad. Un primer experimento en el láser VEGA 2 en CLPU (200 TW, 6 J, 30 fs, 10 Hz) fue realizado para el estudio preliminar del régimen especial de plasma [75]. Esta campaña fue especialmente útil para la puesta a punto del novedoso blanco gaseoso en la exposición a las condiciones extremas de un experimento de este tipo. Una segunda campaña en el láser VEGA 3 en CLPU (1 PW, 30 J, 30 fs, 1 Hz) fue llevado a cabo exitosamente para el estudio detallado de la interacción y la caracterización de la producción de partículas correspondiente.

Se ha prestado especial atención al progreso técnico y conceptual elaborado por el candidato para apoyar esta línea de investigación. Ésto incluye campañas de caracterización del sistema de gas, estudios de la viabilidad de operación del blanco en condiciones experimentales, medidas paramétricas de la densidad del blanco aplicando una metodología de análisis mejorada y la construcción de diagnósticos *tiro a tiro* para la evaluación del daño inducido por en láser en la tobera del sistema de gas y el correspondiente efecto en la calidad del blanco. Además, se muestra la realización de un diagnóstico de interferometría ultra-rápida para medida de densidad de electrones del plasma de densidad crítica a través de un haz sonda ultra-corto.

2.3.3 Tomografía de haz de iones resuelta en energía y medida de espacio de fases

Los haces de partículas acelerados por láser han demostrado experimentalmente tener características espaciales y temporales muy interesantes. Se han medido duraciones temporales de dichos haces excepcionalmente cortas [30, 31] y valores de emitancia transversal muy bajos (lo que significa alta laminaridad y correlación linear entre la coordenada y el ángulo de emisión) [29, 76]. El desarrollo de estas fuentes controladas a alta tasa de repetición puede traer la aplicación práctica de las mismas en industria, medicina o investigación energética. El desarrollo de instrumentación capaz de medir los indicadores de calidad espacial de los haces acelerados por láser a alta tasa de repetición es, por lo tanto, una tarea significativa.

En la tercera parte de la tesis, se describe una novedosa técnica desarrollada para la de medida a alta tasa de repetición del espacio de fases transversal, resuelto en energía, de un haz de protones generado por láser. Se basa en una metodología que combina la técnica de *pepper-pot* [77] y un espectrómetro magnético [65]. Este innovador enfoque presenta varias mejoras técnicas y conceptuales con respecto a los métodos anteriores de medida de espacio de fases de protones acelerados por láser, incluyendo mayor resolución, capacidad de medida en un solo disparo de todo el espectro y el no requerimiento de estructurar el blanco, entre otras. En cualquier caso, la puesta a punto experimental de esta herramienta (a través

de la medida de la fuente de protones resultante de la irradiación de láminas metálicas finas con el láser VEGA 3) arroja valores de emitancia que concuerdan con resultados previos. Se han podido diferenciar características específicas del haz, obteniendo distintos regímenes de laminaridad de los protones para las partes más y menos energéticas del espectro. Por otra parte, se ha probado el uso del mismo aparato como un espectrómetro tipo *Thomson Parabola* resuelto en ángulo, para el análisis tomográfico de una fuente iones generada en interacción láser-plamsa, con la capacidad adicional de diferenciación entre distintas especies de iones.

Chapter 3

Theoretical background

In this chapter, the basic theoretical aspects about laser-driven particle acceleration are presented. First, laser physics, with special emphasis on pulsed beams is outlined. Secondly, laser-matter interaction physics is presented, classified in different regimes in terms of increasing laser intensity: interaction with cold matter is shown, followed by ionization processes explanation, study of relativistic interaction of lasers with a single electron and plasma basics. Finally, several laser-based particle acceleration mechanisms are detailed.

3.1 Properties of a laser beam

Laser is an acronym which stands for "Light Amplification by Stimulated Emission of Radiation". It is a particular type of electro-magnetic (EM) radiation which is normally defined by three fundamental properties, which are, at some extent, spatial and temporal coherence, monocromaticity and directionality. Its operation is based on the capability of an active medium to undergo stimulated transitions, where the propagation of radiation results in an amplification of the energy density of such radiation, with similar wavelength, phase and direction. A possible classification of the laser source can be arranged depending on the composition of its active medium: gas, solid-state, semiconductor, dye, optic fiber, free electrons and more. In order to achieve the energy gain, population inversion should be reached in the active medium. For such purpose, a pump system should be implemented on the active medium, which could be optical, electrical or chemical depending on the laser type. Normally the radiation is stored by a resonating cavity (laser oscillator), where the light interacts and feedbacks with the active medium. Resonators are typically described as pair of reflecting mirrors, one total and other partial, between which the active medium is located. The leak of the partial mirror represents the accessible laser radiation [78–82]. The components of a typical laser resonator are shown in figure 3.1.

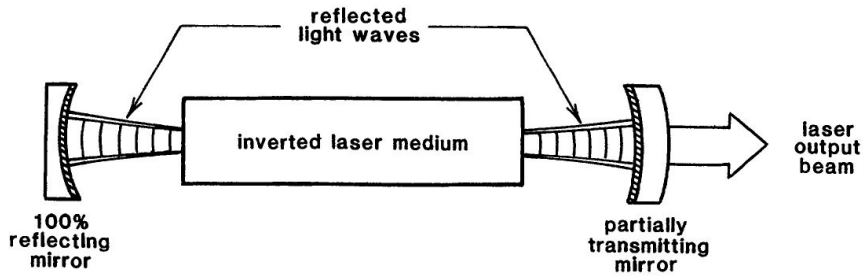

FIGURE 3.1: Sketch of a laser oscillator and its fundamental components, taken from [79].

As long as the population inversion is such that the energy gain is bigger than the losses in a photon round-trip in the cavity, coherent amplification will be achieved, emitting photons with the similar frequencies, direction and phase as the seed radiation.

Classical electrodynamics state that the radiation should obey the Maxwell's equations [78–82]. In vacuum they are given as

$$\nabla \times \mathbf{B} = \mu_0 \left(\mathbf{J} + \epsilon_0 \frac{\partial \mathbf{E}}{\partial t} \right), \tag{3.1}$$

$$\nabla \times \mathbf{E} = -\frac{\partial \mathbf{B}}{\partial t}, \tag{3.2}$$

$$\nabla \cdot \mathbf{E} = \frac{\rho}{\epsilon_0}, \tag{3.3}$$

$$\nabla \cdot \mathbf{B} = 0, \tag{3.4}$$

where $\mathbf{E}$ and $\mathbf{B}$ are the radiation electric and magnetic field respectively and ϵ_0 and μ_0 are the vacuum permittivity and permeability, which define the speed of light in vacuum as $c = 1/\sqrt{\epsilon_0 \mu_0}$. In a source-free medium, electrical charge and current are zero ($\rho = J = 0$). The solutions of these equations in terms of the fields are known as electromagnetic (EM) waves. We can express a coherent EM wave approximately as a plane wave propagating in free space, in terms of the modulus of its electric field (after solving the Maxwell's equations in vacuum) as

$$E(z,t) = E_0 e^{i(\omega t - kz)}, \tag{3.5}$$

where E is the electric field at time t and location (in the direction of propagation) z, E_0 the field amplitude, $\omega = 2\pi\nu$ the angular frequency, ν the wave frequency, $k = 2\pi/\lambda$ the wave vector and λ the wavelength. The term inside the exponential is known as the phase and it contains the information about the periodic behaviour of the wave function. The wavefront is the set of points in space-time with the same phase, which in case of a plane wave as 3.5 are planes with same z coordinate. The magnetic field amplitude will be $B_0 = E_0/c$ and it will oscillate in a plane perpendicular to the electric field but with the same phase. When solving the Maxwell's equation for a wave as 3.5, we find the dispersion relation relates frequency and wave vector through the speed of the wave as

$$\omega = ck. \tag{3.6}$$

Before presenting intense lasers, it is useful to define energy-related quantities (which actually are experimentally measurable) in this approximation, such as the energy density u is given by

$$u(z,t) = \epsilon_0 |E(z,t)|^2 = \epsilon_0 E_0^2 \cos^2(\omega t - kz), \tag{3.7}$$

meanwhile the energy density averaged over a temporal period $T = 2\pi/\omega$ is

$$\langle u \rangle = \frac{1}{2} \epsilon_0 E_0^2. \tag{3.8}$$

The time-averaged power of the laser and the intensity are given respectively by

$$P = \frac{1}{2} c \epsilon_0 E_0^2 s, \tag{3.9}$$

$$I = \frac{P}{s} = \frac{1}{2} c \epsilon_0 E_0^2, \tag{3.10}$$

where s is the beam cross-section.

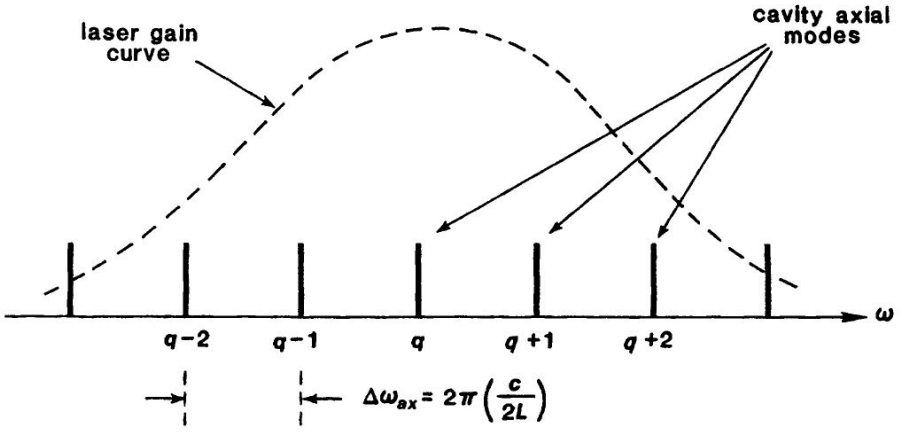

FIGURE 3.2: Longitudinal modes under a Fabry-Perot gain curve for a typical laser oscillator, taken from [79].

The geometry of the cavity defines the longitudinal modes (the frequencies) that will be favoured and therefore amplified, taking into account that a only certain band of frequencies can be emitted for an specific active medium. For the simplified case of a Fabry-Perot resonator (two perfectly plane parallel mirrors), the condition of resonance for the longitudinal modes forces the system to oscillate at frequencies so that the round-trip path length must be an integer of the number of wavelengths at the laser frequency [79], or

$$\frac{2\omega L}{c} = q2\pi, \tag{3.11}$$

$$\omega = q2\pi\left(\frac{c}{2L}\right), \tag{3.12}$$

where q is an integer and L is the cavity length. Moreover, the properties of the active medium (i.e. the energetic levels available for population inversion) will define the gain curve and therefore which frequencies are prone to amplification. Refer to the figure 3.2 for a pictorial sketch of the longitudinal modes and the active medium gain curve.

3.1.1 Gaussian beams

The structure of the system (the geometry of the cavity and the active medium) defines as well the spatial (transversal) properties of the laser beam. The most common (and simpler to formulate) is the Gaussian mode. Also known as TEM_{00} (transverse electro-magnetic wave), it is a solution for the Maxwell's equations which fits in resonators of spherical mirrors, in which the electric and magnetic field polarizations of the electromagnetic wave are perpendicular to each other (inside the $x-y$ plane the selected reference frame for the description) and perpendicular to the the wave propagation direction (z) [80]. Under the paraxial approximation, which is close to reality in most of the practical cases where beams are collimated enough (i.e. the wave evolves slowly in the longitudinal direction $\partial^2 E/\partial z^2 \approx 0$) the solution for electric field is given as [79]

$$E(x,y,z,t) = E_0 \frac{w_0}{w(z)} e^{i(\omega t - kz + \phi_{Gouy}(z))} e^{ik\frac{r^2}{2R(z)}} e^{-\frac{r^2}{w^2(z)}};\ r = \sqrt{x^2+y^2}. \tag{3.13}$$

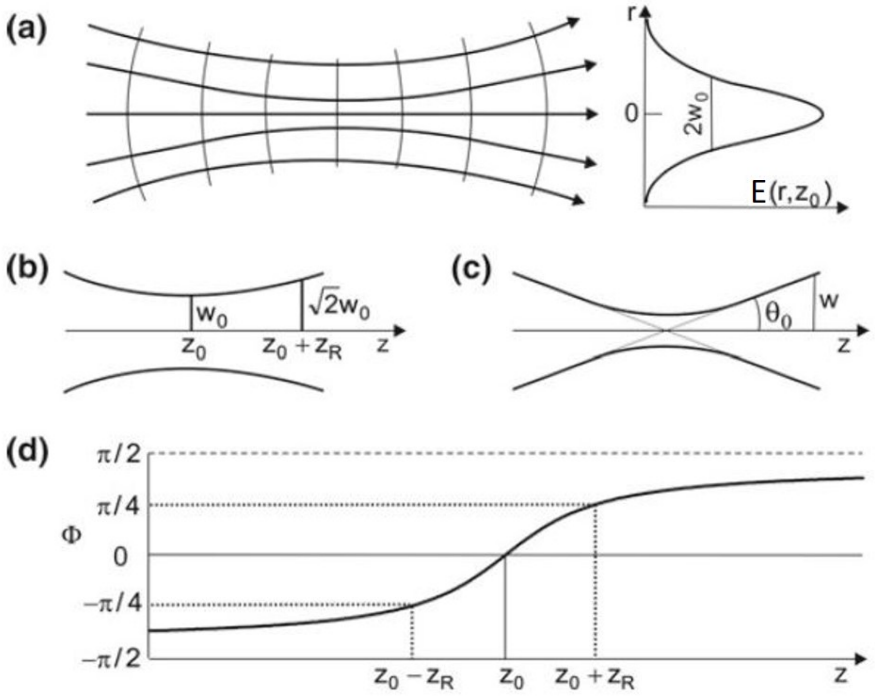

FIGURE 3.3: Gaussian beam characteristics, adapted from [80]. **a**) Propagation direction with wavefront representation and lateral distribution of the field amplitude. **b**) Rayleigh length and waist description. **c**) Divergence. **d**) Gouy phase.

$R(z)$ is the curvature radius of the wavefront, given by

$$R(z) = z - z_0 + \frac{z_R^2}{z - z_0}, \tag{3.14}$$

and $w(z)$ is the transversal radius of the Gaussian profile, defined as the radius at $1/e$ over the electric field value on the beam axis, where it is maximum:

$$w(z) = w_0\sqrt{1 + \frac{(z - z_0)^2}{z_R^2}} = w_0\sqrt{1 + \left(\frac{\lambda(z - z0)}{\pi w_0^2}\right)^2} \tag{3.15}$$

where w_0 is the minimum beam waist radius (see figure 3.3 b) for graphical representation). From 3.15 we see that TEM_{00} has its minimum radius at the waist $\omega(z_0) = \omega_0$, usually referred to as the focal spot.

The Rayleigh length z_R shows the range in which the radius of the beam increase by a factor $\sqrt{2}$. This is considered to be the near-field (or Fresnel) zone.

$$z_R = \frac{kw_0^2}{2} = \frac{\pi w_0^2}{\lambda}. \tag{3.16}$$

Summarizing, for any z the transversal shape of the field amplitude is a cylindrical-symmetric two-dimensional gaussian function, as shown in figure 3.3 a). The beam is convergent up to $z = z_0$, where the beam show a "waist" (the transversal size of the beam is minimum) and the curvature of the wavefront is perfectly plane. For $z > z_0$, the beam diverges. Both $R(z)$ and $w(z)$ increase linearly with $|z - z_0|$ far away from the waist ($|z - z_0| \gg z_R$, far-field (or Fraunhofer) range). In addition, we can define the angle of divergence (see

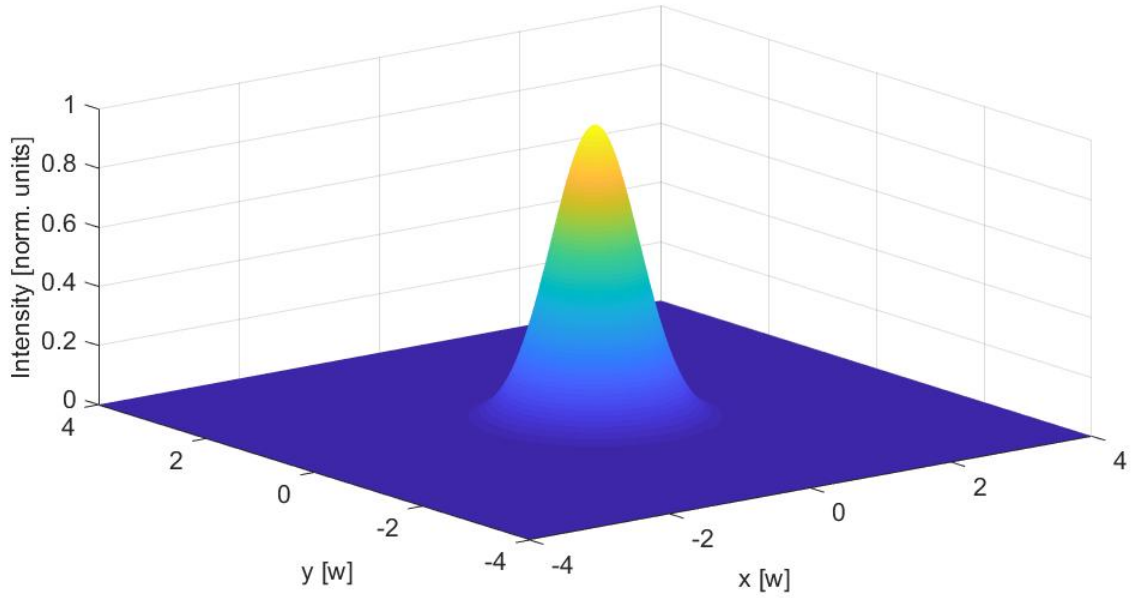

FIGURE 3.4: Normalized gaussian beam intensity.

figure 3.3 c)), only valid at this range, as

$$\theta_0 = \frac{w_0}{z_R} = \frac{\lambda}{\pi w_0}, \tag{3.17}$$

or written differently

$$\theta_0 w_0 = \frac{\lambda}{\pi} = \text{BPP} = \text{constant}. \tag{3.18}$$

The so-called beam product parameter (BPP) [83, 84] shows that the product of the waist and divergence is constant. This is a very important statement for laser-matter interaction physics, as it shows that the faster a beam is focused (i.e. larger θ_0), the smaller will be its minimum diameter.

The term $\phi_{Gouy}(z)$ is the Gouy phase and it is related to a small change in the phase of the beam passing through focus. It is shown in figure 3.3 d), and given by

$$\phi_{Gouy}(z) = \tan^{-1}\left(\frac{z - z_0}{z_R}\right). \tag{3.19}$$

Similarly as in the case of the plane wave, it is useful to define the expressions for the energy density, power and intensity as a function of the beam parameters, as those will be the measurable quantities by experimental detectors. The derived energy density averaged over a oscillation period can be expressed as

$$u(r,z) = \epsilon_0 |E(z,t)|^2 = \frac{1}{2}\epsilon_0 E_0^2 \frac{w_0}{w(z)} e^{-\frac{2r^2}{w^2(z)}}. \tag{3.20}$$

The total power of the laser will be the integral of area

$$P = \int\int u\, ds, \tag{3.21}$$

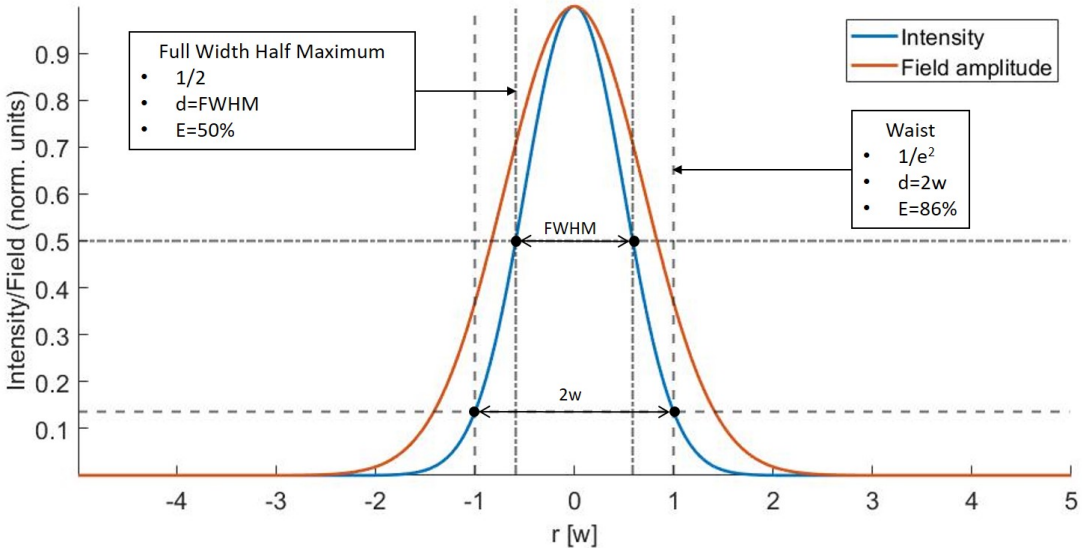

FIGURE 3.5: Gaussian beam field amplitude and intensity profiles. Widths definitions for $1/e^2$ and FWHM.

where ds integrates over the cross-sectional area. The radial intensity variation of the gaussian beam will vary as a gaussian, following

$$I(r,z) = \frac{2P}{\pi w^2(z)} e^{-\frac{2r^2}{w^2(z)}}. \tag{3.22}$$

An amplitude-normalized two-dimensional squared gaussian is shown in figure 3.4 as representation of the intensity of a gaussian beam at any z

As it is clear after 3.22, the intensity scales as the square of the electric field. Therefore, $w(z)$ refers to the radius where the intensity is $1/e^2$ the value on the beam center, as shown in the one-dimensional representation of figure 3.5. A circle of diameter $2w$ centred on the beam contains 86% of a perfect TEM_{00} beam. On the other hand, other standard diameter definition is the Full Width at Half Maximum (FWHM), given by

$$\text{FWHM}(z) = \sqrt{2\ln 2}\, w(z). \tag{3.23}$$

This width express the diameter of the beam where the intensity falls to $1/2$ the value on the axis. The FWHM contains 50% of the laser energy of a perfect Gaussian beam.

3.1.2 Realistic beams

Realistic laser cavities generate certain transverse field patterns in the beam as it propagates and gets amplified in the resonator. The cavity presents transversal dependent diffraction losses, the active medium could be inhomogeneously pumped, the reflectivity profiles of the cavity mirrors are not perfect, and there could be several other items that the laser goes through in the cavity round trip, such as lenses, apertures and the active medium itself, that may be imperfect. These self-reproducible transverse patters are called high order modes (TEM_{ml} with $m, l > 0$) and normally naturally decreased in intensity compared to the perfect Gaussian beam as they propagate since their lateral spread and diffraction is larger than the TEM_{00} mode [80]. They are expressed by the Hermite or Laguerre polynomials depending on their symmetry (rectangular or circular respectively). The resulting emitted beam is composed by a weighted superposition of the different modes supported by the cavity.

M^2 is the parameter which defines the quality of the beam, related to its spatial properties. $M^2 = 1$ implies a perfect Gaussian beam. The larger M^2, the more the beam differs from the TEM_{00} mode. This factor is critical as it gives the relation between waist diameter and divergence for a realistic beam, i.e. this parameter shows how tightly a laser beam can be focused:

$$M^2 = \frac{w_{0,real}\theta_{real}}{w_0\theta}. \tag{3.24}$$

From 3.24, 3.16 and 3.15 we can infer that, for a realistic beam [85, 86]

$$z_{R,real} = \frac{\pi w_0^2}{M^2\lambda} = \frac{z_R}{M^2}\,,\; w_{real}(z) = w_0\sqrt{1+\left(M^2\frac{\lambda(z-z_0)}{\pi w_0^2}\right)^2}. \tag{3.25}$$

Following the propagations rules given for a Gaussian beam, we can deduce how tightly the beam can be focused by some optical element; for instance, by a transmission optic as a lens, or by a reflective one as a parabolic mirror. Any focalizing element is characterized by its focal length f, which is defined as the distance between the optic and the point where an originally collimated beam is made to converge (i.e. focal spot). For the far-field range ($|z - z_0| \gg z_R$, setting from now on $z_0 = 0$ for simplicity) we know that

$$w(z) \approx \frac{w_0(z-z_0)}{z_R} = \frac{\lambda(z-z_0)}{\pi w_0}. \tag{3.26}$$

It is possible to apply this relation to the converging beam geometry; we set the waist (or focus) to be at $z_0 = 0$, then the lens is place at $z = -f$, where the beam diameter is $D = 2w(f)$, yielding a beam diameter at focus as

$$d = 2w_0 = \frac{4f\lambda}{\pi D}. \tag{3.27}$$

A useful dimensionless parameter of the focusing optic is the *f-number*, defined by

$$f^{\#} \equiv \frac{f}{D}, \tag{3.28}$$

so then

$$d = \frac{4\lambda f^{\#}}{\pi}. \tag{3.29}$$

The smaller $f^{\#}$, the more pronounced the focalization and the smaller the focal spot. Other important magnitude is the depth of focus, which is the length in which the beam shows a diameter close to the minimum, and it is defined as

$$2z_R \approx \frac{8\lambda f^2}{\pi D^2} = \frac{8\lambda f^{\#2}}{\pi}. \tag{3.30}$$

From 3.30 we read that shorter focal length systems creates shorter depth of focus. Nevertheless, 3.27 and 3.30 should be corrected when dealing with realistic beams with $M^2 > 1$ as

$$d_{real} = dM^2 = \frac{4M^2 f\lambda}{\pi D} = \frac{4M^2\lambda f^{\#}}{\pi}, \tag{3.31}$$

$$2z_{R,real} = 2\frac{z_R}{M^2}. \tag{3.32}$$

3.1.3 Pulsed lasers

It is possible to classify the lasers depending on their temporal operation [80].

- Continuous Wave (CW) lasers. A stable pumping system keeps the laser oscillation. The output is an uninterrupted EM wave, homogeneous in time-scale larger than the fields oscillations.
- Pulsed lasers. The output is not continuous, but pulsed. They can be arranged in terms of their working principle.
  - Gain switching lasers. The output is pulsed because the pumping system itself is pulsed. The duration of the pulses can be as short as microseconds.
  - Q-switching lasers. By controlling the cavity efficiency, it is possible to pump the active medium until full population inversion is achieved. Then, the cavity is switched to high efficiency (small losses), contributing to the oscillation and amplification of a single laser pulse. Its duration is on the the order of nanoseconds.
  - Mode-locking lasers. This method relies on the use of a broadband gain active medium, which can support amplification of several longitudinal modes of the laser cavity. Mode-locking techniques (active or passive) force all these modes to oscillate in phase (coherently). The result is a train of pulses, with a temporal distance between pulses (the inverse of the repetition rate of the laser) equal to the round-trip transit time. As the resulting wave-packets are coherent addition of different modes and its intensity scales as the square number of longitudinal modes. On the other hand, it important to mention that the field $E(t)$ of an EM wave is the Fourier Transform (FT) of its frequency spectrum $F(\omega)$ and vice versa:

$$E(t) = \int F(\omega) e^{i\omega t} d\omega, \tag{3.33}$$

$$F(\omega) = \frac{1}{2\pi} \int E(t) e^{-i\omega t} dt. \tag{3.34}$$

    In the typical case, we can impose a temporal Gaussian shape for both $E(t)$ and $F(\omega)$. In terms of temporal and spectral intensity we write

$$I(t) = I_0 e^{-\frac{2t^2}{\tau^2}}, \tag{3.35}$$

$$I(\omega) = F_0 e^{-\frac{\tau^2\omega^2}{2}} \tag{3.36}$$

    where τ is the temporal gaussian waist and I_0 and F_0 are normalization factors. The temporal duration τ and bandwidth $1/\tau$ in this case correspond to the ideal minimum bandwidth case referred to as a transform limited pulse. These equations shows that the duration of each pulse is inversely proportional to the total bandwidth of the modes coherently added. For some cases (broadband lasers) the pulses can be as short as a few femtoseconds. However many lasers do not operate at this transform limit and their spectral bandwidth is larger than the given by equation 3.36.

3.1.4 Ti:Sa laser

A very interesting class of mode-locked lasers are the titanium-sapphire (Ti^{3+}:Al_2O_3) lasers. Their active medium (a titanium-doped sapphire crystal) has an extraordinary broadband gain curve thanks to an extended ensemble of vibronic transition levels. Its fluorescence

curve ranges from 700nm to 1050 nm with a relaxation time on the order of μs , meanwhile its absorbs efficiently radiation in the visible spectrum. Normally Ti:Sa crystals are pumped by other lasers radiating on the optical range, such as frequency-doubled Nd:YAG solid state lasers (at 532 nm). Typical pulse duration values for Ti:Sa oscillators are between 5 fs and 100 fs, with energies up to 10nJ per pulse and repetition rates depending on the cavity length, but on the order of MHz.

The development of these lasers led to the achievement of significant laser peak power. If we impose the pulse to have a Gaussian temporal shape, we can approximate its peak power P_p as

$$P_p \approx \frac{E_{pulse}}{\tau_{FWHM}}, \tag{3.37}$$

where τ_{FWHM} is the FWHM duration of the pulse. For typical Ti:Sa oscillator numbers ($E_{pulse} = 10$nJ, $\tau_{FWHM} = 10$fs), this yields to $P_p = 1$MW, still well below to the achievable peak power for Q-switch laser oscillators.

3.1.5 Chirped Pulse Amplification

By means of a $f^{\#} = \pi/2$ focalizing optic, it is possible to get focal spot radius comparable to the wavelength of the laser. In that case, the peak intensity achieved can be approximated by

$$I_p \approx \frac{P_p}{\pi\lambda^2}. \tag{3.38}$$

For typical numbers of a Ti:Sa oscillator, emitting in a central wavelength of 800 nm, yields $I_p \approx 10^{13} - 10^{14}$ W/cm^2.

The search for larger laser intensities led to Strickland and Mourou [5] to develop the technique known as Chirped Pulse Amplification. It is known that ultrashort pulses can be easily *stretched* by means of use of dispersive optics (or by letting them propagate in a dispersive medium). These elements add a quadratic phase term to the pulse spectrum, which elongates the pulse, becoming a chirped wave: different wavelengths composing the wavepacket are separated in time; if dispersion is positive, longer wavelength will be in front of the pulse and shorter ones in the rear side and vice versa. Controlled devices, such as optical grating pairs, can be built to stretch an originally femtosecond pulse into a 100s of picoseconds one. At this point, the spectral content of the laser is still the same but the peak power is several orders of magnitude lower. Picking just a few of these long pulses, at a moderate repetition rate (from 1 Hz to 1 kHz), it is possible to further amplify them by sequential stages in different pumped laser crystals. This step would not be possible with a femtosecond pulse as its intensity would exceed the threshold for non-linear effects that would destroy the beam quality, or exceed the threshold for crystals damage. After the amplification phase, a second dispersive device (opposite to the stretcher) called a compressor has the task to bring the pulse to its minimum available duration, which is normally called a Fourier Limited pulse, given by [80]

$$\tau_{FWHM} \times \Delta\omega_{FWHM} = K \tag{3.39}$$

where $\Delta\omega$ is the laser spectral FWHM and K is a constant which depends on the pulse shape, but is close to $0,4$. Figure 3.6 shows a step-by-step conceptual operation of CPA lasers.

The invention of this technique awarded the inventors the Noble Prize in 2018. As seen in figure 3.7, it meant a major breakthrough in the laser technology, as it made possible the development of laser systems with huge energy levels, up to 100s of Joules for Nd:glass lasers and 10s of Joules in Ti:Sa systems. These lasers become the first to get to the petawatt

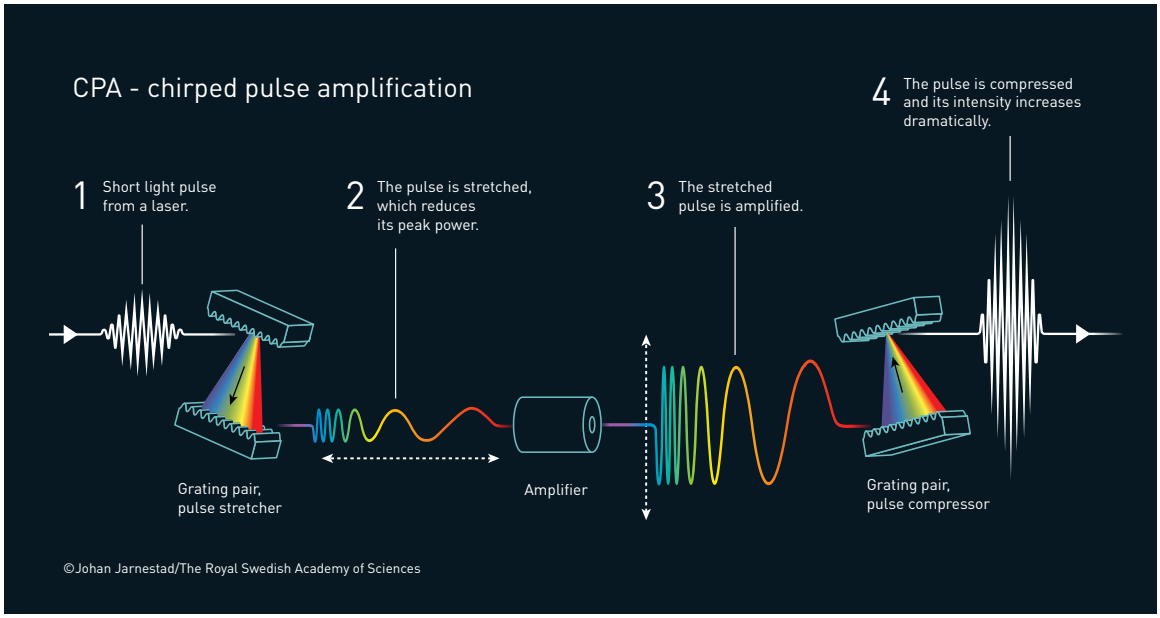

FIGURE 3.6: Conceptual sketch of CPA, from Johan Jarnestad/The Royal Swedish Academy of Sciences [87].

(and higher) power level. For instance, the Ti:Sa PW laser VEGA 3 at CLPU delivers 30J, 30fs pulses at a repetition rate of 1Hz centered at 800nm, which exactly yields 1PW of peak power. With a short enough but ideal focalization optic, it is in theory possible to achieve $I_P = 10^{24}\,\mathrm{W/cm^2}$. Values of intensity over $10^{23}\,\mathrm{W/cm^2}$ have been already experimentally demonstrated for ultrashort PW lasers [88]. Evolution of maximum reachable intensity is shown in figure 3.7.

3.1.6 Laser Contrast

Due to its operation principle, CPA-based can also amplify laser light before and after the pulse peak. One of the well-known results is the amplification of spontaneous emission of the active medium (known as ASE), which acts as a power baseline that can be present several nanoseconds before and after the pulse. Also, the appearance of pulses preceding or following the main pulse is typical. Several sophisticated techniques are used for pulse cleaning, such as the use of plasma mirrors [89], saturable absorbers [90] and cross-polarized wave (XPW) generation [91], which mostly rely on non-linear laser-matter processes that depend on the nth power of the laser intensity, in order to clean as much as possible the front part of the pulse. These pre-pulses are known to create a preplasma before the main pulse reaches the target, affecting the interaction process. An example of a 100s picoseconds long real contrast measurement of the laser system VEGA 3 is shown in figure 3.8

3.2 Laser-Matter Interaction

3.2.1 Maxwell's equations in matter

There are several methods for expressing the interaction between matter and an electromagnetic wave, mainly sorted by the treatment (or not) of both matter and/or light by quantum formalism. We call it "classic EM theory" if both radiation and matter are treated classically.

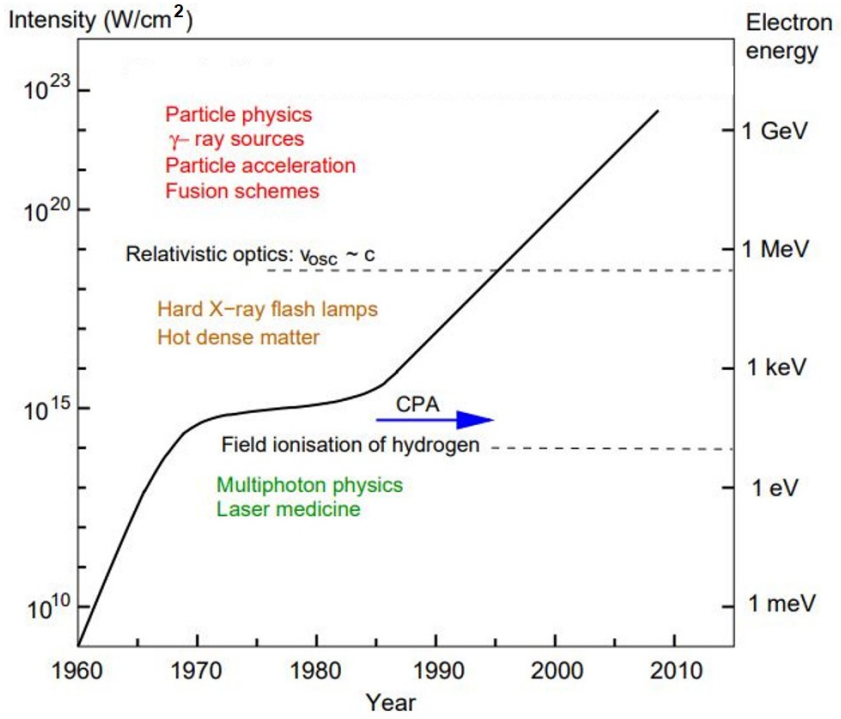

FIGURE 3.7: Progress in peak intensity since laser invention. A clear inflection point appears after the invention of CPA. Right vertical axis corresponds to the characteristic oscillation energy of a free electron in the electric field of a laser with the corresponding intensity. Insets refer to typical applications of such laser intensities. Figure adapted from [69].

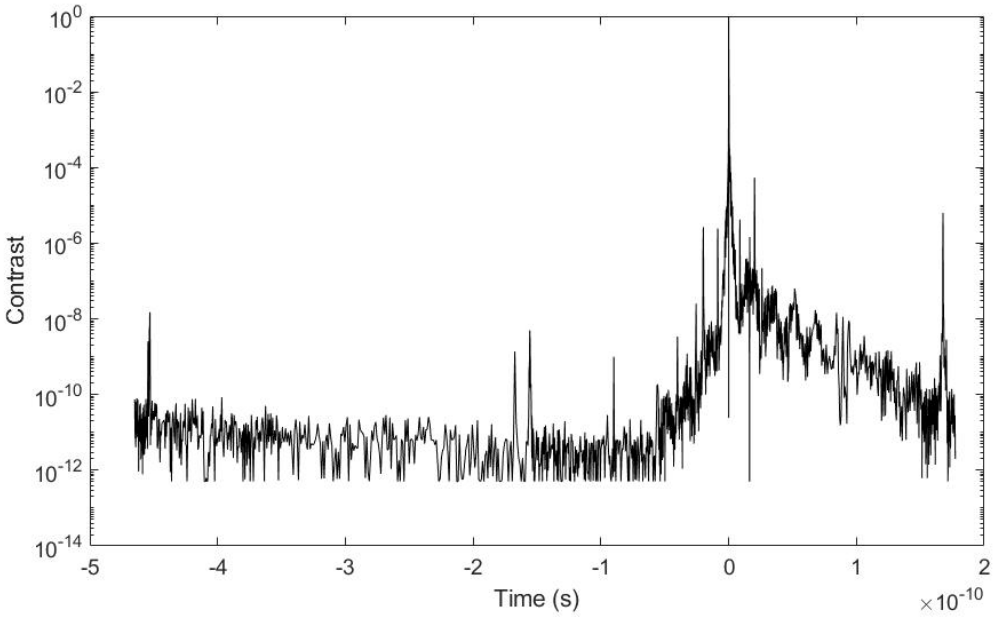

FIGURE 3.8: VEGA 3 laser log-scale contrast measured by high dynamic range third order auto-correlator Sequoia from Amplitude Laser, Inc. [92]. The y-axis, in logarithmic scale, is normalized to the peak intensity, set at $t = 0$.

In the approximation considered in this manuscript, EM fields are given as wave-like solutions of the Maxwell's equations. When the EM fields propagate in a medium, the matter will show a response which will depend on both the wave and the type of matter. The differential representation of the equations is

$$\nabla \times \mathbf{H} = \mathbf{J} + \frac{\partial \mathbf{D}}{\partial t}, \tag{3.40}$$

$$\nabla \times \mathbf{E} = -\frac{\partial \mathbf{B}}{\partial t}, \tag{3.41}$$

$$\nabla \cdot \mathbf{D} = \rho, \tag{3.42}$$

$$\nabla \cdot \mathbf{B} = 0, \tag{3.43}$$

where two additional vector fields are defined: the electric flux density -or electric displacement- $\mathbf{D}$ and the magnetic field strength $\mathbf{H}$. Both are useful as they account for the response of the medium to the fields, following the constitutive equations

$$\mathbf{D} = \epsilon_0 \mathbf{E} + \mathbf{P}, \tag{3.44}$$

$$\mathbf{H} = \frac{1}{\mu_0}\mathbf{B} - \mathbf{M} \tag{3.45}$$

$\mathbf{P}$ is the polarization density of the medium (the electrical response of the matter), and $\mathbf{M}$ the magnetization density. Both can be described as the macroscopic sum of electric/magnetic dipole moments induced by the applied fields. Maxwell's equations are complemented by the charge continuity equation

$$\frac{\partial \rho}{\partial t} + \nabla \cdot \mathbf{J} = 0. \tag{3.46}$$

In vacuum, $\mathbf{P} = \mathbf{M} = 0$, recovering the Maxwell's equation of the form 3.1, 3.2, 3.3 and 3.4. For a non-magnetic material $\mathbf{H} = \mathbf{B}/\mu_0$. Again, for a source-free medium, $\mathbf{J} = \rho = 0$.

Since the divergence of the curl of any vector is zero, 3.43 is satisfied if we set

$$\mathbf{B} = \nabla \times \mathbf{A}. \tag{3.47}$$

Substituting 3.47 into 3.41 we find

$$\mathbf{E} = -\frac{\partial \mathbf{A}}{\partial t} - \nabla \phi. \tag{3.48}$$

$\mathbf{A}$ is known as the magnetic vector potential and ϕ as the electric potential. The previous definition does not define uniquely the new introduced fields. Fixing the Lorenz gauge as a requirement for $\mathbf{A}$ and ϕ [93]

$$\nabla \cdot \mathbf{A} + \frac{1}{c^2}\frac{\partial \phi}{\partial t} = 0, \tag{3.49}$$

we find

$$\nabla^2 \phi - \frac{1}{c^2}\frac{\partial^2 \phi}{\partial t^2} = -\frac{\rho}{\epsilon_0}, \tag{3.50}$$

$$\nabla^2 \mathbf{A} - \frac{1}{c^2}\frac{\partial^2 \mathbf{A}}{\partial t^2} = \mu_0 \mathbf{J}, \tag{3.51}$$

which are in fact the rephrased Maxwell's equations. An EM wave can be therefore fully expressed in terms of $\mathbf{A}$

3.2.2 Cold matter

For simplicity we show first the typical case of interaction, which is the interaction of a monochromatic, linearly polarized wave with a gas of free electrons. We impose the medium to be linear, homogeneous and isotropic. In that case, polarization and electric field are proportional and parallel:

$$\mathbf{P} = \epsilon_0 \chi \mathbf{E}, \tag{3.52}$$

where χ is called the electric susceptibility. Similarly

$$\mathbf{D} = \epsilon \mathbf{E}, \tag{3.53}$$

with the quantity ϵ, the electric permittivity of the medium, defined as

$$\epsilon = \epsilon_0(1 + \chi). \tag{3.54}$$

Similar relation is found for the magnetic quantities, related in this case by the magnetic permeability of the medium as

$$\mathbf{B} = \mu \mathbf{H}, \tag{3.55}$$

with

$$\mu = \mu_0(1 + \chi_m), \tag{3.56}$$

where, by analogy with 3.54, we define χ_m as the magnetic susceptibility. The wave equation for this case reads

$$\nabla^2 \mathbf{E} - \nabla(\nabla \cdot \mathbf{E}) - \epsilon_0 \mu_0 \frac{\partial^2 \mathbf{E}}{\partial t^2} = \mu_0 \frac{\partial^2 \mathbf{P}}{\partial t^2}, \tag{3.57}$$

where P, for the electron free gas, is equal to the addition of the electric dipoles momentum created:

$$\mathbf{P} = q n_e \mathbf{r}, \tag{3.58}$$

being q the electron charge, n_e the electron density and $\mathbf{r}$ the electron position. The equation of motion of the electrons is given by the second Newton's Law:

$$m_e \frac{d^2 \mathbf{r}}{dt^2} = \sum \mathbf{F}, \tag{3.59}$$

where $\mathbf{F}$ is given by the Lorentz force:

$$\mathbf{F} = q(\mathbf{E} + \mathbf{v} \times \mathbf{B}). \tag{3.60}$$

For slow particles $v \ll c$, only the electric field term is important. In the approximations taken (free electrons and monochromatic wave, with electric field linearly polarized in the x axis), the equation of motion of the electrons for an oscillating electric field at angular frequency ω is given by

$$x(t) = \frac{eE_0}{m\omega^2} e^{-i\omega t}. \tag{3.61}$$

The electric current density can be easily calculated with $v(t) = dx/dt$ as

$$J(t) = -e n_e v(t) = i \frac{e^2 n_e}{m\omega} E_0 \, e^{-i\omega t}. \tag{3.62}$$

By equating 3.62 with the Ohm's Law $\mathbf{J} = \sigma\mathbf{E}$ it is possible to find the expression for the frequency-dependent electrical conductivity of the free electron gas

$$\sigma = i\frac{e^2 n_e}{m\omega} \tag{3.63}$$

Joining the expression for the polarization 3.52 and the current density 3.62, and substituting with the electron trajectory 3.61 we get the definition for the electric susceptibility for the free electron gas

$$\chi = \frac{i\sigma}{\omega\epsilon_0} = -\frac{e^2 n_e}{m\omega^2\epsilon_0} \tag{3.64}$$

The medium electric permittivity then reads as

$$\epsilon = \epsilon_0\left(1 - \frac{e^2 n_e}{m\omega^2\epsilon_0}\right) = \epsilon_0\left(1 - \frac{\omega_p^2}{\omega^2}\right), \tag{3.65}$$

where we define the *plasma* frequency as

$$\omega_p = \sqrt{\frac{e^2 n_e}{m_e\epsilon_0}}, \tag{3.66}$$

in practical units

$$\omega_p[s^{-1}] = 5.64 \times 10^4 \left(\frac{n_e}{\mathrm{cm}^{-3}}\right)^{1/2}, \tag{3.67}$$

as a characteristic oscillation period, purely depending on the medium parameters. The dispersion relation 3.6 is then

$$k^2 = \frac{\omega^2}{c^2}\left(1 - \frac{\omega_p^2}{\omega^2}\right). \tag{3.68}$$

The speed of the EM wave in the medium is given by

$$c_m = \frac{1}{\sqrt{\epsilon\mu}}. \tag{3.69}$$

The ratio between the speed of light in vacuum and to that in de medium is denoted as its refractive index. For a nonmagnetic material ($\mu = \mu_0$), then

$$n = \sqrt{\frac{\epsilon}{\epsilon_0}} = \sqrt{1 - \frac{\omega_p^2}{\omega^2}}. \tag{3.70}$$

The propagation of a EM wave in a dispersive medium is ruled by its dispersion relation 3.68, where $k(\omega) = n(\omega)\omega/c$. It is clear that the density of the medium affects severely the EM propagation. For a Gaussian pulse (whose spectrum is considered to follow a Gaussian distribution as well, with central frequency ω_0), it is possible to express the propagated electric field as the sum of individual propagated frequencies as the Fourier Transform (FT) [62]

$$E(z,t) = \int_{-\infty}^{\infty} E(\omega)e^{i\omega t}e^{-ik(\omega)z}d\omega \tag{3.71}$$

It is a good approximation for narrowband pulses to expand 3.68 in Taylor series with respect to the frequency (up to second/third order) and then perform the inverse Fourier

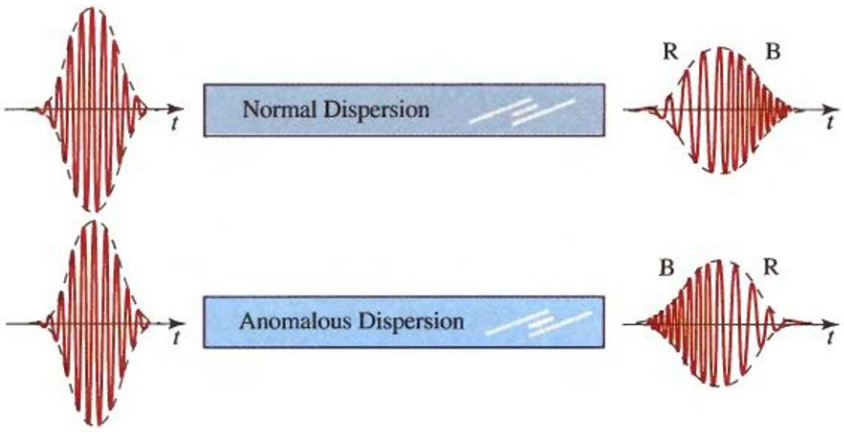

FIGURE 3.9: Propagation of a pulse through media with normal (upper) and anomalous (lower) dispersion. R stands for longer wavelengths and B for shorter. Figure taken from [81].

Transform to get the propagated pulse. Each term of the expansion gives different information about the propagated pulse.

- **0th derivative**: from $k = n(\omega)\omega/c$ we infer $k_0 = k(\omega_0)$ and the phase speed of the wave $v_\phi = \omega_0/k_0$. This quantity stands for the speed of the carrier wave inside the pulse.
- **1st derivative**: the group velocity $v_g = 1/(dk/d\omega)$ gives the speed of the envelope of the pulse. It is then easy to derive

$$v_g = \frac{v_\phi}{1 + \frac{\omega_0}{n(\omega_0)}\left(\frac{dn}{d\omega}\right)_{\omega_0}}. \tag{3.72}$$

  From this expression we see that, depending on the sign of $dn/d\omega$, $v_\phi > v_g$ (normal dispersion), or $v_\phi < v_g$ (anomalous dispersion).

- **2nd derivative**: $d^2k/d\omega^2$ is known as the Group Velocity Dispersion (GVD) and shows how the pulse stretches and compresses (how the pulse chirps) because the difference of speed in the medium of the wavelengths composing the pulse. Specific devices have been designed for proper control of the GVD of pulses (such as compressors, stretchers or Dazzlers/phase modulators) which make CPA possible. Figure 3.9 shows the effect on a laser pulse of normal and anomalous dispersion.
- **3rd derivative**: also known as Third Order dispersion (TOD), this term introduces pulse asymmetry (pre-pulses, steepening, post-pulses...)

Further extensions of the laser-matter theory for more complex and realistic cases are possible.

- **Drude model** [78]: Drude proposed this model for interaction between EM waves and metals. He proposed the valence electrons to form a conducting band to be responsible of carrying heat and current through the material. This model treats these electrons to be free but they are damped by collisions with the ions, which is characterized by its mean collision period $\tau_c = 1/\gamma$. The equation of motion reads

$$\frac{d^2x}{dt^2} = -\gamma\frac{dx}{dt} - \frac{eE_0}{m_e}e^{-i\omega t} \tag{3.73}$$

This model gives more complex expressions for the electric permittivity and the conductivity:

$$\epsilon = \epsilon_0 \left(1 - \frac{\omega_p^2}{\omega^2} \frac{1}{1 + i\gamma/\omega}\right), \tag{3.74}$$

$$\sigma = \frac{e^2 n_e}{m_e} \frac{1}{\gamma - i\omega}. \tag{3.75}$$

- **Lorentz model** [78]: extension of the Drude model for more generic materials, which imposes damped oscillator harmonic movement for the electrons, which is characterized by the oscillator constant $k = m\omega_0^2$. The equation of motion is given by

$$\frac{d^2x}{dt^2} = -\omega_0^2 x - \gamma \frac{dx}{dt} - \frac{eE_0}{m_e} e^{-i\omega t}. \tag{3.76}$$

This model yields

$$\epsilon = \epsilon_0 \left(1 - \omega_p^2 \frac{\omega^2 - \omega_0^2 - i\omega\gamma}{(\omega^2 - \omega_0^2)^2 + \omega^2\gamma}\right). \tag{3.77}$$

- **Molecular dipole (gas) approximation** [78]: for small field amplitudes, we can suppose some materials (normally gases) to be composed by molecules which are polarizable (i.e. they show electric and magnetic moments under the influence of an external field) [78]. Imposing isotropic nonmagnetic substances, we can define the effective field $\mathbf{E}'$ as the field actually acting on the molecule, which can be different from the field applied $\mathbf{E}$. So

$$\mathbf{p} = \alpha \mathbf{E}', \tag{3.78}$$

where α is the molecular polarizability [78, 94], which accounts for the sensitivity of the molecule to be polarized and it is function of the EM frequency and the molecule structure itself. The total polarization density is then

$$\mathbf{P} = N\mathbf{p} = N\alpha\mathbf{E}', \tag{3.79}$$

where N the molecular number density of the gas. Considering that $\mathbf{P}$ is homogeneous in the space between molecules and $\mathrm{P} = 0$ *inside* the molecule, one can estimate

$$\mathbf{E}' = \mathbf{E} + \frac{1}{3\epsilon_0}\mathbf{P} \tag{3.80}$$

Joining 3.52 and 3.80, it is possible to find an expression which relates the electric permittivity (electrical response of the medium) and the molecular polarizability (property of the medium):

$$\epsilon = \epsilon_0 \frac{1 + \frac{2N\alpha}{3\epsilon_0}}{1 - \frac{N\alpha}{3\epsilon_0}}. \tag{3.81}$$

In terms of the refractive index, it is called the Lorentz-Lorenz formula [95, 96]

$$\frac{n^2 - 1}{n^2 + 2} = \frac{N\alpha}{3\epsilon_0}. \tag{3.82}$$

- **Anisotropic media**: some materials (for instance crystals) have an internal structure which provides direction-dependency material response. In this case, both susceptibility and permittivity need to be expressed as a tensor, which results in birefringence (different refractive index for different polarization directions) and polarization

dichroism (different absorption depending on polarization). This effects are useful for the design of beamsplitters, waveplates and other specific polarization dependent optical setups.

- **Nonlinear media**: [81, 97] for sufficiently large laser amplitudes (specially relevant for pulsed lasers) the response of some medium could be nonlinear. In this case, the equation of motion of the of the electron is given by the anharmonic oscillator approximation

$$\frac{d^2x}{dt^2} = -\frac{eE_0}{m_e}e^{-i\omega t} - \gamma\frac{dx}{dt} - \omega_0^2 x - \alpha x^2 + \cdots \tag{3.83}$$

which is normally solved by perturbation theory. This is translated into a expansion of the polarization

$$\mathbf{P} = \epsilon_0\left[\chi\mathbf{E} + \chi^{(2)}\mathbf{E}^2 + \cdots\right] \tag{3.84}$$

where $\chi^{(j)}$ are the nonlinear susceptibilities of order j. It is possible to define then the j-order nonlinear polarization response of a medium as

$$\mathbf{P}^{(j)} = \epsilon_0\chi^{(j)}\mathbf{E}^j. \tag{3.85}$$

For $j = 2$

$$P^{(2)} = 2\epsilon_0\chi^{(2)}EE^* + (\epsilon_0\chi^{(2)}E_0^2e^{-i2\omega t}). \tag{3.86}$$

For a material with non-zero second order susceptibility, which is irradiated by an intense laser, there is a contribution to its total polarization oscillating at 2ω. From classical electrodynamics [78, 93], it is known that a charged particle oscillating at 2ω will radiate at that same frequency. This frequency-doubled outcoming radiation is called second harmonic generation (SHG), which has become a very common practice in laser laboratories as a high efficiency technique for wavelength conversion. One of the conditions for an efficient SHG is the phasing of the material microscopic dipoles so the field emitted by each of them adds coherently. This is known as *phase matching*, and it applies when

$$\Delta k = 2k_\omega - k_{2\omega} = \frac{2\omega}{c}(n_\omega - n_{2\omega}) = 0. \tag{3.87}$$

Unfortunately, for most materials the dependence of the index of refraction with ω is not constant, complicating the phase matching condition. Nevertheless, phase matching is possible by means of the use of anisotropic crystals as non-linear media. As explained above, these crystals show different refractive index depending of the EM wave polarization direction. For certain laser frequencies, polarization and incidence angles, there are crystals which meet 3.87, such as the Beta Barium Borate (BBO) for $\lambda = 800$ nm at an incidence angle of $\theta_{PM} \approx 29^\circ$ with respect to their main optical axis.

With $j = 3$ we define the third order effects, such as third harmonic generation (THG) or the Kerr effect. The latter can be defined in terms of the third order polarization (getting rid of the second order effects and the third harmonic contribution) as

$$P_{Kerr} = \epsilon_0(\chi^{(1)} + 3\chi^{(3)}A^2)E_0 0e^{-i\omega t} = \epsilon\chi_{eff}E_0e^{-i\omega t}. \tag{3.88}$$

By analogy, we define a non-linear refractive index:

$$n_{NL} = \sqrt{1+\chi_{eff}} = \sqrt{n^2 + 3\chi^{(3)}E_0^2} \approx n + \frac{3\chi^{(3)}E_0^2}{2n}. \tag{3.89}$$

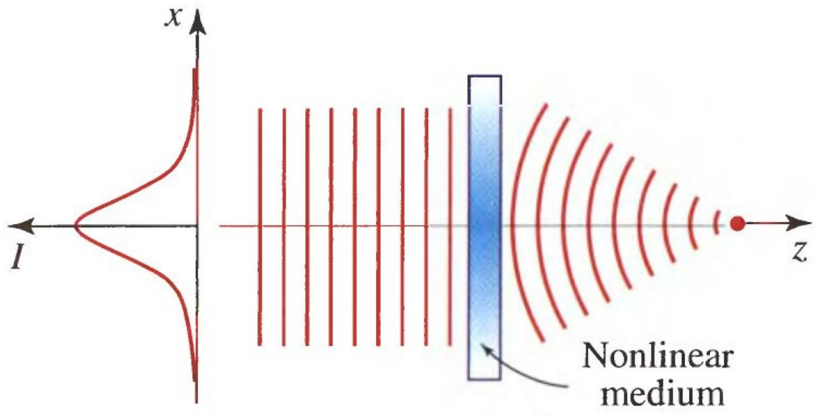

FIGURE 3.10: Self-focusing scheme, taken from [81].

We summarize this result in the expression

$$n_{NL} = n + n_2 I \tag{3.90}$$

with

$$n_2 = \frac{3\chi^{(3)}}{4n^2\epsilon_0 c}. \tag{3.91}$$

This means that for sufficiently bright lasers -with inhomogeneous spatial profile, the EM wave will propagate through an intensity-dependent refractive index. This has consequences both in the transversal and longitudinal propagation coordinates. For a gaussian beam, whose intensity radial profile follows 3.22, the resulting refractive index is then

$$n(r) = n + n_2 I_0 e^{-\frac{-2r^2}{\omega^2}}. \tag{3.92}$$

The result is that a homogeneous material reacts as a graded-index medium, providing radially symmetric phase shift, curving the beam wavefront and culminating in the laser so-called *self-focusing* [98], as shown in figure 3.10.

There are also temporal effects arising from the intensity dependence of the index of refraction. Specifically, the self phase modulation (SPM) [99] accounts for the generation of new frequencies for an intense pulse after travelling through the non-linear media of length L, as

$$\phi = -n_{NL}(I)kL = -\frac{\omega}{c}(n + n_2 I)L. \tag{3.93}$$

As $\omega = \partial\phi/\partial t$, the interaction with an intensity dependent pulse (for instance, a gaussian-enveloped pulse) results in the generation of new frequencies; an effect which is proportional to n_2.

A parameter for identifying the threshold between non-linear and linear regimes is the accumulated non-linear phase, the so-called B-integral, which is given by

$$B = \frac{2\pi}{\lambda}\int n_2 I(z)dz. \tag{3.94}$$

Values above 1 are considered over the threshold for self-focusing SPM, and other non-linear effects, such as self-steepening [100] or self-reflection [101].

In addition to these intensity dependent phase shift effects, the refractive index can also be a complex value, depending on the relation between the laser frequency and the medium properties:

$$n = n^{(R)} + in^{(I)}. \tag{3.95}$$

In this case propagation is expressed as

$$\mathbf{E} = E_0 e^{i\mathbf{k}\cdot\mathbf{r}}\mathbf{u}_r = E_0 e^{-kn^{(I)}z} e^{ikn^{(R)}z}\mathbf{u}_r, \tag{3.96}$$

being $\mathbf{u}_r = \mathbf{r}/|\mathbf{r}|$ the unitarian vector of position. For $n = n^{(R)}$, the medium is transparent and the the index of refraction accounts for the wave velocity and dispersion. On the other hand, in the case $n = n^{(R)} + in^{(I)}$, the medium is absorbent with an extinction coefficient $\alpha_{Att} = 2kn^{(I)}$ and

$$I(z) = I_0 e^{-\alpha_{Att}z}. \tag{3.97}$$

We define the skin depth as $L_{Skin} = 2/\alpha_{Att}$. For the simple case of the free electron gas, after 3.70, it is possible to determine that:

- for $\omega > \omega_p$ the refractive index is real, and the waves propagate without damping. As $n < 1$ the phase velocity v_ϕ of the wave is faster than c, which does not contradict Einstein Special Relativity Theory, as the information and power of the pulse travels with the pulse group velocity $v_g < c$.
- for $\omega > \omega_p$ the refractive index is complex and the wave gets severely damped after the skin depth. If we consider a pulse incident from vacuum to the medium, after solving Maxwell's equations at the interface, it follows that some percentage of the wave will be reflected on the medium transition.

Another interesting case to examine is the solution of the EM waves at media discontinuities. It is easy to obtain [78] the so-called Snell Reflection Law

$$\sin\theta_i = \sin\theta_r, \tag{3.98}$$

which shows that part of the energy of the wave will be reflected in an angle θ_r of same tilt as the incidence angle θ_i with respect to the discontinuity surface normal. See figure 3.11 for a geometrical clarification of the incidence. On the other hand, the response of the transmitted wave, given by the Refraction Snell law, shows that the transmission direction θ_t depends on the speed of the wave on each medium as

$$n_i \sin\theta_i = n_t \sin\theta_t, \tag{3.99}$$

being n_i and n_t the corresponding indices of refraction. In the most general case, the EM can be expressed in terms of the electric field vectorial components with respect to the incidence geometry. The vectorial component parallel to the plane defined by the incident k-vector and the surface normal is usually called *p-polarization* and the perpendicular component as *s-polarization*. See figure 3.11 for a schematic view of the problem. Applying field continuity at the surface for each component, it is possible to derive the reflection and transmission coefficients of the surface given by the Fresnel equations

$$R_p = \left|\frac{E_r^p}{E_i^p}\right|^2 = \left|\frac{n_t\cos\theta_i - n_i\cos\theta_t}{n_t\cos\theta_i + n_i\cos\theta_t}\right|^2, \; R_p + T_p = 1, \tag{3.100}$$

and

$$R_s = \left|\frac{E_r^s}{E_i^s}\right|^2 = \left|\frac{n_i\cos\theta_i - n_t\cos\theta_t}{n_i\cos\theta_i + n_t\cos\theta_t}\right|^2, \; R_s + T_s = 1. \tag{3.101}$$

For the particular case of normal incidence [69]

$$R_p = R_s = \left|\frac{1-n_t}{1+n_t}\right|^2, \tag{3.102}$$

and

$$T_p = T_s = \frac{4n_i n_t}{(n_i+n_t)^2}. \tag{3.103}$$

In the most general (as seen above, for instance, in the case of the free electron gas when $\omega > \omega_p$), the index of refraction can take complex values [78]

$$n = n^{(R)} + in^{(I)}. \tag{3.104}$$

Including this into the dispersion relation of the EM wave 3.68 a complex wavevector is also obtained.

$$k = \frac{2\pi(n^{(R)} + in^{(I)})}{\lambda}. \tag{3.105}$$

In such a case the electric field is given as

$$\mathbf{E}(z,t) = \Re\left[\mathbf{E}_0 e^{i(kz-\omega t)}\right] = \Re\left[\mathbf{E}_0 e^{i(2\pi n^{(R)} z/\lambda - \omega t)}\right] e^{-2\pi n^{(I)} z/\lambda}, \tag{3.106}$$

an the intensity as

$$I(z) = I_0 e^{-4\pi n^{(I)} z/\lambda}. \tag{3.107}$$

This means that in an absorbing medium, the EM wave power decays exponentially with an absorption coefficient of $\alpha = 4\pi n^{(I)}/\lambda$ and a corresponding penetration depth $\delta_p = 1/\alpha$. When the EM wave encounters a discontinuity from a transparent medium to an absorbing one, following Snell Law 3.99, the transmission angle needs to be complex, leading to a transmitted evanescent wave which will be absorbed by the second medium.

3.2.3 Multiphoton interaction

Multiphoton ionization (MPI)

One of the most famous examples of laser-matter interaction is the photoelectric effect, predicted by Einstein in 1905 [102], which was experimentally validated a few years later by Millikan [103]. This is one of the first examples of a quantum treatment of the laser-matter interaction, which awarded Einstein with the Nobel Prize in 1921. It explains the extraction of an electron from the atomic structure by interaction with a single photon, which is considered the minimal quantum unit of the EM radiation. The condition for the photoelectric effect is that the photon energy should be equal or higher than the atomic potential barrier $\hbar\omega \geq E_{ion}$. For typical E_{ion}, even for outer shell electrons, the required photon energy is over several eV level, which corresponds to a wavelength range ultraviolet (UV) up to keV (X-rays), much shorter wavelengths than the typical laser sources available, which lie in the infrared (IR) and optical range. However, in 1931 Göppert-Mayer proposed a theory for simultaneous absorption of several photons, known now as MPI [104], whose total energy could be larger than the atomic barrier $n\hbar\omega \geq E_{ion}$. Nevertheless, the probability of this non-linear effect is proportional to the n-th power of the light intensity. For this reason this effect could not be demonstrated until sufficiently high laser intensities were reached

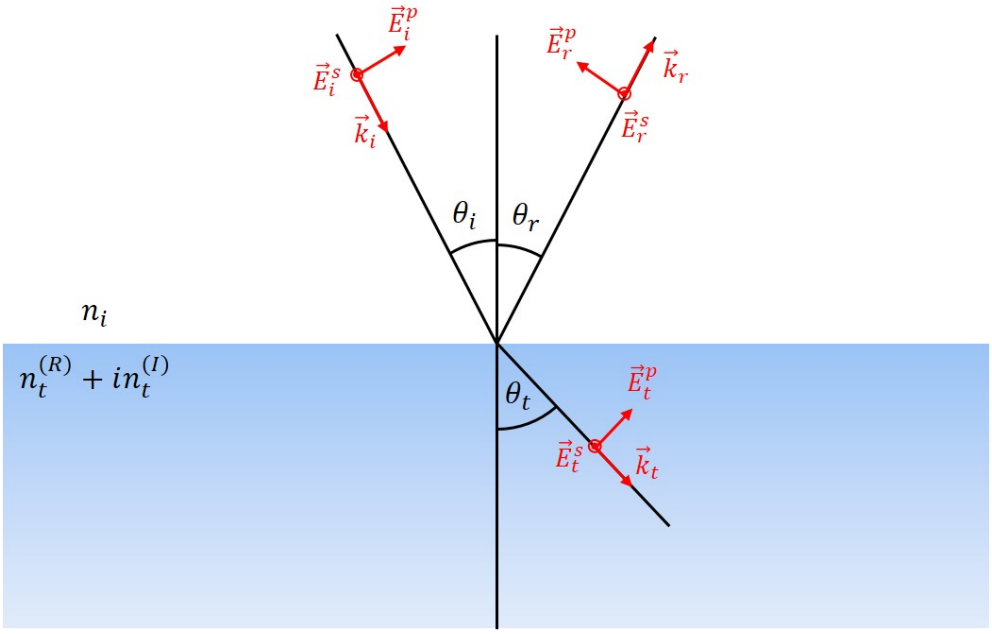

FIGURE 3.11: Sketch of the reflection and refraction Snell laws.

(10^{10}W/cm^2), after the the invention of the laser, 30 years later [105]. For larger intensities, more photons can be absorbed, and the resulting free electrons will have significant energy gain equal to

$$E_{free} = (n+s)\hbar\omega - E_{ion}, \tag{3.108}$$

where s is the number of extra photons absorbed. This is called Above Threshold Ionization (ATI) [69]. The energy level diagram of these processes is shown in figure 3.12.

Barrier Suppression Ionization

From Bohr's model of the atom, the radius of the atom is expressed as

$$a_B = \frac{4\pi\epsilon_0\hbar^2}{m_e e^2} = 5.3 \times 10^{-9}\,\text{cm}. \tag{3.109}$$

By means of Coulomb's Law, it is possible to infer the corresponding electric field strength which binds the electron to the nucleus as

$$E_a = \frac{e}{4\pi\epsilon_0 a_B^2} = 5.1 \times 10^{11}\,\text{V/m}. \tag{3.110}$$

Substituting E_a in equation 3.10 for the field amplitude, we obtain the *atomic intensity*

$$I_a = \frac{\epsilon_0 c E_a^2}{2} = 3.51 \times 10^{16}\,\text{W/cm}^2, \tag{3.111}$$

which stands for the equivalent EM intensity which a laser needs to reach to match the atomic potential. When irradiating an atom with laser intensities larger than I_a, the polarization field of the laser will overcome the electrons atomic binding field, and it will become instantly ionized, known as Barrier Suppression [69]. For sufficiently intense radiation, the atom can be completely ionized.

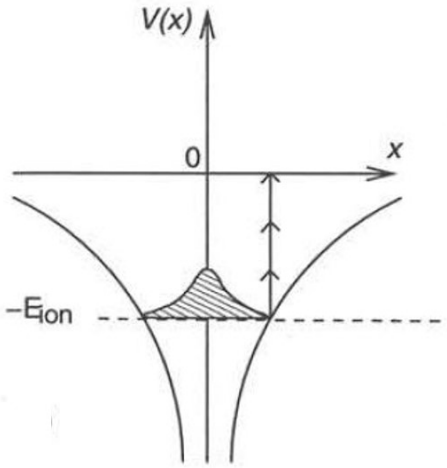

FIGURE 3.12: Conceptual drawing of MPI and ATI, taken from [69]. V(x) stands for a one-dimensional projection of the potential well generated by the positive charge of the atom nucleus, where the arrows represent the energy absorption of individual photons.

Tunneling ionization: High Harmonic Generation

For the nonrelativistic case ($v \ll c$), imposing a plane EM wave, we solve the Lorentz force for a single free electron

$$m_e \frac{d^2\mathbf{r}}{dt^2} = q\mathbf{E}. \tag{3.112}$$

Imposing linearly polarized light

$$\mathbf{E} = E_0 \cos(\omega t)\mathbf{u}_x, \tag{3.113}$$

then

$$\mathbf{r} = \frac{e}{m_e\omega^2} E_0 \left[1 - \cos(\omega t)\right] \mathbf{u}_x \tag{3.114}$$

and

$$\mathbf{v} = \frac{q}{m_e\omega} E_0 \sin(\omega t)\mathbf{u}_x. \tag{3.115}$$

These are the equations of the quiver motion of an electron under an oscillating plane laser wave. The instantaneous kinetic energy reads as

$$E_{kin} = \frac{e^2 E_0^2}{2m_e\omega^2} \sin^2(\omega t). \tag{3.116}$$

E_{kin} averaged over one cycle is consider as the ponderomotive potential of the laser field, expressing quiver energy acquired by the electron

$$U_p = \frac{e^2 E_0^2}{4m_e\omega^2}. \tag{3.117}$$

For the case of a single atom irradiated by a EM wave with laser intensities well below I_a, the perturbative approach of the MPI holds true. When the laser intensity is comparable to this value, the polarization field itself modifies the total field perceived by the electrons.

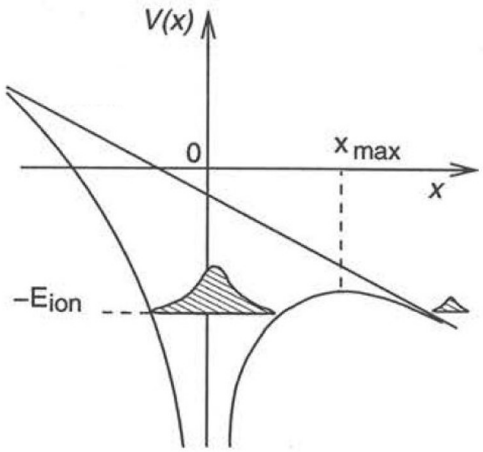

FIGURE 3.13: Conceptual drawing of tunnelling/barrier suppression ionization, taken from [69]. $V(x)$ of the electron gathers both contributions from parenting ion and the laser electric field.

We can write an electric potential as

$$V(x) = \frac{1}{4\pi\epsilon_0}\frac{Ze^2}{x} - exE, \tag{3.118}$$

where Z is the atomic number. This was firstly introduced by Keldish [106], who introduced the parameter

$$\Gamma = \sqrt{\frac{E_{ion}}{2U_p}}. \tag{3.119}$$

$\Gamma > 1$ implies an interaction at the MPI regime, meanwhile for $\Gamma < 1$ strong field is considered. In the latter case, for an oscillating $\mathbf{E}(t)$, there is a time of the laser period in which there is a local maximum in $V(x_{max})$. If $V(x_{max}) < -E_{ion}$, then the electron is free and the atom is ionized by barrier suppression method. As shown in the previous section, laser intensities available nowadays are orders of magnitude higher; in such cases normally most of the target material is completely ionized well before the arrival of the main part of the beam. Therefore, the laser interacts with a plasma.

On the other hand, if $V(x_{max}) > -E_{ion}$ still there is a possibility for the electron to escape the atomic potential by quantum Tunnel effect. The corresponding energetic levels of the barrier suppression and quantum tunnelling regime are depicted in figure 3.13. Tunneling means that, for a certain intensity range, ionization of selected electrons can be triggered in a relatively short and controlled interval (around the electric field maxima, where the range is shorter than half optical cycle). These electrons, after one laser oscillation period can be sent back to their parent ion and recombine with them, emitting by a highly nonlinear process the so-called HHG. This mechanism, which can only be properly explained in a fully quantum approach, was first demonstrated by several groups in the late 80s [107, 108].

The nature of the interaction gives the cut-off energy that a single photon can reach by HHG (meaning the maximum accessible harmonic order) as [109]

$$E_{max} = E_{ion} + 3.17U_p. \tag{3.120}$$

For typical numbers, this means that HHG is an efficient converter of infrared radiation into

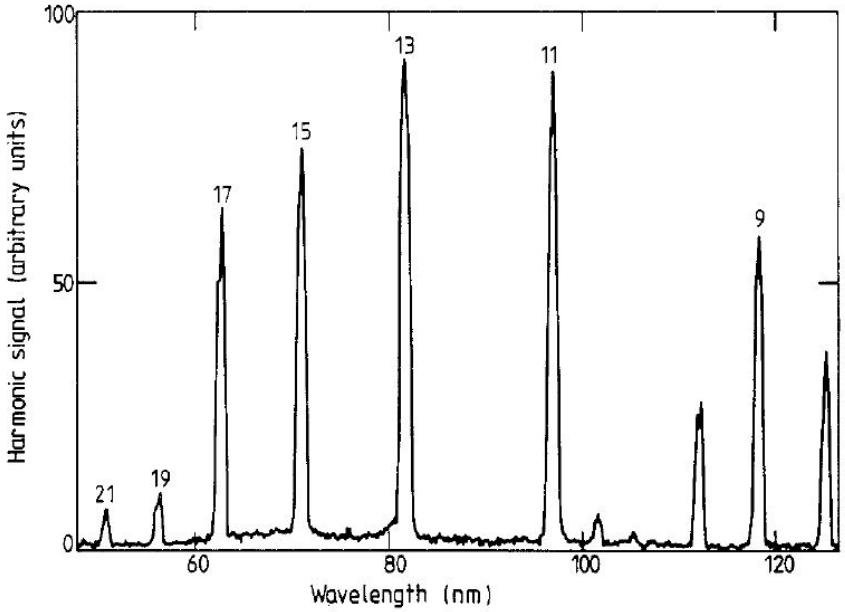

FIGURE 3.14: Typical experimentally measured HHG spectrum between 9^{th} and 21^{st} harmonic orders. In the case shown, for a Nd:YAG laser ($\lambda = 1064\,\text{nm}$) irradiating Xe gas with $I = 3 \times 10^{13}\,\text{Wcm}^{-2}$, up to 21st harmonic order was detected. Figure taken from [108].

EUV. A typical HHG spectrum is shown in figure 3.14. The resulting radiation inherits some properties from its parent radiation, as the spatial and temporal coherence. The different harmonics are phase-locked with a much shorter central wavelength and wider bandwidth, which paved the way for the generation of attosecond EUV pulses [54].

3.2.4 Interaction with single electron

For the available laser intensities nowadays, well above the barrier suppression threshold, atoms will be partially of fully ionized before the arrival of the main part of the laser pulse. Therefore, we are interested in the interaction of the EM wave with free electrons and plasmas. As the rest mass of the lightest ion (the proton) is approximately 2000 times the electron mass, the EM fields will have a larger influence on the latter. This is the reason why we study first the interaction of lasers with single electrons [69, 110].

First it is important to note that, from now on, we will introduce our interaction description for accounting for relativistic effects. The reason behind this is easily understandable if we calculate the quiver energy of an electron oscillating in the electric field of a typical ultra-intense laser focus ($I = 10^{19}\,\text{W/cm}^2$, $\lambda = 800\,\text{nm}$). After substitution 3.10 in 3.117 we get $U_p = 0.598\,\text{MeV} \approx 0.511\,\text{MeV} = m_e c^2$. When the rest mass of a particle is comparable to its kinetic energy, a relativistic approach should be considered.

A common figure of merit which is normally used for differentiating relativistic and non-relativistic regimes is the dimensionless parameter a_0, which corresponds to the normalized amplitude of the oscillating particle speed. It can be thought as the peak momentum of the oscillating electron, in units of $m_e c$. By derivation of 3.61 it is immediate to find

$$a_0 = \frac{eE_0}{m_e \omega c}, \tag{3.121}$$

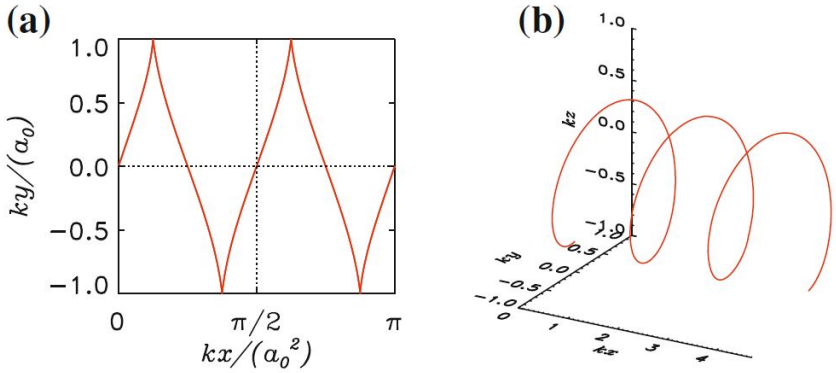

FIGURE 3.15: a) Electron trajectory in monocromatic EM wave of amplitude a_0 linearly polarized in the y direction. b) Electron trajectory for circularly polarized wave of amplitude $a_0 = 2$. Figure taken from [110].

or alternatively in practical units

$$a_0 = \left(\frac{I\lambda^2}{1.37 \times 10^{18}\ \mathrm{Wcm^{-2}\mu m^2}} \right)^{1/2}. \tag{3.122}$$

If $a_0 \approx 1$, then $v \approx c$ and relativistic formalism should be applied. It can be related to the intensity by

$$I = \frac{c\epsilon_0}{2} \left(\frac{m_e c\omega}{e} a_0 \right)^2. \tag{3.123}$$

The relativistic Lorentz Force equation of an electron is

$$\frac{d\mathbf{p}}{dt} = -e\left(\mathbf{E} + \mathbf{v} \times \mathbf{B}\right), \tag{3.124}$$

where $\mathbf{p} = \gamma m_e \mathbf{v}$ is the relativistic momentum and γ is the relativistic factor, given by

$$\gamma = \sqrt{1 + \left(\frac{p}{m_e c} \right)^2} = \frac{1}{\sqrt{1 - \frac{v^2}{c^2}}}. \tag{3.125}$$

It is clear from 3.124 that for intense fields, the transversal velocity imposed on the electron is significant, hence the magnetic term cannot be ignored. The motion of the electron should also fulfil the energy equation

$$\frac{dE_e}{dt} = \frac{d(\gamma mc^2)}{dt} = -e\mathbf{v} \cdot \mathbf{E}. \tag{3.126}$$

For simplicity ,the case of an EM plane wave propagating along the z-axis is considered. EM waves can be represented in terms of its vector potential ($\mathbf{A} \cdot \mathbf{u}_z = 0$) as

$$\mathbf{E} = -\frac{\partial \mathbf{A}}{\partial t}, \tag{3.127}$$

$$\mathbf{B} = \nabla \times \mathbf{A} = \mathbf{u}_z \times \frac{\partial \mathbf{A}}{\partial z}. \tag{3.128}$$

We note with the subscript $\perp$ to refer to the components of the vectors in the transverse plane with respect to the laser propagation direction (z-axis). Then $\mathbf{A} = \mathbf{A}_\perp$ which leads to

the equation of conservation of transversal momentum

$$\frac{d}{dt}\left(\mathbf{p}_\perp - e\mathbf{A}\right) = 0. \tag{3.129}$$

Joining 3.124, 3.126 and 3.129, the conservation law of longitudinal momentum is derived

$$\frac{d}{dt}\left(p_z - m_e\gamma c\right) = 0. \tag{3.130}$$

Assuming an initially at rest electron and no field at that time, the conservation equations give

$$\mathbf{p}_\perp = e\mathbf{A}, \tag{3.131}$$

$$p_z = mc(\gamma - 1), \tag{3.132}$$

yielding a unique relation between the longitudinal and transversal momentum of the electron and $\mathbf{A}$

$$p_z = \frac{\mathbf{p}_\perp^2}{2m_e c} = \frac{e^2\mathbf{A}^2}{2m_e c}. \tag{3.133}$$

For an arbitrary polarization, the vector potential can be defined as

$$\mathbf{A} = A_0\left[\delta\cos(kz-\omega t)\mathbf{u}_x + \sqrt{1-\delta^2}\sin(kz-\omega t)\mathbf{u}_y\right], \tag{3.134}$$

where $\delta \leq 1$ is the polarization parameter. Inserting this form of the potential yields

$$\mathbf{p}_\perp = eA_0\left[\delta\cos(kz-\omega t)\mathbf{u}_x + \sqrt{1-\delta^2}\sin(kz-\omega t)\mathbf{u}_y\right] \tag{3.135}$$

$$p_z = \frac{e^2A_0^2}{4m_e c}\left[1 + (2\delta^2-1)\cos(2kz-2\omega t)\right]. \tag{3.136}$$

It is clear that the longitudinal momentum oscillates at frequency 2ω. Another conclusion is that there is a net longitudinal momentum, which can be calculated by averaging p_z over an oscillation cycle

$$p_d = \langle p_z\rangle = m_e c\frac{a_0^2}{4} \tag{3.137}$$

which we call drift momentum. The first order approximation of the drifted position of the electron is given by

$$\langle z\rangle = v_d t \approx \frac{a_0^2}{a_0^2+4}ct. \tag{3.138}$$

It is interesting to show two specific EM polarization cases. For linear polarization $\delta = 1$ (or 0) the motion is restricted in the xz (or yz) plane, with oscillation frequency 2ω in the longitudinal direction and ω in the transversal. For circular polarization ($\delta = \pm 1/\sqrt{2}$), then the component at 2ω vanishes and $p_z = \langle p_z\rangle$. Trajectories for this both cases are shown in figure 3.15.

When transforming to a reference frame at constant v_d, the electron orbit is a closed circle for the circularly polarized case, meanwhile for linear polarization it describes a "figure of eight", as shown in figure 3.16.

3.2.5 Ponderomotive Force

One of the conclusions from 3.133 is that for an infinite plane EM wave, if the vector potential is zero $\mathbf{A} = 0$ then the electron is at rest $\mathbf{p} = 0$. If the EM wave is pulsed (i.e. the vector

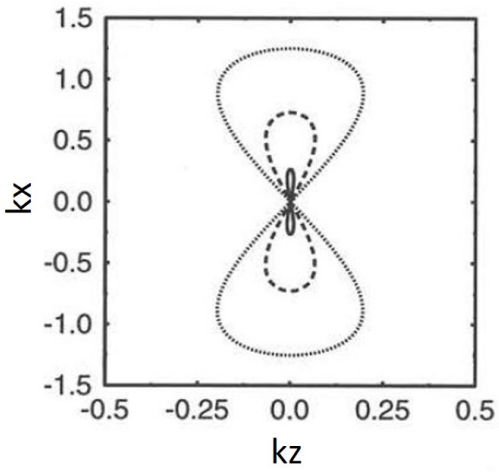

FIGURE 3.16: Electron orbit at the drift velocity frame for a linearly polarized EM wave (in the y direction), with $a_0 = 0.3$ (solid line), $a_0 = 1$ (dashed line) and $a_0 = 3$ (points line). Figure adapted from [69].

potential is zero sufficiently before and after the pulse peak: $\mathbf{A}(t = 0) = \mathbf{A}(t = \infty) = 0$), the electron will be at rest after the interaction and will not gain net energy after interaction with the fields. This is different if the EM wave is finite in transverse size, as it is found in nature for more realistic cases, such as for a focused laser beam, which can present a strong radial intensity gradient on the order of a few wavelengths. Supposing that the EM fields (almost) average to zero over a period, but that the envelope does not, it is possible to decompose the electron motion into a fast component (oscillating term) and a slow component on the time scale of the the envelope gradient, which represents the motion of the "oscillation center" of the particle. In the non-relativistic limit, considering gradients larger than laser wavelength, a second order approximation of the equation of motion of the oscillating centre is given by

$$m_e \frac{d^2\langle \mathbf{r} \rangle}{dt^2} = \frac{e^2}{2m_e\omega^2} \nabla \left\langle \mathbf{E}^2 \right\rangle \equiv \mathbf{f}_p. \tag{3.139}$$

The conclusion from 3.139 is that, especially for focalized laser beams, there is an effective cycle-averaged force which expels the electrons from the higher intensity regions. For a quasi-gaussian beam ($M^2 \approx 1$), this means that the electrons will be ejected away from the laser axis. It is important to note from 3.117 that this effective force is actually the gradient of the ponderomotive potential

$$\mathbf{f}_p = -\nabla U_p. \tag{3.140}$$

For the general relativistic case, the ponderomotive force should be expressed in terms of the electron oscillation energy. If we approximate the electron momentum to be fully restricted in the transversal coordinates, $\gamma = \sqrt{1 + a^2/2}$ and the electron kinetic energy is

$$E_{kin} = m_e(\gamma - 1)c^2 \approx m_e c^2 \left(\sqrt{1 + \frac{a^2}{2}} - 1 \right) \tag{3.141}$$

which is known as the "Ponderomotive Scaling" of the electron energy [111]. Therefore

$$f_p = -m_e c^2 \nabla \left(\sqrt{1 + \frac{\langle a \rangle^2}{2}} \right). \tag{3.142}$$

3.2.6 Plasma

Usually called the fourth state of matter, plasmas compose 99% of the observable universe. On Earth, plasmas can be found in the ionosphere, lighting, industry, fusion facilities and research laboratories where they are generated and studied. Shortly after the interaction of a high-intensity laser with matter, a percentage of the target atoms will be ionized, resulting in a quasi-neutral gas of electrons, ions and atoms which we call plasma [112, 113]. Coulomb forces between charged particles dominate the plasma behaviour, even at large distances, which results in collective effects in response to perturbations. These processes are critical for low-density plasmas, where they rule the interaction over particle collisions, in the so-called collisionless plasma regime.

For a three-dimensional Maxwellian temperature distribution of the form

$$f(v) = n_e \left(\frac{m_e}{2\pi k_B T} \right)^{3/2} e^{-\frac{mv^2}{2k_B T}}, \tag{3.143}$$

where k_B is the Boltzmann constant, the average kinetic energy of the plasma is

$$E_{av} = \frac{3}{2} k_B T. \tag{3.144}$$

In that context, we can define one fundamental characteristics of the plasmas, which is the Deybe shielding. Plasmas are able to shield, thanks to charge redistribution, electric potentials that are applied to it. Considering again that electrons move much faster than the ions, after solving to the first order the Poisson equation 3.50 in equilibrium we find

$$\phi = \phi_0 e^{-\frac{r}{\lambda_D}}, \tag{3.145}$$

where λ_D is the Debye length, defined as

$$\lambda_D \equiv \sqrt{\frac{\epsilon_0 k_B T_e}{n_e e^2}}, \tag{3.146}$$

or in practical units

$$\lambda_D[\mathrm{cm}] = 743 \left(\frac{T_e}{\mathrm{eV}} \right)^{1/2} \left(\frac{\mathrm{cm}^{-3}}{n_e} \right)^{1/2}. \tag{3.147}$$

This means that any electrostatic perturbation in the plasma will be shielded by a sheath of plasma charge-carrier particles of thickness λ_D, proportional to $\sqrt{T_e/n_e}$. For a system of typical dimension L large enough (or dense enough) so $\lambda_D \ll L$, any local charge concentration on external potential applied to the system will be shielded in a short distance compared to L, causing the quasi-neutrality of the plasma. Nevertheless, this effect is only realistic if enough charged particles are present in the plasma. We define N_D as the number of particles present in the *Debye sphere*

$$N_D = n_e \frac{4}{3} \pi \lambda_D^3. \tag{3.148}$$

The collective behaviour condition requires that $N_D \gg 1$. The condition that should be satisfied for electromagnetic interactions to dominate over particle collisions is

$$\omega_p \tau_c > 1, \tag{3.149}$$

where τ_c is the mean time between collisions and ω_p is the typical plasma oscillation frequency that, by analogy with the free electron gas case, is the plasma frequency defined in 3.66.

The response of the plasma to EM fields will be ruled, similar to the free electron gas case explained above, by the relation between the laser frequency ω and the plasma frequency ω_p. As it is normally the case in laser facilities, it is simpler to change the target composition and density than the wavelength of the laser source, therefore it is more convenient to define the interaction in terms of electronic densities. The critical density is given by

$$n_c = \frac{m_e \epsilon_0 \omega^2}{e^2}, \tag{3.150}$$

or in practical units

$$n_c[\mathrm{cm}^{-3}] = 1,1 \times 10^{21} \left(\frac{\mu\mathrm{m}}{\lambda}\right)^2. \tag{3.151}$$

This value corresponds to the plasma resonance frequency ($\omega = \omega_p$). This expression yields a definition for the refractive index of refraction in terms of its density:

$$n = \sqrt{1 - \frac{n_e}{n_c}}. \tag{3.152}$$

For the central wavelength of Ti:Sa lasers ($\lambda = 800$ nm) the critical density lies at $n_c \approx 2 \times 10^{21}$ cm^{-3}. This threshold leads to the three classical laser-plasma interaction regimes:

- Underdense plasmas ($n_e < n_c$): these plasmas are transparent to the EM radiation, so they are traversed by intense laser pulses, nevertheless absorbing part of the laser energy by different mechanisms such as particle collisions and non-linear plasma wave generation and wavebreaking. It is technically simple to achieve this kind of target on the laboratory, as $n_e \approx 10^{19}$ cm^{-3} is the typical electron concentration of atmospheric pressure air or gaseous target in experimental chambers.

- Overdense plasmas ($n_e > n_c$): these plasmas are opaque to the EM radiation and act as a mirror for a large percentage of the pulse energy, nevertheless providing energy to the target by collisions, skin effects and other collisionless non-linear methods. Solid target, such metals ($n_e \approx 10^{23}$ cm^{-3}) and liquids ($n_e \approx 10^{22}$ cm^{-3}) are normally used as overdense targets.

- Near-critical plasmas ($n_e \approx n_c$): mixed effects are found in this regime, volumetric heating effects and plasma shock wave can be triggered. These targets are especially difficult to achieve in the laboratory, as they lie right between the typical solid and gas ranges, which are difficult to find in nature.

Departures from the classical plasma description are given by the coupling and degeneracy parameters [113]. A strongly coupled plasma is defined by the ion Coulomb coupling parameter

$$\Gamma_i = \frac{\langle E_{pot} \rangle}{\langle E_{kin} \rangle} = \frac{(Ze)^2}{k_B T_e a_i}. \tag{3.153}$$

where $a_i = (4\pi n_i/3)^{-1/3}$ is the average ion spacing. When $\Gamma_{ion} >> 1$ (dense/cold plasmas), inter-particle electrostatic coupling dominates over collective effects. On the other

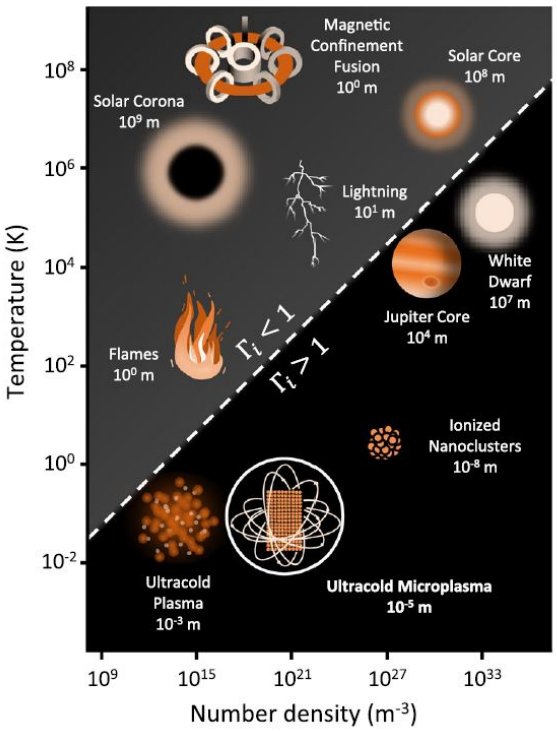

FIGURE 3.17: Chart of temperature versus number density for plasmas. Insets show typical plasmas found in nature or laboratories and their characteristic dimension. Weakly-coupled (classical) plasmas correspond to $\Gamma_i < 1$. Laser-produced plasmas are placed in the middle of the graph, at $T_e \approx 10^2 - 10^3$ eV and $n_e \approx 10^{24} - 10^{30}$ m^{-3}, with characteristic length of $10^{-4} - 10^{-2}$ m. Image taken from [114].

hand, quantum effects are important when the average particle spacing start to be comparable to its de Broglie wavelength. Again, this depends purely on the plasma temperature and density through the degeneracy parameter

$$\Theta = \frac{k_B T_e}{E_F} \tag{3.154}$$

when it smaller than the unity. $E_F = \hbar^2 (3\pi^2 n_e)^{3/2}/2m_e$ is the Fermi energy. These regimes can be achieved when heating solid-density plasmas to a few eV and it is normally referred as Warm Dense Matter (WDM). Unless stated otherwise, the theoretical description in this manuscript will consider weakly-coupled classical plasmas. Types of plasmas are classified in the chart of figure 3.17.

For a non-magnetized *cold* plasma (i.e. ignoring thermal effects) transverse electromagnetic wave solutions are obtained with the same dispersion relation as in the free electron gas case. On the other hand, it is important to note that Maxwell's equation in this medium allow for longitudinal electrostatic (ES) wave solutions, where the electrons oscillate along the direction of the k-vector at frequency ω_p, with arbitrary group velocity [113]. In this special solution -normally called *plasma waves*- the wave group velocity vanishes. Solving Poisson equation 3.50, we see that these waves are linked to charge perturbations on the plasma as

$$\nabla \cdot \mathbf{E} = -\frac{e}{\epsilon_0}(n_e - Z n_i) \tag{3.155}$$

being n_i the ion number density and Z its charge. Considering *warm* plasmas (i.e. taking into account the thermal velocity of the electrons $v_{th} = \sqrt{k_B T/m_e}$), the dispersion relation is modified to

$$\omega^2 = \omega_p^2 + 3k^2 v_{th}^2. \tag{3.156}$$

It can be shown that these waves can be damped (without the action of particle collisions) via resonant energy transmission to the electrons with velocities close to the wave phase velocity $v_p = \omega/k$. Such a process is known as *Landau damping*.

As seen before, when irradiating the plasma with a sufficiently large amplitude laser (above 10^{18} W/cm^2, what is normally called *relativistic amplitude*) the motion of the electrons becomes relativistic. In that case, the plasma behaviour becomes non-linear due to the importance of the magnetic term and the non-linear relativistic relation between speed and momentum. In the most simple relativistic case (circularly polarized laser $\mathbf{v}_e \times \mathbf{B} = 0$ and $\mathbf{p}_e \cdot \mathbf{k} = 0$) we find the non-linear equation motion

$$\frac{d}{dt}(m_e \gamma v_e) = -e\mathbf{E}. \tag{3.157}$$

The dispersion relation in this case reads

$$k^2 = \frac{\omega^2}{c^2} - \frac{\omega_p^2}{c^2 \gamma}, \tag{3.158}$$

which yields a non-linear refractive index

$$n = \sqrt{1 - \frac{\omega_p^2}{\gamma \omega^2}}. \tag{3.159}$$

Summarizing, the refractive index (so the propagation and dispersion of the pulse) is affected by the local amplitude of the laser itself. Several propagation effects result from this dependency, such as *relativistic self-focusing* and *relativistic transparency*. An interesting result for the first is the appearance of a threshold laser power value for this effect: $P_{cr}[GW] \approx (n_c/n_e)$ uniquely dependent on the electron density [115]. The second effect is easily understandable from 3.158; we can define an effective *relativistic* plasma frequency (and wavelength) as

$$\omega_p' = \frac{\omega_p}{\sqrt{\gamma}}\ ,\ \lambda_p' = \frac{2\pi c}{\omega_p'} = \lambda_p \sqrt{\gamma}. \tag{3.160}$$

The effective critical density is then

$$n_c' = n_c \gamma > n_c, \tag{3.161}$$

which means, for the simple case of the circular polarization, that the laser can propagate in plasmas above the non-relativistic critical density.

This simplified picture of wave propagation in plasmas is just an example of the wide variety of the possible solutions that can be found depending on the local plasma conditions, applied magnetic and electric fields and so on. There are several theoretical approaches that are useful for dealing with these problems, which are applied depending on the length and time scale of interest. Longitudinal plasma wave solutions can be found by assuming that each charged particle component of density and velocity behaves like a fluid interacting with each other through the fields. This is the idea behind the *two-fluid* or *hydro* method, in which ions and electrons fluids are considered separately imposing Maxwellian distributions. The more rigorous *kinetic* theory is based on solving the particle phase-space

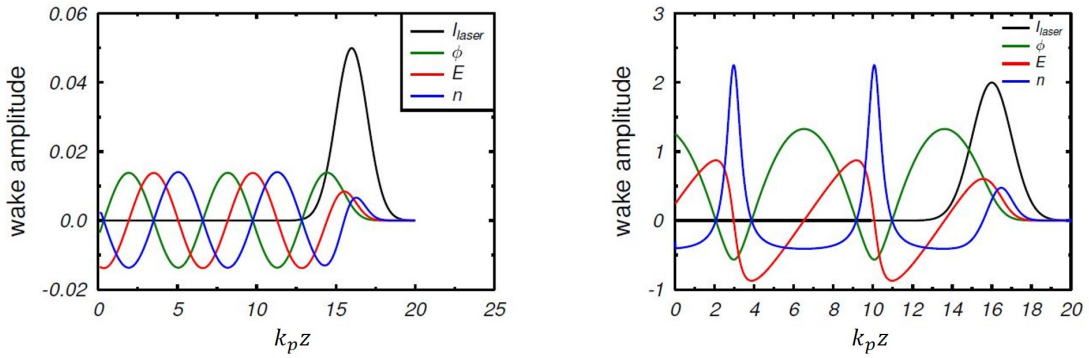

FIGURE 3.18: Wakefield excitation after interaction with linear (left) and non-linear (right) short pulse travelling to positive z. The black line stands for the laser amplitude, the green for the electrostatic potential, the red for the electric field and the blue the electronic density. Figure adapted from [17].

Vlasov-Boltzmann equation, which is the basis for kinetic phase space solvers. One can also solve for the motion of individual particles in the self consistent electric and magnetic fields as is done in the well-established Particle-in-Cell (PIC) simulation codes [69].

One of the interesting cases to study for LPA is the effect of a perturbation (such an intense laser pulse and the associated ponderomotive force) crossing an underdense plasma. As no restriction is made to the plasma wave group velocity, by construction it will be equal to the perturbative force (i.e. the laser). Causality forces the plasma oscillation to appear in the region after the front part of the laser in the form of a *wake*. For the linear case [7, 116], i.e. for small laser amplitudes and short pulses, the wake is characterized with an electron velocity as (1D simplification)

$$v = v_0 \sin(k_p z - \omega t), \tag{3.162}$$

where z is the laser propagation coordinate and v_0 the velocity amplitude. This is translated into a density change (from background electron density $n_{e,0}$) of the form

$$\delta n_e = n_e - n_{e,0} \approx n_{e,0} \frac{v_0}{v_f} \sin(k_p z - \omega_p t), \tag{3.163}$$

where k_p is the wavenumber of the plasma wave, and v_f the plasma wave phase velocity. By solving the Poisson equation, it is possible to deduce the electrostatic longitudinal electric field generated

$$E \approx \frac{m_e c \omega_p}{e} \frac{v_0}{v_f} \cos(k_p z - \omega_p t). \tag{3.164}$$

A linear wakefield is shown in figure 3.18 (left). It is easy to appreciate the sinusoidal shape of both the electric field and plasma waves. Nevertheless, for laser amplitudes above $a_0 = 1$, relativistic effects bring non-linearities to the ruling equations of the wake. Figure 3.18 (right) shows a wake created by a relativistic pulse. Clear steepening of the charge concentration is seen which is translated into higher electrostatic fields.

Nevertheless, the maximum reachable ES field sustained by a wake is ruled by the wave-breaking limit. When the fields are strong enough, the speed of the particles is faster than the phase velocity of the plasma wave and the structure of the wave itself is lost. Such a limit is given by

$$E_{wb} = \frac{m_e c \omega_p}{e} \sqrt{2(\gamma_p - 1)} \tag{3.165}$$

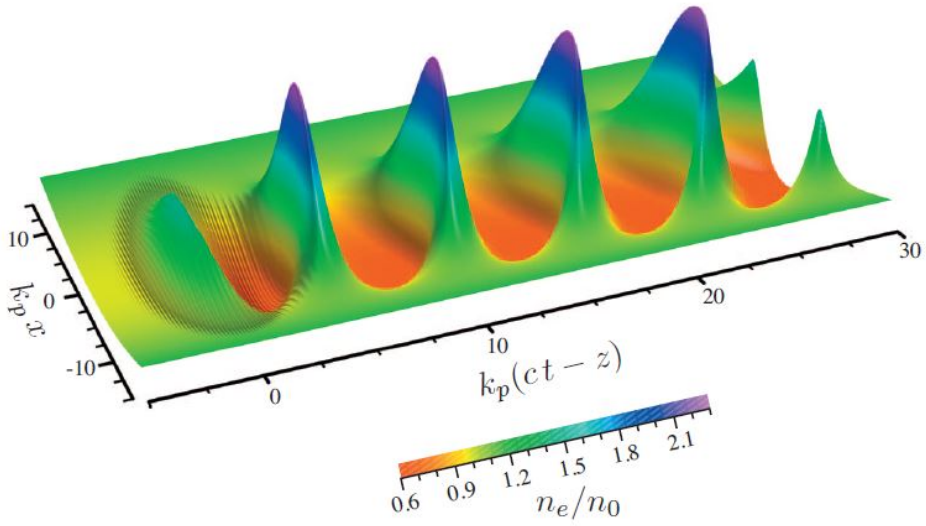

FIGURE 3.19: Two-dimensional representation of non-linear plasma wake generated by a $a_0 = 1.5$ gaussian laser pulse, taken from [7].

where γ_p is the relativistic factor of the plasma wave.

The real scaling of the plasma and field structures changes when translating to two or three dimensions. A two-dimensional PIC simulated plasma density plot of a non-linear wake is shown at figure 3.19 for illustration.

3.3 Laser-driven accelerators

Tajima and Dawson [20] realized that such enormous electric fields sustained by *plasma cavities*, that can reach values above 100 GV/m (several orders of magnitude over the typical values of conventional radio-frequency accelerators) were perfect candidates for new schemes of particles accelerators.

It is standard to classify the laser-plasma driven particle accelerators in terms of the transparency regime of the interaction: under dense, over dense and near critical plasmas.

3.3.1 Under dense plasmas

During the beginning of the century, as the CPA laser technology advanced and shorter and more intense pulses were achieved, several acceleration regimes were proposed and demonstrated [7, 19, 116]. These experiments proved the technical feasibility of acceleration of electrons at the underdense regime (energies below the GeV level, with a rather broadband spectrum) thanks to the electric field sustained by the plasma cavities generated by picosecond (or 100s of femtoseconds) long laser pulses. The Laser Beat Wave regime [117], the Self Modulated Laser Wakefield [118] and the Force Laser Wakefield [119] can be mentioned. In addition there are other mechanisms, such as the Direct Laser Acceleration [120], where electrons are accelerated by the laser fields, acceleration by wavebreaking [121], and the Plasma Wakefield Acceleration [122], a method in which the plasma cavity is driven by an electron bunch, which could be accelerated by other laser-based method.

Pukhov and Meyer-Ter-Vehn [123] were the first proposing the Bubble Regime, or blow-out, which was experimentally demonstrated shortly after [124–126]. The wide effort on the study of this method and its use has granted its name as simply Laser Wakefield Acceleration (LWFA). In this relativistic regime ($a_0 > 2$) [7, 19, 127], the laser energy is concentrated

in a very short pulse (half of a plasma wavelength), so the ponderomotive kick of both front and rear edges of the pulse are resonant with the plasma oscillation, enhancing enormously the charge depletion right after the laser pulse. On the other hand, in order to favour the formation of a *bubble* of positive charge behind the pulse, it should be focalized to a diameter close to the plasma wavelength ($k_p w_0 \simeq \sqrt{a_0}$), and kept like this during the acceleration length, helped by the relativistic self-focusing. The electrons expelled by the pulse travel on the bubble border until the cavity rear side, where they are self-injected into the longitudinal electric accelerating field. As the location of injection is small and the initial conditions of the injected electrons are similar, the phase-space of the accelerated bunch is similar, which means rather monoenergetic and collimated electron beams, perfect for applications.

The generation of such energetic electrons beams rely upon sustaining of the acceleration structure for sufficient range, normally on the order of centimetres. Despite the use of long focal optics for focusing onto the target ($f^{\#}$ large), typical Rayleigh lengths are much shorter than the optimal acceleration distance. Nevertheless, laser channelling into micrometric-wide centimetre-long filaments is possible thanks to the dynamic competition of relativistic self-focusing effect, which tends to concentrate the beam, and the anomalous dispersion of the beam due to the ionization gradient, which locally changes the index of refraction and defocus the beam. Such a process, known as *filamentation* [128], is highly dependent on the laser parameters (intensity profile, pulse duration and focusing length) and the target density and atomic composition. Limitations on the maximum energy achievable in LWFA are given mainly by the electron bunch outrunning the plasma wave (called dephasing) and by the loss of laser energy during the process up to a point in which the bubble cannot be sustained (called depletion). The maximum acceleration lengths allowed by both limiting processes are approximately (it depends on the analytical model considered) [127]

$$L_{deph} = \frac{4}{3}\frac{\lambda_p^3}{\lambda^2}\sqrt{a_0}c \tag{3.166}$$

and

$$L_{depl} = \frac{\lambda_p^2}{\lambda^2}c\tau_{FWHM}. \tag{3.167}$$

Thanks to the huge electric field sustained by the bubble, 1 mm of acceleration length is enough to reach 100s of MeV electrons. Classical scaling laws [7, 19, 127] for the maximum possible energy gained by electrons limited by dephasing is

$$\Delta E_{kin,max} \simeq m_e c^2 \left(\frac{P}{m_e^2 c^5/e^2}\right)^{1/3}\left(\frac{n_c}{n_e}\right)^{2/3}, \tag{3.168}$$

or alternatively, in practical units

$$\Delta E_{kin,max}[\text{GeV}] \simeq 1,7\left(\frac{P_{Laser}}{100\ \text{TW}}\right)^{1/3}\left(\frac{10^{18}\ \text{cm}^{-3}}{n_e}\right)^{2/3}\left(\frac{0,8\ \mu\text{m}}{\lambda}\right)^{4/3}. \tag{3.169}$$

In the blow-out regime, the control of the beam properties is critically linked to the conditions of injection of the electrons into the accelerating wakefield. Proper control of the target conditions and laser parameters makes possible the repetitive achievement of the blow-out regime; in such case, mJ-class lasers (operating at $\sim kHz$ repetition rate) are sufficient to drive wakefields. Kilohertz repetition rate operation of laser-driven electron acceleration is nowadays feasible [44]. Nevertheless, pure self-injection does not allow fine tuning of parameters tuning and does not achieve acceptable reproducibility for practical applications. Several controlled injection schemes have been proposed and tested, most of them relying on optical or target engineering.

- Ionization injection [56, 129, 130]: a method to control the injection is by using mixes of high-Z and low-Z gases as a target. Due to the large difference of ionization potential between both species, low-Z electrons will escape the atoms when encountering the front edge of the pulse, working as background plasma to sustain the wakefield, meanwhile inner-shell electrons from the high-Z component will be ionized only when the intensity is large enough, typically close to the pulse peak. This differential ionization leads to the latter electrons being efficiently trapped by the bubble. This method leads normally to broader electron spectra but reducing the laser intensity requirements and increasing the beam charge. Complex two-stage setups based on this process (first with gas mixture for injection, second with pure low density gas for acceleration) have been experimentally demonstrated [131].

- Density gradient injection [132–134]: another common method for injection control is the use of targets with density downramp gradient. When travelling in a density downramp, the plasma wake suffers elongation and its phase velocity is decreased as a consequence of the gradual increase of λ_p. This relaxes the conditions for electron trapping. Proper tailoring of the target gives access to electron bunch properties control. Two-stages setups have been demonstrated as well following this idea [135].

- Colliding pulse [136]: the use of two counter-propagating pulses for driving the plasma wave leads to the acceleration of stable, tunable and monoenergetic electron beams. This process relies on the beatwave created when two counter-propagating coherent lasers cross each other, which appears to be an efficient ponderomotive kick for electron injection. As the action is triggered only when both pulses overlap in space in time (which for ultrashort pulses is extremely short), injection is very fast compared to the wake evolution, so monoenergetic beams are achieved. Beams as short as few femtoseconds have been measured following this procedure [31], leading to kA currents.

By means of these new methods (or their combination [137]) a new generation of laser-based tunable electron accelerators have emerged. From pC to nC of charge, low-divergence beams with controlled spectral bandwidth are now commonly available at high-intensity laser facilities, with cutoff energies up to GeV. In order to achieve higher energies, different strategies, such as laser guidance in preformed plasma channels, have been carried out [43].

Off-axis injection of the electrons into the accelerating structure brings an interesting secondary effect. Due to the restoring force towards the centre of the charge cavity, the electrons will perform transversal oscillations, known as Betatron oscillations. It is well known in the conventional acceleration community that the transverse oscillation of a relativistic charged particle bunch emit forward Doppler-upshifted radiation. This is a direct consequence of the Liénard-Wiechert potential formula, which gives the intensity dependence with the particle trajectory in the direction of observation $\mathbf{n}$ as [93]

$$\frac{d^2I}{d\omega d\Omega} = \frac{e^2}{16\pi^3\epsilon_0 c}\left|\int_{-\infty}^{+\infty} e^{i\omega(t-\mathbf{n}\cdot\mathbf{r}/c)}\frac{\mathbf{n}\times[(\mathbf{n}-\boldsymbol{\beta})\times\dot{\boldsymbol{\beta}}]}{(1-\boldsymbol{\beta}\cdot\mathbf{n})^2}dt\right|^2 \tag{3.170}$$

where $\boldsymbol{\beta} = \mathbf{v}/c$. From this equation is clear that the emission is favoured when the acceleration is perpendicular to the observation point, but increased when the particles have relativistic velocities towards the observer. Actually, the radiation is relativistically contracted into a cone of angle $\theta \sim K/\gamma_e$, where γ_e is the longitudinal Lorentz factor of the electron bunch and K is known as the wiggler parameter, which is guideline for differentiating from soft (undulator regime $K < 1$) or strong transversal oscillations (wiggler regime $K > 1$). In conventional accelerators, such orbits are achieved thanks to the addition to the beamline

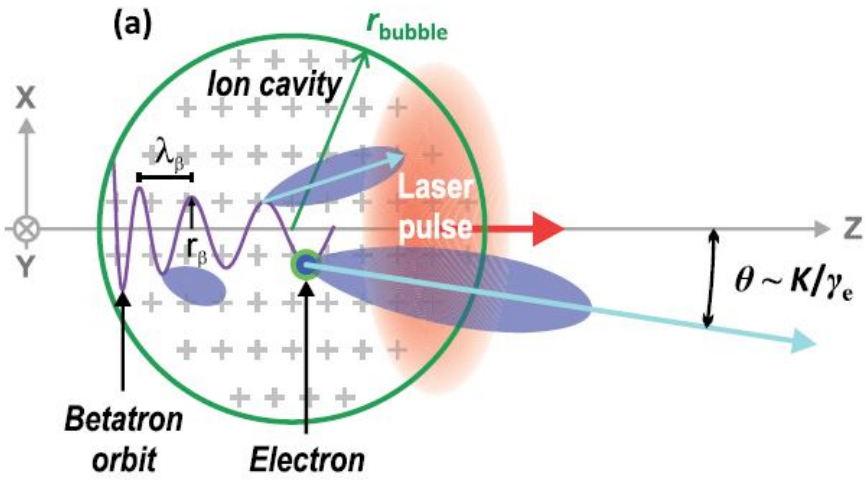

FIGURE 3.20: Sketch of electron acceleration and consequent betatron generation due to the relativistic transversal electron oscillation in the positive-charged cavity. Figure taken from [61].

of magnetic dipoles, in devices known as Synchrotrons or Undulators/Wigglers. Nevertheless, in the case of plasma accelerators, Betatron oscillations are native to the interaction process; Betatron radiation is inherent to LWFA process [8, 24, 61, 138, 139].

The betatron oscillation period is a function of the plasma wavelength (i.e. the plasma density) and the electron energy:

$$\lambda_\beta = \lambda_p \sqrt{2\gamma_e}. \tag{3.171}$$

The K parameter is defined in Betatron as

$$K = \gamma_e k_\beta r_\beta \sim \theta \gamma_e, \tag{3.172}$$

where r_β is the amplitude of the betatron oscillation, normally smaller than the bubble radius.

In the undulator regime ($K < 1$), the photons are measured in the laboratory frame at the basic Doppler-shifted energy

$$\hbar\omega = \frac{2\gamma_e hc}{\lambda_\beta(1 + K^2/2)}. \tag{3.173}$$

Nevertheless, when wiggler regime is applicable, the photons will be emitted along the harmonics of this fundamental frequency, so close to each other that create a continuous spectrum. Such radiated power by a single wiggling electron will have a synchrotron-like spectrum such

$$\frac{dW_\beta}{d\omega} \simeq \sqrt{3} N_\beta \frac{e^2}{2\pi\epsilon_0 c} \gamma_e \frac{\omega}{\omega_c} \int_{\omega/\omega_c}^{\infty} K_{5/3}(\xi) d\xi \tag{3.174}$$

where N_β is the number of oscillations, K_n is the modified Bessel function of the second kind and

$$\hbar\omega_c = \frac{3}{2} K \gamma_e^2 \frac{hc}{\lambda_\beta} \tag{3.175}$$

is the so-called *critical frequency*, which represents the median frequency of the Betatron spectral intensity (i.e. half of the energy is emitted with photons avobe $\hbar\omega_c$ and half below

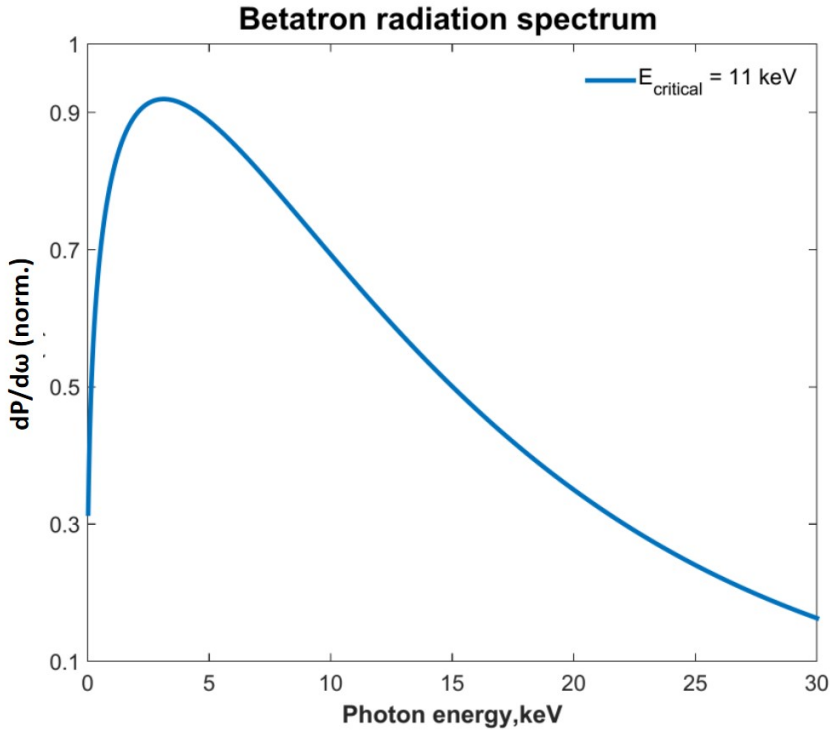

FIGURE 3.21: Power of synchrotron emission as a function of the photon energy for $E_c = 11$ keV.

that value). A typical spectrum is shown in figure 3.21. The number of emitted photons is proportional to the number of emitting electrons (they add incoherently) and to the K parameter. Nevertheless, the picture of Betatron generation is not homogeneous during the acceleration length. Due to the dependence of the radiation properties with γ_e, it is obvious that the most important contribution to the spectrum will be at final stages of acceleration, during the last oscillations, where the electron energy is larger.

The considerable relativistic factor of LWFA electrons (and the double Lorentz contraction between reference frames, which yields to the dependency $E_c = \hbar\omega_c \propto \gamma_e^2$) makes the Betatron spectrum to be centred around hard X-rays. Further extension of this photon energy (up to gamma-ray range) have been achieved by resonantly enhancing the Betatron oscillations by direct interaction with the rear part of the driver pulse [140]. Moreover, other emission mechanisms have been studied by the laser-driven electron beam, such as non-linear Thomson Scattering [141] or Compton scattering with a second laser pulse [142], which also reached gamma-ray energies.

Summarizing, LWFA are also powerful sources of broadband, ultrashort (few tens of femtosecond-long, this is 3 orders of magnitude shorter than typical synchrotron-source pulse duration), highly-directional ($\sim$ 20mrad), high energy photons (from X-ray to gamma-rays). Despite reaching the typical pulse duration of FELs, Betatron sources are still behind in terms of beam reproducibility, bandwidth control and brightness (typical Betatron yield is 10^8 photons/sr/0.1%BW/shot, several orders of magnitude less than FEL [50]).

It is worth to mention the use of Betatron sources for Phase Contrast Imaging technique. Such a radiography approach measures the change of the real part of the refractive index of matter $n^{(R)}$. This method has proven to be useful when carrying out radiography of soft matter, which is normally transparent to X-rays and regular absorption radiography fails. This measurement is only possible for highly transversally coherent photon beams. Tomography reconstruction of biological samples have been demonstrated [52, 53].

It has been shown for both electron LWFA (and subsequently for Betatron radiation generation) that the requirements to reach different acceleration regimes and injection schemes are linked to the target density through the dependency of the plasma wavelength with the plasma electron density. For instance, resonance between the plasma oscillation frequency and the pulse duration ($c\tau \sim \lambda_p/2$) has been proven to be favourable to achieve the bubble acceleration regime. Also, from 3.168 it is possible to note the stronger dependence of the beam energy on the target density, rather than the laser intensity. Also, sharpness and shape of the gas target profile and edges will define as well the properties of the emitted radiation [143]. These are a few of the main reason for the extensive study of ultrafast plasma density diagnostics.

3.3.2 Over dense plasmas

The picture of the interaction of short and intense pulses with overdense plasmas is completely different to the underdense case. Any overdense target such as a metallic foil is rapidly ionized by the front edge of the laser pulse, after a few optical cycles of sufficiently large amplitude. The rest of the pulse (the most energetic part) will interact with the resulting plasma slab, where $n_e > n_c$ and therefore, encountering a medium with complex refractive index, consequently acting as a reflective surface for a large percentage of the laser energy. The coupling of the radiation energy into the overdense plasmas depends mostly on the laser intensity, pulse duration, polarization and target type, normally mixing several mechanisms simultaneously [69].

Once the fast ionization of the overdense plasma layer starts, ablation mechanism pushes plasma away from the bulk of the target, creating a plasma density gradient of typical scale length L [144]. Assuming that this coronal plasma expands isothermally, we can approximate

$$L \approx c_s \tau_{FWHM}, \tag{3.176}$$

where c_s is the ion speed sound of the plasma

$$c_s = \sqrt{\frac{Z k_B T_e}{m_i}}, \tag{3.177}$$

where Z the average ion charge of the plasma. The neutrality condition yields

$$n_e = Z n_i = \frac{Z N_A \rho_m}{A}, \tag{3.178}$$

where ρ_m is the non-ionized mass density, A the atomic number and N_A the Avogadro number.

Alternatively, in terms of the plasma profile

$$L = \left(\left| \frac{d}{dx} \log n_e \right|_{x=L_t} \right)^{-1}. \tag{3.179}$$

This *preplasma* illustrates one of the crucial differences between *long* pulse and *short* pulse interaction (considering the latter as $\tau_{FWHM} < 1$ps). A nanosecond-long pulse creates a plasma scale length of hundreds of microns; a non-negligible part of it will be underdense, so transparent to the laser but also partially absorbing due to collisions in the plasma. The laser can then efficiently transfer its energy to the plasma at or below the critical density surface. On the other hand, a subpicosecond laser will create a much steeper preplasma of $L/\lambda \approx 0.01 - 0.1$. The main part of the laser interacts basically with a solid-density plasma

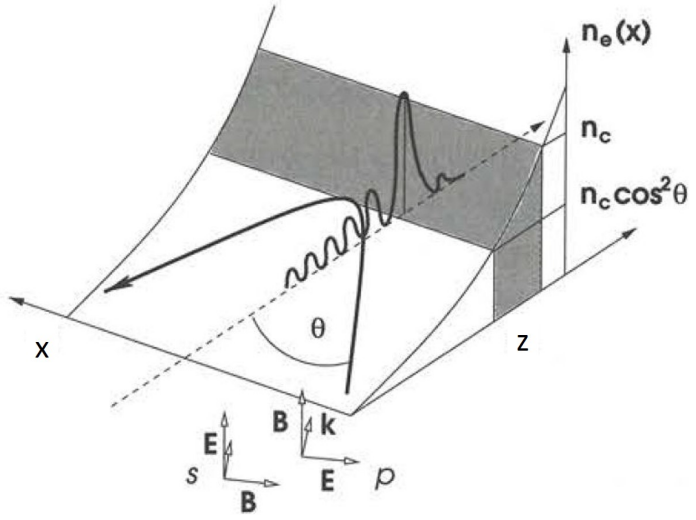

FIGURE 3.22: Geometrical sketch of for p(s)-polarized EM wave, with angle of incidence θ into a preplasma gradient density from an initially overdense target. Figure adapted from [69].

which reacts to first order as a mirror, following Snell laws as seen before. As in the case of the reflection on a metal, reflection yields to the appearance of an standing wave in front of the target, and a evanescent wave with skin depth $L_{skin} = c/\omega_p$ into the plasma. Nevertheless, as the transversal component of the wavevector k_y has to be conserved, when substituting into the Maxwell equations we see that the the reflection occurs at the surface where $n_e = n_c\cos^2\theta$, referred to as turning point (see figure 3.22). Thanks to the different preplasma scale lengths and profile shapes created and the wide range of available laser pulse duration, intensities, and wavelengths, a rich set of absorption mechanisms are feasible for both long and short pulse interaction, often mixed and competing with each other. Some of these methods are depicted in the following list [69].

- Collisional absorption [144, 145]: For non-ideal plasmas, when $N_D \approx 1$, screening effects are reduced and the behaviour of the plasma is dominated by collisions. In intermediate regimes the absorption can be described by electron heating and consequent energy transfer to ions by collisions between electrons and ions (also known as inverse Bremsstrahlung), and it is normally linked to nanosecond-long laser pulse, as it occurs mainly in the underdense (but almost critical) part of the plasma gradient, so it is favoured when $L/\lambda > 1$. Nevertheless, the fact that denser and steeper preplasmas are highly collisional also favours this mechanisms. As in the Drude model, the equation of motion of electrons is considered as

$$m_e\frac{d^2\mathbf{r}}{dt^2} = -e(\mathbf{E} + \frac{d\mathbf{r}}{dt}\times\mathbf{B}) - m_e\nu_{ei}\frac{d\mathbf{r}}{dt}, \tag{3.180}$$

  where the Coulomb electron-ion collision frequency is given by

$$\nu_{ei} = \frac{\pi^{3/2}n_eZe^4}{\sqrt{2}(4\pi\epsilon_0)^2m_e^2v_{te}^3}\ln\Lambda. \tag{3.181}$$

  In this expression, v_{te} is the electron thermal velocity $v_{te} = \omega_p\lambda_D = \sqrt{k_BT_e/m_e}$, and $\ln\Lambda$ is the Coulomb logarithm, related to the electron-ion cross section $\Lambda = 9N_D/Z$.

In practical units, the collision frequency is

$$\nu_{ei}[s^{-1}] = 2.9 \times 10^{-6} \ln\Lambda \left(\frac{n_e}{\mathrm{cm}^{-3}}\right) \left(\frac{\mathrm{eV}}{T_e}\right)^{3/2} \tag{3.182}$$

Similarly as in the Drude model, after solving the Maxwell equations we define locally the index of refraction of the plasma as

$$n(z) = \sqrt{1 - \frac{n_e(z)}{n_c} \frac{1}{1 + i\frac{\nu_{ei}(z)}{\omega}}} \tag{3.183}$$

or alternatively, in the form of dispersion relation

$$k(z) = \frac{\omega}{c} \left[\cos^2\theta - \frac{\omega_p^2(z)}{\omega(\omega + i\nu_{ei}(z))}\right], \tag{3.184}$$

already taking one-dimensional plasma expansion and fixed incidence angle θ, as shown in figure 3.22, and considering s-polarized wave. One of the conclusions for this approximation after 3.182 and 3.183 is that the index of refraction (and therefore the absorption) in this approximation depends purely on both the local values of electron density and temperature. Taking a closer look at the dependencies, it is clear that the absorption is more pronounced where $n_e \approx n_c$. In the case of a soft gradient scale-length ($kL \gg 1$), considering a plane wave, it is possible to apply the Wentzel-Kramers-Brillouin (WKB) approximation, linearising the solutions and forcing the field quantities to have harmonic time-dependency with ω. Thus, absorption of laser energy is

$$\eta = 1 - e^{-2\delta} \tag{3.185}$$

where δ is the line integral

$$\delta = 2\Im \int_0^{L_t} k(z')dz', \tag{3.186}$$

where L_T is the turning point. Furthermore, neglecting weak dependencies of the collision frequency and keeping simply its relation to the electron density $\nu_{ei}(z) = \nu_{ei}(n_c)n_e(z)/n_c$, and imposing a specific density profile $n_e(z)$, analytical solutions can be found for the total absorption. For instance, assuming a linear density profile ($n_e(z) = n_c z/L$) yields

$$\eta = 1 - e^{-\frac{32\nu_{ei}(n_c)L}{15c}\cos^5\theta}. \tag{3.187}$$

The case of an exponential profile ($n_e(z) = n_c e^{-z/L}$) yields

$$\eta = 1 - e^{-\frac{8\nu_{ei}(n_c)L}{3c}\cos^3\theta}. \tag{3.188}$$

It is obvious that the absorption is maximum for normal incidence and null for grazing incidence. In the limit $L \to 0$, Drude's model Fresnel equations 3.100 and 3.101 are recovered [78], often referred as Normal Skin Effect: the transmitted part of the wave penetrates as an evanescent wave at the skin layer l_s, which drives electron oscillations which are later absorbed by collisions.

- Collisionless absorption [69]: for sufficiently high intensities (above $10^{15}\mathrm{W/cm}^2$), the plasma is heated sufficiently such that the collision frequency drops and absorption start to be dominated by other mechanisms:

- Resonance absorption: this mechanisms only appears for p-polarized light, as it has an electric field componenet along the direction of the density gradient. This creates density fluctuation (i.e. excites a plasma waves) at the surface in which the plasma resonantly responds; that is, in the critical surface. This method leads to maximum absorption at some off axis angle of incidence dependent on the ratio of density scale length to laser wavelength and it is especially effective in for short to intermediate plasma scale lengths.
- Vacuum (or Brunel) heating: for very sharp density profiles (i.e. shorter pulses), charge oscillations driven by p-polarized light can have amplitudes larger than the plasma scale length, and therefore escape the plasma bulk (further than λ_D) and be exposed directly to the laser field. When the field reverses its direction, the electrons will be injected back into the plasma with net acceleration, where they will be eventually absorbed.
- $\mathbf{j} \times \mathbf{B}$ heating: if the plasma electrons are exposed to linearly-polarized relativistic laser intensities, the magnetic component of the Lorentz force is noticeable, especially at normal incidence. As predicted by [111], the driver force at frequency 2ω appears (see 3.136). In this case, the energy acquired by the electrons scales with the irradiance [111], as shown in 3.141.

As soon as the laser energy starts to be transferred to the plasma, its temperature will increase. Heating of the target will affect how the rest of the laser energy couples to the plasma, so both heating and absorption are in fact linked and their behaviour is entangled. Perfect analytical solutions do not exist and the use of numerical simulations as such kinetic or PIC codes is necessary. The advent of the high-intensity femtosecond pulse lasers made possible the absorption of the energy in almost unperturbed targets, beneficial for fast electron generation or fast ignition fusion schemes. Energy transfer to hot electrons has been estimated to be in the $10\% - 30\%$ range, with crucial dependence on polarization, prepulse and incidence angle [22]. In any case, in a characteristic time of picoseconds -longer than the typical femtosecond pulse duration- heat will be transferred to the vicinity of the interaction point and plasma (including ions) expansion will begin. On the other hand, for some applications (such as symmetrical compression of targets) the presence of a controlled plasma scale length at the arrival time of the laser is desirable; this can be achieved in short pulses with a controlled laser pedestal or with a second laser pulse prior to the main one (a prepulse).

Early experiments of ultra-intense laser interaction with overdense target (metallic or plastic foils), either with long [146] and short pulses [147, 148], showed ion acceleration in the backward direction with broad angular distribution. Their origin was attributed to acceleration in the expanding plasma plume. Nevertheless, several groups demonstrated forward acceleration of protons above the MeV level under the same kind of laser irradiation conditions [149–151]. This acceleration mechanism was firstly explained by Wilks *et. al.* [152], and named Target Normal Sheath Acceleration (TNSA) [21, 22].

Hot electrons energized at the front surface of the target can travel through the target towards the rear face of the foil, generating currents up to several MA. The study of hot electrons transport is an important research area as it is a critical component in Fast Ignition in ICF. The transport of electrons in this kind of experiment is a non-trivial topic, as it gets complicated when taking into account electron refluxing, target heating and the presence of a return current for compensating the hot electron stream. When the hot electrons cross the rear boundary of the target, they try to escape but they are retained in the vicinity of the plasma due to the electrostatic field generated by the charge imbalance, generating therefore a sheath of negative charge of length $L_s \sim \lambda_D$. The magnitude of the electrostatic

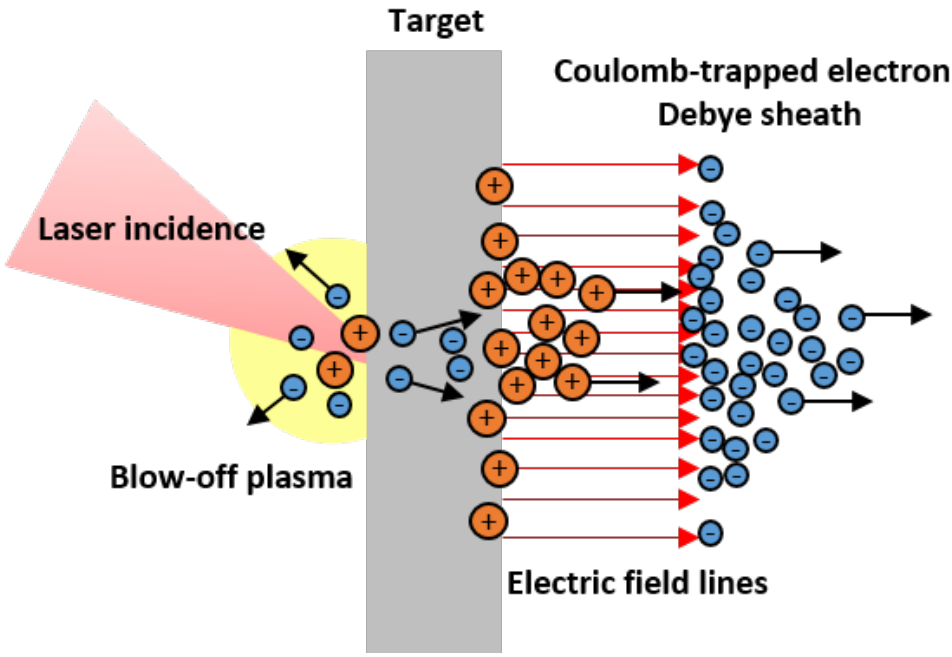

FIGURE 3.23: Sketch of TNSA ion acceleration mechanisms.

field, directed along the normal to the target surface, can be approximated by

$$E_s \sim \frac{T_e}{e\lambda_D}. \tag{3.189}$$

From 3.189 is possible to find for typical experimental irradiance numbers the estimated electric fields: $E_s \sim 10^3$ GV/m. Such enormous field ionizes light atoms of the contamination layer at the rear surface, usually composed by hydrocarbons or deposited water vapour. Light ions, specially protons due to their high charge-to-mass ratio $q/m = 1$, are easily accelerated in the direction of the surface normal. Nevertheless, protons can also originate from the bulk of the target if made of H-rich material (plastic). Once a sufficiently high number of ions move through the Debye sheath, charge balance starts to be locally restored; when the accelerated ions leave the target they drag a co-moving electron beam from the sheath. The result of this process is, not taking into account the associated electron beam, is a multi-species, high charge, high-divergence and extremely broadband MeV-energy ion beam.

Evidence for the origin of the ions at the rear surface was made clear performing the experiment on metallic foil targets, but only after cleaning the rear surface from impurities. In such a case, proton yield is extremely reduced, and the charge balance is of the sheath not achieved so fast. Therefore, heavier ion species are accelerated over a longer time scale [153]. Spectral measurements show a quasi-Maxwellian ion spectrum with a sharp cut-off E_{cut}, which has been modelled by several different theoretical models under different assumptions [21, 22]. An extensive study of the scaling of E_{cut} with the laser and target parameters has been carried out over the last decades. The cutoff energy seems to follow a positive scaling with the laser intensity I (usually, the higher the laser intensity and energy, the larger the proton cut-off). Proton deflectometry experiments have demonstrated the existence of the accelerating sheath [154]. Models also describe the dependency of the ion yield and its spatial and angular characteristics with respect to the sheath spatial distribution, and therefore on the target properties affecting electron propagation. Experiments show this dependency as they generate inhomogeneous beams with larger cutoff energies

in the central part of the beam and lower ones in the edges. Resistivity and thickness of the target (as well as the the structure of the rear surface) define the size, shape and magnitude of the electron sheath. For instance, conducting targets show smooth proton beam profiles with sharp boundaries, meanwhile insulator target as plastic, which are prone to electron stream filamentation, show inhomogeneities at the sheath (and therefore in the ion beam shape). There is also a crucial dependency on the ion density scale length at the rear surface, which has been demonstrated with experimental suppression of the ion acceleration when a preplasma is formed on the rear surface.

Some other important aspects of TNSA are decisive for a proper understanding of the mechanism. Thicker targets in TNSA normally yield lower E_{cut} as they imply a longer path for hot electrons until the rear surface and the formation of a weaker sheath. Nevertheless, it has been observed that the scaling with target thickness is coupled to the level of contrast of the laser system [155]. The presence of a preplasma generated by the laser pedestal in the front surface affects the coupling between laser energy and hot sheath electrons. For sub-micron targets it could led to the target vanishing prior to the main pulse arrival. Nevertheless, for certain thickness range it seems that the preplasma could enhance hot electron conversion and therefore the proton yield. Control and measurement of the laser contrast have become a crucial requirement in intense laser laboratories nowadays.

On the other hand, TNSA is not the only laser-solid target ion acceleration mechanism. Other mechanisms include:

- Radiation Pressure Acceleration (RPA) [6] this regime is divided in two different subclassifications: the Hole Boring regime (HB) for thick targets and the Light Sail regime (LS) for thin ones. This mechanisms is based on the effect of radiation pressure onto the front surface of the target overdense plasma. Light momentum is transferred to electrons and hence to the ions by charge separation. When the target is thinner than the skin depth of the interaction, complete hole boring occurs and the target can be accelerated as a whole; in LS regime there is not a plasma background to screen the laser fields. This regime requires of ultra-clean laser pedestal and it is favoured by circular polarization (which prevents from excessive electron escaping). Because of its scaling of the ion cut-off energy as $E_{cut} \sim I/(An_i c)$, RPA has become a promising acceleration mechanism when ultra-relativistic laser irradiances become accessible.

- Break-Out Afterburner (BOA) [156]: when ultrathin foils are irradiated by pedestral-free ultra-intense laser pulses, it is possible to access the relativistic transparency regime. As described in 3.161, this is caused by the effective change of the plasma frequency (and therefore the plasma opacity threshold) due to the inertia acquired by the relativistic quiver electrons. In this regime, volumetric heating of the plasma slab can be achieved and access to stronger accelerating fields is possible.

A secondary effect of the laser-solid interaction is also remarkable the generation of high-energy photons due to the deceleration of relativistic electrons in the bulk of the plasma, following equation 3.170, in a process known as Bremsstrahlung. Also, as a result of recombination of heavy ionized atoms, K-line emission is also generated. The combination of these two X-ray sources are intrinsic to the laser-overdense plasma interaction, but with rather broad emission angle. However high X-ray and γ-ray photon energies can be achieved of interest for deep penetration X-ray imaging when compared with Betatron sources.

3.3.3 Laser-driven acceleration in NCP

The interaction of short and intense pulses with plasmas of electron density $n_e \sim 0.1 - 1\, n_c$ -the so called near-critical regime- has attained lately plenty of attention, as it is predicted to

enhance the energy coupling between the laser and the plasma due to volumetric effects [71, 157, 158]. An intense laser pulse focalized onto a near-critical plasma can trigger a strong charge separation along the longitudinal direction, which can drive an electrostatic shock wave [159, 160]. The charge separation can be caused directly by the hole boring effect on the opaque region (if any) of the plasma [158, 160, 161] as shown in the previous section, or indirectly by the pressure gradients associated with the laser heating of the bulk electrons in a transparent inhomogeneous plasma [73, 162–164]. The shock wave, which propagates with supersonic velocities, travels through the plasma and it will reflect background ions at twice the shock velocity ($v_{ion} = 2v_{sh}$) if their initial kinetic energy is smaller than the potential barrier of the shock ($Ze\Phi > m_i v_i^2/2$). The mechanisms of shock acceleration triggered by electron energization is normally known as Collisionless Shock Acceleration (CSA). Depending on the target conditions, CSA may be accompanied by other acceleration mechanisms as TNSA [158, 160] or magnetic vortex acceleration [165–169]. Simulations have shown (and experiments have demonstrated up to a point) that the proper combination of these mechanism can yield up to 100 MeV level monoenergetic collimated ion beams. Such beam characteristics, along with a high averaged particle flux thanks to the high repetition rate of the new laser and target systems, would mean a breakthrough milestone for the ion beams for medical applications, where 100 to 200 MeV proton energies are desirable.

It is worth to outline at this point that MeV electron beam acceleration of remarkable charge have been demonstrated in near-critical plasmas as well [170, 171]. Alternatively, radial [172] and forward [173] ion acceleration has been demonstrated in underdense plasmas. Such an effect is attributed, similarly as in LWFA, to the electrostatic fields generated in the electron depletion channel formed after the ponderomotive laser pushes out electrons.

The production in the laboratory of near-critical plasmas remains a nontrivial task, especially when high repetition rate ion sources are needed. From 3.151, density values required for the widely available near infra-red ultrashort lasers ($\lambda \sim 1$ μm) are around 10^{21} cm^{-3}, which lies above atmospheric pressure gases but below liquid and solid densities. Experimental realization of such target has been shown by the use of exploding foils (using either the laser pedestal or a second separated prepulse) [161, 174–176], nano-wire arrays [177], foam targets [157, 171, 178] or high-density gas jets [74, 162–164, 170, 179]. The latter has the advantage of being intrinsically compatible with debris-free high repetition rate operation of the Ti:Sa laser systems. Nevertheless, moderate intensity lasers are available at other wavelengths range, such as the mid-infrared CO_2 laser at $\lambda \sim 10$ μm, for which $n_c \sim 10^{19}$cm^{-3}; this is a typical moderate pressure gaseous target. Monoenergetic (1% spread) proton beams of 10s of MeV have been achieved in this regime with CO_2 laser pulses of only $a_0 \sim 2$ [72].

Despite the enormous experimental effort worldwide in NCP-laser interaction experiments, it is important to outline that most of these shock acceleration experiments have relied on high-energy ($\sim$ 100 J), picosecond duration low-repetition-rate Nd:glass lasers. Significant CSA detection observed in HRR petawatt femtoseconds-class lasers have been only reported in the transverse direction of the laser to the date [164], never in the forward axis. The experimental achievement of CSA acceleration in the forward direction remains unaccomplished. Its experimental demonstrations with gaseous dense targets would set the principles for a debris-free HRR-compatible ion acceleration program.

3.3.4 Charged Particle Beams

In terms of spatial quality, the ideal particle beam consists of individual particles whose trajectories never intersect as in a laminar fluid. Such a "laminar" beam should follow the conditions [77]:

- Particles at certain positions should have identical transverse velocities. If the beam propagates in the z-axis, then identical velocities in x-axis and y axis.
- The magnitude of the transversal slopes $x'(z) = \frac{dx}{dz}$ and $y'(z) = \frac{dy}{dz}$ should be proportional to the displacement from the z-axis. This is also referred to as a beam with *linear correlation*.

It is common in beam physics to consider the paraxial approximation since $p_{x,y} \ll p_z \approx p$. In such a case $x' \approx p_x/p$ and $y' \approx p_y/p$. Particles in a realistic beam (non-laminar) have a distribution of transverse velocities at the same locations, and therefore a spread in directions. The achievement of perfectly laminar beams in the laboratory is difficult due to the nature itself of the beam generation mechanism, misalignments and chromatic effects of the beam transport and acceleration devices or simply by the collective effect produced by the beam itself via the Coulomb interaction, the so-called *space charge* force. The degree of the laminarity of the beams is often referred to as the beam quality; laminar beams are quite desired for applications, as they are easier to transport and can be focused to smaller spot sizes.

The propagation of the beam is defined by its 6D phase space (x, p_x, y, p_y, z, p_z). According to Liouville theorem if no dissipative forces are applied, neither particles created or lost and no binary collisions are considered, the space occupied by a beam in the phase space is conserved. Moreover, if the forces are uncoupled in each axis the theorem holds for each reduced phase space $(x, p_x), (y, p_y), (z, p_z)$ [180]. When p is constant (no longitudinal acceleration considered) the phase space is equivalent to the trace space (x, x') as $p_x \approx x'p$. A perfect laminar beam shows a perfect linear correlation between coordinate and momentum, therefore it would be represented in the trace space by a straight line, meanwhile realistic beams occupy larger areas. Example of a imperfect beam trace space is shown in figure 3.24.

The geometrical emittance is considered as figure of merit of the quality of the beam, as it increased with the area occupied by the beam in the trace space. It can be expressed separately for each transverse direction of the beam in terms of the statistical moments of the distribution function $f(x, x', z)$ of the trace space, in which case it is called rms (root mean square) geometrical emittance. It is given as

$$\epsilon_{rms,x} = \sqrt{\langle x^2 \rangle \langle x'^2 \rangle - \langle xx' \rangle^2}. \tag{3.190}$$

$\langle x^2 \rangle$ and $\langle x'^2 \rangle$ are the corresponding x and x' distribution variances, whose square roots are the standard deviation of the distribution projected in the corresponding axis $\sigma_x = \sqrt{\langle x^2 \rangle}$ and $\sigma_{x'} = \sqrt{\langle x'^2 \rangle}$. They are given by

$$\langle x^2 \rangle = \frac{\int_{-\infty}^{\infty} \int_{-\infty}^{\infty} (x - \langle x \rangle)^2 f(x, x') dx dx'}{\int_{-\infty}^{\infty} \int_{-\infty}^{\infty} f(x, x') dx dx'} \tag{3.191}$$

and

$$\langle x'^2 \rangle = \frac{\int_{-\infty}^{\infty} \int_{-\infty}^{\infty} (x' - \langle x' \rangle)^2 f(x, x') dx dx'}{\int_{-\infty}^{\infty} \int_{-\infty}^{\infty} f(x, x') dx dx'} \tag{3.192}$$

where $\langle x \rangle$ and $\langle x' \rangle$ are the mean position and pointing of the beam

$$\langle x \rangle = \frac{\int_{-\infty}^{\infty} \int_{-\infty}^{\infty} x f(x, x') dx dx'}{\int_{-\infty}^{\infty} \int_{-\infty}^{\infty} f(x, x') dx dx'} \tag{3.193}$$

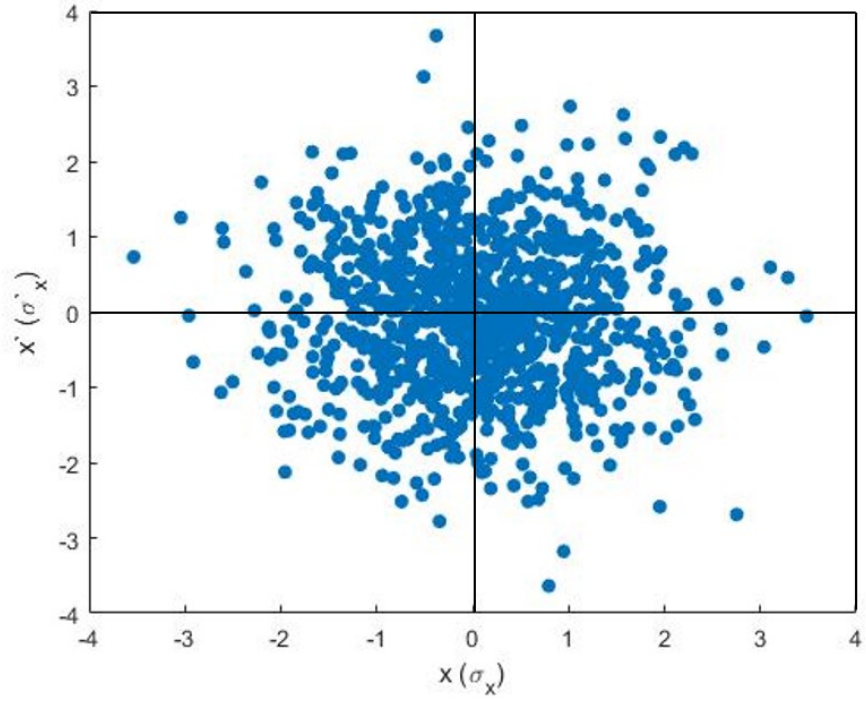

FIGURE 3.24: Trace space representation of a normal (in each axis) particle distribution. The axis units are given in terms of the standard deviation of each quantity for the given distribution.

and

$$\langle x' \rangle = \frac{\int_{-\infty}^{\infty}\int_{-\infty}^{\infty} x' f(x,x') dx dx'}{\int_{-\infty}^{\infty}\int_{-\infty}^{\infty} f(x,x') dx dx'}. \tag{3.194}$$

The correlation term (often called covariance) is defined in an similar way

$$\langle xx' \rangle = \frac{\int_{-\infty}^{\infty}\int_{-\infty}^{\infty} xx' f(x,x') dx dx'}{\int_{-\infty}^{\infty}\int_{-\infty}^{\infty} f(x,x') dx dx'}. \tag{3.195}$$

Furthermore, it can be shown that for a phase-space with no area but with a non-linear correlation ($x' \propto x^n$ with $n > 1$) then $\epsilon_{rms,x} \neq 0$. Therefore, the emittance is simultaneously a measurement of the non-linearity of the beam correlation.

Other useful definition (especially when the beam is exposed to accelerating fields) is the normalized emittance, where the transverse momentum is used instead of the divergence:

$$\epsilon_{N,rms,x} = \sqrt{\langle x^2 \rangle \langle p_x^2 \rangle - \langle x p_x \rangle^2}. \tag{3.196}$$

The reason behind this definition is that $\epsilon_{N,rms,x}$ is conserved during longitudinal acceleration as p_x is not affected, meanwhile x' is reduced as p increases. For a small energy spread beam both emittance definitions can be related by

$$\epsilon_{N,rms,x} \approx \beta\gamma\epsilon_{rms,x}. \tag{3.197}$$

Generation of ultralow emittance (i.e. excellent quality) beams have been demonstrated both in electron beams accelerated by LWFA [76, 181, 182] and in ion beams accelerated by TNSA [29, 35]. In the latter case, the low emittance is attributed to the ultrafast nature

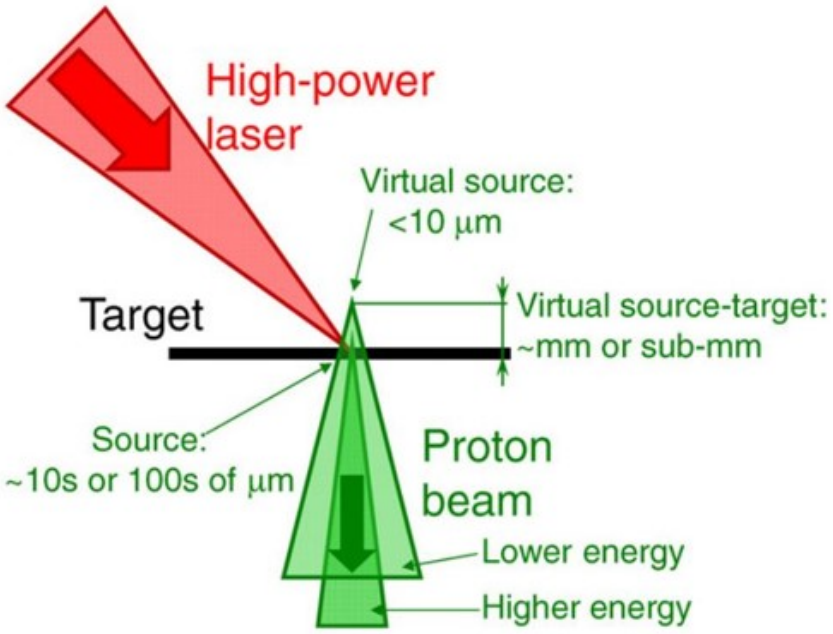

FIGURE 3.25: Diagram of the virtual source emission of a high-laminar laser-driven beam. The beam appears to be originated from a smaller diameter source before the target. Higher energy components are normally found to be concentrated in the center of the beam. Image taken from [21].

acceleration mechanism (i.e. the charge separation generating the strong accelerating field) whose duration is on the order of the driver pulse length, emerging from an initially unperturbed non-ionized surface. Laminarity is favoured when interacting with conducting materials, as they prevent from filamentation of the electron stream towards the rear surface, creating a smooth Gaussian-like accelerating field shape. Also, the beam transversal quality is benefited from the facts that the sheath field self-consistently evolves with the ions and thanks to the suppression of space charge effects as the ions are quasi-neutralized by a co-moving electron beam during part of the acceleration process. Measurements by grid method [35, 183, 184] and groove imaging technique [29, 34, 185] yield as best result $\epsilon_{N,rms} \sim 0.004$ mm mrad, this is two orders of magnitude better quality than conventional radiofrequency accelerators (e.g. proton RF-linac at CERN presents a normalized emittance > 5 mm mrad).

Even if the origin of the particle beam is a region of a given dimension (for the case of TNSA ions, it has been experimentally determined onto an area of approximately 100s micrometers of diameter at the rear surface of the target), these divergent quasi-laminar beams can be understood as being generated from a very small source behind the target [186]. Such result is just an interpretation of the (linear) correlation between particle coordinates and momenta given by the phase space. A comprehensive sketch of this interpretation can be found in figure 3.25.

Delivery, control and measurement of low-emittance beams is a key step in the way for achieving wider application range of the laser driven accelerated particles. Referring to electron beams, high charge and short pulse duration beams (i.e. high peak current) with minimized energy spread and transverse emittance (as low as a few π mm mrad) are required for applications, such as high-field THz sources [187] or high-brightness free-electron laser [188]. On the other hand, most of applications of ion beams (such as hadrontherapy [42]) require proper transport and focalization of the particles. The laminarity that the laser-driven ions demonstrate is a perfect characteristic for post-acceleration

beam control, either by all-optical methods [33], conventional magnetic [32] or electromagnetic (solenoid) lensing [189] or directly by target engineering. Spectrum shaping, beam transport and focusing of laser-generated protons has been experimentally demonstrated. Moreover, the short lived charge imbalance which is the origin of the proton bunches makes them as short as a few picoseconds, orders of magnitude shorter than conventional radiofrequency accelerator bunches.

In addition, combination of short duration and low emittance makes these beams useful for specific applications as proton radiography. The interest of this technique comes from the sensitivity of the proton trajectories to the electric and magnetic fields inside the sample, resulting in a powerful field probing method [64]. The low emittance of the beam brings high spatial resolution when performing these experiments by back-illuminating a sample, which can be a laser-driven transient plasma that can be temporally resolved thanks to the short beam duration.

Chapter 4

Experimental methods

This chapter presents the different methodological and technical aspects of the equipment and diagnostics systems for laser-driven particle acceleration relevant for this work. Firstly, the ultrashort ultraintense laser system VEGA is introduced, which was the driver laser of all the experiments shown in this manuscript. Secondly, the working principle of several techniques for gaseous target characterization are shown, as well as the their potential use for ultrashort probing for transient plasma density measurements. Finally, several ion beam diagnostics are presented, including Thomson Parabola spectrometers and beam emittance monitors.

4.1 VEGA laser system

The experiments shown in this manuscript were carried out at the Spanish Centre for Pulsed Lasers (Centro de Láseres Pulsados, CLPU) at Salamanca, Spain; more specifically in the VEGA 2 and VEGA 3 laser facilities. VEGA is a unique and versatile CPA Ti:Sa pulsed laser whose dedicated architecture was designed to provide three different and independent outputs, all of them synchronized as they share the front end as a seed for amplification (see figure 4.1). The front-end generates low energy pulses at MHz repetition rate, and several Pockels cells are used to select the pulses that are injected into each line and consequently amplified. Three different amplification chains and compressors yield three increasing power outputs, as summarized in the table 4.1.

The broad spectrum of VEGA is shown at figure 4.2. Its bandwidth is centred at 800 $\pm$ 10 nm. The spatial beam profile is super-gaussian ($M^2 \approx 1,5$, FWHM $\approx$ 225 mm), with $<$ 7% rms modulation on the plateau.

Control of the energy is achieved by modification of the amplification chain (adjusting amplification steps or varying the delay between active medium pumps and seed pulse) and the pulse duration is controlled by means of either pulse compressor modification (change of the distance between the compressor gratings) or spectral phase corrections with a acousto-optic programmable dispersive filter (or Dazzler by Fastlite company) [190]. Both energy and pulse duration are monitored shot to shot thanks to calibrated leaks and reflections from the main beam. Energy is measured by pixel integration of the picture of the

Laser	Power (TW)	Pulse energy (J)	Pulse duration (fs)	Rep. rate (Hz)
VEGA 1	20	0.6	30	10
VEGA 2	200	6	30	10
VEGA 3	1000	30	30	1

TABLE 4.1: Summary of VEGA laser system parameters.

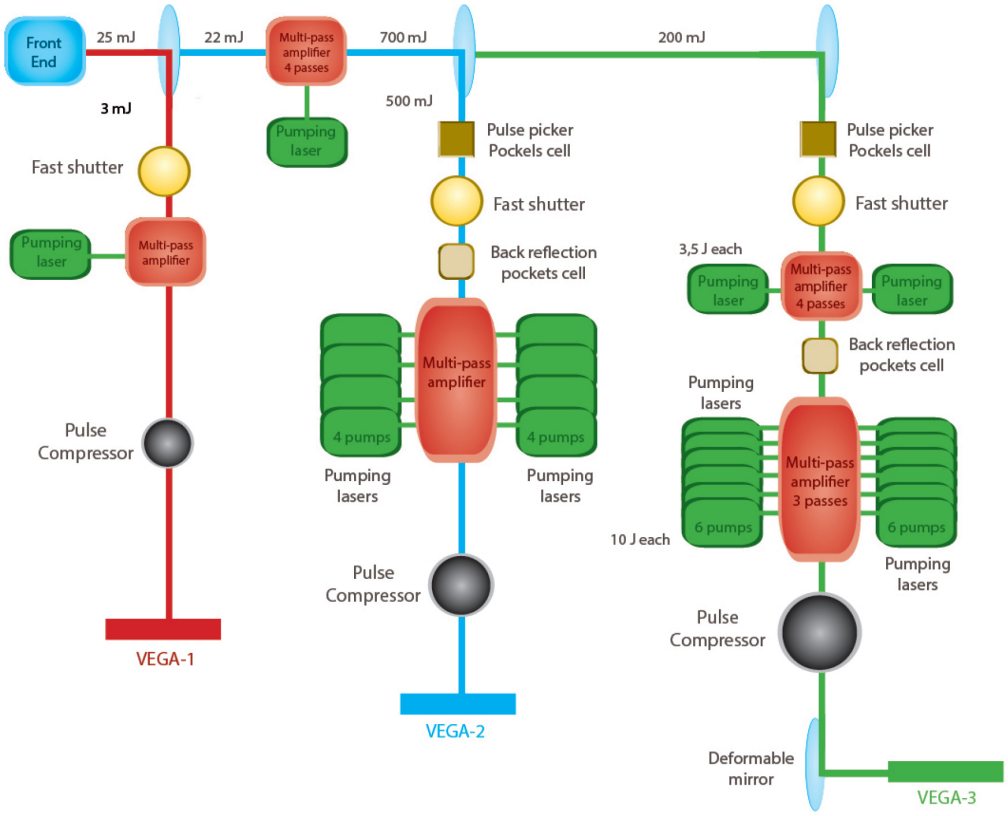

FIGURE 4.1: Sketch of VEGA laser system. The amplification chains of the three outputs are drawn vertically.

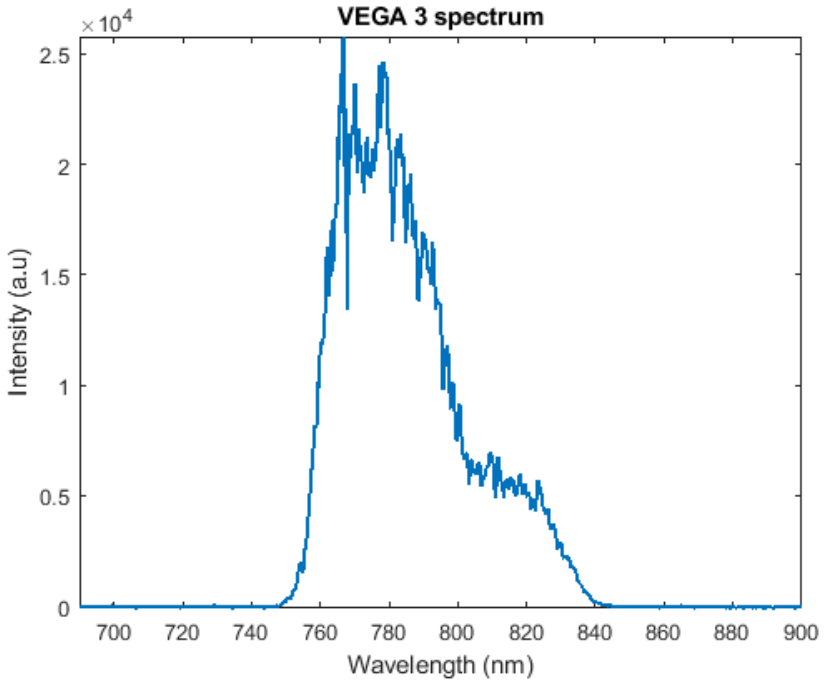

FIGURE 4.2: VEGA 3 spectrum measured with CCS/200 optical spectrometer from Thorlabs Inc.

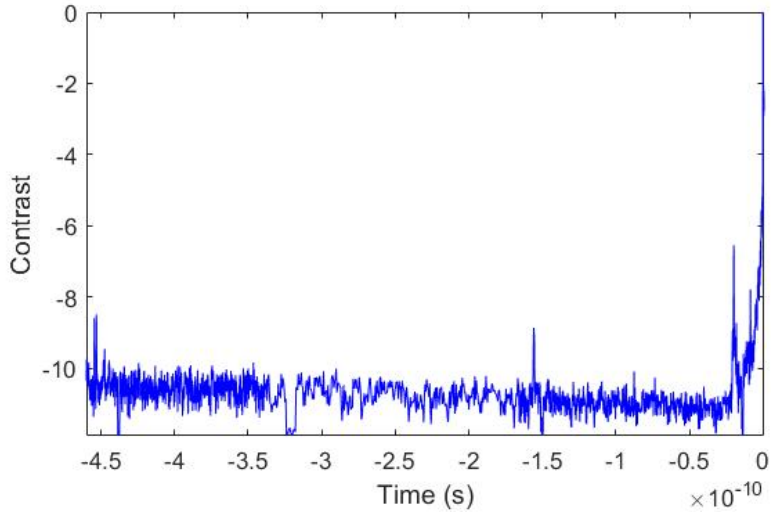

FIGURE 4.3: VEGA 2 laser log-scale contrast measured by high dynamic range third order auto-correlator Sequoia from Amplitude Laser, Inc. [92]. The y-axis, in logarithmic scale, is normalized to the peak intensity, set at $t = 0$.

Contrast				
Laser	@ >100 ps	@ 10 ps	@ 5 ps	@ 1 ps
VEGA 2	5×10^{-10}	1×10^{-9}	5×10^{-7}	6×10^{-5}
VEGA 3	5×10^{-12}	8×10^{-9}	5×10^{-8}	2×10^{-5}

TABLE 4.2: Level of contrast of the VEGA system measured at different times before the pulse peak.

near-field image of one of those leaks at the laser main amplifier exit. The energy on target is calculated by considering a energy loss factor from the compressor entrance to TCC (around 0.66 for VEGA 3), calibrated before the experiment. Meanwhile the pulse duration is measured at two separated points of the beam transport: one right after the compressor by means of a SPIDER (spectral phase interferometry for direct electric-field reconstruction [191]) and other before the focalization point, in the Target Area (TA), by a second order single-shot autocorrelator (ASF-15M by Avesta Ltd.) The pulse contrast (i.e. the intensity measured at some time prior to the pulse peak, normalized to the intensity maximum) is minimized by means of the XPW system, reaching values as good as shown in the Table 4.2. Refer to figure figure 3.8 for an actual contrast measurement by third order auto-correlator Sequoia device of VEGA 3. The pulse contrast for VEGA 2 is shown in figure 4.3.

After its pass through the compressor and being delivered to the experimental area, the beam is transported in vacuum by means of dielectric or metallic mirrors (with the corresponding reflection losses) until the interaction chamber, where the beam is normally focused by an off-axis parabolic (OAP) mirror onto the interaction point, which is normally referred as target chamber center (TCC). The spatial profile quality factor of the beam (and its aberrations) and the focusing geometry of the OAP mirror will define the size and shape of the beam at the waist. Furthermore, relative position between target and focal position will define the intensity profile of the laser at the interaction. For the experiments shown in this manuscripst, the VEGA Target Area operators were in charge of the focal spot optimization (Dr. J. A. Pérez-Hernández and Dr. J. I. Apiñaniz) meanwhile the pulse duration measurement was carried out by Dr. J. A. Pérez-Hernández and Dr. R. Lera.

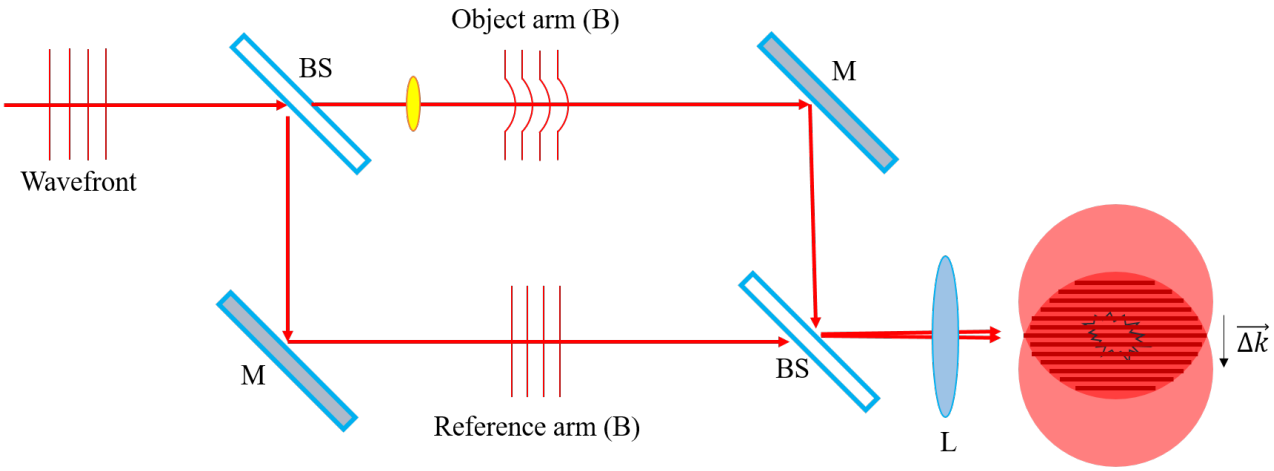

FIGURE 4.4: Basic Mach-Zehnder interferometer operation. M stands for mirrors, meanwhile BS for beams-plitters and L for an imaging lens.

4.2 Gas target characterization

As seen in Chapter 2, the density of the target in a laser-plasma interaction experiment is a fundamental parameter. Actually, the classification of such experiments is normally arranged as a function of the transparency regime of laser and plasma, which is a function of the laser wavelength and plasma electronic density. In the underdense case ($n_e < n_c$), both for LWFA and HHG [192], normally moderate-pressure gas structures (jets or cells) are used as targets in these experiments. Also, it has been proven that experiments at the near-critical density regime (for near-IR lasers) are feasible in gas with dedicated high-pressure systems [74, 162–164, 170, 179].

Gas targets have the advantage to be transparent to optical radiation (before and after ionization). Therefore, optical measurements of the density profile of the gas are possible prior to ionization, or even off-line target calibration can be done in parallel to the experiment (between laser shots) or previously in dedicated characterization campaigns. From the information retrieved about the neutral gas density, a prediction about the expected ionization degree can be made (depending on the laser intensity and gas ionization potential) and an estimation of the electronic density can be obtained [66, 67, 193, 194].

Gas jets operation is based in three different basic components. Firstly, there should be a reservoir filled with the desired gas (or controlled mixture) at a certain backing pressure. Such reservoir connected to a valve inside the interaction chamber thanks to a series of high pressure hoses to the valve. The valve is a normally-closed remotely-controlled electro-mechanical device; when a specific voltage is applied to the valve, it opens and let the gas flow into the chamber for a certain period of time (normally on the order of tens of milliseconds). Finally, the gas flow into the chamber is shaped by a nozzle, which is directly attached to the valve orifice. The dimensions and geometry of the nozzle, the backing pressure, gas species and valve opening time are the defining elements of the target which will shape the target density profile in the vicinity of the nozzle.

A list of different diagnostics tools for gaseous density measurement (relevant for this work) is elaborated in this section.

4.2.1 Interferometry

Interferometers are practical tools for measuring the phase of laser beams and they are commonly used for characterizing gaseous targets by means of optical components and

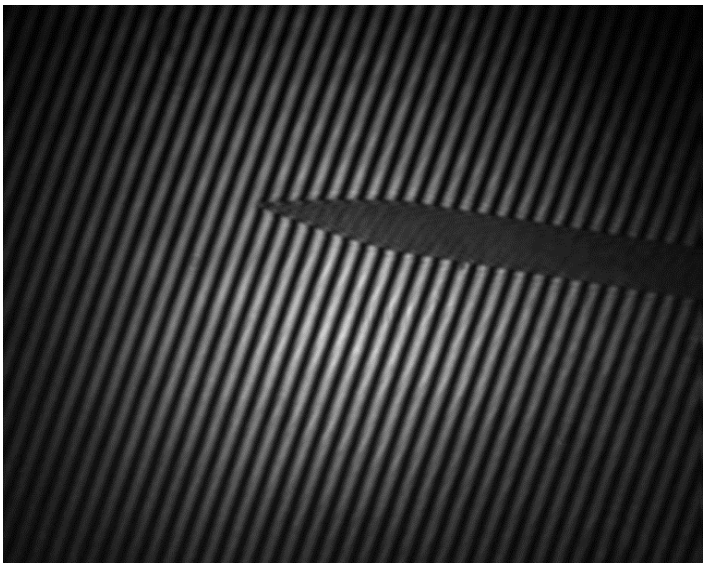

FIGURE 4.5: Interferogram generated by a Mach-Zehnder interferometer. A known object (a needle) was placed at the object plane for space calibration purposes.

measuring their refractive index [63, 195]. The method shown here is mainly based in the work of [67, 70, 194, 196] and similar references. As shown in figure 4.4, the operation principle is based on the splitting and recombination of a laser beam. Along their separate paths, one of the arms will act as a reference beam (B), meanwhile the other (A) will go through the gas, acquiring an extra optical phase. Simplifying the beam as a plane wave, the electric field of each arm can be written as

$$\mathbf{E}_A = \mathbf{E}_{A,0} e^{i(\mathbf{k}_A \cdot \mathbf{r} - \omega t + \phi(\mathbf{r}) + \phi_0)} \tag{4.1}$$

$$\mathbf{E}_B = \mathbf{E}_{B,0} e^{i(\mathbf{k}_B \cdot \mathbf{r} - \omega t)} \tag{4.2}$$

where $\phi(\mathbf{r})$ is the phase difference acquired by the arm A due to the object, and ϕ_0 is any other phase difference between the arms. The object is imaged into a imaging sensor chip with the help of a lens system. The condition for interference fringes at the detector plane is that both beam polarizations have parallel components (or they are totally parallel, $\mathbf{E}_{A,0} || \mathbf{E}_{B,0}$) which is naturally achieved in a Mach-Zehnder interferometer (MZI) as the one depicted in figure 4.4. Intensity (i.e. the square of the total electric field) is the physical quantity that the pixels of the imaging sensors measure, being in this case

$$I_{AB} = |\mathbf{E}_A + \mathbf{E}_B|^2 = E_A^2 + E_B^2 + 2\Re(E_A E_B^*) = E_{A,0}^2 + E_{B,0}^2 + 2E_{A,0}E_{B,0}\cos(\Delta\mathbf{k} \cdot \mathbf{r} + \phi(\mathbf{r}) + \phi_0). \tag{4.3}$$

This is, a slow-evolving term (depending on the beams amplitude profile inhomogeneities) and a fast beating term (the fringes, i.e. the cosine term in equation 4.3) which has the information about the object $\phi(\mathbf{r})$, coded as a shift in the fringes. An example of a non-perturbed fringe pattern is seen in figure 4.5, meanwhile the shift caused by the presence of gas can be observed in figure 4.6. The fringe geometry (orientation and thickness) is determined by the angle between both beams ($\Delta\mathbf{k} = \mathbf{k}_A - \mathbf{k}_B$, see figure 4.4), and it can be experimentally controlled by independent tilt control of A and B beams.

The phase term can be retrieved by Fourier Transform (FT) analysis of the interferometry pictures.

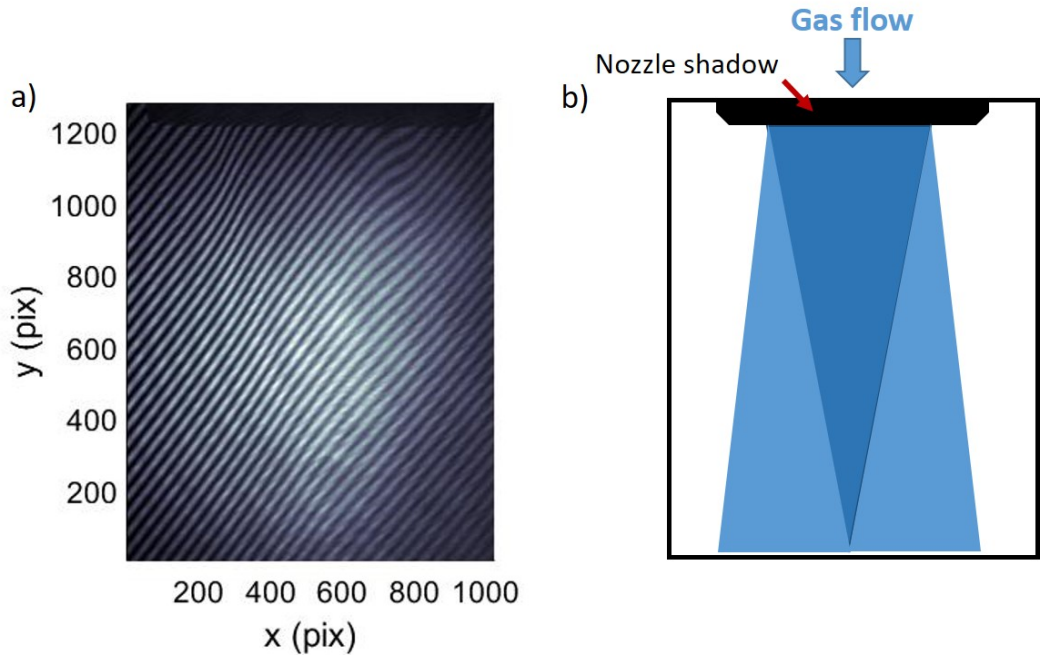

FIGURE 4.6: a) Interferometry taken during the stream of a Nitrogen gas jet target. The shadow at the image top is the nozzle. Fringe shift can be appreciated. Data taken for a nozzle with external orifice of $\sim$ 2 mm backed with 70 bars of Nitrogen. b) Schematic interpretation of the interferometric picture.

- First, a two-dimensional Fourier Transform of the picture is performed. Fast Fourier Transform (FFT) [197] algorithm is used.
- After applying a square mask around the spatial frequency of the fringes (see figure 4.7), the inverse FFT is performed.
- The argument (phase) of the inversed FT is calculated (see figure 4.8).

A reference interferogram can be obtained by repeating the measurement without the presence of the target. In such case

$$I_{AB,ref} = E_{A,0}^2 + E_{B,0}^2 + 2E_{A,0}E_{B,0}\cos(\Delta\mathbf{k}\cdot\mathbf{r} + \phi_0). \tag{4.4}$$

If the same process is applied to the reference, information of $\phi(\mathbf{r})$ is available after phase subtraction, as shown in figure 4.9.

It is easy to relate this extra optical phase with respect to the reference case in vacuum ($n = 1$) to the index of refraction of the gas by the line integral

$$\Delta\phi = \frac{2\pi}{\lambda}\int (n-1)dl. \tag{4.5}$$

Finally, it is possible to relate the index of refraction the gas to its density via the Lorenz-Lorentz equation seen in Chapter 2. For most gases, where $n \approx 1$, expanding to the first order of the Taylor series, the Lorentz-Lorenz equation 3.82 becomes

$$N = \frac{2\epsilon_0}{\alpha}(n-1). \tag{4.6}$$

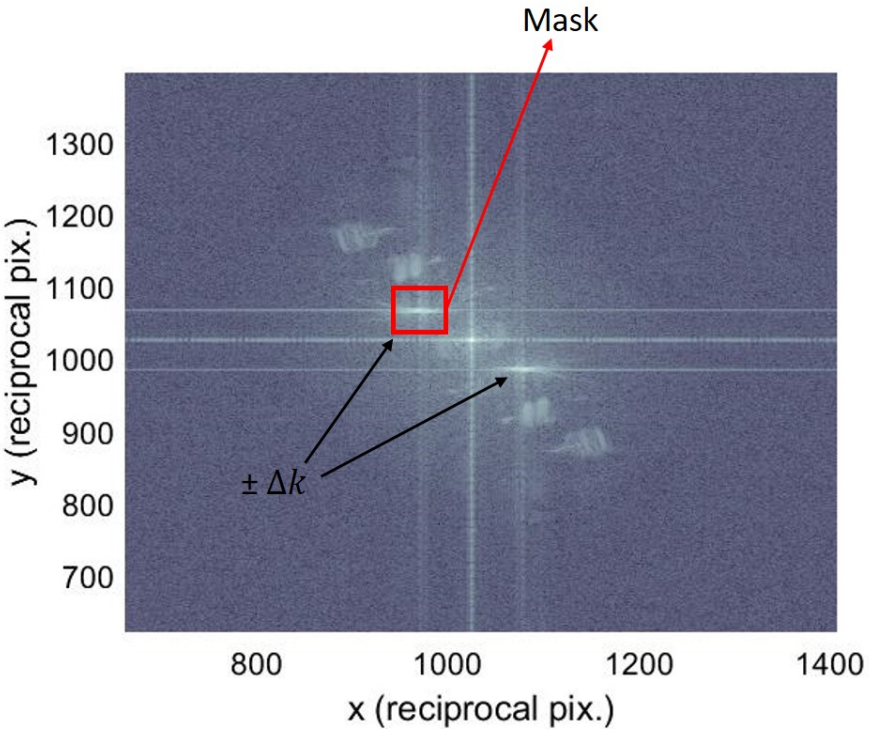

FIGURE 4.7: Log-scaled modulus of the FT of 4.6.

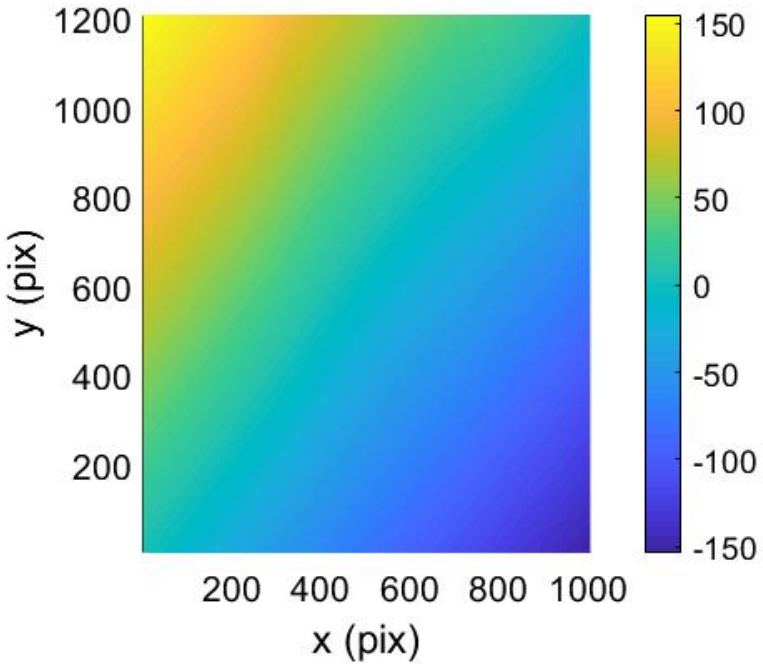

FIGURE 4.8: Phase (in radians) retrieved from inverse FT of masked 4.7.

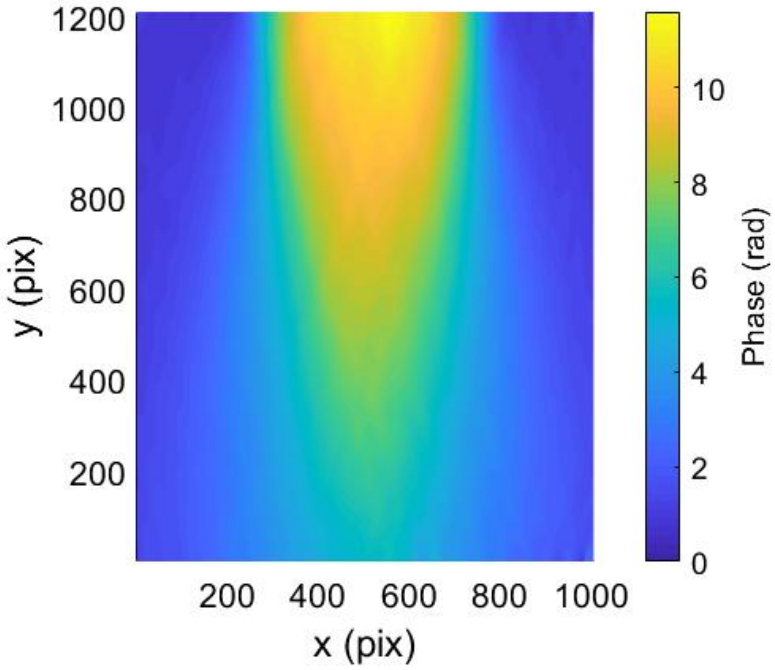

FIGURE 4.9: Optical phase acquired by the laser due to its travel through the gas jet.

Therefore, relating the extra optical phase measured by the interferometer to the density of the gas is straightforward. Nevertheless, there are different possibilities to deal with the integral 4.5 and obtain an expression for the local refractive index:

- For some nozzle geometries, such as for rectangular output orifices [196], it is a reasonable assumption (but not totally true) to take the gas jet profile as a flat top with a fixed plateau value (which depends on the distance to the nozzle edge) above the orifice, and zero elsewhere. In that case 4.5 is

$$\Delta\phi = \frac{2\pi}{\lambda}(n-1)L, \tag{4.7}$$

  with L the nozzle length (in the probing direction). This means

$$N = \frac{\epsilon_0\lambda}{\pi\alpha L}\Delta\phi. \tag{4.8}$$

- For a cylindrically symmetrical nozzle (for instance, a conical nozzle) it is a good assumption to consider the gas jet itself as symmetrical around its central axis (in figure 4.9 the projection of the jet can be considered symmetrical around the central Cartesian x-axis). Therefore, from the two-dimensional projection of the integrated phase measured by the interferometer it is possible to infer the three-dimensional (or radial) profile of the gas following the mathematical transformation called Abel Inversion [198, 199] (in each pixel line):

$$\phi(r) = -\frac{1}{\pi}\int_r^R \frac{d(\Delta\phi(x))}{dx}\frac{1}{\sqrt{x^2-r^2}}dx = A^{-1}(\Delta\phi(x)). \tag{4.9}$$

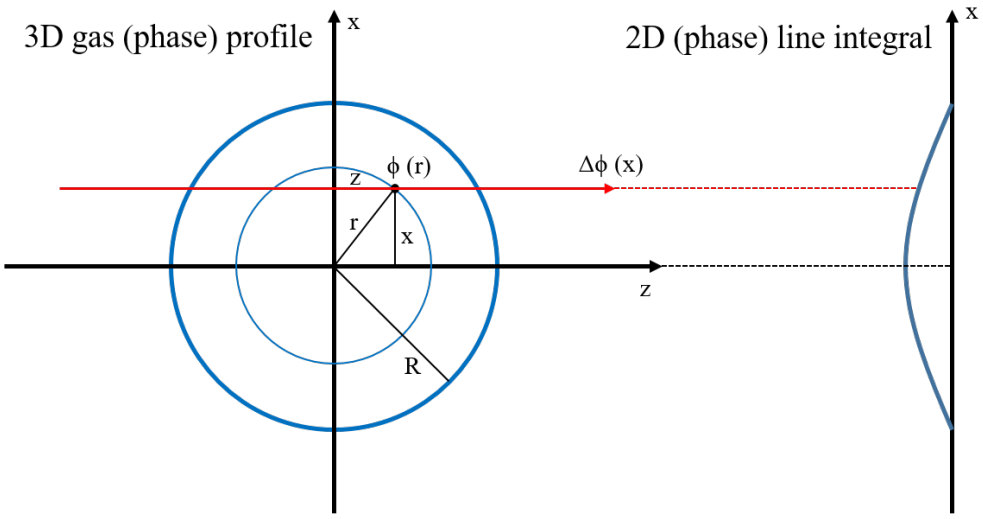

FIGURE 4.10: Abel inversion scheme. Cartesian axis orientation is equivalent to the example phase map 4.9. The red line represents the probing laser direction, meanwhile the blue lines are gas density contour lines. R is the radius at which the density ideally vanishes.

See figure 4.10 for a geometrical sketch of the Abel inversion. Joining equation 4.9 and equation 4.5 yields

$$\frac{2\pi}{\lambda}(n(r)-1) = A^{-1}(\Delta\phi(x)). \tag{4.10}$$

The final expression for the local molecular density has to account for the variable transformation, as the Abel inversion is performed in units of pixels. Therefore

$$N(r) = \frac{\epsilon_0\lambda}{\alpha\pi\vartheta}A^{-1}(\Delta\phi(x)), \tag{4.11}$$

where ϑ is the spatial calibration of the image given in [length/pix] (i.e. the lateral size of a pixel multiplied by the imaging system magnification).

It is a standard procedure to average left and right sides of around the symmetry axis (before applying the Abel inversion) in order to minimize possible errors coming from asymmetry. The inversion can be numerically solved, for instance, by means of the 3-points method following [200] or by Fourier-series-based algorithms as in [198]. In the later case, different upper frequency limits (UPF) can be applied; this is the order cosine expansions in which the inversion is reconstructed

$$A^{-1}(r) = \sum_{n=0}^{\text{UPF}} C_n f_n(r), \tag{4.12}$$

where C_n is a weighting constant and

$$f_0(r) = 1,\ f_n(r) = 1-(-1)^n\cos\left(n\pi\frac{r}{R}\right). \tag{4.13}$$

The selection of the UPF is important for noise-filtering, as its choice acts as a low-pass filter for very small values, but could erase potential structure features. Different profile geometries may required from appropriate UPF choice for best reconstruction. Finally, after inverting the profile for each y (distance to the nozzle), the full three-dimensional map of the gaseous target density is achieved, as shown in fig 4.11,

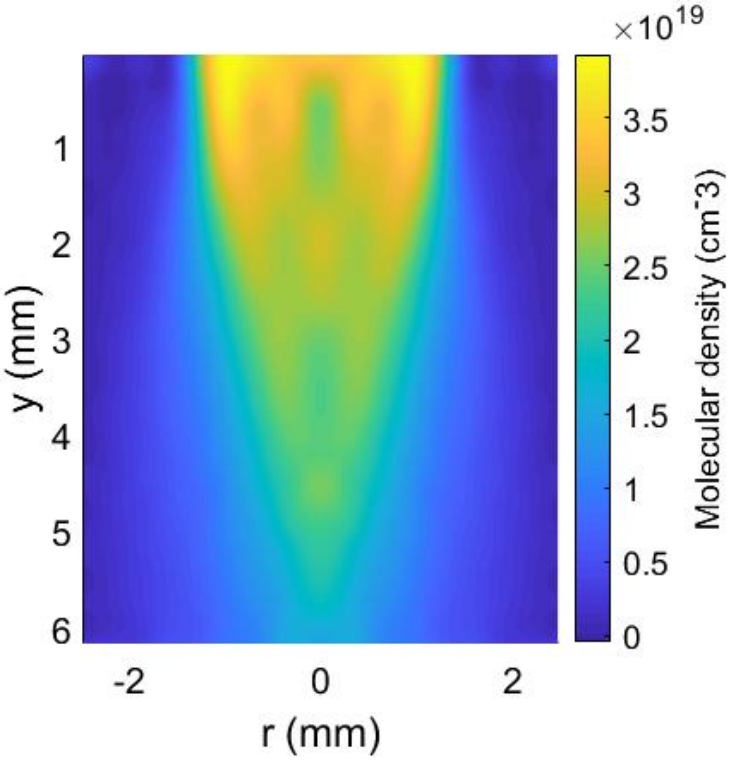

FIGURE 4.11: Typical conical nozzle gas density profile after analysis of 4.6. The coordinate origin is set at the nozzle edge ($y = 0$) and on the center of the nozzle (i.e. the symmetry axis $r = 0$).

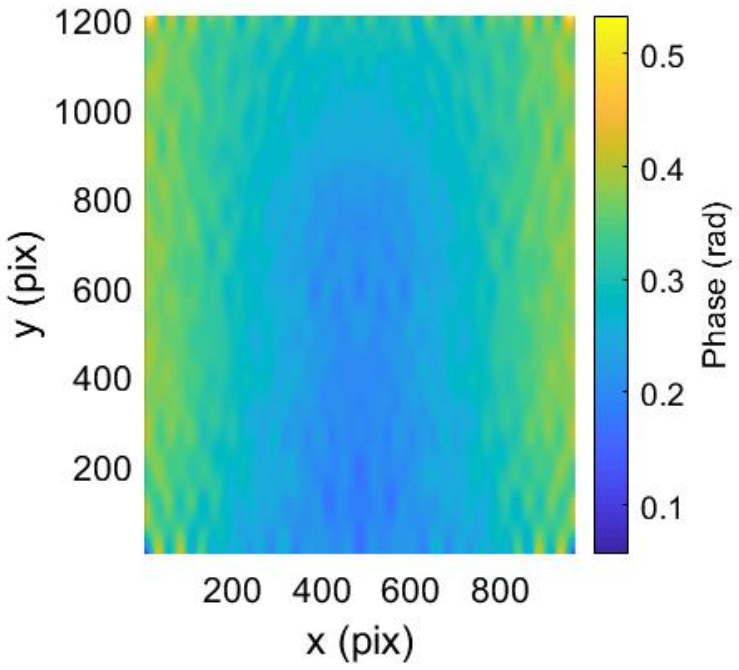

FIGURE 4.12: Standard deviation of phase maps over 5 measurements, constructed with reference (no gas) interferograms.

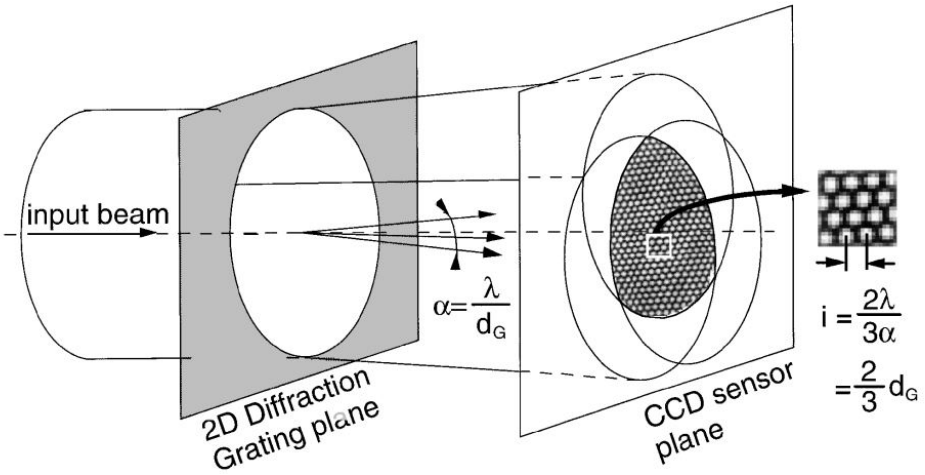

FIGURE 4.13: Working principle of a 3-wave lateral shearing interferometer. Image taken from [201]. α is the tilt angle of each replica beam with respect to the input beam axis. i is the inter-fringe spacing and d_G is the characteristic grating pitch.

accounting now for the spatial calibration of the imaging system and the sensor pixel size.

In order to estimate the stability of the applied method, we follow the procedure proposed in [67]. Figure 4.12 shows the noise map of the phase shift, after repeating several times the reference measurement. Small fluctuations appear due to setup instabilities that introduces phase disturbances for every shot. The average standard deviation is 0.3 rad $\approx \lambda/20$ given by figure 4.12. This noise level is below 3% of the expected phase shift for the gas targets (comparison with figure 4.9).

4.2.2 n-wave Lateral Shearing Interferometer

There are other possible interferometry-based techniques for measuring phase shifts (and therefore capable of evaluating gaseous target densities). Originally developed as an ultrashort laser wavefront quality diagnostic [201, 202], n-wave shearing interferometers are simple but very flexible tools. Their operation (depicted in figure 4.13) is based on the use of a two-dimensional transmission grating plane. This optic create n tilted replicas of the input beam (with angle α). Defining the EM complex amplitude of the laser (similarly as equation 4.2) as

$$E(\mathbf{r}) = E_0 e^{iW(\mathbf{r})}, \tag{4.14}$$

where W stands for the wavefront, then the tilted replicas can be expressed as

$$E_i(\mathbf{r}) = E_0 e^{i[W(\mathbf{r})+\mathbf{k}_i\cdot\mathbf{r}]}, \tag{4.15}$$

where $\mathbf{k}_i$ is the wave vector of the i-th beam replica. The irradiation at the splitting plane is then

$$I_g(\mathbf{r}) = \left|\sum_i^n E_i(\mathbf{r})\right|^2 = 3E_0 + \sum_{i\neq j}^n e^{i[(\mathbf{k}_i-\mathbf{k}_j)\cdot\mathbf{r}]}. \tag{4.16}$$

After some propagation distance L, the irradiance reads as [203]

$$I_L(\mathbf{r}) = I_g(\mathbf{r}) - \frac{L}{k}[\nabla I_g(\mathbf{r})\cdot\nabla W(\mathbf{r}) + I_g(\mathbf{r})\cdot\nabla^2 W(\mathbf{r})] \tag{4.17}$$

PHASICS SID4-HR	
Pupil dimension	$9.98 \times 8.64\,\mathrm{mm}^2$
Spatial resolution	$24\,\mu\mathrm{m}$
Resolution (phase)	$< 2\,\mathrm{nm}$ RMS
Sampling	416×360

TABLE 4.3: SID4-HR specifications.

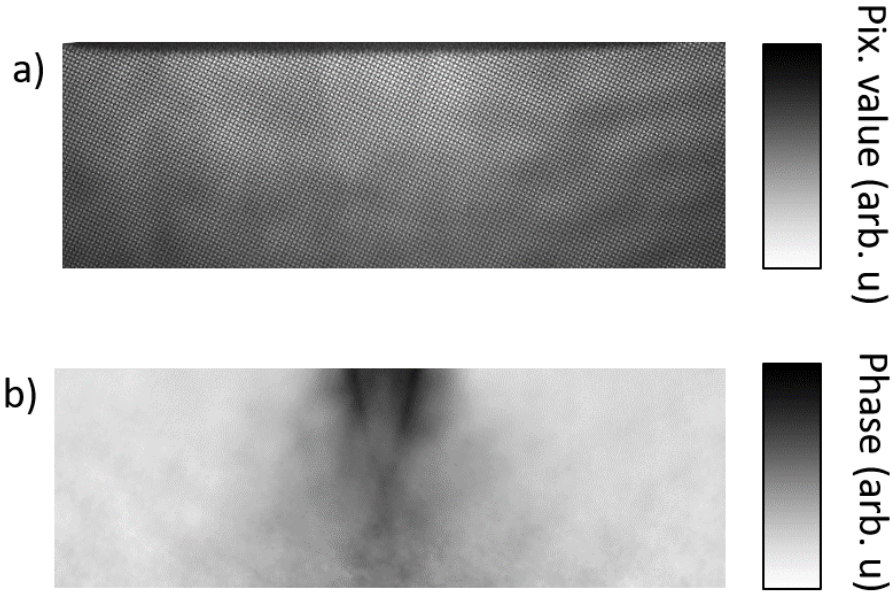

FIGURE 4.14: a) Raw interferometric data taken with SID4 and b) retrieved phase map of a supersonic shock gas jet (external orifice 400 μm) backed with 400 bars of Nitrogen.

This interference pattern can be analysed by Fourier analysis. The Fourier transform of such expression consist of a continuum term plus $n!/(n-2)!$ harmonics. When isolating such harmonics in the Fourier space, the wavefront gradient $\nabla W(\mathbf{r})$ in the directions $(\mathbf{k}_i - \mathbf{k}_j)$ can be obtained by performing the inverse FT. This method works for ultrashort (broadband) lasers as the n arms are geometrically equivalent and the interference pattern is achromatic (the interfringe spacing depends purely on the grating pitch d_G).

An advantage of this tool is that it works as an in-line interferometer as no reference arm is needed for interferogram generation, simplifying enormously the setup close to the investigated sample. Once the phase maps (with and without the target) are measured, their subtraction yields the contribution of the gaseous target to the extra optical path. Then the density can be calculated following the procedure depicted in the previous section.

This technology is patented by the company Phasics SA and sold as 4-wave lateral shearing interferometers. In the experiments shown in this manuscript, the model used was the SID4-HR, whose relevant specifications can be found in table 4.3. Figure 4.14 shows the interferometric raw data and the estimated phase map from a supersonic shock jet.

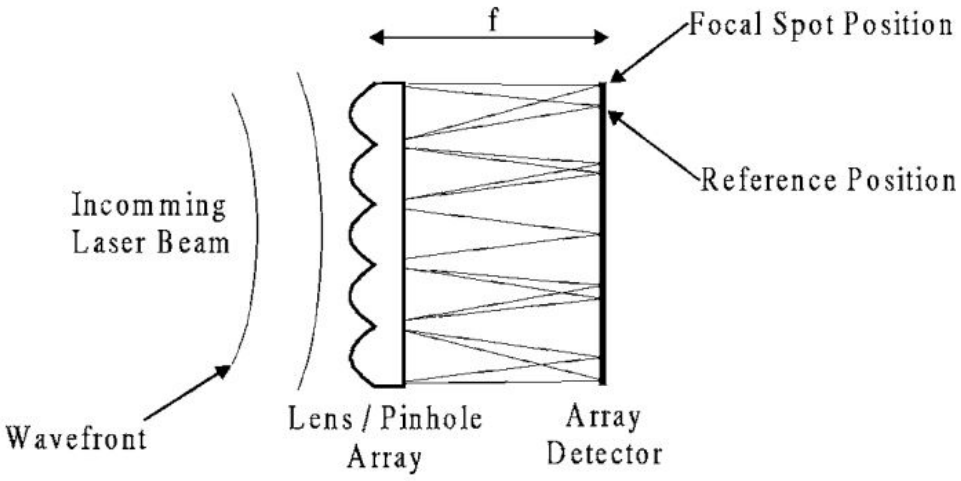

FIGURE 4.15: Working principle of a Shack-Hartmann wavefront detector. Image taken from [204].

ImagineOptic HASO4 FIRST	
Pupil dimension	$4.6 \times 3.6\,\text{mm}^2$
Spatial resolution (lateral size of micro-lenses)	110 µm
Resolution (phase)	$< 4\,\text{nm}$
Sampling	40×32

TABLE 4.4: HASO4 FIRST specifications.

4.2.3 Shack-Hartmann wavefront detector

Another classical tool for laser wavefront measurement is the so-called Shack-Hartmann detector [204]. Originally developed by R. Shack (based on the idea of the 19th century astronomer F. Hartmann), as shown in figure 4.15, its operation principle is straightforward. The input laser is broken down into multiple elementary beams by using a matrix of micro-lenses and each of them is focused on the detector of a camera. The first local derivative of the wavefront of the original beam can be then measured in each micro-lens, as it is proportional to the deviation of each focal spot from the reference point (taken with a reference beam with no aberrations).

Similarly to the lateral shearing interferometers, no reference arm is needed for studying the beam wavefront, which simplifies the measurement setup. Furthermore, their operation can be partially achromatic as the position of the spot on the camera does not depend on the beam wavelength. On the other hand, the expected spot size has an effective dependency with the wavelength. The micro-lenses are normally built so they have a very large *f-number* (> 30), so the focal spot are normally diffraction limited and their size is simply proportional to the beam wavelength.

Nowadays, there are a wide range of commercially available Shack-Hartmann wavefront sensors. Their software includes calibration files for the reference points and an automatized analysis algorithm able to retrieve the wavefront information from each individual measurement. In the experiments shown in this manuscript, the HASO4 FIRST from ImagineOptic company was used. Relevant specifications of the HASO4 are shown in table 4.4. Raw and analysed signals of a gas jet can be found respectively in figures 4.16 and 4.17.

Analogously as in the interferometer case, once the beam phase is known the information about the sample density can be estimated. Measurements of gas densities [205] and electronic plasma densities [206, 207] have been reported in the literature with this method.

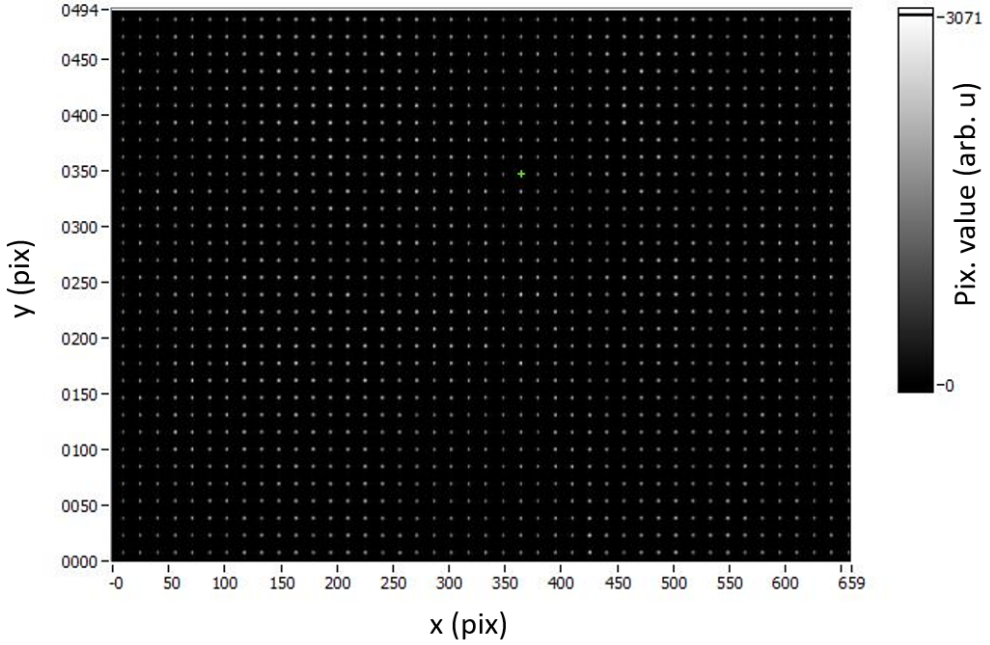

FIGURE 4.16: Typical raw signal from SH wavefront detector. The multiple foci generated by the micro-lenses array can be appreciated. Data taken with HASO4 detector, back-illuminated with a expanded He-Ne laser.

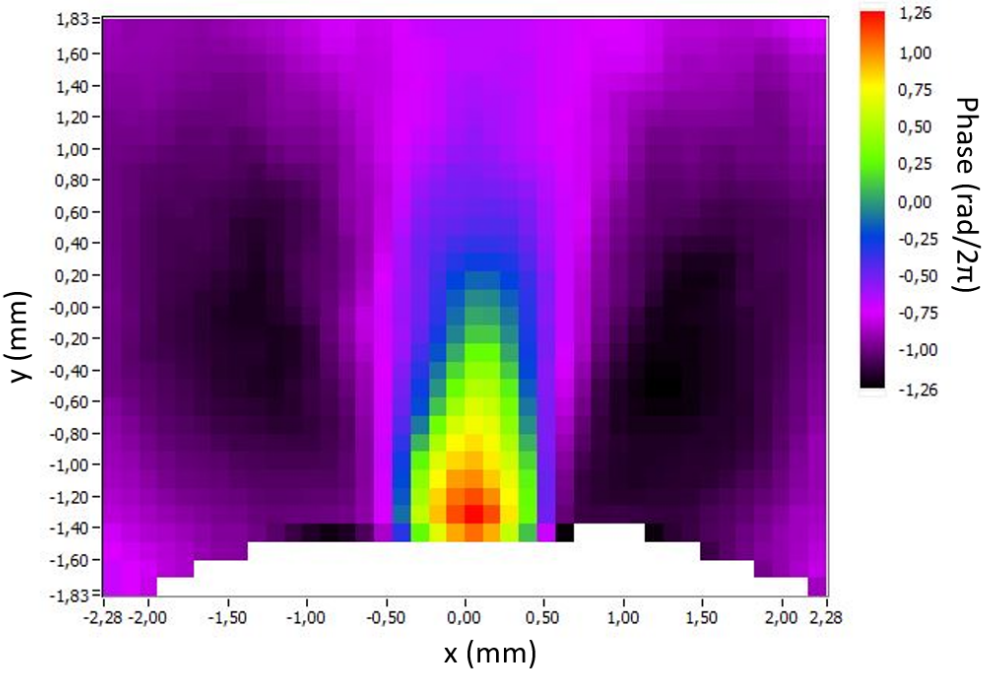

FIGURE 4.17: Example of phase map retrieved with the SH wavefront sensor HASO4 corresponding to a shock gas jet (0.4 mm outer diameter) backed with 400 bars of Nitrogen. The horiziontal and vertical axis (in millimetres) are given in the detector plane. Non-analysed data points in the bottom of the image correspond to the nozzle shadow.

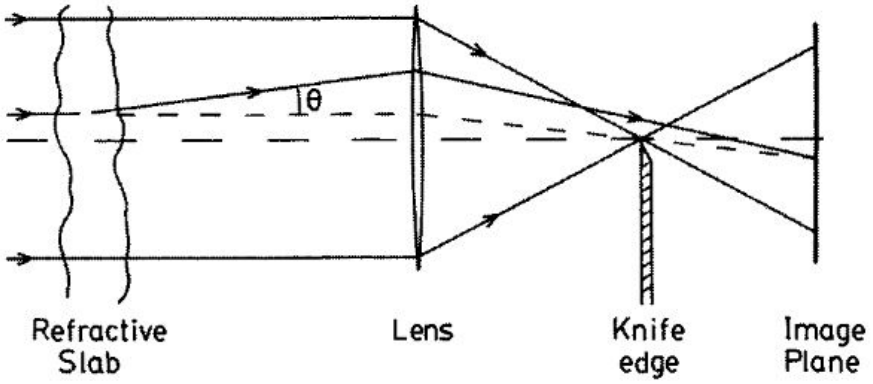

FIGURE 4.18: Working principle of Schlieren imaging. Image taken from [63].

4.2.4 Schlieren Imaging

The density of a sample can be estimated as well by means of the so-called Schlieren Imaging (also known as strioscopy) [63]. Such method is based on the refraction effect of the radiation. It is known that, when crossing a medium with inhomogeneous refractive index, a light ray will be deviated by an angle proportional to the index gradient. In plasmas this would mean

$$\theta_{refraction} = \int \nabla n \, dl \approx \frac{1}{2} \int \frac{\nabla n_e}{n_c} dl. \tag{4.18}$$

As outlined in Chapter 2, focalization of a good-quality laser beam ($M^2 \sim 1$) results in a quasi-gaussian spot. If the beam is modified by refraction when crossing an inhomogeneous refractive index sample, the non-deviated rays will cross the center of the focal spot, meanwhile the refracted components of the beam (higher modes over TEM_{00}) will skip this central point. When a knife edge (a needle) is place exactly at the center of the focal spot, low spatial frequency modes are stopped at the object and the deviated rays go through. Re-imaging of this beam onto a detector shows intensity variations which are proportional to the spatial derivative of the index of refraction of the sample.

Full calibration of this detection mechanisms is not straightforward as it is related to the first derivative of the refractive index. Nevertheless, this method can be a very useful tool for qualitative assessment of the density of the target. If a fast device is used as detector for the Schlieren beam, a time-resolved (but qualitative) idea of the target evolution can be obtained.

For instance, a photo-diode, which is several orders of magnitude faster than the characteristic evolution time of a gas jet ($\tau_{PD} \sim$ 1ns and $\tau_{gas} \sim$ 1ms) can be used to understand from a single measurement the evolution of a gas jet (normally, density ramp-up right after opening the valve, density plateau when keeping it open and gradual vanishing of the density when closing the valve). The drawback of photodiodes is that they are zero-dimensional detectors (only one *pixel* is available), so this method is sensitive to alignment and can only retrieve the information from one integral line.

4.3 Plasma detectors: probes

The interaction of high-intensity lasers with matter results in generation of plasmas. As it is known, plasmas can be rated depending on their transparency to optical radiation. Both underdense plasmas and near-critical plasmas (for near-IR wavelengths) are transparent to radiation in the optical range. On the other hand, interaction with overdense targets produces plasma gradients in the front surface of the irradiation, which at some extent are transparent as well. Optical laser beams can be used to traverse such accessible plasma volumes and be subsequently measured, obtaining indirectly some plasma attributes (e.g. electronic density).

The interaction with fs-long pulses (as VEGA lasers system) determines the characteristic time of the plasma evolution. Therefore, ultrashort lasers pulses (~ 30 fs) -commonly named *probe*- are valuable tools for inspection of fs-long laser driven plasmas. In this kind of experiments, the laser driving the interaction is referred as *pump*.

The ideal characteristics of a probe laser for inspection of ultrafast intense laser-driven plasmas would be

- Ultrashort duration (< 100 fs). The shorter the probe pulse, the finer the temporal resolution (more dynamical process can be seen).
- Few mJ energy: this is required in order to overcome the pump-driven plasma self-emission and other driver laser optical scattering. Control of the energy is desirable.
- Shorter wavelength than the pump. This is useful for two reasons: firstly, shorter wavelengths are more penetrating into denser plasmas than longer ones, so NCP or slightly overdense plasmas for the pump can still be traversed. Secondly, choosing a different wavelength between pump and probe can be use for wavelength discrimination at detection of the probe (with color/bandpass filters).
- Defined geometry and polarization, depending on the diagnostic tool to analyse the beam.
- Intrinsic synchronization between pump and probe. The inspection of the plasma requires both spatial and temporal overlap of the phenomenon of interest and the probe. Therefore, the probe should be properly timed with the pump driving the interaction. This is specially complex when dealing with ultrashort lasers, as their duration is smaller than any electronic detector time resolution.

Different choices can fulfil some of these requirements. A dedicated ultrashort laser system separated from the pump but properly synchronized with the pump (e.g. sharing the laser oscillator). Unfortunately this option was not available at the VEGA laser facility at that time. Other possibility is to create a probe beam with a piece of the pump, by separating a small percentage of the beam energy into a different path; this was the approach taken in VEGA in the work in this manuscript.

There are several ways to create a probe beam from an originally multi-TW fs-long beam. The two choices done at CLPU are shown in figure 4.19. Firstly, the use of a low-transmission beam-splitter creates a second separate beam, which is normally narrowed into a smaller diameter beam. The other option is to place a small mirror in the path of the beam to physically separate this part of the beam and transport it in another direction. As long the size of the pick-up mirror is much smaller than the size of the beam, it has been experimentally proven than the quality of the focal spot is not noticeably worse. This second choice has a major disadvantage: due to the hard cut with the mirror edge, it creates diffraction fringes both in the transmitted and reflected beams. This issue can be addressed

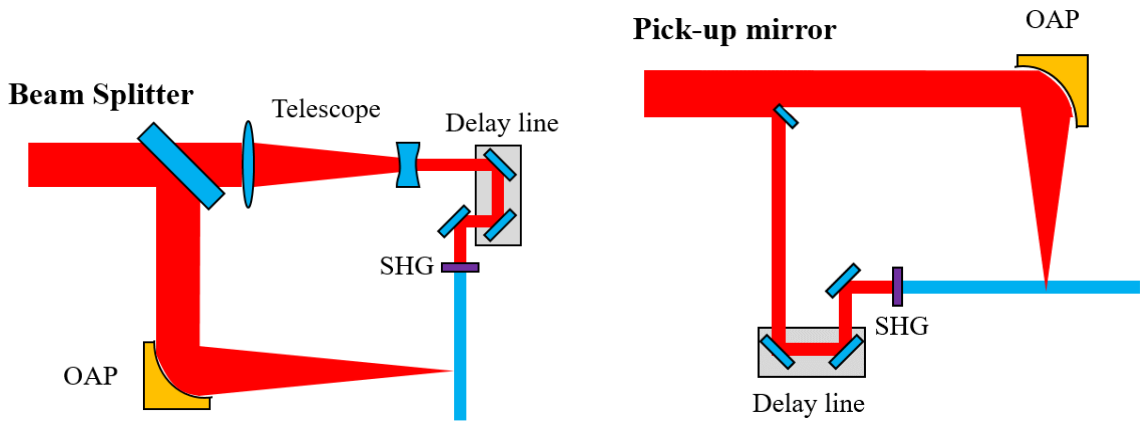

(A) Probe setup with a beam splitter.

(B) Probe setup with a pick-up mirror.

FIGURE 4.19: Simplistic sketches of probe beam construction used in VEGA.

partially by the use of a Graded Reflectivity Mirror (GRM). In any case, the transmitted fringes at the probe designs at VEGA were characterized in realistic experimental conditions and the local fluence enhancement was determined to be smaller than the damage threshold of the beamline optics downstream. On the other hand, these two methods have the advantage to be intrinsically synchronized (without any jitter) with the pump.

A frequency conversion is normally applied to probes, in order to go through the plasma with a different wavelength than the pump, as well as to have deeper penetration power into the plasma due to the higher critical density value for shorter wavelengths. In probe taken from VEGA, second harmonic generation (SHG) in BBO crystals (Type 1) was performed. Other optical elements are normally added to the probe beam path for controlling other characteristics, such as energy control device ($\lambda/2$ waveplates followed by a linear polarizer), polarization control devices, aperture control, telescopes for beam size control, and so on. Care should be taken with the accumulated B-integral if many transmission optics are added (or if a very high-intensity probe is built).

One of the most important components of the probe beamline is the delay line. It is a motorized retro-reflector mirror configuration that allows for fine control of the timing between the arrival of the probe with respect to the pump to the interaction region. Repeating an experiment with different positions of the delay line gives different timed *frames* of the interaction, being able to reconstruct then the dynamics of the plasma process. Such an option is really valuable in HRR facilities as VEGA, with repetition rates $\sim$ 1 Hz, where the experiment can be repeated hundreds (even thousands) of times in a single day. The time-resolution of such *movie* is proportional to the minimum step of the delay line motor $\Delta t = 2 \times \Delta s_{\text{min}}/c$. In VEGA, delay lines are mounted on high precision linear stages PLS-85 1' VSS42 MLS HV from Pi miCos GmbH, with a minimum step of 200 nm yields $\Delta t \approx 1.5$ fs.

A critical point for the probe design to be consider is the synchronization between pump and probe, which is specially challenging for fetmosecond duration laser pulses. Once the beam path is defined until the interaction point, a very fine measurement between the arrival times of pump and probe is desired. For such purpose, different methodology have been developed depending on the required synchronization requirements, which can rely either on electronic detectors (for a slow -or coarse- synchronization, with accuracy > 1 ps) or on optical techniques (for fast -or fine- synchronization, with accuracies < 1 ps.

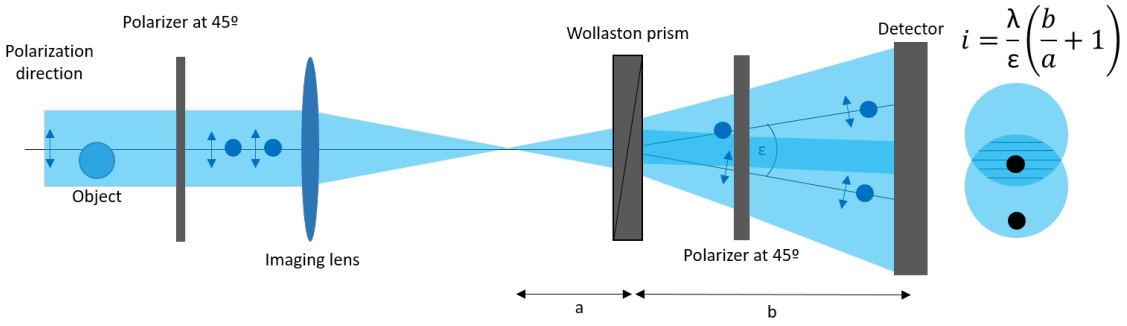

FIGURE 4.20: Nomarsky interferometer sketch. The equation shows the formula for the inter-fringe spacing, where ε is the Wollaston angle. Blue arrows represent the probe polarization direction.

- Coarse (electronical) synchronization can be performed thanks to time-resolved detection of pump and probe pulses by a fast electronic device, such as a fast photodiode (connected to a oscilloscope), with typical accuracy of $\sim$ 100 ps, or a streak camera (time accuracy $\sim$ 1 ps, see A). The accuracy of these methods is given by the speed of such electronic-based detectors. Both pump and probe can be simultaneous detected if some dispersive object is placed in the interaction point, scattering both beams. Also, a partially reflective object can be placed in TCC at a specific angle so part of both beams (one in transmission, the other in reflection) are collinear and sent to the detector.

- Fine synchronization relies on optical methods which only appear when both pulses overlap in space and time, such as interferometric fringe generation or SHG (the latter only in a non-linear crystal). Other methods can rely on fast laser-matter interaction products, as the appearance of photo-ionized free electrons (by the pump) on a sample which can be detected by the probe via the induce absorption caused by such free charge carriers. In any case, coarse synchronization is recommended before performing the fast one in order to narrow the time (space) interval to be spanned by the delay line when searching for the pulse overlap.

The probe beam can be then analysed in order to obtain information of the plasma. Information about the local variation of the index of refraction can be achieved by simply imaging the probe (the so-called Shadowgraphy [208]), meanwhile the internal magnetic can be estimated (by Faraday rotation effect) in a polarimetry setup [209]; both diagnostic can be combined simultaneously [210].

As the index of refraction of the plasma is a function of electronic plasma density, both wavefront sensors [143] or interferometers can be applied for such study.

4.3.1 Plasma interferometer

Interference with ultrafast lasers is not trivial as due to their very short coherence length (similar to the pulse duration). Simplified, this means that both arms have to overlap in time and space order to interfere on the detector plane, which is not an easy task for ultrashort pulses. For this reason, Nomarsky interferometers (also known as Wollaston-based interferometers) are normally built for short-pulse interference. A sketch of a typical Normarsky interferometer is shown in figure 4.20.

The operation is based on the use of a Wollaston prism for separating both interferometer arms. This item is the junction of two wedged birefringent crystal prisms whose principal axes are rotated 90° with respect with each other. The resulting prism will separate

the two linear polarization components of the incoming beam with an small angle, which is a function of the crystal birefringence and wedge angle. If the incoming beam is linearly polarized at 45° with respect to the prism axis, two identical beam replicas orthogonally polarized will be created. A linear polarizer set at 45° after the prism makes both beams polarization direction parallel so they can interfere. The overlap region of both pulses will show interference fringes that are measured in the detector plane (normally a camera). In order to image the object to study (and also to enhance the overlap region of both beams) a converging lens should be properly placed and aligned between plasma and prism. The design of Wollaston-based interferometer is quite complex as it should follow several constrains. The distances between optics, prism angle and focal length should be chosen so the fringe area covers the imaged object (but still being confined to only one half of the probe beam) and the inter-fringe spacing should be larger than the image resolution. Furthermore, the image should cover all the desired region of interest of the object with proper magnification. On the other hand, several advantages of this scheme can be outlined. First of all, this design is a single-split configuration (no need of construction of a separate reference arm) where the arms are naturally synchronized, being therefore specially useful for ultrashort pulses [63].

Similarly as in the first step for gas interferometry, once the 2D accumulated phase is retrieved by the interferometer, a reference phase map should be obtained, replicating the target (gas) conditions but avoiding the plasmas precursor (the driver laser). Subtraction of both phase maps yields the phase difference generated by the plasma. Afterwards, the same process for the Abel inversion can be applied if cylindrical symmetry is imposed for the plasma sample (which is a reasonable assumption ,up to some extent, around the laser focalization axis). The relation between refractive index and phase is again given by the formula 4.10. Nevertheless, in plasmas the refractive index is expressed as a function of the electron density

$$n = \sqrt{1 - \frac{n_e}{n_c}}. \tag{4.19}$$

For underdense plasmas ($n_e \ll n_c$) the refractive index can be approximated as $n \approx 1 - n_e/(2n_c)$, so

$$\frac{n_e}{n_c} \approx -\frac{\lambda}{\pi\vartheta} A^{-1}(\Delta\phi(x)). \tag{4.20}$$

Note that for plasmas $n < 1$, so the phase shift ϕ is negative. The expression for the electron density is more complex when the underdense approximation is not taken

$$\frac{n_e}{n_c} = -\left(\frac{\lambda}{2\pi\vartheta} A^{-1}(\Delta\phi(x))\right)^2 - \frac{\lambda}{\pi\vartheta} A^{-1}(\Delta\phi(x)). \tag{4.21}$$

4.4 Particle beam detection

A wide range of diagnostic techniques has been developed for inspection of spatial, temporal and spectral properties of the laser-driven accelerated particles. Some of these tools are inherited from the accelerator community and in some cases adapted to the special conditions of the laser-driven beams (for instance, hostile detection environment near the source or high peak currents). The general goal of these particle diagnostics is to detect single ion bunch with resolution in space and time at the operational repetition rate of the driver laser system and in a non-destructive way when possible (i.e. the beam is not modified by the measurement).

Ion diagnostics can be sorted in several different manners. Related to their operational purpose, a division between on-line diagnostics and ion detectors with post-processing can

be used [65]. Radiochromic films (RCF) stacks , imaging plates (IP), CR-39 and nuclear activation detectors, despite being quite reliable and flexible, can be assigned to the latter group as normally they require to be extracted from the experimental area and studied by some device (e.g. an scanner). Depending on their configuration in the experiment, these tool can measure spatial profile, dose, ion species, divergence, spectrum and many other beam properties. On the other hand, on-line detectors are accessible from outside the experimental chamber and are better fitted for high-repetition rate operation of the new fs-long high-power laser generation. Scintillators sensitive to radiation can be used for on-line measurement of ion beam divergence and spectrum, imitating the working principle of RCF stacks [211]. Also, microchannel plates (MCP), whose operation is depicted in Appendix A, and semiconductor or crystalline detectors, working in time-of-flight configuration, yield an electrical signal proportional to the dose absorbed, with a gain that can be regulated by an external applied bias voltage. Furthermore, large MPCs can be coupled to phosphor screens so two-dimensional beam information can be recorded. The type of information recorded will be as well a function of the diagnostic technique used with this device. It is important to note that the majority of these diagnostics are destructive for the particles.

In this section, two ion measurement techniques relevant for the work of this manuscript are presented. Thomson Parabola (TPs) spectrometers -for ion spectrum and species measurement- and pepper-pot -for emittance investigation- are shown. When coupled to active detectors, these tools can be operated on-line.

4.4.1 Thomson Parabola

Due to the special spectral characteristic of the multi-species laser-driven ion accelerated beams, one of the key diagnostics for their investigation are the Thomson parabola spectrometers, first developed by Thomson in 1907 [212]. TPs are in-line diagnostics capable of rating the particles depending on their energy, momentum and charge-to-mass ratio [65]. The element of the spectrometer sensible to particles can be either a passive detector -for instance, imaging plates (IPs) or CR39 nuclear track detector [213]- which require post-processing for retrieving the data, or an active one -microchannel-plate [214] or plastic scintillators [211]-, well fitted for HRR operation, due to its capability of performing on-line measurements for every single laser shot. The main drawback of an ordinary TP is the incapability of deconvolving the angular distribution of the measured beam, as only a particular angle of the beam (with an insignificant angular spread) is measured, as the particles measured have to pass through a pinhole. This fact also makes this detector specially sensitive to alignment.

The Thomson parabola works according to magnetic and electric sector spectrometer principles. The entrance pinhole selects a beamlet -composed by ions with a specific charge-to-mass ratio q/m, with $q = Ze$ the ion charge- which is deflected by magnetic B and electric E fields of length l_2 (see fig. 4.21). Deflection directions of the two fields are mutually orthogonal, allowing species separation (by electric field, in x-axis) and energy separation (mostly by magnetic field, in y-axis) after some propagation distance l_3. The ions are measured on a two-dimensional spatially-resolved particle sensitive detector. In the small deflection approximation $\sin(\theta) \approx \theta$, considering perfectly sharp and homogeneous fields and nonrelativistic particle energies, the deviation coordinates at the detector plane caused by the Lorentz force are given by

$$x = \frac{qEl_2l_3}{2E_{kin}}, \tag{4.22}$$

$$y = \frac{qBl_2l_3}{\sqrt{2mE_{kin}}}, \tag{4.23}$$

where E_{kin} is the kinetic energy of the ion. When combinating (4.22) and (4.23) we get the parabolic equation

$$y^2 = \frac{q}{m}\frac{B^2 l_2 l_3}{E}x. \tag{4.24}$$

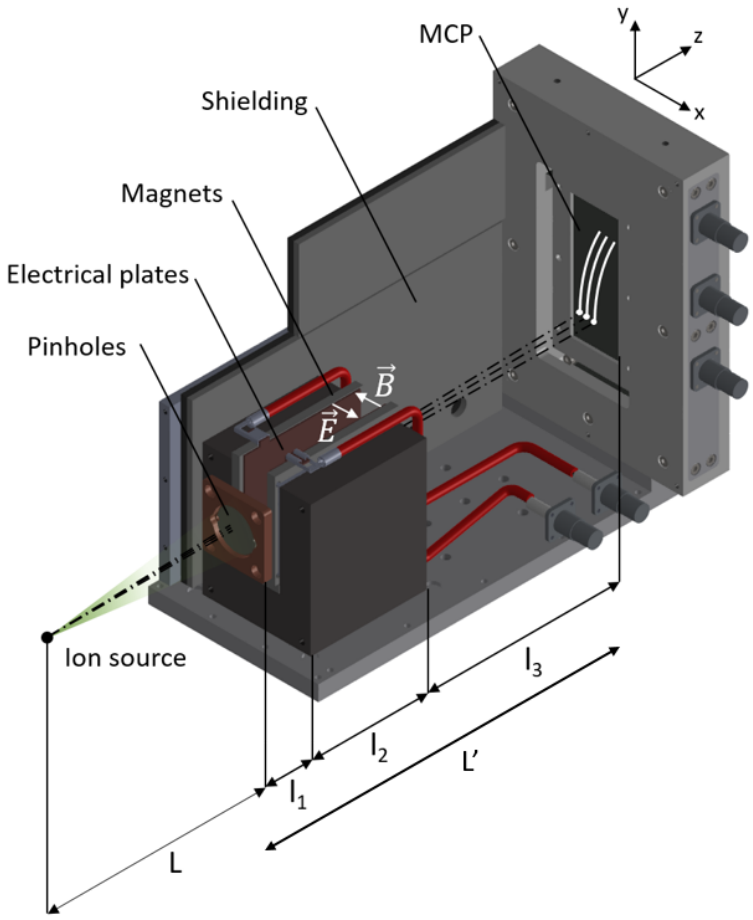

FIGURE 4.21: Multi-pinhole TP spectrometer design. L is the distance from source to pinhole, l_1 is the distance from pinhole mask to the fields gap (in this design both magnetic and electric fields overlap in space), l_2 is the length of the dipole/plates and l_3 is the distance from fields to detector. $L' = l_1 + l_2 + l_3$ is the flight distance from entrance pinhole to the detector, and it determines the magnification effect if operating the device as a perfect pinhole-camera as $M = L'/L$.

Ions with the same charge-to-mass ratio will reach the same parabolic trace on the detector plane, meanwhile their position along the trace will define their energy. Photons are not deflected by the fields and travel straight through the source/pinhole axis and impact the MCP, providing the zero deflection reference (used for spectrum data interpretation).

The ultimate energy resolution of the TP depends on the magnetic spatial separation at the active area of the detector (related to the magnetic field B, its length l_2 and the distance to MCP l_3), the magnification of the imaging system collecting MCP photons and the minimum particle trace thickness δ. In the considered approximation, δ (which is inversely proportional to the spectrometer resolution) is given by the setup geometry and the pinhole diameter d, similarly as in a pinhole camera, as $\delta = d + (s + d)L'/L$, being L the distance

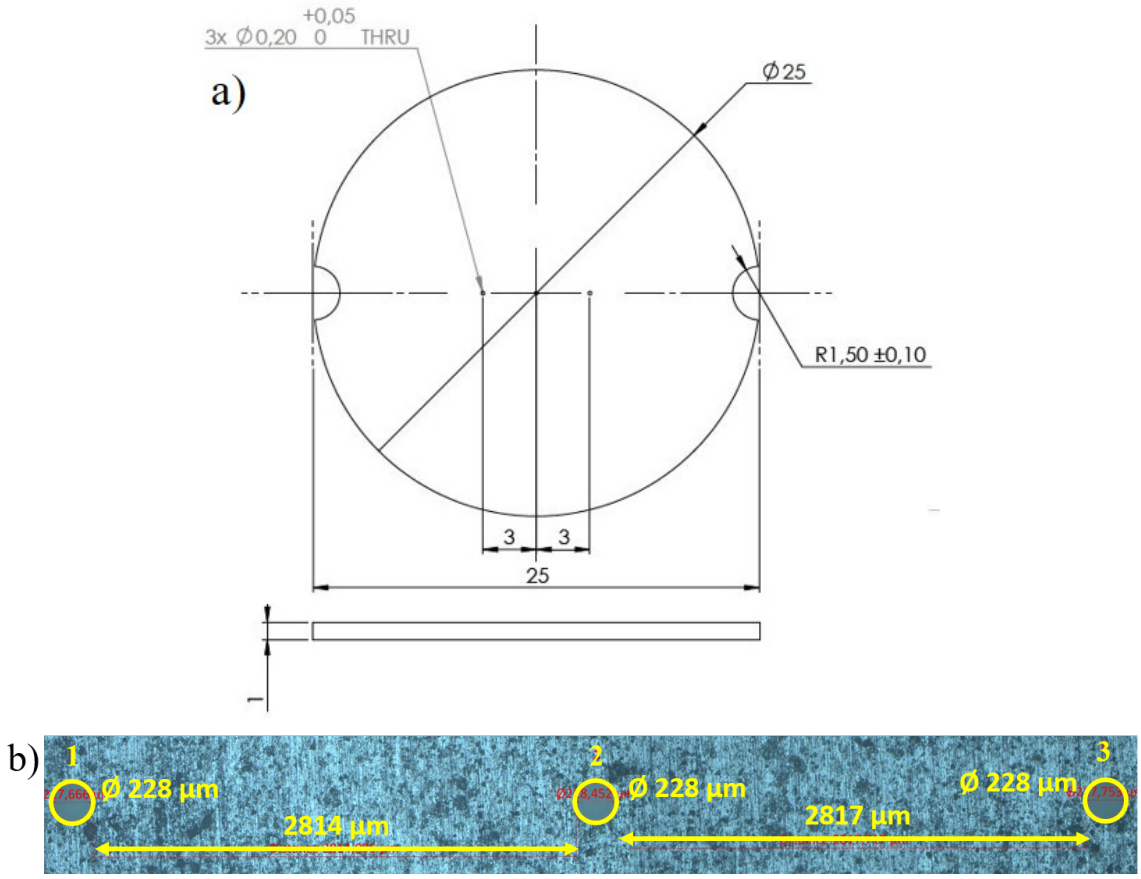

FIGURE 4.22: Tungsten mask of 3 pinholes in line with diameter $d \approx 230$ µm and separation between centres of $a \approx 3$ mm. a) Mask design. b) Detailed optical microscope picture.

from source to pinhole and $L' = l_1 + l_2 + l_3$ the distance from pinhole to detector and s the source size [215].

In the recent years several conceptual modifications have been proposed as improvements of the basic functioning of TPs, such as a tunable magnetic dipole [216] or electromagnet [214] for adaptable energy resolution, exotic electrode geometry (trapezoidal or wedged) [216–218] for extended retrieval of lower part of the spectrum, transient electric field for time-gated measurement of the beam [219], designs with two in-line entrance pinholes for spatially resolved measurements of the ion source [220], or simultaneous measurement of ion and electron [221] or plasma-emitted extreme ultraviolet radiation spectra [222].

4.4.2 Multi-pinhole Thomson Parabola

In order to retrieve angular-resolved spectral information about the beam, radiochromic film (RCF) or scintillator stacks are practical diagnostic tools [34, 211], yielding nevertheless a discretized spectrum of typically $\Delta E \approx 1$ MeV, much coarser when compared to the continuous spectral TP resolution [65]. Moreover, these diagnostics cannot discriminate between different q/m ionic species. These facts are compensated in some experimental layouts by the combination of perforated RCF stacks and TPs [223], so part of the beam reaches the latter. Despite yielding complementary information, this method is limited in spectral resolution for most of the beam.

The design and development of a multi-pinhole Thomson Parabola spectrometer is presented, which combines sharp spectral/angular precision, besides the ionic species sorting capability [224]. Moreover, the use of a MCP as an active detector device allows for single-shot HRR acquisition [225]. The design of the device is a modification of the basic TP arrangement consisting of the substitution of the pinhole by a horizontal array of pinholes. This array chops the incoming cone of particles in several beamlets which are simultaneously detected. In this way we provide a measurement in different locations (and divergences) adding angularly resolved spectral information. Similar strategies were already proposed [186, 220, 226–233] most of the cases, dismissing the electric field for charge-to-mass ratio inspections, as the authors claim to accelerate a single ion species (protons). Some references [234] showed the possibility of joining different ion diagnostics in order to have extended information about the beam, but lacking of ion discrimination capability at different subtended angles. A few works have proposed [216] or demonstrated [235] an absolute capability of angular-spectral-q/m resolution but with strong limitations in the available species to be investigated -and their subtended angles- due to data analysis constrains: ion traces from different beamlets are not allowed to cross at the detector plane. We show here a more general multi-pinhole TP spectrometer, including the use of electric and magnetic fields for identifying different q/m ions, angular selection of beamlets and a more generic post-processing method which does not limit the available ion species to be investigated.

The original configuration of the detector consisted of a *line* of three pinholes of diameter $d = 200\,\mu m$, separated by a distance of $a = 3\,mm$ aligned along the x-axis (electric deflection direction), as shown in figure 4.22. These were drilled into a 1 mm thick 25 mm diameter tungsten plate. Detail of the pinholes is shown in figure 4.22. A copper nosepiece was designed to easily exchange between these substrates, with different pinhole array combinations with pre-set alignment orientations. A $B = 0.4\,T$, $l_2 = 75\,mm$ long permanent dipole magnet is located $l_1 = 13.5\,mm$ after the pinholes. The direction of the magnetic field $(-x)$ deflects the ions upwards $(+y)$. Magnets are attached to an iron yoke, leaving a gap between poles of 16 mm, on-axis with respect to the central pinhole. Two thin copper electrodes are placed over the magnet poles. A variable voltage difference can be applied between electrodes, up to $U = 10\,kV$ which deviates the particles parallel to the field lines. After a propagation distance $l_3 = 135\,mm$ a $80 \times 30\,mm^2$, a single stage MCP with attached phosphor screen (Hamamatsu F283-12P, 12 µm channel diameter) converts the two-dimensional ion traces into visible photons at the rear side of the TP. This signal is acquired by an image recording system properly calibrated, in order to retrieve particle data for every laser shot. All the components are light-tight covered by a shielding made of overlapped layers of Al, polyethylene and Pb, whose goal is to protected the MCP from secondary radiation sources. The full assembly is 10 kg mass and $130 \times 255 \times 175\,mm^3$ in volume, which makes it relatively easy to set and align inside an experimental vacuum chamber.

A 3D numerical solver was developed for trajectory simulation to provide expected traces in MCP and energy/position relation for all the required charged species. It consisted on a second order Verlet algorithm and the numerical error was estimated by comparison to analytical results to be 0.23% at 20 MeV. The magnetic field was mapped by a Hall probe in the central vertical plane (between dipole magnets) and implemented in the code for realistic trajectory calculation (see figure 4.23). The electric field could not be measured for the moment, being therefore implemented in the code as as perfectly sharp and homogeneous field between plates, ignoring edge effects. To account for this imperfection, the voltage value in the simulation had to be increased by $\sim 10\%$ to make the theoretical traces to coincide with the experimental ones. The numerical simulation provided precise energy/position calibrations, accounting for the exact trajectory of particles coming from

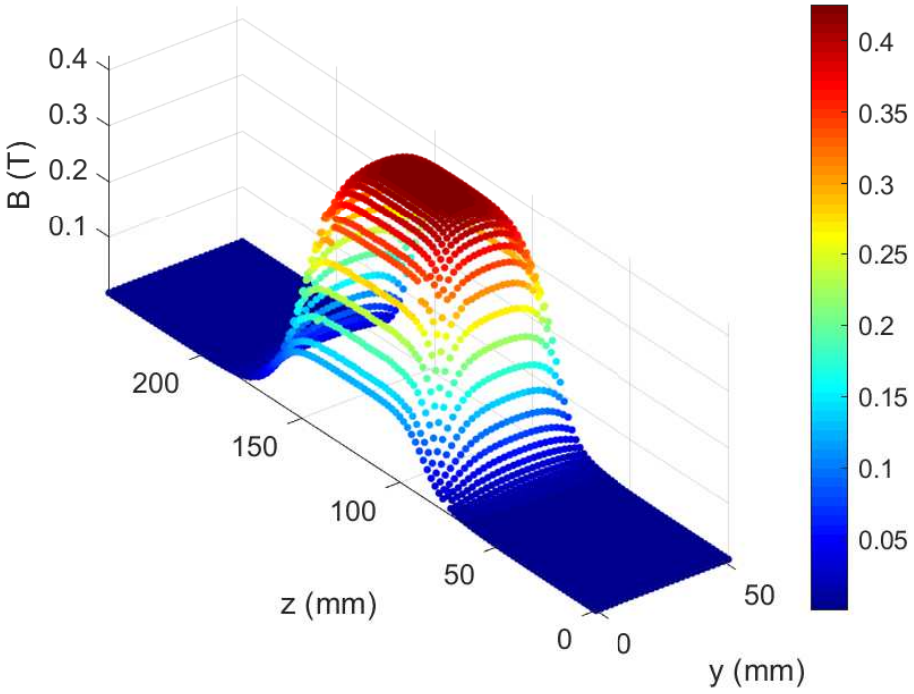

FIGURE 4.23: Measured magnetic field distribution. Ions propagate in z-direction through the field towards the MCP, being deflected on the y-direction by the Lorentz force.

each pinhole of the array. A precise calibration of the electromagnetic field deflection is foreseen at an accelerator facility.

In the presented design, proton energies between 300 keV and 25 MeV are accessible. The ultimate energy resolution of the TP spectrometer is determined by the energy separation at the MCP position ($\Delta E/\Delta x$) and the trace width. For instance, at 20 MeV, $\Delta E/\Delta x = 4.33\,\mathrm{MeV/mm}$, with a measured trace width of $\delta = 0.30\,\mathrm{mm}$ the resolution is $4.33\,\mathrm{MeV/mm} \times 0.3\,\mathrm{mm} = 1.3\,\mathrm{MeV}$.

4.4.3 Emittance measurement

Several methods are employed at conventional acceleration facilities for direct or indirect measurement of the emittance of the beams, depending on the nature of the particles and the beam measurement requirements. They can rely on measurement of secondary radiation generated by the beam (such a X-ray pinhole camera detecting X-ray synchrotron radiation from a relativistic electron beam [236]). Other destructive methods consist on direct measurement of the spatial properties of the beam, such as the slit (or pepper-pot) method which is presented below.

Slit-method (or Pepper-pot)

This method splits physically the beam in different pieces (or beamlets) with the help of a mask. The spatial properties of these beamlets are measured (position, divergence, size) after a propagation distance L', with a spatially resolved detector (it can be a scintillating screen or a MCP). Depending on the geometry of the mask and orientation (it can be an ensemble of slits or pinholes) a *discretized* measurement of the one-dimensional transversal trace space (horizontal or vertical for the slits) or two-dimensional one (for the pinhole

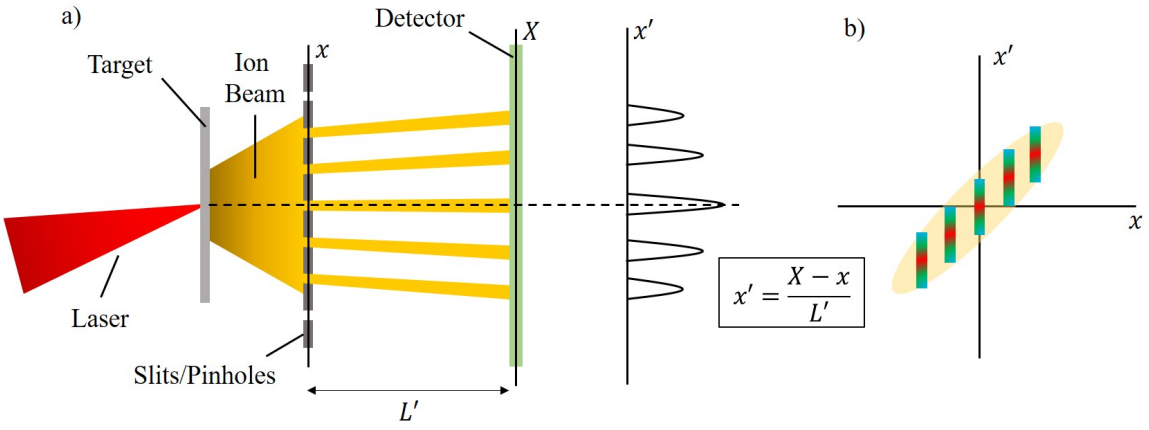

FIGURE 4.24: Scheme of the slit/pepper-pot measurement method. a) Experimental layout. x stands for the transversal coordinate at the mask plane, meanwhile X refers to the transversal coordinate at detector plane. b) Data retrieved transferred to trace space. Inset shows the conversion from spatial to divergence coordinates in this setup (for small angle approximation) which is applied for calculating the trace-space.

mask) can be retrieved. The basic operation of this technique is sketched in the figure 4.24. From such trace-space, an estimation for the 1D (2D) geometrical rms emittance can be obtained. The method for the pinhole mask is similar to the slit one but applied twice in each direction. For simplification the slit method is presented [237]. It is important to note that the emittance estimation is retrieved from a subset of particles instead the of the full beam. Examples of the possible mask are shown in figure 4.25.

The emittance estimation presented here requires certain working hypothesis:

- Paraxial approximation is considered, so $\tan(x/L') \approx x/L'$.
- The width of the slits (or pinhole diameter) d is considered very small when compared to the beam size, and all of them are similar.
- Space-charge effects are not taken into consideration in the free path from mask to detector.
- Non-relativistic particles are considered ($\gamma \sim 1$).
- The signal given by the detector is supposed to be proportional to the number of particles arriving to the detector.

Moreover, a condition should be complied for good resolution emittance measurement

$$L' > \frac{\Delta X p}{2x'} \tag{4.25}$$

where ΔX is the detector spatial resolution and p the number of slits or pinholes.

In the presented formalism two different coordinates are used to refer to the beamlet position. x is used at the plane of the slits, meanwhile X is used at the detector plane. The measurement is valid at the plane of the mask (x), meanwhile the distance L' is given so effective beamlet divergences can be measured at plane X

As shown in figure 4.24, the spatial coordinates axis of the trace space (x) are simply the pinhole positions, meanwhile the divergence axis (x') is given by the lineouts of the diverged beamlets on the detector plane. From the discretized trace space, the emittance is

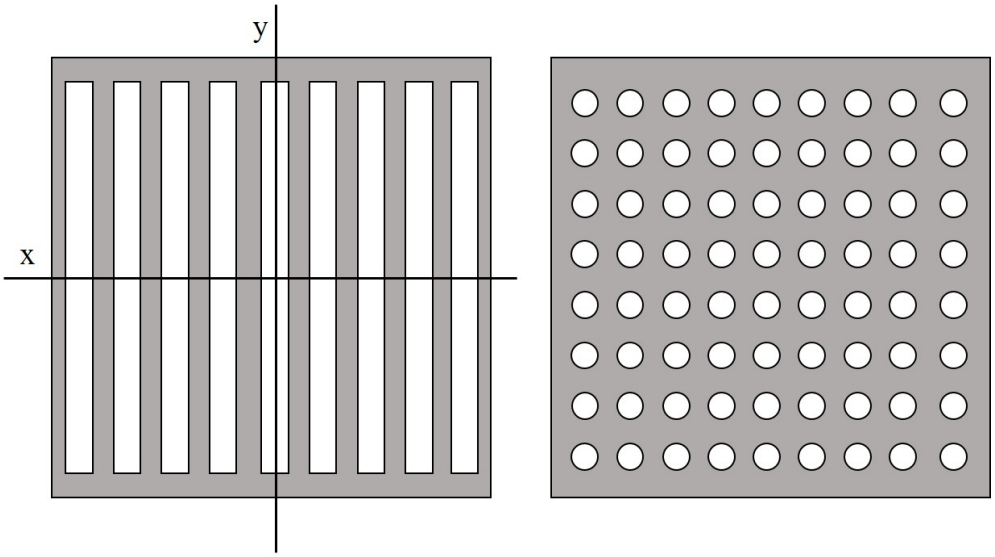

FIGURE 4.25: Beam masks for trace space measurement: slit mask (left) and pepper-pot (pinhole) mask (right).

estimated, similarly as explained in chapter 3 via the second order moments of the particle distribution, as

$$\epsilon_{rms,x} \approx \frac{1}{N}\sqrt{\left\{\sum_i^p n_i(x_i - \langle x\rangle)^2\right\}\left\{\sum_i^p \left[n_i\sigma_i'^2 + n_i(\langle x_i'\rangle - \langle x'\rangle)^2\right]\right\} - \left\{\sum_i^p (n_i x_i \langle x_i'\rangle) - N\langle x\rangle\langle x'\rangle\right\}^2}. \tag{4.26}$$

All the terms in this formula are given by measured quantities:

- p is the number of pinholes,
- $n_i = \sum_{i,pix} f_{i,pix}$ is the normalization factor of the particles of the i-th beamlet, (i.e. the integral of the signal of the individual beamlets on the detector). $f_{i,pix}$ corresponds to the pixel value function of the i-th beamlet,
- $N = \sum_i^p n_i$ is the normalization factor of the particles (integral of the signal on the detector),
- x_i is the i-th pinhole or slit position,
- $\langle x\rangle = \frac{1}{N}\sum_i^p n_i x_i$ is the mean position of the pinholes or slits,
- $\langle x_i'\rangle = \frac{\langle X_i\rangle - x_i}{L'}$ is the mean divergence coordinate (i.e. pointing) of the i-th beamlet (where $\langle X_i\rangle = \frac{1}{n_i}\sum_{i,pix} f_{i,pix} X_{i,pix}$ is the mean position of the i-th beamlet on the detector),
- $\langle x'\rangle = \frac{1}{N}\sum_i^p n_i \langle x_i'\rangle$ is the mean divergence coordinate (i.e. mean pointing) of all the beamlets combined,
- $\sigma_i' = \frac{\sigma_i}{L'}$ is the rms divergence of the i-th beamlet,
- $\sigma_i = \sqrt{\frac{1}{n_i}\sum_{i,pix} f_{i,pix}(X_{i,pix} - \langle X_i\rangle)^2}$ corresponds to the rms signal size of the i-th beamlet on the detector.

Energy-resolved emittance measurement

Techniques for emittance measurements at conventional accelerators are adapted to the specific properties of their beams. For instance, due to the accurate control of the beam energy (and its narrow band) at conventional accelerators, an spectrally-resolved emittance measurement is not required. Nevertheless, this is not the case for protons accelerated by laser-driven TNSA. Extremely broadband, ultra-low emittance, non-relativistic ion beams are generated via TNSA. Existing works have already addressed the emittance measurements for laser-driven ion beams, but with severe limitations.

In the work of Borghesi *et al.* [35] the emittance is estimated by analysing the imaging properties of the source by performing proton radiography of a structured sample (a grid). Nevertheless, such analysis did not take into account the covariance term of the definition of emittance, yielding $\epsilon_N \sim 0.3$ mm mrad for 15 MeV protons.

Cowan *et al.* [29] micro-structured the rear surface of the irradiated target. Such pattern was observable in the beam profile, and the emittance was estimated to be $\epsilon_N < 0.015$ mm mrad for 7 MeV, $\epsilon_N < 0.008$ mm mrad for 9 MeV and $\epsilon_N < 0.004$ mm mrad for 10 MeV (i.e. a clear trend to higher quality beams with increasing energy). Nevertheless, this method has the disadvantage of modifying the soft profile of the beam coming from a plane surface. Furthermore, the laminarity of a beam generated in a micro-structured target may be different from a flat target due to electron filamentation and/or sheath field modification [34].

Nürnberg *et al.* [34] and Roth *et. al.* [185] present a compendium of trace-space and emittance measurements at different high-power laser facilities following the target *grooving* method of Cowan *et al.* [29]. Disparity of results is found probably caused by the experimental configuration differences and the fact that diverse laser sources of different energies and pulse duration were used in each case. In any case, the normalized emittance values range from 1.6 mm mrad to 0.03 mm mrad.

On the other hand, Ter-Avestiyan *et. al.* [238] utilized the grid proton radiography method for a two-dimensional emittance estimation. This work proposes the existence of two distinct proton acceleration mechanisms when the driver pulse laser is ultrashort ($\sim$ 30 fs), one regime for the high-energy part of the proton spectrum with a smaller emittance ($\epsilon_N \approx 0.2$ mm mrad) related to a transient electron cavity formation at the interaction point, and the classical TNSA scenario for the low-energy part of the spectrum with larger emittance ($\epsilon_N \approx 0.9$ mm mrad).

In the formerly mentioned cases, the poor spectral resolution of the RCF used as proton detectors was a limiting factor, neither high repetition rate was possible with such screens as they need to be extracted from the experimental chamber after each shot, scanned and post-processed. Furthermore, RCF stacks are not intrinsically able to differentiate between different ionic species, as normally not only protons are accelerated during TNSA. Additionally, the grid method only estimates an upper limit for the emittance value, as it is retrieved by reconstructing the proton virtual source, where an upper limit for the particle phase distribution area in the trace space can be given by $\epsilon = \sigma_x \sigma_{x'}$.

Finally, it important to acknowledge the recent work of Wu. *et. al.* [239], where the emittance of a proton beam was characterized in three different stages of a focusing beamline by three different methods: pepper-pot, quadrupole scan technique and the so-called *single-shot measurement* (which works by evaluation of the image proton focal spot) [240]. The three mentioned methods are designed to obtain the proton beam emittance in a very narrow spectral range (5 MeV with an energy spread of 2%), and HRR-compatibility was demonstrated in the latter one by means of a scintillating screen. Their results vary (depending on the stage of the beamline) between 0.02 mm mrad and 0.1 mm mrad.

A method for simultaneous spectrum and emittance measurement was developed at CLPU, consisting on the combination of the pepper-pot method and the Thomson Parabola working principle. The use of the multi-pinhole TP in a high magnification configuration ($L'/L >> 1$) gives the required resolution so trace thickness on the detector can be measured accurately, well above the spatial resolution limit of the HRR active detector used (a BC-400 scintillator). The choice of a properly dimensioned pinhole array chops the beam similarly as in the pepper-pot method; the fields downstream deviate the resulting beamlets accordingly to their specie, charge and energy. The result on the detector plane is a signal of several traces with accessible spatial properties linked to a specific energy at different trace position, therefore having access to the energy-resolved descretized trace-space information, namely rms values of beam position, emission angle, size, divergence, laminarity and emittance. The technique, thoroughly described in Chapter 7, presents several operational and conceptual improvements when compared with previous methods, as the HRR operation capability, an extended energy and spatial resolution and the lack of requirements of target structuring.

Several limitations have been encountered in this first prototype of the detector, as a limited acceptance angle ($< 10^{\circ}$) and the impossibility of measurement of several ion species due to the overlapping of their signals on the detector plane. These restrictions, and others as the scaling of the detector towards higher particle energies ($\sim$ 100 MeV), can be overcome in a future version of the device, with specifically designed pinhole arrays, larger dipole separation and increased active scintillator area.

Chapter 5

Underdense target investigation for laser-matter experiments

As seen in Chapter 2, the density of the target in a laser-plasma interaction experiment determines completely the nature of the interaction. In the case of electron acceleration via a laser-driven wakefield, it is known that the gas density shape and composition are key parameters for efficient acceleration and control of the different electron injection mechanisms. In the case of HHG, it has been shown that the high-harmonic yield is highly dependent on the product NL_{med}, where N is the density of the gas and L_{med} the length of the interaction region [192]. An increase of both N or L_{med} results in a larger number of harmonic emitters; nevertheless, propagation effects, reabsorption and macroscopic phase matching confines the optimum conversion efficiency to a certain NL_{med} product.

The dependency with the target conditions for these (and other) cases is the reason behind the extensive characterization of gaseous targets that is normally carried out in this kind of experiments. In this chapter, the underdense gaseous targetry developed at CLPU is presented, as well its characterization, performed at CLPU with home-made interferometers. Comprehensive characterization of nozzles and jets is achieved. Optimal conditions for gas operation in the ultra-intense experiments are found for different electron acceleration and harmonic generation experiments.

Each design, setup and analysis presented in this chapter was developed by C. Salgado in collaboration with L. Rego, at that time a undergraduate student at the University of Salamanca carrying out an internship at CLPU. The Abel inversion algorithm was taken from the MATLAB Central File Exchange [199].

Some relevant optical and thermodynamics properties of the gas species used at CLPU for underdense plasma experiments are shown in the table 5.1.

Gas	$n-1\ (10^{-5})$	$\alpha\ (10^{-41}\,\mathrm{F\,m^2})$	γ_c
He	3.492	2.3	1.67
N_2	29.79	19.62	1.4
Ar	28.12	18.52	1.67

TABLE 5.1: Index of refraction (n) of various gases at normal conditions (273 K and 1 atm) for the probe laser wavelength 632.8 nm. Also, polarizability (α) of such gases at 632.8 nm is given, as well as their specific heat capacity ratio γ_c. Values taken from [94, 241].

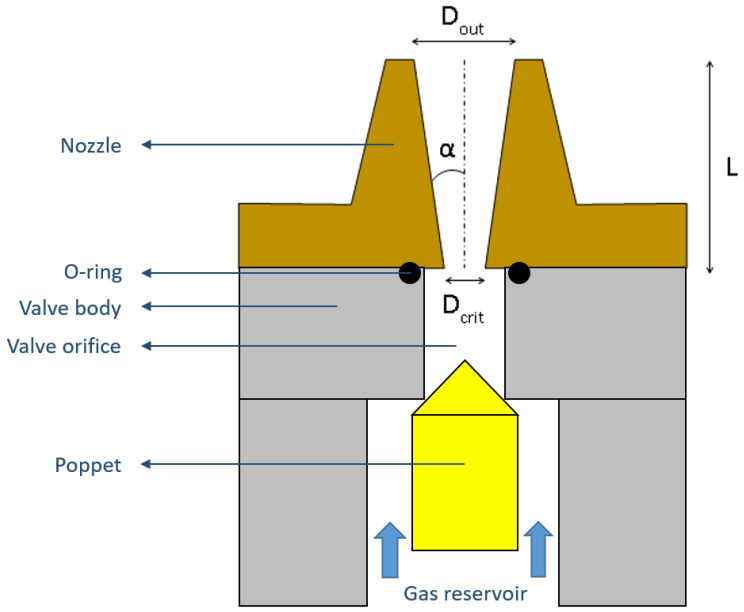

FIGURE 5.1: Sketch of the central section of a conical nozzles connected to its valve. Dashed line represents the symmetry axis. The gas is pressurized before the valve poppet, which moves inwards (downwards on the paper) when fed with the proper voltage, allowing the gas to travel through the valve and nozzle orifices, coming out to the chamber though D_{out}.

5.1 Conical nozzles for laser wakefield electron acceleration

Underdense target experiments carried out at VEGA 2 and VEGA 3 laser facilities normally have employed the moderate pressure gas jet system of CLPU. Its basic operation and elements have been explained in Chapter 3. The specific components of the system are shown in the following list.

- **Valves:** Two different electro-valves from the Series 9 of Parker Hannifin have been used.
  - 009-1643-900 with an orifice size of 0.99 mm.
  - 099-1671-900 with an orifice size of 0.79 mm.
- **Gas jet reservoir**: 200 bar bottles work as gas containers. Argon, Helium and Nitrogen (with less than 5 ppm of impurities) are the chosen gases for characterization. A pressure regulator installed in the output of the bottle controls the gas pressure downstream, from 0 to 100 bars.
- **Pipes:** 1/4' diameter Swagelok hoses and fittings are used to connect all gas jet system components.

Once the valve opens, the gas flows through the valve orifice into the vacuum chamber. Dedicated nozzles are then used to shape and control the density in the proximity of the valve. Furthermore, nozzles are useful tools to spatially confine the gas close to the laser focus, where the interaction is meant to occur. Proper synchronization between the valve opening and the laser arrival is recommended, in order to avoid unnecessary filling of the vacuum chamber and undesired interaction before the focal volume.

For most of the electron acceleration experiments conical nozzles (or de Laval nozzles) are chosen to create the gaseous jets to be irradiated. Their conical design is used in order

Conical nozzles at CLPU	D_{out} (mm)	D_{crit} (mm)	L (mm)	α (°)
BM2_1	2.74	0.83	14,22	3.84
BM5_1	4.98	1.02	10,85	10.37
BM5_2	4.78	0.80	10,45	10.78

TABLE 5.2: Nomenclature, basic dimensions and halve-angles of the conical nozzles studied at CLPU.

to achieve supersonic gas velocities, creating slowly expanding (in the radial direction) jets in the interaction area. A sketch of the geometry of these kind of nozzles is shown in figure 5.1. Conical nozzles have useful characteristics for the experiments.

- Cylindrically symmetric design: this fact facilitate the alignment with respect to the laser axis. If this property is assumed as well on the resulting gas jet then it is possible to perform Abel inversion when analysing the density profiles and therefore be capable of estimating their complete density profiles from a single probing angle.
- The resulting supersonic gas jet has a longitudinal profile with a quasi-flat top shape [66, 70], with fast transitions from vacuum to a density plateau close to the nozzle.
- Known scaling laws for the density with respect to the minimum (D_{crit}) and maximum (D_{out}) nozzle aperture diameters.

The experimental investigation of the density of such gaseous targets was performed following the Mach-Zehnder interferometric methodology explained in Chapter 3. A more detailed sketch of the setup used is shown in figure 5.2. The laser source was a commercial He-Ne laser ($\lambda = 633$ nm) from Thorlasbs Inc. (HNLS008L-EC), a CW laser with < 1 mW, linear polarization and remarkably good spatial quality (TEM_{00} above 95%). In order to cover a sufficiently significant volume of the gas jet, a ten-fold beam expander was built before the interferometer. The beam was inserted in the vacuum chamber with the help of transparent windows, where the interferometer was mounted. The experiment was carried out with a background vacuum level of 5×10^{-6} mbar (the expected vacuum pressure level in the vacuum system of the laser system VEGA). The beam -with the information about the gas density coded in its phase- leaves the chamber through another window. Finally, the gas jet plane is imaged onto a scientific camera (Blackfly PGE-23S6M-C) with the help of a converging lens. By changing the relative position between lens and camera, the imaging magnification was controlled within values of $M = 0.8$ and $M = 1.2$, so jets of different sizes could fit onto the CMOS sensor.

By means of the analysis methodology presented in the Chapter 3, the phase is retrieved from the interferometric data. Afterwards, by imposing cylindrical symmetry and choosing a symmetry axis in the phase map, the Abel inversion is performed (in each horizontal pixel line) and a three-dimensional density map is obtained from a single probing frame. The molecular polarizability values of the gases under analysis, which are required for the conversion of refractive index to density (via the Lorentz-Lorenz formula 4.6) are given in the table 5.1.

5.1.1 Analysis of a single gas jet

A detailed analysis of a single interferometric data is shown in the this section. Such case is the resulting jet of the nozzle BM2_1, use of valve 099-1643-900 with diameter 0.99 mm (i.e. the minimum diameter of the nozzle throat is then 0.83 mm) with 70 bar of N_2. This configuration is chosen as Nitrogen has a large index of refraction (compared to some noble

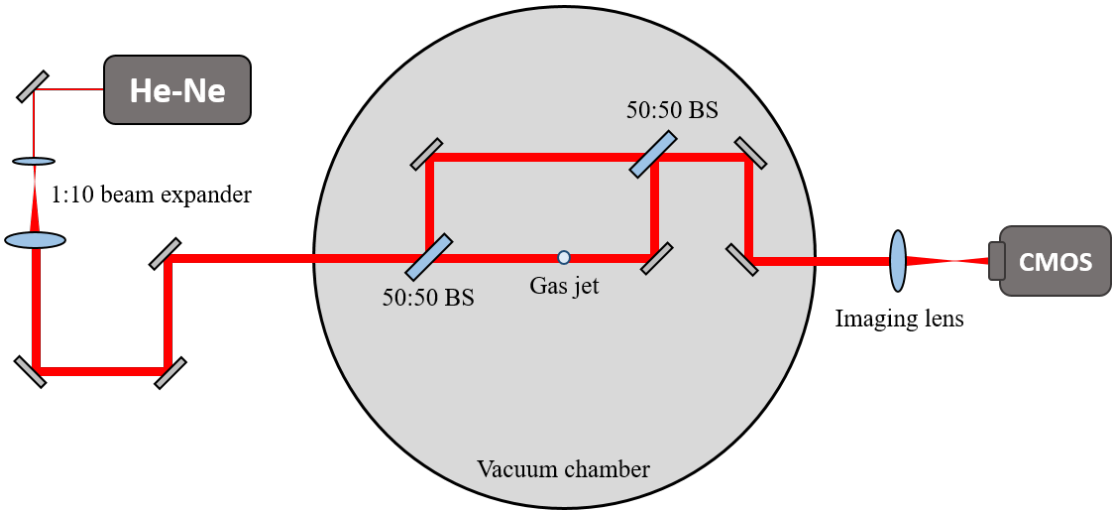

FIGURE 5.2: Sketch of the MZ interferometer built for cylindrical nozzle gas jet investigation.

gases, for instance), and the density scales with the pressure. Therefore, good signal-to-noise ratio is expected. The resulting complete phase map can be seen in figure 5.3.

As it as been already explained, a definition for the axis of symmetry is needed (in each pixel line) in order to perform the Abel inversion. In this case, the symmetry axis has been imposed to be a the same pixel column (same x-axis coordinate in the phase maps) for all the pixel lines. This hypothesis actually imposes that the jet image and the CMOS sensor are properly aligned (axis of symmetry and CMOS axis are parallel), assumption which is valid with a proven tolerance below 0.5° in this case. The pixel representing the symmetry axis was then calculated by estimating the centroid of the transversal coordinates (x) of the phase maps. In order to smooth possible differences between left and right sides, both are averaged and the result is the profile in which the Abel inversion is applied.

The result is a quasi flat-top profile close to the nozzle, which is smearing and smoothing as it expands into the vacuum chamber. This effect is evident when showing individual profiles at different distances as in figure 5.4.

As expected, the transition vacuum to the density plateau is steeper when closer to the nozzle end. The density modulations in the plateau are typical from supersonic flows and are caused by the Mach waves which propagate through the nozzle, reflecting on the walls of the cone and crossing with each other at the nozzle exit [70]. Also, it is important to note that some systematic source of error could contribute to these fluctuations.

- The selection of the mask on the FT for filtering only the fringe information is done manually. The mask has to be small enough so the contributions of the low frequencies (e.g. spatial profile of the laser beam itself) are removed, but it cannot be extremely large, if faster frequencies are included on the mask, discontinuities can appear in the fringe reconstruction, causing failure on the phase unwrapping algorithm. This manual selection may cause that some relevant information about the jet phase to be removed from the analysed data.

- The selection of axis of symmetry is not perfect, meanwhile the imposition of symmetry (averaging both sides) is a further restrictive approximation. This will enhance any error on the phase close to the axis of symmetry, as the Abel inversion diverges when $r \to 0$

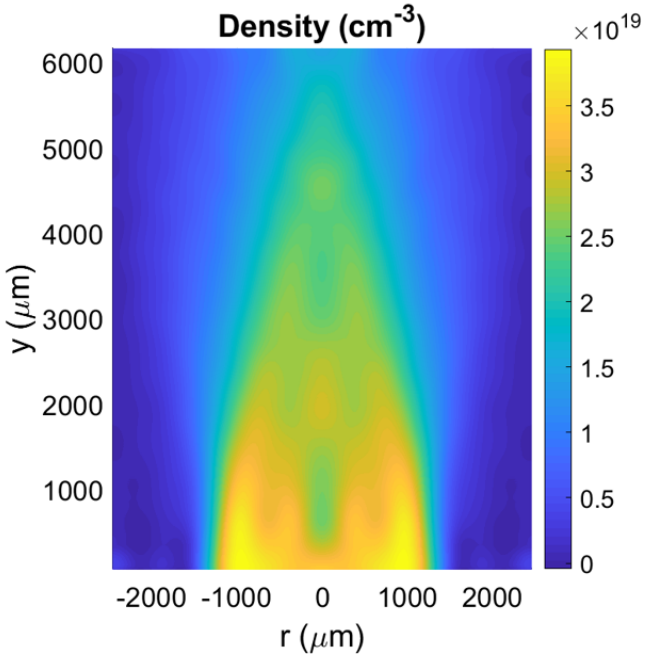

FIGURE 5.3: Molecular density map for the nozzle BM2_1 with 70 bar of nitrogen gas. $y = 0$ set the edge of the nozzle. The gas flow upstream.

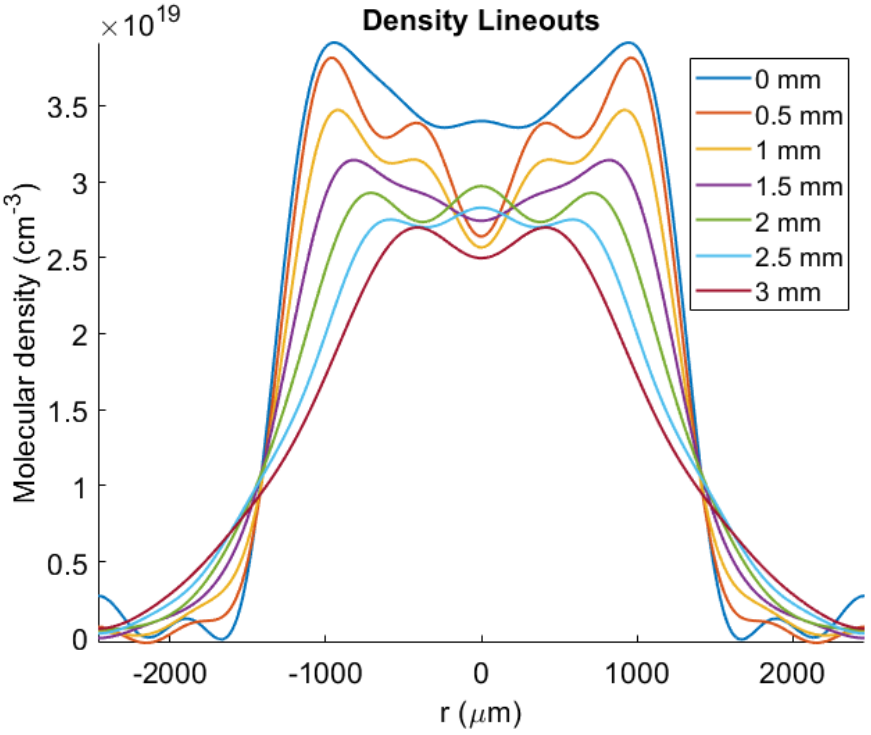

FIGURE 5.4: Density lineouts at different distances to the nozzle taken from figure 5.3.

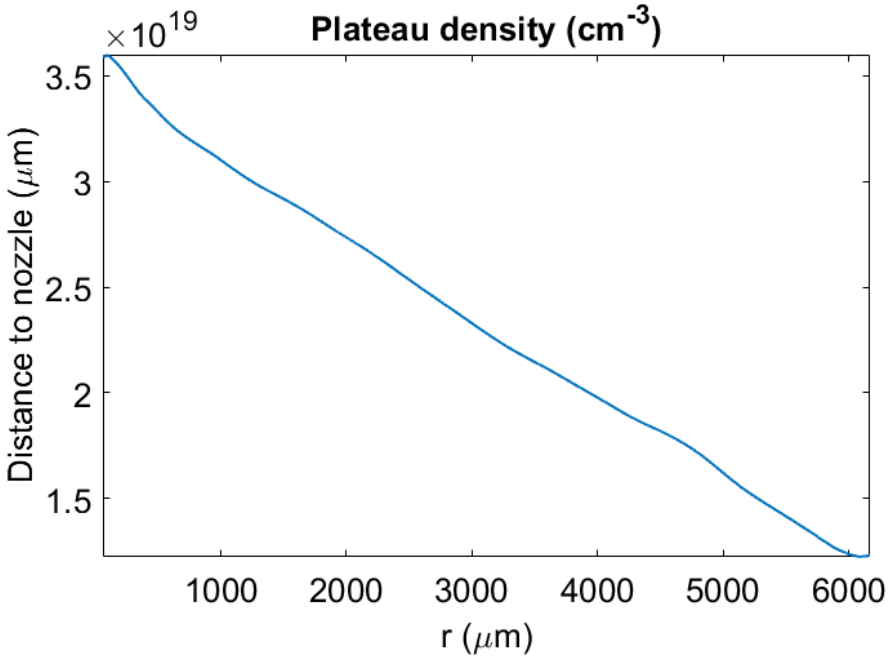

FIGURE 5.5: Average value of the density plateau versus the distance to the nozzle, calculated from the density map of figure 5.3.

- The Abel inversion method used is based on reconstructing the unknown distribution in Fourier-series [198, 199], which could amplify the sinusoidal trend of these fluctuations. Nevertheless, the Fourier-series was chosen to be limited to the 8^{th} order, which somehow acts as a low-pass filtering effect.

In any case, to double check the density of some representative lineouts, these were also calculated with the help of the software for fringe analysis IDEA [242] (developed at the Technical University of Graz, Austria), yielding similar results as the presented analysis.

The average plateau density calculated at each pixel line (i.e. at different distances to the nozzle end by means of averaging density values in a segment of length $\approx 0.9 D_{\text{out}}$) is shown in 5.5, where a clear decreasing trend is observed.

Keeping the same nozzle configuration, the experiment can be repeated at different backing pressures. The resulting chart of the density plateau value for each pressure and distance to nozzle is shown in figure 5.6. These kind of plots are extremely useful for a potential usage of the gaseous target in a laser-plasma experiment, as they allow to know exactly which pressure and distance from the nozzle should be chosen in order to achieve a specific molecular density value. Plasma density can be calculated by imposing a determined ionization degree of the gas Z_i^* (depending on a_0) as

$$n_e = N \sum_i Z_i^* \, n_{i,at}, \tag{5.1}$$

where the index of the summation index refers to each atom type in the molecule and $n_{i,at}$ is the number of atoms of the i-kind that compose that molecule. The case of pure nitrogen at very high intensities ($a_0 \gg 1$, i.e. full ionization) is straightforward as $Z^* = 7$ and $n_{at} = 2$ so $n_e = 14N$. The case of mono-atomic molecules as the noble gases is even simpler. For laser-wakefield experiments, determination of the target density is critical in order to match the laser parameters to the plasma density so efficient acceleration can be achieved.

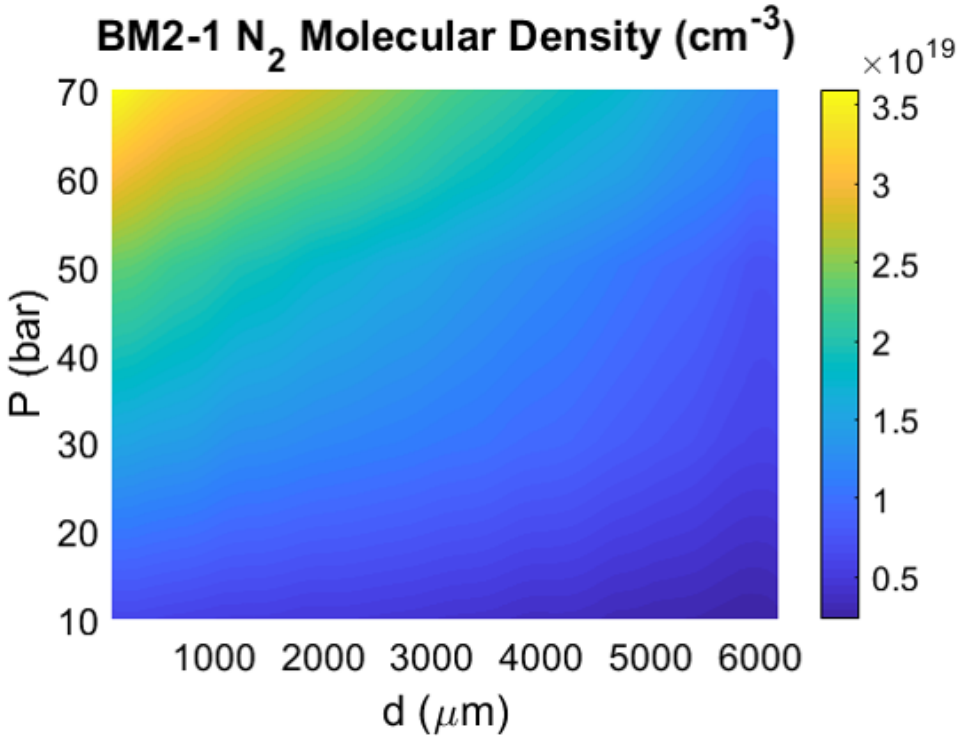

FIGURE 5.6: Average plateau density for different pressures at different distances to the nozzle, for the nozzle BM2_1 fed with N_2. The measured values were taken with 70, 60, 50, 30 and 10 bars of gas backing pressure; the values in between are interpolated.

5.1.2 Gas jet evolution

It was also of interest for the experiments to perform a time-resolved characterization of the jet. For such purpose, repetitions of the interferometric measurement were done with different delay between gas jet trigger and CMOS acquisition time. The time-resolving power is given in this case by the short acquisition time of the CMOS, as small as tens of μs, compared to the typical evolution time of the jet (around ms).

This time-resolved study was performed with the same configuration as shown before: nozzle BM2_1, Nitrogen gas and valve 099-1643-900. The valve controller allows for regulation over the valve opening time, the voltage supplied to the valve and the duration of the initial voltage burst which pushes the valve's poppet in order to allow the gas flow. Following the specifications of the used valve and the pressure conditions of the experiments, the voltage was set to 20 V and the burst duration to 320μs. It was experimentally determined that the valve would malfunction when the backing pressures is above 50 bar if such parameters were not followed.

The operation of the jet is well summarized in figure 5.7, where the phase acquired by the laser is shown at different delays between acquisition and gas jet trigger signal. An increasing density ramp appears right after the valve opening, which last around 2 ms. After this the jet achieve a steady state where the density is more or less constant while the valve is kept open. When the voltage of the valve is shut down, it takes the valve around 0.5 ms to close down.

Such a characterization was of major importance for the usage of the jet in a real experimental environment. From the results of this experiment, a threshold of 2.7 ms of minimum delay between valve opening and laser arrival was set for all the experiments using these kind of gas jets at both VEGA 2 and VEGA 3. In such way, the laser would arrive to TCC

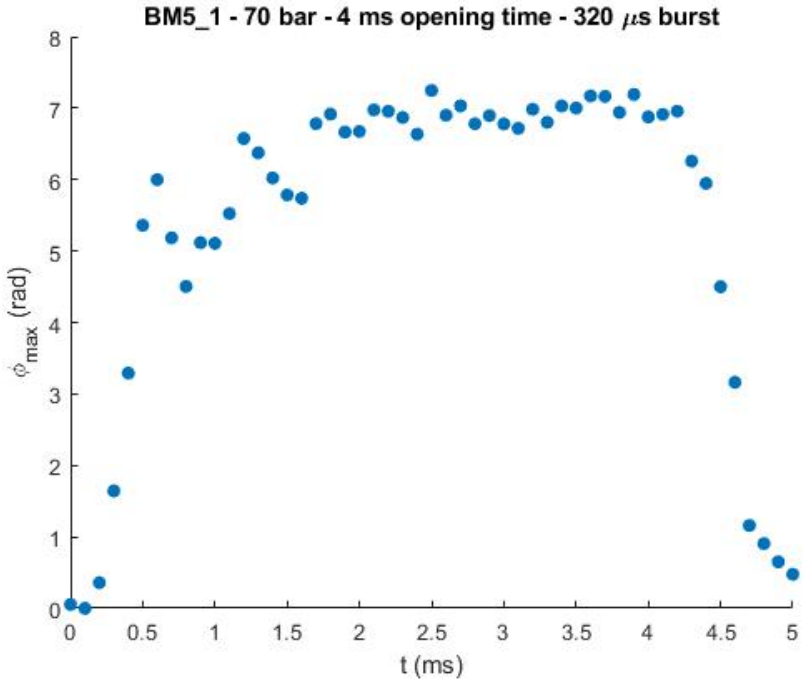

FIGURE 5.7: Time evolution of the maximum phase (measured by the interferometry system) created by the gas jet of the nozzle BM5_1 fed with 70 bars of nitrogen. The valve was set to open during 4 ms.

at the time of the jet with maximum and constant density, but with still with a minimized amount of gas inside the vacuum chamber. Furthermore, after this study the valve opening time could be minimized for not overloading the vacuum equipment as the turbo-molecular pumps. If not specified otherwise, all the gas measurements presented in this Chapter were taken in the stability plateau of the jet evolution.

5.1.3 Comparison between gases

By simply changing the feeding bottle the characterization of the jet can be obtained for other type of gases, as in this case for Helium. Due to its very small refractive index (and polarizability), the acquired phase shift of the probing laser is much smaller and in some cases comparable to the noise, so the measurements are less precise than in the case of Nitrogen.

In order to compare the results of Helium, some representative density plateau values of the Helium jet (for different pressures) at 0.45 mm from the nozzle end are plotted in figure 5.8 together with results for Nitrogen under the exactly same experimental conditions. As it is clear, both set of measurements show a linear relation between the density value and the pressure for both cases. Experimental results yield that the scaling of density with pressure seems to be 1.13 times larger for Helium than for Nitrogen. This fact can be explained by one-dimensional analytical models [70], considering the nozzle to be perfect and the gas to behave as an ideal gas (which in fact is not totally accurate in the case of the Nitrogen, as its behaviour is better depicted by the Van der Waals equation). This model gives the following scaling for the density along the nozzle expansion:

$$\frac{N}{N_0} = \left(1 + \frac{\gamma_c - 1}{2} M^2\right)^{-\frac{1}{\gamma_c - 1}}, \tag{5.2}$$

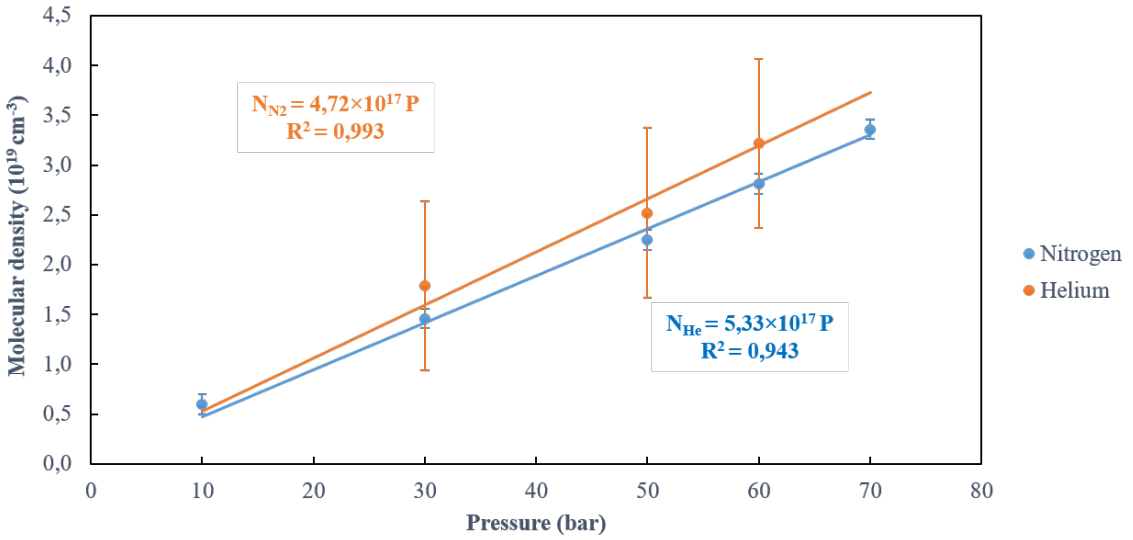

FIGURE 5.8: Plot of the average plateau density for the same gas jet (nozzle BM2_1) and same distance to nozzle (450 µm, for different pressures of Nitrogen (blue) and Helium (orange). Insets show the linear regression and the fitting parameters R^2 of both data sets; the linear fit forces the regressions to cross the origin. Following Chapter 4, the error bars are estimated by considering the averaged standard deviation of consecutive phase shifts of reference shots (i.e. without gas). The measurement error for Helium is larger as $\frac{n_{N_2}-1}{n_{He}-1} \sim 8.5$, yielding a much smaller phase shift in that case.

where N_0 is the density in the gas reservoir and M is the expanding gas local Mach number. In this one-dimensional analytical model the Mach number is given by the gas properties and the nozzle diameter as

$$\left(\frac{d_{\text{crit}}}{d}\right)^2 = M\left[1+\frac{\gamma_c-1}{\gamma_c+1}(M^2-1)\right]^{-\frac{\gamma_c+1}{2(\gamma_c-1)}}, \tag{5.3}$$

where d is the diameter of the nozzle at a certain height. The resulting Mach numbers for 70 bar in the given nozzle geometry are then $M_{N_2} = 4.02$ and $M_{He} = 5.22$ for Nitrogen and Helium respectively. Supposing the density in the gas reservoir before the nozzle to be the same in both cases (i.e. $N_{0,He} = N_{0,N_2}$, which even for same pressure and temperature is not completely true when one of the gases differ from ideal gas behaviour), the ratio between the expected densities at the nozzle exit for both cases can be calculated with equation 5.2. The estimated theoretical result is $N_{He} \approx 1.15 N_{N_2}$. Such a result agrees with the scaling factor calculated experimentally. This scaling was extended to other nozzles (as long as their Mach number can be calculated) for estimating the expected plasma density resulting from pure Helium gas jets at the experiments in VEGA. Same kind of scaling comparison is found in the literature for Helium and Hydrogen [194]. The problem of the small signal-to-noise ratio in the case of Helium can be addressed experimentally by building a double-pass interferometer as shown in [67], where Helium and Argon are also compared.

5.1.4 Comparison between conical nozzles

Full characterization of the Nitrogen density was also performed for the jets generated by two other nozzles:

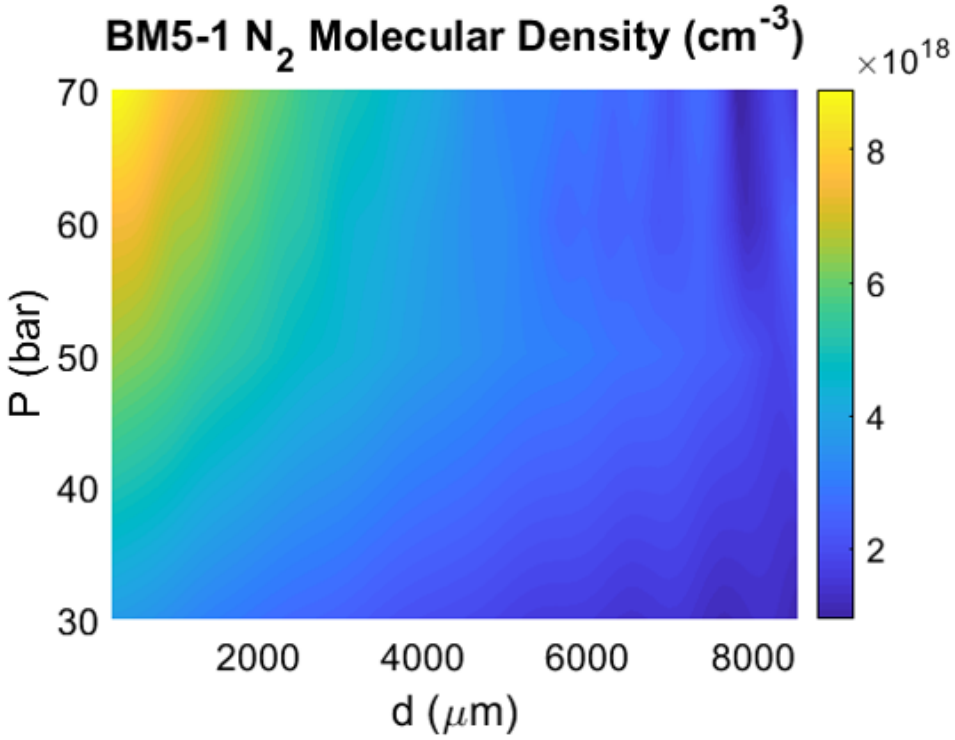

FIGURE 5.9: Average plateau density for different pressures at different distances to the nozzle, for the nozzle BM5_1 fed with N_2. The measured values were taken with 70, 60, 50 and 30 bars of gas backing pressure; the values in between are interpolated.

- Nozzle BM5_1 with valve 099-1643-900 (critical diameter $\sim$ 1 mm, exit diameter $\sim$ 5 mm).
- Nozzle BM5_2 with valve 099-1671-900 (critical diameter $\sim$ 0.8 mm, exit diameter $\sim$ 5 mm).

The complete graphs of the plateau density for different pressures and distance to nozzles are shown in figures 5.9 and 5.10.

In order to compare both nozzles, similarly as in the gas species comparison, the average density values of both cases at a fixed distance to the nozzle for different backing pressures are plotted in figure 5.11. Again the linear trend with the pressure is clear. The same 1D analytical model, after equation 5.3, yields $M_{\mathrm{BM5\_1}} = 4.94$ and $M_{\mathrm{BM5\_2}} = 5.50$ in the nozzle edge. This would mean, after equation 5.2 that in the border of the nozzle the ratio of the expected density is $N_{\mathrm{BM5\_1}}/N_{\mathrm{BM5\_2}} = 1.57$, which is indeed similar to the critical orifice area (i.e. $\pi D_{\mathrm{crit}}^2/4$) ratio between the nozzles (as the outer diameter D_{out} is similar for both). Nevertheless, the experimentally measured density ratio according to the fittings from 5.11 is noticeably different ($N_{\mathrm{BM5\_1}}/N_{\mathrm{BM5\_2}} = 2.77$).

The main reason for this discrepancy may be the use of two different valve models in the two characterization campaigns. The gas flow dynamics can be severely determined by the valve used. Most likely, the valve used for the BM5_2 did not fully open. Other smaller corrections to explain the difference between the prediction and the experimental data are given in the following list.

- The analytical model is a simplistic one-dimensional approximation, where higher-dimension effects are not taken into account. The transversal dimension of these nozzles is larger than in the case of the BM2_1 (i.e. larger cone angle), then is reasonable

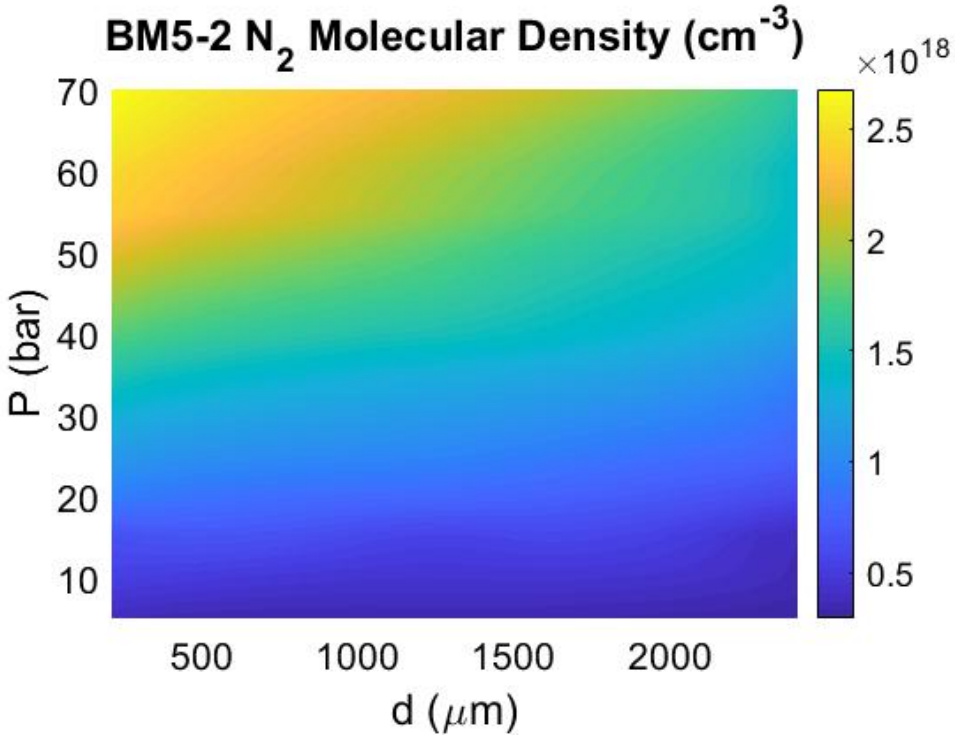

FIGURE 5.10: Average plateau density for different pressures at different distances to the nozzle, for the nozzle BM2_2 fed with N_2. The measured values were taken in regular intervals of 5 bar of gas backing pressure; the values in between are interpolated.

to think than the hypothesis is not optimal for this case.

- The prediction of the density relation is given in the edge of the nozzle by the model. Nevertheless the measurements were carried out a few hundreds of microns far away from the nozzle, which was the available measurement point closer to the nozzle in the experimental configuration. For extrapolation of the density scaling to that point, the model should take into account the gas flow into the vacuum chamber and its resulting divergence.
- The characterization of the jet created by the nozzle BM5_2 was performed in a different experimental setup. This jet was measured in a Nomarsky interferometer dedicated to measure shock jets (see Chapter 3 and 5). However the same analysis algorithms were used in both cases.

These results indicate the importance in measuring the actual gas jet profile for every experimental situation in order to have an accurate gas density profile.

5.1.5 Application in Laser Wakefield Acceleration

The previously presented conical jets have been used as underdense targets at VEGA 2 and VEGA 3 laser facilities in more than 5 different experimental campaigns. The goal of these experiments was mostly laser-driven electron wakefield acceleration and betatron generation, but also a couple of experiments based on high harmonic generation and Relativistic Thomson Scattering were carried out.

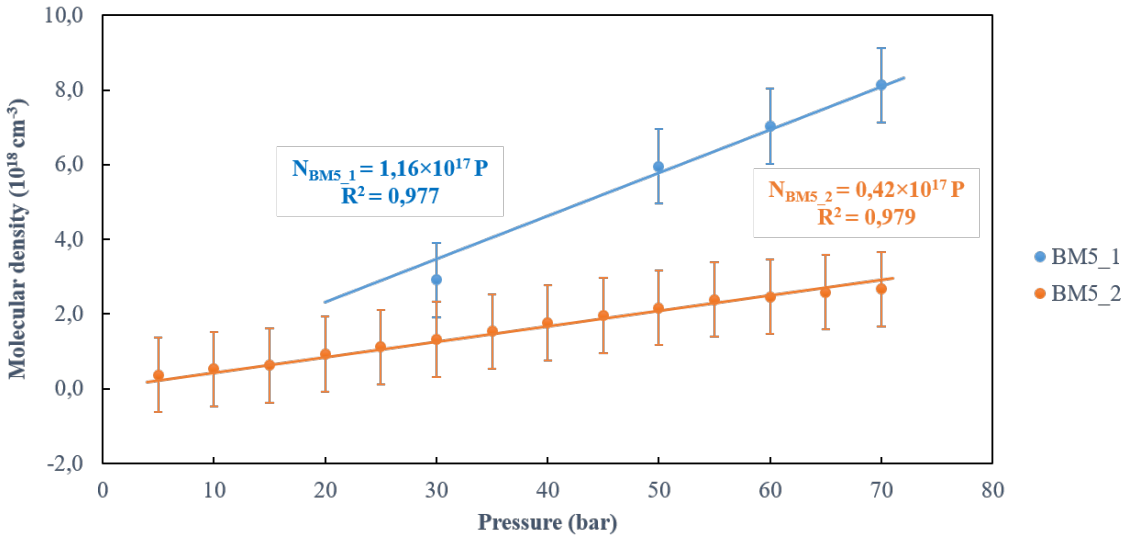

FIGURE 5.11: Plot of the average plateau density at different Nitrogen pressures for the nozzle BM5_1 (blue) and BM5_2 (orange) at the same distance to nozzle (230 µm). Insets show the linear regression and the fitting parameters R^2 of both data sets; the linear fit forces the regressions to cross the origin. Error bars are calculated similarly as in figure 5.8

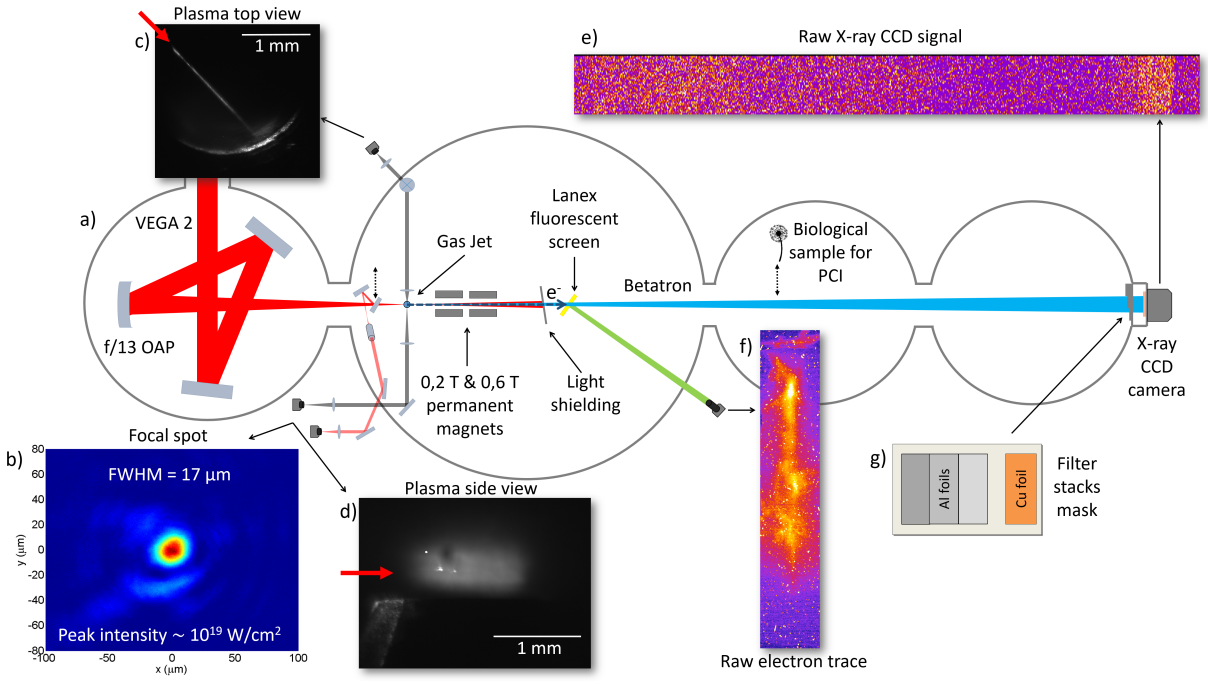

FIGURE 5.12: a) General setup of the LWFA commissioning experiment at VEGA 2. b) Laser focal spot. c) Zenithal plasma image (red arrow points the laser direction) d) Lateral plasma image (red arrow points the laser direction). e) Raw X-ray CCD signal of the Betatron radiation. f) Electron spectral trace measured on Lanex screen. g) Step-filter configuration for Betatron characterization.

The first experiment were these targets were successfully tested was the VEGA 2 commissioning experiment based on electron acceleration. The experiment led by Prof. R. Fedosejevs from the University of Alberta, Canada, was focused in the use of the ultrashort X-ray pulses resulting from the Betatron oscillation as a probe for ultrafast abortion spectroscopy of Warm Dense Aluminium [51]. The study of this kind of matter is relevant for a large number of areas, including inertial confinement fusion and astrophysics. Profit can be taken from the femtosecond lasers to generate non-equilibrium warm dense matter, but an ultrafast probe is required for instantaneous measurement of their ionization states and equation of state. Betatron radiation from a laser-driven electron beam is an ideal candidate for such probe, due to its ultrashort duration, wavelength and intrinsic synchronization with the warm dense mater heater beam. For such diagnostic to work efficiently, maximization of the Betatron yield around the K absorption line of Aluminium ($\sim 1.5\,\mathrm{keV}$) was needed. Being the typical critical energy of the Betatron spectrum around 10 keV, the optimization of these photons is achieved by maximization of the electron charge self-injected and accelerated in the plasma [56], not by optimizing the maximum electron energy or quality. This is the reason why plasma densities above the bubble regime matching conditions were generated in this experiment.

A detailed sketch of the experimental setup for electron beam and betatron characterization can be found in figure 5.12. The VEGA 2 laser pulses (nominal energy on target 4 J, 30 fs length) were focalized by a $f^{\#} = 13$ off-axis parabolic mirror onto a 17 µm FWHM focal spot, resulting in a peak intensity of $\sim 10^{19}\,\mathrm{W/cm^2}$ ($a_0 > 2$). We used as target the gas jet resulting from the nozzle BM5_1 with Helium at large pressure, yielding a electronic plasma density $n_e \sim 1.3 \times 10^{19}\,\mathrm{cm^{-3}}$, supposing full ionization. It is important to note that the density requirement for 30-fs long pulses for the bubble regime

$$c\tau = \frac{\lambda_p}{2} \tag{5.4}$$

means that the optimal electron density is $3 \times 10^{18}\,\mathrm{cm^{-3}}$, 4-fold smaller than the density experimentally achieved. Two perpendicular imaging systems of the scattered photons in the plasma were built in order to control the relative alignment between laser and gas target. A high magnification imaging system evaluated the focal spot quality. By means of a magnetic dipole combination and a Lanex scintillating screen, a broadband electron spectrometer was built. Figure 5.13 shows an example of an electron spectrum obtained. As expected, due to the plasma regime chosen, quite broadband multi-100-MeV electron energy spectra are measured. Thanks to the extensive literature for calibration of the Lanex screens response to electrons [243], the beam charge could be estimated to $\sim$ 50 pC in the typical case. The broad electron spectrum retrieved (with very poor shot-to-shot repeatability) and the target utilized are indications of a electron self-injection regime into the plasma wave.

On the other hand, the Betatron spectrum was measured by Ross-filter technique, which is based on the estimation of the transmission of the X-rays after different stacks of filters [138]. In this case, different stacks of Aluminium and Copper were used and the photons detected with a X-ray CCD camera. The best fit for a synchrotron-like spectrum for the data taken was for a critical energy $E_{\mathrm{crit}} = 10 \pm 1$ keV. The analysis, carried out in collaboration with S. Malko and R. Fedosejevs yielded a brightness of $\sim 10^8$ photons/sr/0.1%BW/shot.

This Betatron source was used as well as a spatially-coherent back-lighting X-ray source for a phase contrast image of biological samples. Measuring the transmitted X-ray beam with a X-ray CCD camera and setting a experimental magnification $M \sim 2$, the details of the sample were recorded with 13 µm spatial resolution. Details about this experiment can be found in G. Zeraouli Ph.D. manuscript [244].

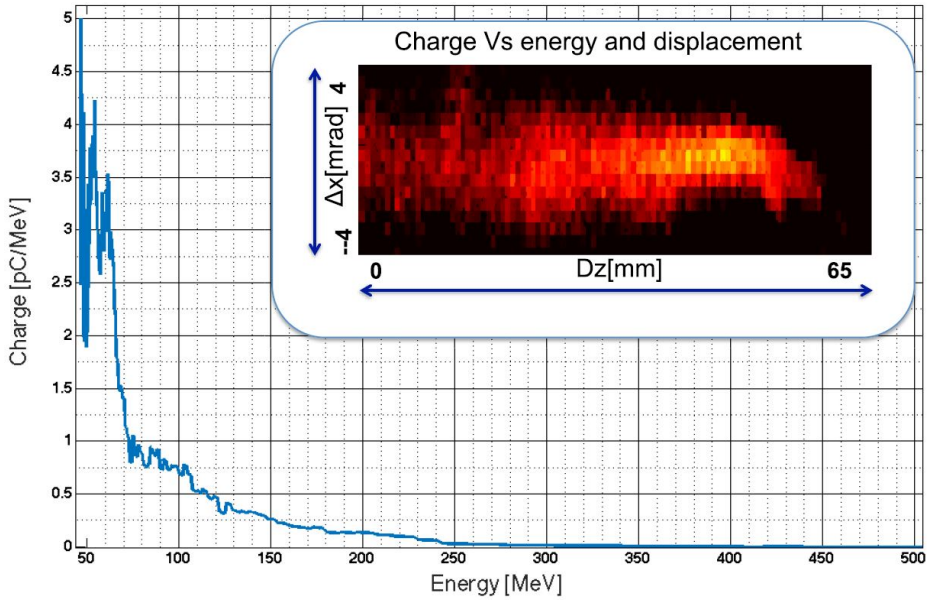

FIGURE 5.13: Typical electron spectrum and filtered Lanex signal (inset) of a single shot of the VEGA 2 electron acceleration commissioning experiment, taken from [60]. Analysis in collaboration with G. Gatti.

5.2 Rectangular nozzle for High Harmonics Generation experiment

The brightness of the HHG sources is limited by several factors, including a very small conversion efficiency (10^{-5} to 10^{-7}) and the necessity to operate in a very narrow range of intensities to avoid plasma formation (it depends on the ionization potential of the target atoms, but always around $10^{15}\,\mathrm{W/cm^2}$), which are normally achieved around the focal volume of the driving lasers. Many experimental techniques have been proposed to increase the harmonic yield; the focal cone high harmonic generation (FCHHG) is one of them [245, 246]. The main idea is to place the gas target at a specific position of the converging focal cone of the laser (where the condition for the laser intensity is fulfilled), and in return allowing a much larger interaction area, enhancing therefore the total energy accepted for the driver laser and increasing the number of potential harmonic emitters. Furthermore, this coherent radiation generation process in such experimental configuration would create a converging harmonic beam, which when optimized could led to ultra-intense XUV focal spot.

A FCHHG experiment was successfully commissioned at the VEGA 3 petawatt facility in CLPU, in a competitive access collaborative experiment of the University of Alberta, Canada (Principal Investigator Prof. R. Fedosejevs) and the CLPU. Implementation of the FCHHG scheme into the VEGA 3 focalization geometry ($f/11$ OAP, $f' = 2500$ mm) requires from a quasi-homogeneous jet with a transversal dimension larger than the beam diameter at a specific distance to focus. A rectangular nozzle was designed and built for such purpose (which can be adapted to the Parker Series 9 valve), whose characteristics are shown figure 5.14. In this case low gas densities of $10^{17}\mathrm{cm}^{-3}$ to $10^{18}\mathrm{cm}^{-3}$ were required.

Gaseous characterization was necessary in order to experimentally determine the harmonic efficiency scaling with the gas density. Similarly as in the case of the conical jets, the characterization was performed via interferometry. For the nozzle geometry given, the probing direction for phase accumulation should be in the jet larger dimension, so the accumulated phase is maximized and the signal to noise ratio is improved. For this reason, a MZI with vertical probing direction was built directly in VEGA 3 experimental chamber,

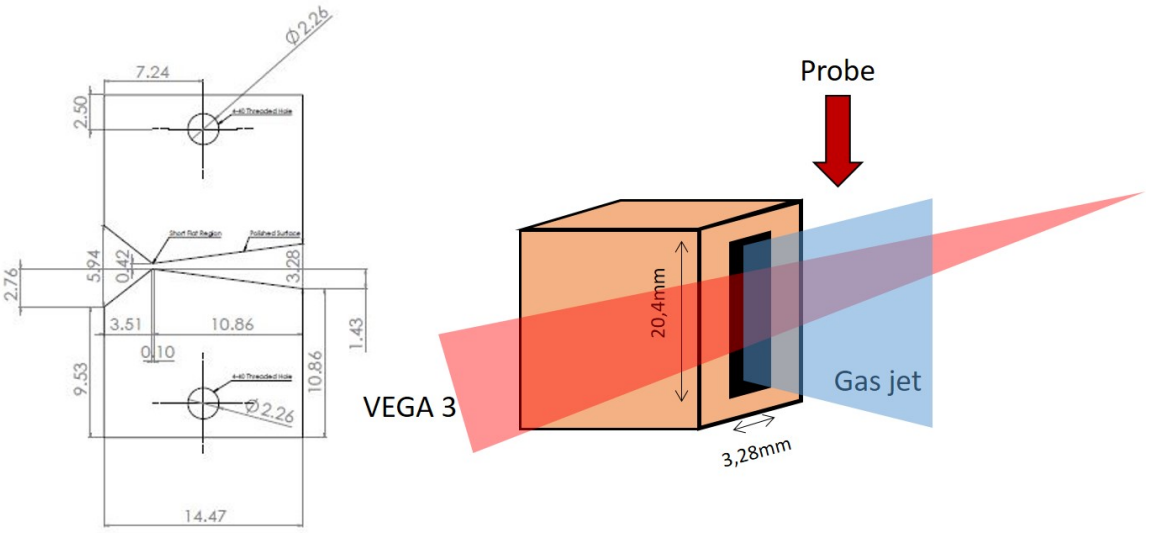

FIGURE 5.14: Nozzle transversal section plane (left) and irradiation geometry (right).

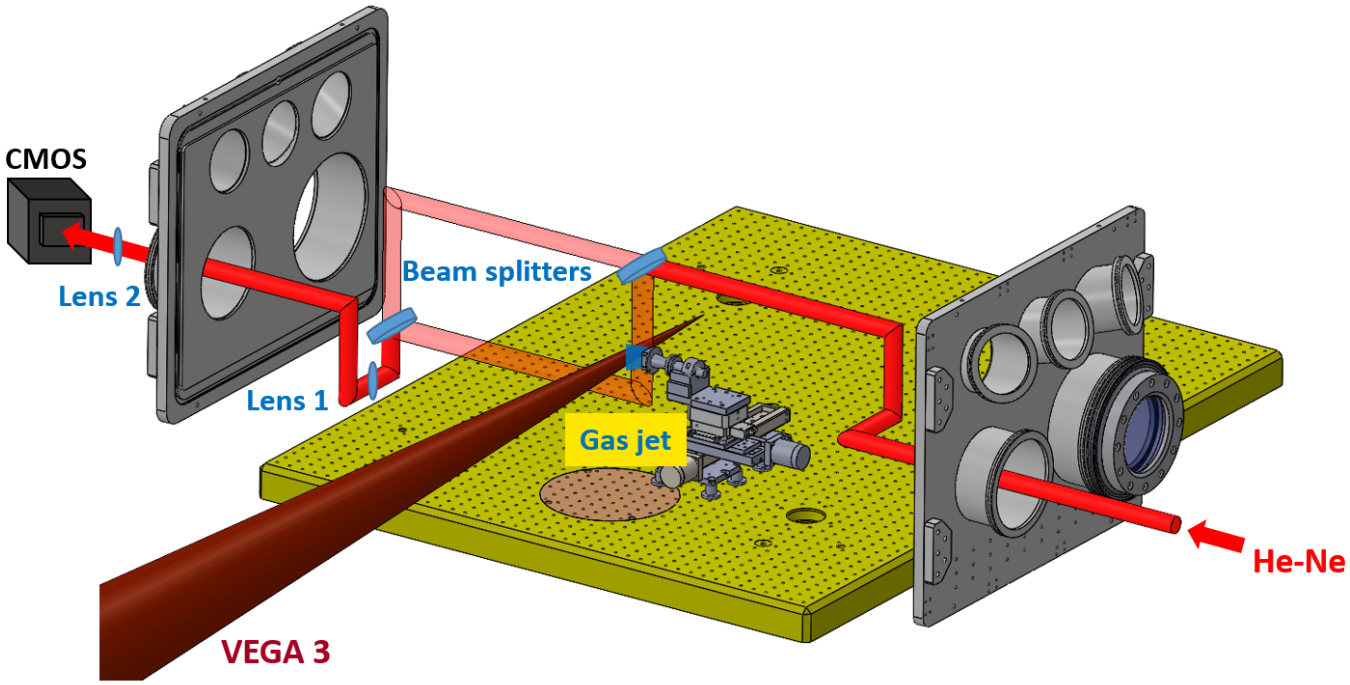

FIGURE 5.15: SolidWorks drawing of the gaseous target configuration, driver beam focalization geometry and gaseous characterization interferometric setup for the focal cone HHG experiment.

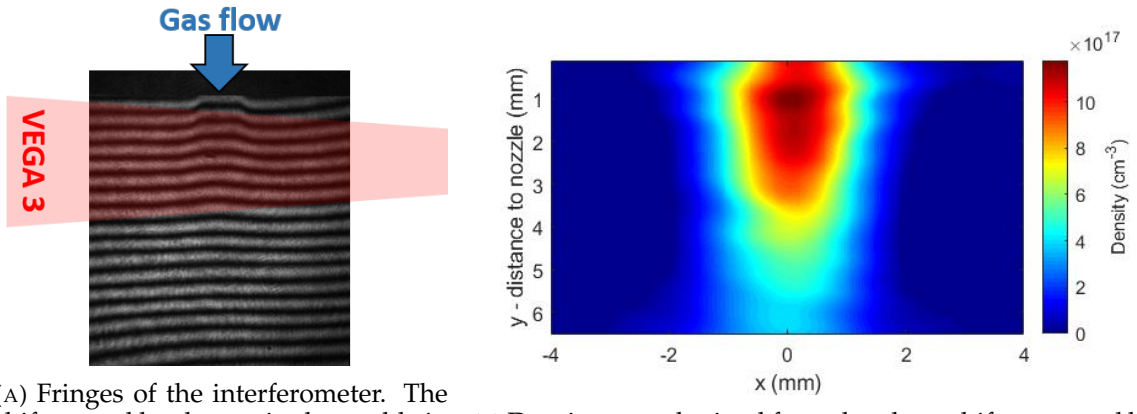

(A) Fringes of the interferometer. The shift caused by the gas is observable in the center of the image.

(B) Density map obtained from the phase shift measured by the interferometer.

FIGURE 5.16: Typical raw interferometric signal and density map of the rectangular gas jet with 50 bar of Argon.

where the gas density was characterized previous to the laser beam time. Despite of its complexity when probing vertically (several periscopes were required) a MZI was chosen due to its flexibility and its large field of view when large diameter optics are used. The plane of the interferometer is shown in figure 5.15.

A double converging lens imaging system imaged the central plane of the gas jet onto a scientific CMOS (Hamamatsu ORCA-flash, 2048 × 2048 pixels of 6.5µm lateral size). The magnification of the imaging system was $f_2'/f_1' = 0.33$, resulting in a spatial calibration of 19.8 µm/pix. Following the interferometric methodology for rectangular nozzles described in Chapter 3, imposing flat-top profile in the jet longitudinal direction of the nozzle the density is obtained with equation 4.8. The typical fringe shift and corresponding density chart are shown in figure 5.16 for a gas shot with 50 bar of Argon.

A time-resolved framed density acquisition was performed for this jet. The opening time of the valve was set to 7 ms and the feeding gas was 50 bars of Argon (the gas used during the experiment). The resulting density values for different delays between valve and camera triggers are shown in figure 5.17. This graph was used to optimize the required delay between valve trigger and VEGA 3 arrival for minimization of the gas inside the chamber and avoid of harmonics reabsorption. Density estimates for other backing pressures was obtained by assuming linear scaling with P.

The experiment was carried out after the gas characterization at VEGA 3 laser facility. HHG was demonstrated in the focal cone geometry for a range of driver laser energies (1-12 J) and pulse durations (30-300 fs). The gas jet was set in a motorized XYZ stage which allowed the jet to be placed between 50 mm and 250 mm before focus (with corresponding beam diameters of 22 mm and 4.4 mm. By means of a UV transmission grating, odd harmonics (as expected in Argon) between the 19^{th} and the 37^{th} order were identified, with conversion efficiencies ranging 10^{-7} - 10^{-6}. Furthermore, the existence of the harmonic spot was indirectly demonstrated by knife edge technique [247]. Details of the experiment will be found in future publication, in preparation at the time of the writing of this manuscript.

It should be noted that the underdense gas targets characterized by the author have been used in a number of other experimental campaigns at VEGA 2 and VEGA 3 laser facilities, including:

- **Proton/Electron Beams' Space/Time Characterization**
  Mar/2020 (4 weeks beam-time) at VEGA 2 (200 TW), CLPU, Salamanca, Spain. PI: G. Gatti (CLPU, Spain).

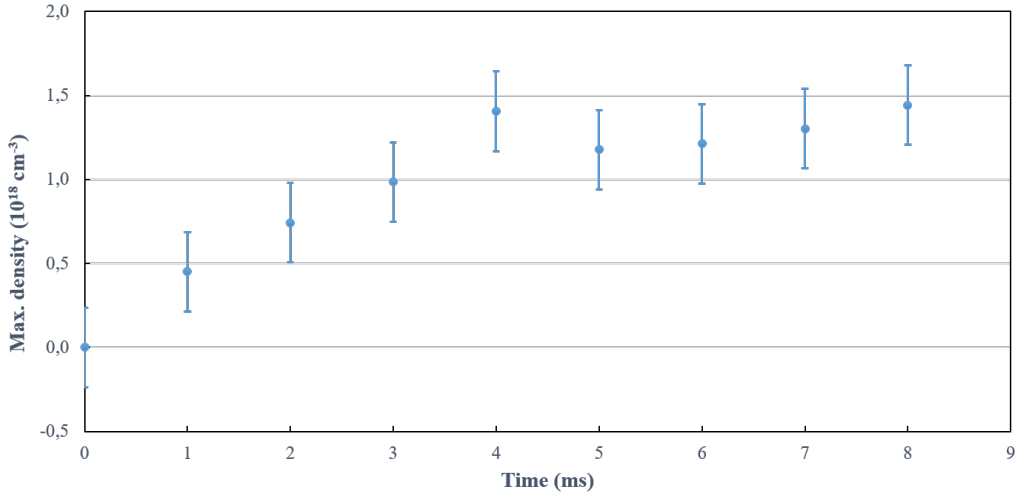

FIGURE 5.17: Time evolution of the maximum density generated by the rectangular nozzle fed with 50 bar of Argon and valve opening time of 7 ms. Error bars are calculated from comparison between reference shots (i.e. without gas).

Participation of the candidate: setup construction, including gas target, counter-propagating beam and mid-infrared beamline for transition radiation diagnostics.

- **Relativistic Thompson Scattering based vacuum gauge**
  Jul/2018 (2 weeks beam-time) at VEGA 2 (200 TW), CLPU, Salamanca, Spain. PI: W. T. Hill (University of Maryland, USA).
  Participation of the candidate: gas target setup.
  Publication: 10.1364/OE.27.030020.

- **Betatron enhancement with orbital angular momentum laser beams**
  Jun/2018 (3 weeks beam-time) at VEGA 2 (200 TW), CLPU, Salamanca, Spain. PI: R. Fedosejevs (University of Alberta, Canada).
  Participation of the candidate: gas target handling, implementation of orbital momentum beamline and probe beam construction.
  Publication: 10.1364/OL.387363.

- **Braided electron beams and X-ray radiation emission from interacting wake-fields.**
  Apr/2018 (3 weeks beam-time) at VEGA 2 (200 TW), CLPU, Salamanca, Spain. PI: O. Lundh (Lund University, Sweden).
  Participation of the candidate: beamline alignment and gas target handling and analysis.

Chapter 6

Diagnostics for laser-driven ion acceleration in near-critical plasmas

Chapter 3 introduced the high density gas jets as one of the most promising techniques for near-critical target generation. Their high-repetition rate potential and debris-free interaction are critical aspects favouring their employment as targets for laser-driven particle accelerators for future industrial or medical applications.

In the frame of the Bordeaux University Excellence Initiative: Laser and Photonics in Aquitaine, "project IonGasJet", a collaboration between numerous different laboratories in Europe was accomplished, including CLPU, Centre d'Etudes Nucléaires de Bordeaux-Gradignan (CENBG), Commissariat a l'Énergie Atomique (CEA), Technische Universität Darmstadt, Prague Asterix Laser System (PALS), Institute of Plasma Physics and Laser Microfusion (IPPLM) and led by the research group of J. J. Santos from Centre Lasers Intenses et Applications (CELIA), Bordeaux, France. A research program focused on laser-driven ion acceleration with high density gaseous targets was carried out during several years. Several gas characterization campaigns of such target were performed both in CELIA and CLPU, whose results are presented in this thesis. The first ion acceleration experiment in a multi-TW facility (VEGA 2) in 2018 is also described here. An extended set of specific diagnostics were developed in order to distinguish between the different possible plasma mechanisms at play. Special emphasis is made on the results of target and plasma diagnostics which were under responsibility of the candidate at that time, including plasma interferometry and gaseous characterization. A more detailed examination of the rest of diagnostics can be found in the thesis manuscript of Dr. M. Ehret [248]. A preprint with the experimental outcomes, simulations and interpretation was published in [75], with Dr. M. Ehret and C. Salgado as principal authors. Following this research line, the candidate completed a three-month research internship at CELIA, distributed in several time intervals between 2016 and 2019. In this period, the candidate participated in the technical commissioning of the gas jet system and its first characterization campaigns before the experiment at VEGA 2, and he carried out the analysis of the optical diagnostics after such experiment.

The experience gained in the operation and limitations of the use of a high density gaseous target in a ultra-intense laser environment was applied to improve the setup of a follow-up experiment at the VEGA 3 laser facility. This experiment used as a target a modified version of the gas system better adapted for the experimental conditions, improved versions of all the plasma and particle diagnostics and better control over the laser parameters. Details of the experimental results can be found in Dr. V. Ospina-Bohórquez Ph.D. manuscript [249], who was the main responsible for experimental design and coordination. In this case, the Ph. D. candidate assumed the role of host facility coordinator. This chapter shows the main experimental outcome of this campaign, placing special emphasis on the tasks assumed by the candidate, as gas target characterization, driver-laser axis control and probe laser construction, among others.

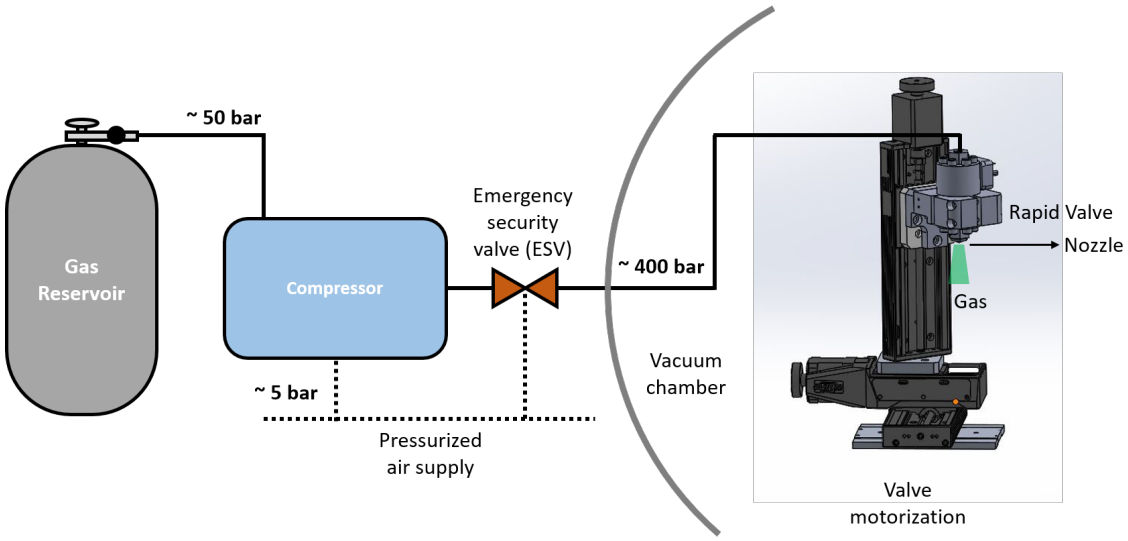

FIGURE 6.1: Sketch of the high pressure gas system SL-GT-10 from SourceLab. Solid lines represent the high pressure tubes with the gas of interest. Dashed lines show indicate the pressurized air system.

6.1 High density gas jet system

The gas system used in this research was the commercial system SL-GT-10 developed by SourceLab [74]. Its operation it is summarized in figure 6.1. A gas compressor -which works as a pneumatic device- is fed both with the desired gas and with a high flux compressed air supply (which comes from the centralized pressurized air system of the facility). A piston with a surface ratio of 75 between both faces is cyclically pushed by the pressurized air line (whose pressure is regulated in the compressor input) in order to compress the gas of interest. This gas is then able to reach 75 times the pressure of the air line. With a maximum available cutoff of pressurized air of 5.6 bar, the gas can be squeezed up to 420 bars. This is precisely the pressure limit of the hoses and connections of the system. These high pressure but flexible hoses connect the compressor with the vacuum chamber wall feedthrough and subsequently with the rapid valve. The output valve, which is controlled with a pulsed voltage generator, opens and closes in the millisecond range controlling the gas flow into the chamber. As in the case of conventional gas jets, in order to shape the gas jet density close to the valve, a dedicated nozzle is attached to the valve output. The valve is motorized in 3 degrees of freedom in order to position it relative to the laser focus. An emergency security valve (ESV) is placed between compressor and vacuum chamber; this pneumatic valve closes when a certain pressure gradient threshold is reached in the connection hoses, which prevents the complete discharge of the compressor content into the vacuum chamber in case of an output valve failure.

The system can work with any kind of nozzle, including the rectangular or cylindrical types presented in Chapter 4. Nevertheless for a proper interaction between laser and plasma it is advantageous to create a near-critical density but reduced volume gas target at a considerable distance from the nozzle edge so laser-induced damaged can be minimized. For such purpose, the so-called shock nozzles are used. Figure 6.2 shows a typical density map of this kind of nozzles (taken with Nitrogen at 400 bars), meanwhile depicting the nozzle geometry. This submillimeter nozzles resemble the conical type but include a cylindrical section before the edge (often called rim) where the divergent flow is reflected. This stream converges in a position in space separated from the nozzle edge, crating a high density volume that it is called the shock point. Depending on the specific geometry and

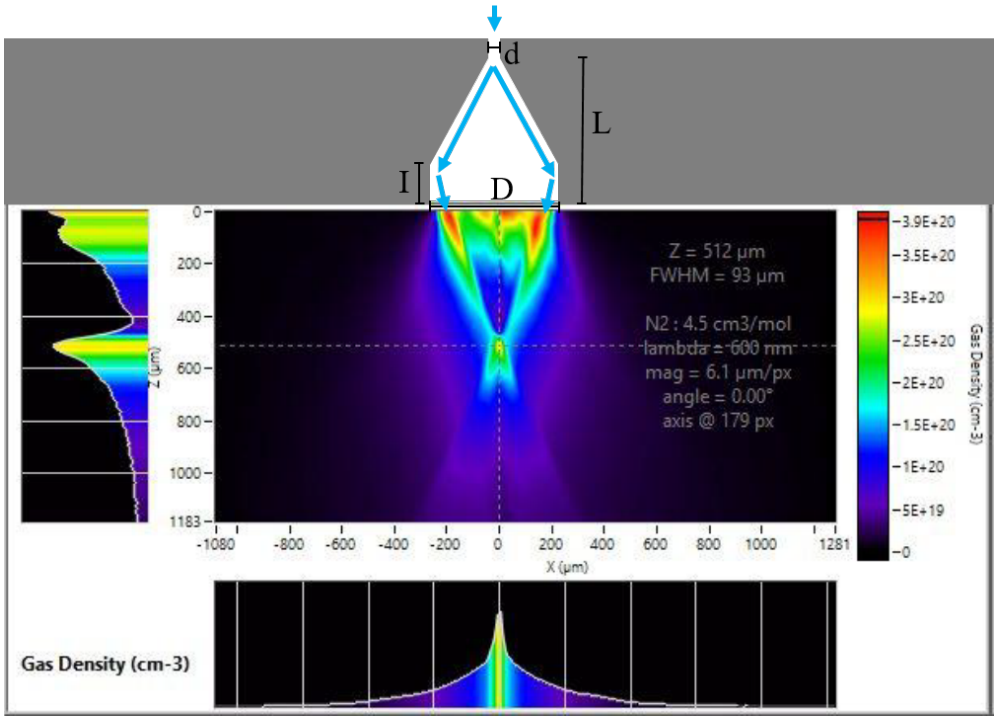

FIGURE 6.2: Typical gas density map of a fully developed gas jet generated by a shock nozzle backed with 400 bars of nitrogen. Density map provided by the company SourceLab. Left and bottom plots are vertical and horizontal lineouts crossing the shock point. Top drawing shows typical shock nozzle geometry.

Mach number of the nozzle design, the shock point will have different sizes and shapes and its distance to the nozzle edge will vary.

The plasma effect sought for ion acceleration in this research line (collisionless shock acceleration) was presented in Chapter 2. Being a purely electromagnetic effect, ions with higher charge to mass ratio will be favoured by this mechanism. Therefore hydrogen would be the best candidate for the target composition. Despite its benefits, since the proper operation of the system was not guaranteed with H_2 and due to its explosive nature, Hydrogen gas was discarded. In addition, the host facility was not ready for handling of explosive gases. The second best candidate would then be Helium ions. An extensive study of the performance of the valve (with shock nozzle attached) fed with Helium was first addressed. Due to its design being normally open, the rapid valve systematically failed to close once opened. This fact resulted in the filling of the vacuum chamber with gas, despite the ESV closing) and the subsequent braking of the turbo-molecular pumps, which creates considerable stress and a rapid reduction of their service life. On the other hand, this behaviour was not observed when working with heavier gases such as Nitrogen, although not providing the best ions for acceleration. A compromise solution was found by the use of a gas mixture of Nitrogen gas doped with a small percentage of Helium. For such purpose the gas mixing system of CLPU was helpful. This device, which is represented in figure 6.3, allows for the creation of a precise mixture of the various gas species, its storage in an auxiliary bottle (limited up to 100 bars of pressure) and in addition a remote controlled output. The mixture generation process is simple. Firstly, gas impurities are removed from the reservoir dedicated for the gas mixture and the gas lines with the help of a vacuum (rotatory) pump. Secondly, the reservoir is partially filled with the gas type which will become the dopant of the mixture. Afterwards, the reservoir is filled with the bottle containing the gas which

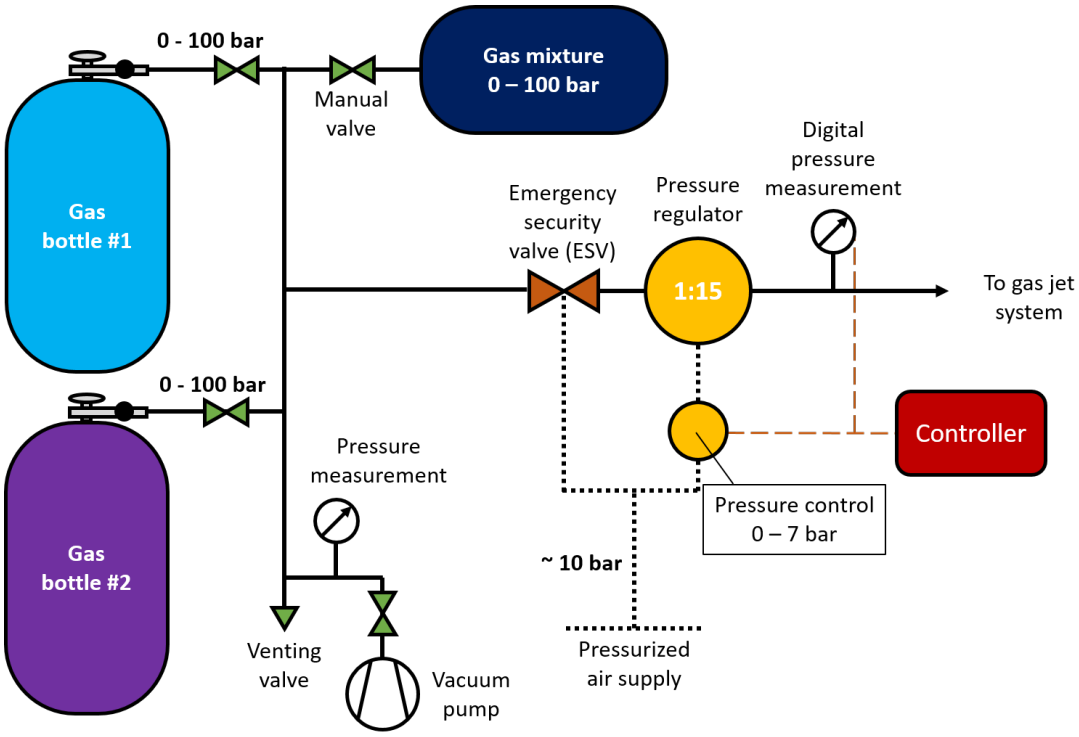

FIGURE 6.3: Sketch of the gas mixing system of CLPU. Solid lines represent the high pressure tubes with the gas of interest. Dashed black lines indicate the pressurized air system.

will be the predominant part of the mixture. Dalton's Law of the additivity of pressures states that the pressure of a mixture is equal to the sum of the individual gases; therefore the calculation for the mixture percentage is straightforward. For instance, if the tank has to be filled to the maximum capacity (100 bars) and the gas composition sought is 5% Helium and 95% Nitrogen, then the reservoir should be simply filled with 5 bars of Helium and later with Nitrogen up to 100 bars. In this case, the atomic ratio would be then 2.5%, as the Nitrogen is a diatomic molecule.

The system connects the gas reservoir with the compressor of the gas jet via a pneumatic pressure regulator, which is supplied by a controlled pressurized air line. The cylinder surface ratio of this regulator is 1 to 15, so the feeding air pressures range from 0 to 6.67 bars for corresponding output gas pressures between 0 and 100 bars. A digital pressure measurement device is placed downstream for the fine pressure estimation, which is connected through a electronic controller with the air regulator, creating therefore a closed loop for fine pressure control. Additionally, a pneumatic valve is placed in the main tube for security reasons; this valve can be manually activated or alternatively controlled by an external rule from other device, as a vacuum gauge interlock from the interaction chamber, protecting in such way the vacuum equipment.

6.1.1 Nozzle list

The table 6.1 shows the dimensions of the shock nozzles used in the investigation relevant for this thesis manuscript. The measurements were done with an optical microscope at CLPU. On the other hand, a conical nozzle of 500 µm output orifice diameter was also tested for comparison. All the nozzles are made of stainless steel.

	TUCAN	HT1	HT2	J2020	LOLA
d (µm)	220	219	223	212	200
D (µm)	467	564	513	393	500
L (µm)	210	1000	860	900	175
I (µm)	110	78	60	60	-

TABLE 6.1: Dimensions of the shock nozzles used in this work (except LOLA, which is a conical nozzle without a rim). d and D are respectively the smaller and larger orifice diameters, L is the length of the nozzle and I is the extent of the *rim*, as shown in figure 6.2.

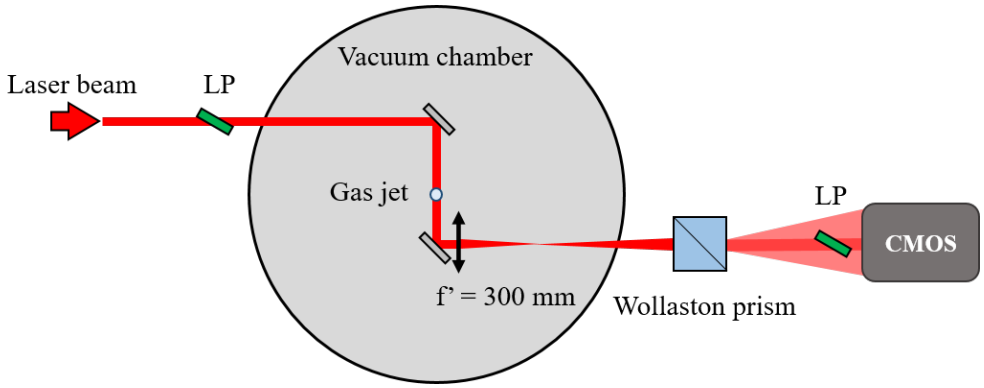

FIGURE 6.4: Basic sketch of the Nomarksy interferometer built for characterization of high-density gas jets. LP stands for the Brewster linear polarizer, which were set at 45° with respect to the Wollaston prism orientation axes.

6.2 Experiment at VEGA 2

As already introduced, the gas targetry system was first commissioned at the VEGA 2 laser facility in CLPU. This section first depicts the effort on target characterization carried out before the experiment. Later, the experimental configuration is reviewed, putting special emphasis on the diagnostics under the responsibility of the Ph.D. candidate.

6.2.1 Gas characterization by interferometry

In order to properly understand the target and to measure and test the gas jet in the real experimental environment, several gas characterization campaigns were carried out at CLPU within the IonGasJet project. Only the campaigns where C. Salgado had an active role are presented here. Depending on different aspects and the specific campaign purpose, several methods were used, mostly limited by the physical constraints of the laboratory at the time of the experiment. In any case, in order to perform a complete study of the target, the necessary parameters to scan were the nozzle model, type of gas used, compressor backing pressure, valve opening time and delay between valve trigger and measurement.

The first attempt for characterization of the target, prior to the experiment in VEGA 2, was simultaneous to the characterization of the underdense gas jet target BM5_2 shown in the Chapter 4, so the same setup was utilized. It consisted on a Nomarsky interferometer (already introduced in Chapter 3, see figure 4.20) composed by a 1° quartz Wollaston prism and thin film Brewster linear polarizers. The interferograms were imaged onto a Blackfly PGE-23S6M-C CMOS optical camera by a converging lens of focal length 300 mm, resulting in an imaging magnification of 2.2. The light source used for this experiment was the commercial He-Ne laser ($\lambda = 633$ nm) from Thorlasbs Inc. (HNLS008L-EC), with excellent

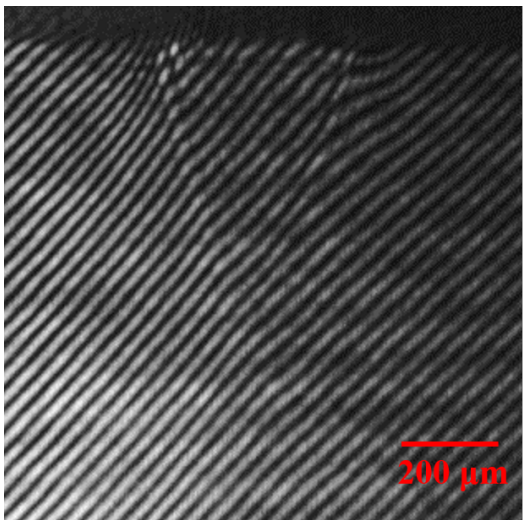

FIGURE 6.5: Typical Nomarsky interferometric picture of a fully developed shock jet (TUCAN, outer orifice diameter 400 µm), backed with 400 bars of nitrogen, measured 12 ms after the valve opening.

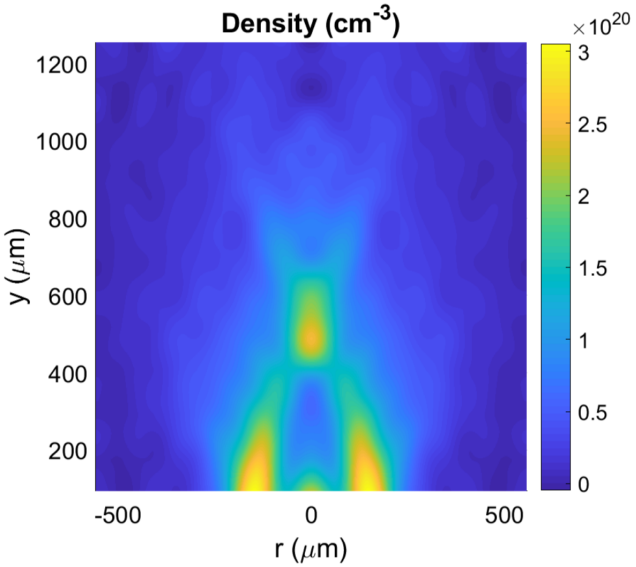

(A) Molecular density map retrieved from the interferogram in figure 6.5. $y = 0$ corresponds to the nozzle edge.

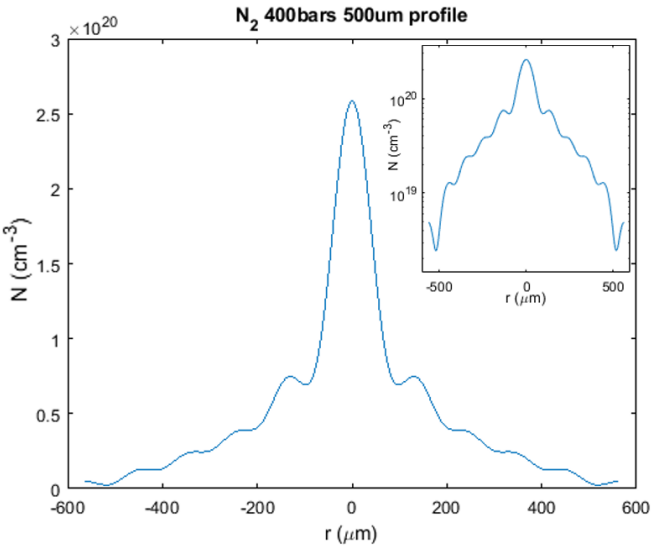

(B) Density lineout at shock height (500 μm) taken from 6.6a. Inset shows the same lineout in logarithmic scale.

FIGURE 6.6: Molecular density of the gas jet generated by the shock nozzle TUCAN backed with 400 bars of nitrogen, measured 12 ms after valve opening. The inset plot in logarithmic scale helps the reader to evaluate the extent of the gas far from the jet center.

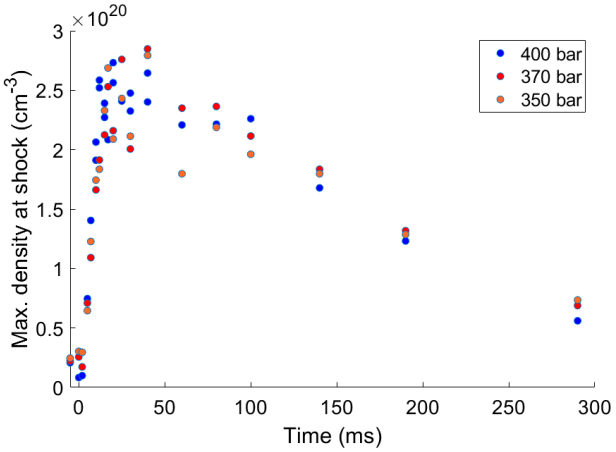

(A) Time evolution of the molecular density of the shock point density for TUCAN nozzle for different backing pressures of Nitrogen.

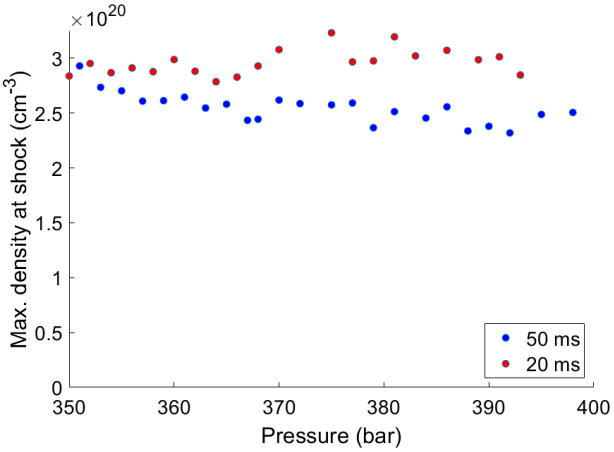

(B) Dependence with pressure of the shock point molecular density for TUCAN fed with Nitrogen, measured at different times after the valve opening.

FIGURE 6.7: Dependence with time and pressure of the density of the shock point for TUCAN nozzle fed with Nitrogen.

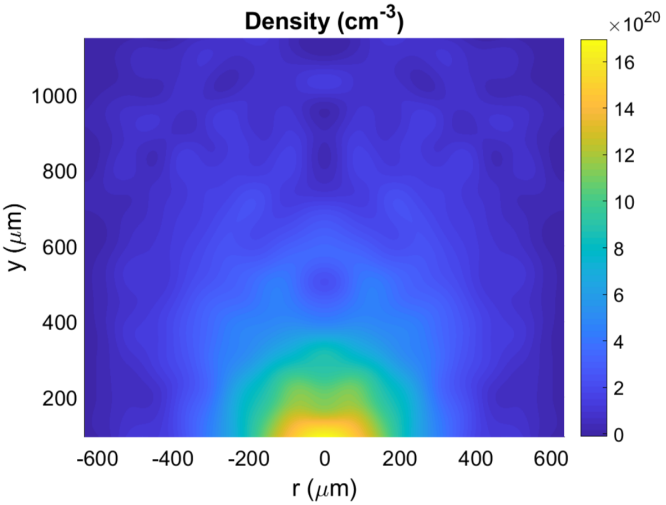

(A) Density map retrieved from interferometric technique of nozzle LOLA.

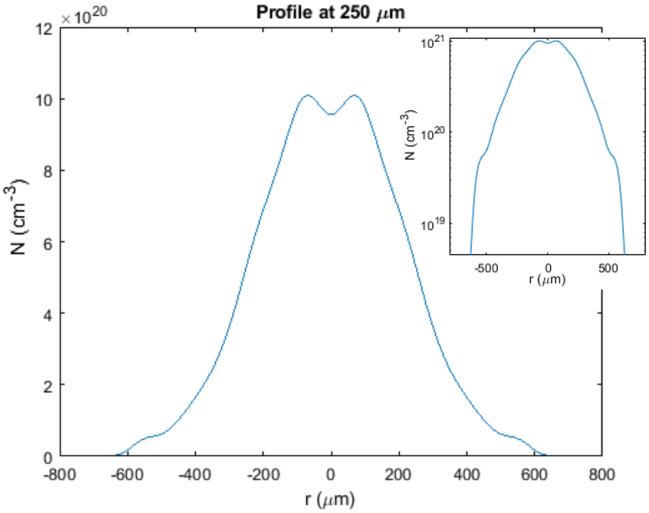

(B) Density lineout at 250 μm from nozzle end taken from 6.8a. Inset shows the same lineout in logarithmic scale.

FIGURE 6.8: Density of the gas jet generated by the cylindrical nozzle LOLA backed with 400 bars of Helium, measured 20 ms after valve opening. The inset plot in logarithmic scale helps the reader to evaluate the extent of the gas far from the jet center.

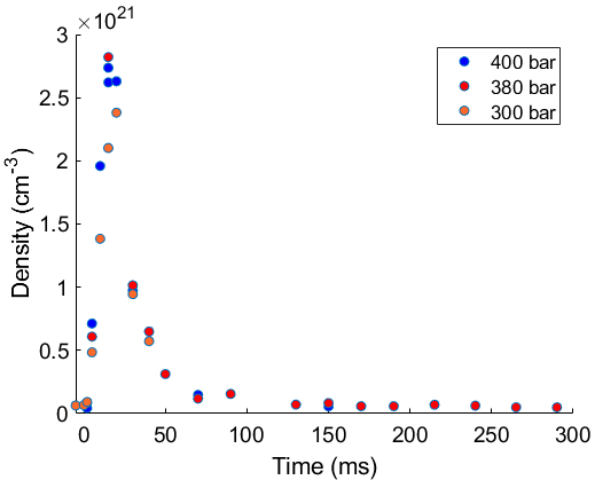

(A) Maximum molecular density (close to the nozzle) for LOLA conical nozzle with different backing pressures of Helium.

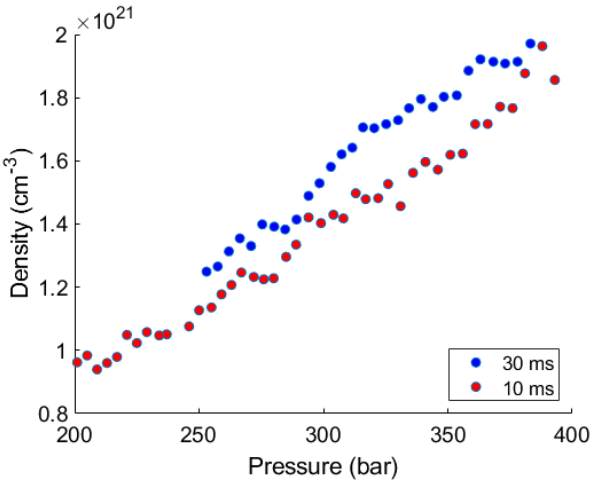

(B) Dependence with the pressure of the maximum density for LOLA conical nozzle fed with Helium, measured at two different delays after valve opening.

FIGURE 6.9: Dependence with time and pressure of the molecular density for LOLA conical nozzle fed with Helium.

spatial quality. Similarly as in the case of the conventional gas jets, the time resolution is given by the short acquisition time of the camera. A simplified sketch of the setup for this experiment is shown in figure 6.4. An example of the resulting interferometric fringes are shown in figure 6.5.

Imposing cylindrical symmetry, the same analysis process as in the cylindrical nozzles explained in Chapter 4 is followed. The Fourier-based method for the Abel inversion implementation (with a cut-off upper frequency of 13) is used. The typical density map of the shock nozzles is presented in figure 6.6a, showing the high density point at a distance 500 µm from the nozzle end. The radial profile at such distance can be observed in figure 6.6b. The quasi-parabolic profile shows a FWHM of $\approx$ 175 µm and a maximum molecular density around $2.5 \times 10^{20}\,\mathrm{cm}^{-3}$ (i.e. $n_e = 3.5 \times 10^{21}\mathrm{cm}^{-3} = 1.75\,n_c$ for full ionization).

In order to study the behaviour of the density with respect to the system parameters, a set of measurements were done under factory specifications (4.9 ms of aperture voltage and backing pressure up to 400 bars). Due to the aforementioned malfunction of the valve when a shock nozzle is attached, the results shown here for the nozzle TUCAN are only with Nitrogen gas. Figure 6.7a represents the evolution of the density of the shock point with time for different backing pressures, obtained by varying the delay time between gas and acquisition trigger signals. Despite being fed by a very short voltage ($<$ 5 ms), the valve keeps injecting gas into the vacuum chamber for a long period ($\approx$ 0.5 s). Three differentiated stages can be observed: from 0 to $\sim$ 10 ms jet formation, from $\sim$ 10 to $\sim$ 50 density plateau (gas jet is relatively stable) and finally from $\sim$ 50 to $\sim$ 500 ms, density ramp-down. Such long aperture time is of course detrimental for the vacuum equipment, as much more gas than needed is sent into the chambers. Density maxima are consistently found between 10 and 30 ms after opening. On the other hand, 6.7b shows the dependency of the dense shock for a small range of pressures. From this analysis is observed that the maximum density value does not vary considerably within the studied range of pressures. From the combined data after time and pressure scans, it seems that the jet presents slightly higher densities at the shock point at later times of the plateau.

For sake of comparison, the same analysis procedure was performed to the same gas system but using a conical nozzle (LOLA in table 6.1). Exchange between nozzles changed the gas flow dynamics in such a way that the valve malfunction (found with Helium and

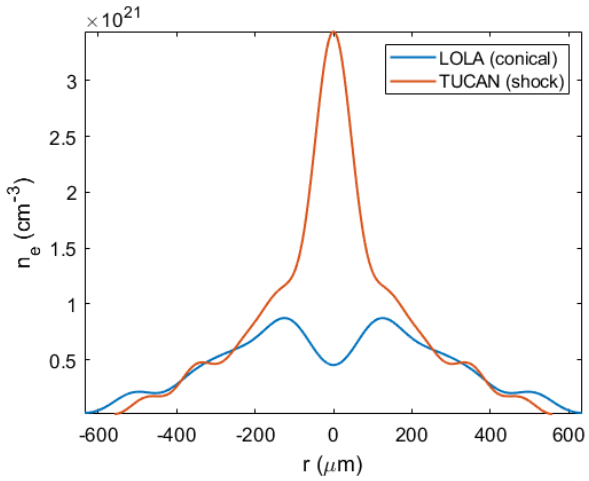

(A) Transversal lineouts of the expected electron density at shock height for TUCAN (shock, orange) and LOLA (conical, blue).

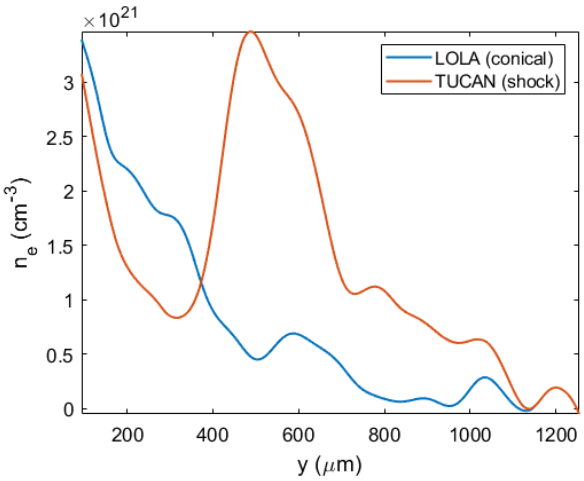

(B) Vertical lineouts of the expected electron density along the jet symmetry axis of the for TUCAN (shock, orange) and LOLA (conical, blue).

FIGURE 6.10: Lineouts of interest taken from 6.6a and 6.8a of the electron number density (imposing full ionization) of the studied jets. Measurements of nozzle TUCAN (shock, orange) were done with N_2 and nozzle LOLA with He.

shock nozzle) did not occur when using the conical nozzle. Therefore the measurements with the conical nozzle were done with high pressure Helium. The valve opening time was set to 4.9 ms as well following the provider specifications. Figure 6.8a show the typical density map for this nozzle, meanwhile 6.8b presents the radial density lineout at 250 μm from the nozzle end, considering this distance as potentially accessible for the the laser interaction. Nevertheless, this distance would not be enough for preventing from severe laser-induced damage on the nozzle if interacting with a multi-TW laser. Referring to the density measurement, a flat-top-like profile is measured close to the nozzle, whose shape spreads very quickly with increasing distance from the nozzle. The molecular density of the plateau measured is $N \approx 10^{21}\,\mathrm{cm}^{-3}$, which corresponds to $n_e \approx 2 \times 10^{21}\,\mathrm{cm}^{-3} \sim n_c$ at full ionization for Helium.

Similarly as in the case of TUCAN, the time evolution of the conical jet and its dependence with the pressure are shown respectively in figure 6.9a and 6.9b. The time behaviour is noticeable different than in the shock jet; the closure of the valve is much faster in this case and no evidence of gas is measured 100 ms after the valve opening. On the other hand, the linear dependence with the pressure is much more clear in this case, as demonstrated in Chapter 4, being the jet better formed 30 ms after opening rather than 10 ms.

The purpose design of the shock nozzles is well justified when comparing both conical and shock jets, as in figure 6.10. Figure 6.10a shows both electron density transversal lineouts (supposing full ionization of the neutral gas) at 500 μm from the nozzle edge, which coincides with the shock density point of TUCAN. On the other hand, figure 6.10b illustrates the longitudinal lineouts along the jet symmetry axis. With the shock geometry a high dense peak of $n_e \approx n_c$ (with *low* density lateral prolongations) is created at some distance from the nozzle. In a realistic high power laser experimental setup, this ensures a "clean" interaction of the high power laser with the higher density part of the target, trying to minimize as much as possible energy interchange before, minimizing as well undesired absorption before the shock point and avoiding potential plasma shaping by laser prepulses. Furthermore, the distance between the intense laser axis and the nozzle border (and the fact that there is a local density minimum between them) will help to minimize the

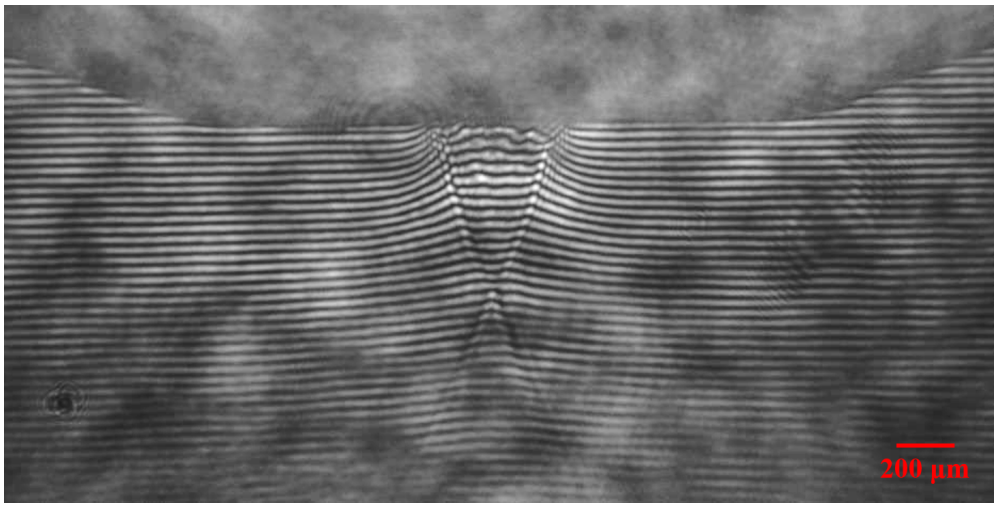

FIGURE 6.11: Ultrafast Nomarsky interferogram (with a femtosecond-class laser source) of a fully developed shock jet (TUCAN, outer orifice diameter 400 µm), backed with 400 bars of nitrogen.

laser-induce damage onto the nozzle structure.

The use of ultrashort laser sources to perform gas characterization was also demonstrated by means of the same Nomarsky interferometer after its adaptation to a new wavelength. The second harmonic ($\lambda = 400$ nm) of the Ti:Sa CEP-stabilized laser at CLPU (Femtopower Pro CEP, $\sim$ 2 mJ, 25 fs, 1 kHz), was successfully used as backlighting for the Normasrky interferometer of figure 6.4, obtaining interferograms as the one shown in figure 6.11. This test was the first experimental demonstration of an ultrashort interferometry diagnostic (based on a Wollaston prism) at CLPU, and it worked as a training for the plasma interferometry planned for the experiments at VEGA with such target. The analysis of a few exemplary cases yielded similar results as the ones measured with the CW laser source.

6.2.2 VEGA 2 experiment description

A competitive access experiment at VEGA 2 laser facility was carried out by the research group. The experimental interaction of ultrashort ultraintense laser pulses with the high-density gas jet was studied at CLPU [75]. The major aim of this experiment was the preliminary study of the nature of the interaction of a near-critical plasma generated by the high-density gas jet system with high-power fs-long laser pulses. This included the commissioning of the target system in a realistic high-power laser environment and the deploy of a remarkable amount of diagnostics for the target, plasma and particle yield. Enhanced absorption of the laser energy was expected (when compared with underdense and overdense plasmas), meanwhile some evidence of a potential collisionless shock formation was searched (as the case of monoenergetic ion acceleration).

Laser configuration

VEGA 2 pulses with 3 ± 0.36 J energy, 30 fs long, were focused by a $f^{\#} = 4$ OAP gold-coated mirror into the high-density gas target, as seen in the drawing of figure 6.12. A more realistic setup sketch is presented in figure 6.13. The focal spot was measured daily at low energy by a high magnification imaging system. A constant FWHM of 7 µm was achieved yielding a peak intensity around 10^{20} W/cm^2. This spot was aligned everyday into a precise point in space (TCC) which the help of the spatial reference given by a motorized small needle

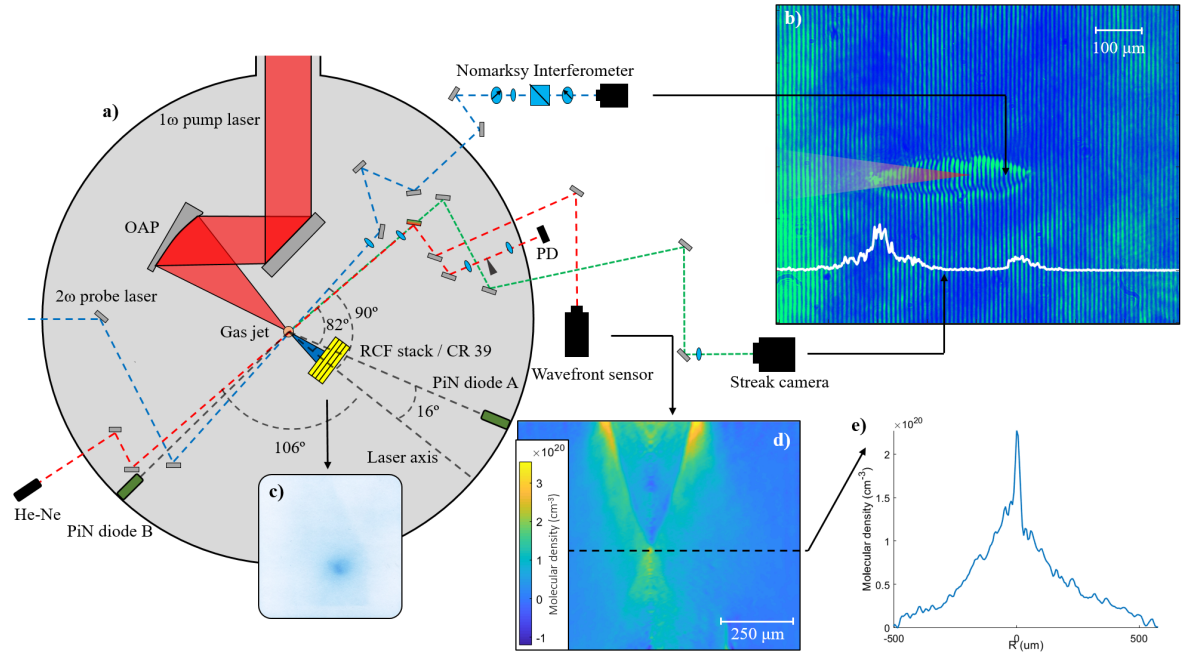

FIGURE 6.12: (a) Zenithal view of the experimental setup. (b) Raw data of the ultrafast interferometry. A lineout of the plasma prompt emission measured by the streak camera (white curve) and a sketch to scale of the laser envelope in vacuum (transparent red triangle) are overlaid. (c) Typical RCF signal. (d) Molecular density map of the gas jet prior to interaction as measured by the wavefront sensor (the nozzle edge is located 300 µm above the image). (e) Molecular density lineout at the shock height.

(∼ 10 µm of tip diameter). The pulse duration was verified shot by shot with the help of an auto-correlator, yielding 28 ± 1 fs. The temporal laser contrast was measured once by means of an third-order auto-correlator (Sequoia from Amplitude Laser, Inc.) shortly before the experiment, yielding the results shown in Chapter 3.

Plasma diagnostics

A series of diagnostics were employed to carry out a detailed investigation of the laser-driven plasma. An imaging system which looked at the target at 82° (in the experiment equatorial plane) with respect to the laser axis was used to collect the prompt plasma prompt emission optical photons. The plasma image was (one-dimensionally) measured by a fast streak camera (Hamamatsu C7700) with picosecond resolution. The basic operation of streak cameras is shown in Appendix A. The combination of the imaging system built for this diagnostic and the built-in optics of camera yielded a spatial calibration of ∼ 1 µm/pixel and a spatial resolution diffraction limit of ≈ 11 µm. The NIR photons elastically scattered from the driver laser were partially attenuated by means of a BG38 colour filter. The streak sweep range selected for plasma measurements was 2 ns, much longer than the required time for the laser to cross the field of view of the camera (∼ 3 ps). Therefore the prompt emission from the laser-plasma interaction (mainly originated from elastic and inelastic photon scattering and other non-linear effects in the plasma) appears *frozen* (i.e. in the same time coordinate) in the streak camera images. An example of the optical emission measurement is shown in figure 6.14 (c).

The other specific plasma diagnostic prepared was an ultrafast plasma Nomarksy interferometer. Its operation was already detailed in Chapter 3. A pick of VEGA 2 was taken by

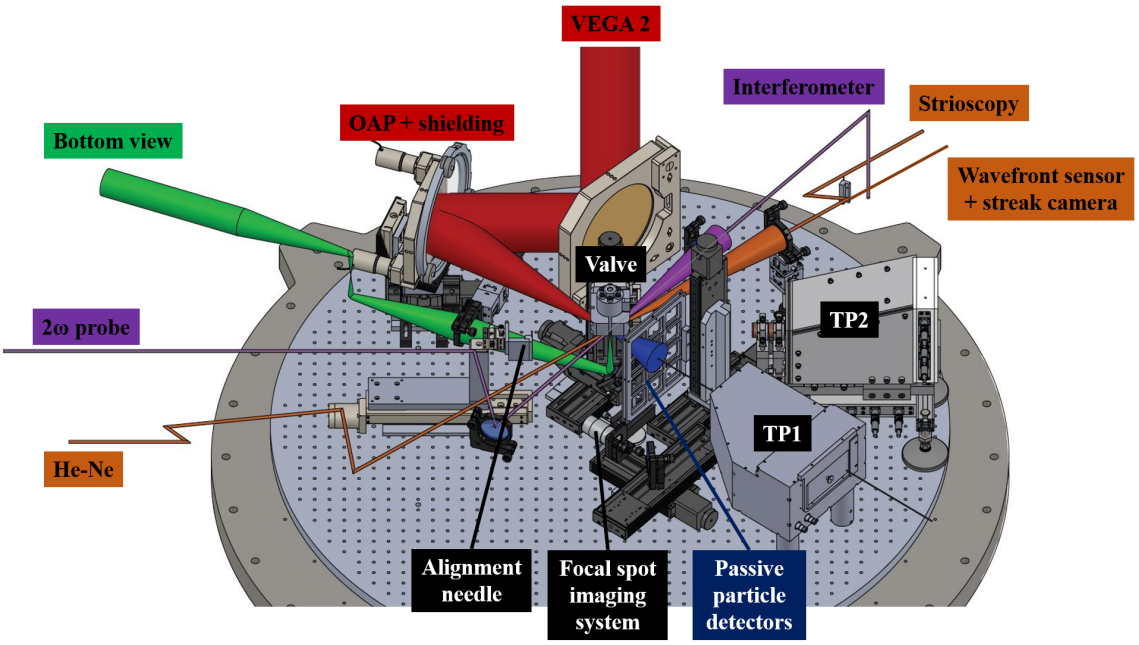

FIGURE 6.13: SolidWorks drawing of the experimental setup of IonGasJet-VEGA 2 experiment.

insertion of a 25 mm dielectric mirror similarly as shown in figure 4.19b. A centimetre-scale delay line controlled the delay between pump and probe in a range of $\sim$ 200 ps. Frequency-doubling is achieved downstream with the help of a Type I BBO crystal; the probe beam crosses TCC and overlaps the laser-driven plasma orthogonally to the laser axis direction (this means that the angle between streak imaging and interferometry lines is 8°). The synchronization between pump and probe at TCC was studied by measuring the scattered light of both beams with the fast streak camera. The physical constrains of the beam transport limited the accessible probe delay (with respect to the main) between 1 and 1,1 ns, much later after the interaction occurs. The imaging system of the interferometer magnifies the plasma image yielding a spatial calibration of 5 µm/pixel and spatial resolution diffraction limit of $\approx$ 7 µm. Figure 6.12 (b) shows a lineout of the emission in the plasma measured with the streak camera overlaid to a typical raw interferometric picture (with the spatial coordinates corrected, taking into account the projection into the interferometry line of sight).

Imposing cylindrical symmetry, the methodology for plasma interferometers shown in Chapter 3 can be followed. Figure 6.14 illustrates the combined results of these plasma diagnostics, analysis carried out by the candidate. Since the plasma was probed 1 ns after the interaction, the plasma was able to expand and homogenize, yielding the average density measured $\approx 0.1 n_c$. Furthermore, both the systematic evidence of noticeable plasma density and measurement of prompt optical emission after the shock point ($x > 0$) for most of shots are evidence of an important deposition of the energy downstream, either directly or through secondary ionization process.

The Abel inversion code used in this case is based on the 3-point method [200]. For sake of comparison, this same interferogram was analysed with the Fourier-based method [198] (the same used for the neutral gas in Chapter 4). Figure 6.15 shows such different analysis results of both methods; in the case of the Fourier-based method, different frequency cutoffs are applied. Clear structure difference are seen between the different analysis techniques. The higher the upper frequency limit, the finer the details and more complex radial structure is appreciated. The case of the 3-point method shows additionally sharp edges on the plasma borders. Nevertheless, in all cases the density in the bulk of the plasma is similar,

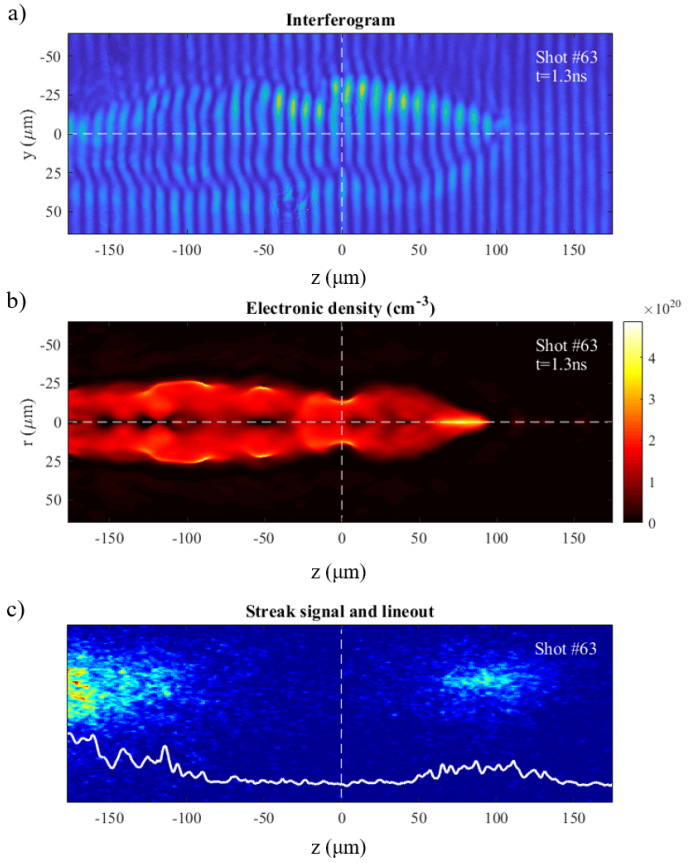

FIGURE 6.14: Optical plasma diagnostics show strong emission from dense regions of the plasma. For the same VEGA 2 laser shot #63 onto the high density pure helium jet (a) the raw interferogram of the plasma probe 1 ns after the interaction starts, (b) the retrieved electron density of the plasma and (c) the raw streak camera measurement of the prompt plasma emission, including a line-out in white representing the time integrated measurement (in arb. units). The laser travels from left to right in the pictures and in this shot its focus in vacuum coincides with $x = y = z = 0$, the same coordinates of the jet shock point. Vertical dashed line represent the jet symmetry axis and horizontal dashed lines illustrate the laser focalization axis.

ranging from $n_e = 1 \times 10^{20}\text{cm}^{-3}$ to $n_e = 2 \times 10^{20}\text{cm}^{-3}$. Further optimization of the analysis process is beyond the scope of this thesis.

Particle diagnostics

On-line energy spectra of the accelerated particles were acquired by two Silicon PiN diodes, working in time-of-flight (ToF) operation mode, located vertically inclined at an angle 19° above the horiziontal plane at 67 cm from the interaction point. Each diode was place at a different horizontal angle: PiN A at 16° and PiN B at 106° with respect to the driver laser propagation axis. In such way both transversal and longitudinal acceleration of particles can be studied. PiN A was shielded for low energy photons and particles with a single layer of aluminized (40 nm) Maylar foil (2 μm thick), meanwhile PiN B was covered by two layers. Signal acquisition with a 1 GHz oscilloscope (Tektronix DPO4104) was performed at maximum sampling rate of 200 ps per sample. 20 dB attenuation was applied to both

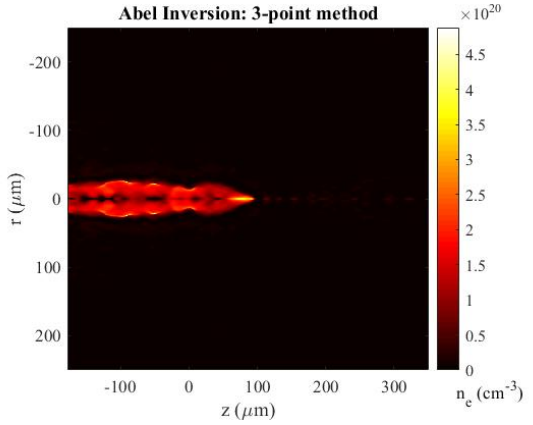

(A) 3-point method.

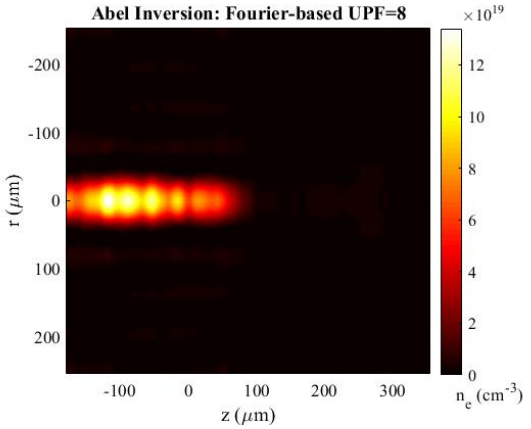

(B) Fourier method with low-pass filter of 8.

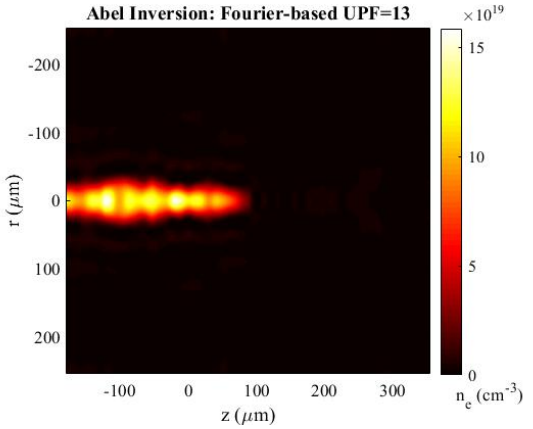

(C) Fourier method with low-pass filter of 13.

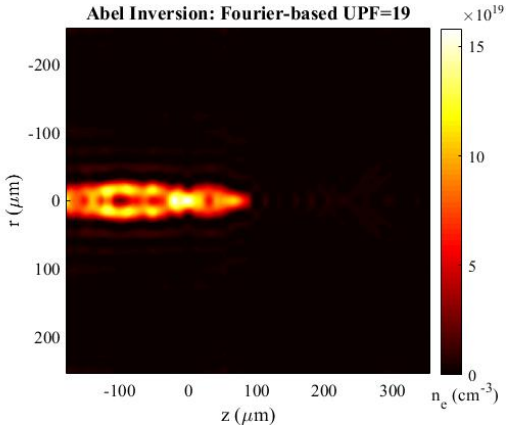

(D) Fourier method with low-pass filter of 19.

FIGURE 6.15: Comparison of the near-critical plasma electron density obtained from different analysis methodologies of interferogram shown in figure 6.14 (a).

channels. The ToF technique requires from an accurate measurement of the time difference of arrival to the detector between the interaction-induced X-ray photo-peak (considered as a clear evidence of the interaction) and the arrival of the particles under study. If overlapping occurs between the fall time of the photo-peak signal and the particle signal, dedicated measurement of the photo-peak only should be accomplished in order to deconvolute the signal. Unfortunately, the photo-peaks measured in the experiment, considered as the PiN signal measured after poor interaction conditions, showed very slow exponential decays ($\tau \approx 20$ ns) when compared to the fast PiN diode response function ($\tau \approx 3$ ns). Then, it is not certain that the photo-peaks were particle-free, which jeopardizes the ToF data. An example of the extended photopeak raw data and the raw signal of a regular laser shot into the target is shown in figure 6.16. In addition, these *extended* photo-peaks overlapped with the signal from Helium ions of energy higher than 9 MeV. Note that the ToF analysis procedure has been successfully used to analyze PiN diode data in other experiment, where the obtained proton spectra were validated with deconvolved spectra from RCF analysis [60].

Solid state passive particle detectors were also deployed to capture the spatial and spectral properties of the forward accelerated beams in single shots, with stacks of RCF or pieces of CR-39, shielded by 10 μm Al filters. These detectors were set at 60 mm from the interaction point facing perpendicular to the laser axis and wrapped in 2 μm thick Maylar foils

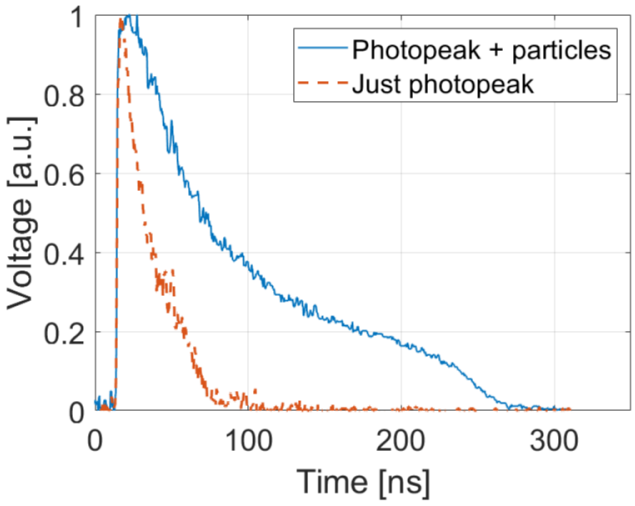

FIGURE 6.16: Comparison between the detector raw signal comprising the *extended* photopeak and all accelerated particle species (blue full line) and a signal with the *extended* photopeak only (orange dashed line). Data taken from [75].

with 40 nm Al coating.

Additionally, as depicted in figure 6.13, two Thomson Parabola spectrometers were aligned at 0° and 30° from the laser axis (in the horizontal plane). In an attempt for high-repetition rate diagnostic operation, Lanex scintillating screens (coupled with scientific cameras) were used as active detectors for the TP traces. The poor sensitivity of Lanex for ions (and the small solid angle acceptance of the TPs $\approx 10^{-6}$ sr) were probably the reason why ions were not detected with devices.

Details of the analysis of these detectors can be found the ArXiV preprint [75] and in the Ph.D. manuscripts M. Ehret [248] and V. Ospina [249].

On-line gas measurement and laser-induced damage

A specific diagnostic was prepared by the candidate for target assessment between shots. The wavefront sensor SID4 from Phasics company, which was depicted in Chapter 3, was utilized for evaluation of the target density between shots. In this case, a high quality CW He-Ne laser (model 30991 from REO Precision Optical Solutions) was the laser source backlighting the target for phase-shift purposes. Although the gas target operation was characterized before the experimental period -although not for all the shock nozzles- this shot-to-shot diagnostic was necessary to determine the gas jet shape as well as for the position of the shock point. This was also required to monitor possible worsening of the jet quality due to laser-induced damage on the nozzle. Furthermore, in this way a measurement of the density lineout as close as possible to the real experimental conditions is achieved.

The necessity of this diagnostic is justified following figure 6.17. It shows the density map (and density lineouts at both the shock height and laser-shot height) of three Phasics measurements done before three consecutive laser shots. The shots shown were part of the preparatory phase of the experiment as the nozzle used (HT2) forms the shock very close to the nozzle edge ($\sim$ 300 µm), which would lead to fast degradation of the nozzle when the laser-plasma interaction occurs. After each shot the quality of the shock point noticeably changes. The width of the shock point increases in consecutive shots, the maximum density value decreases and the shock point *moves* further away from the nozzle edge.

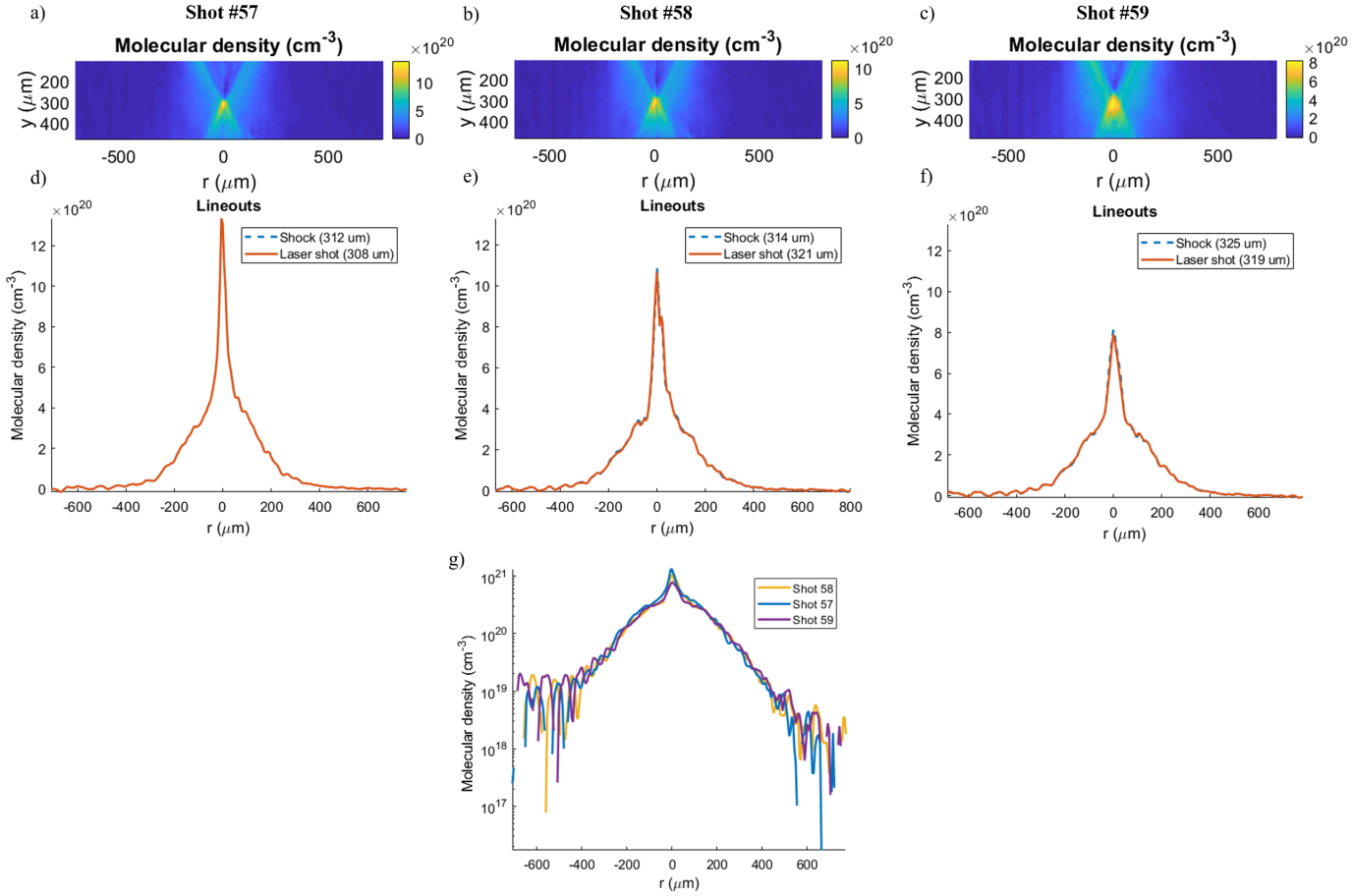

FIGURE 6.17: Gas density maps of the HT2 jet (backed with 400 bars of Nitrogen) before (a) shot 57, (b) shot 58 and (c) shot 59 measured by the Phasics in-line interferometer. (d-f) show the corresponding density lineouts at shock height (dashed blue) and laser shot axis (solid orange). (g) shows the the density lineouts of (d-f) at the laser axis in logarithmic scale for an easier visualization of the gas density far from the jet shock point, not varying considerably in consecutive shots.

When severe damage occurs (normally after $\sim$ 10 shots), the jet losses its symmetry (therefore the Abel inversion becomes useless) and the shock point moves both vertically and horizontally and finally vanishes (as it can be observed in figure 6.18). Optical inspection of the nozzle laser-induce damage is shown in figure 6.19.

The protocol defined for the shot-to-shot operation was:

- Prior to the experiment, the TCC is defined with the help of an alignment needle (small tip of $\sim$ 10μm of diameter), which can be measured and set as reference for the imaging systems.
- VEGA 2 focal spot is optimized and brought to TCC by means of beam transport mirrors and OAP tilts.
- With the help of the XYZ motorization stages holding the valve, this is moved until an approximate position close to TCC, where the jet image fits inside the field of view of the Phasics sensor. The longitudinal and transversal position can be set close to the final position with the help of a bottom view imaging system (see figure 6.13), which faces the nozzle's surface and helps to asses for the laser damage on them.

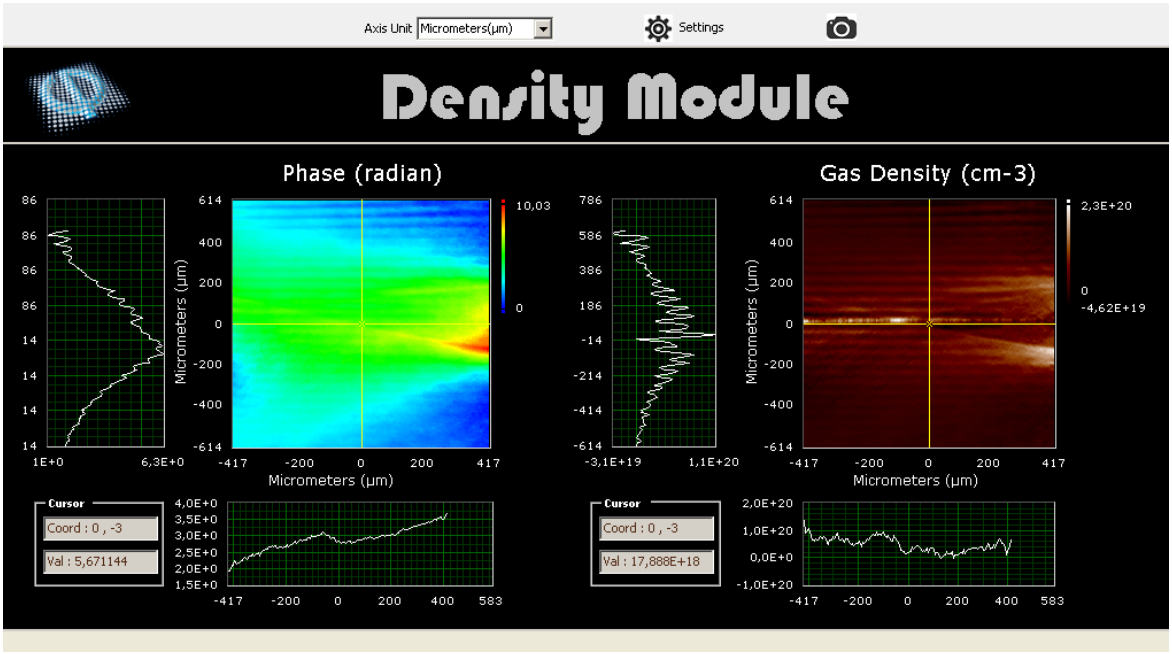

FIGURE 6.18: Snapshot (taken online during the experiment) of the gas density analysis module from Phasics, which analyses the retrieved phase maps. Left picture shows a phase map measured from the severely damaged TUCAN jet, with 400 bars of backing pressure of 9:1 N_2/He mix. Right side shows the automatic analysis performed by the software, supposing pure Nitrogen gas.

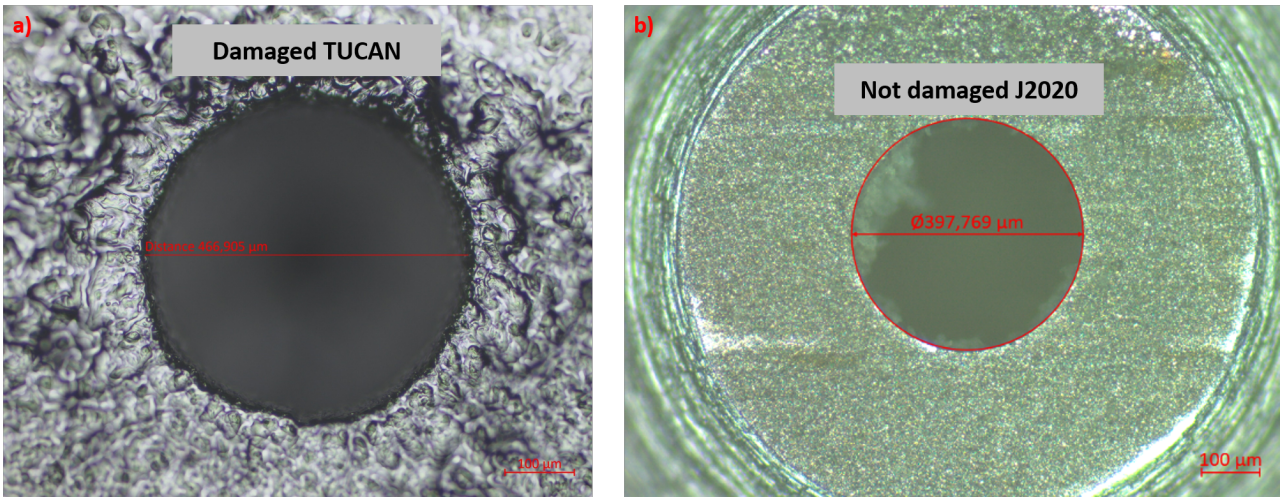

FIGURE 6.19: Optical microscope images of the outer orifice of a) TUCAN nozzle after irradiation at VEGA 2 experiment and b) damage-free J2020 nozzle.

- The wavefront sensor records a phase diagram of a single gas jet and reveals the shape of the shock point and its relative positions with respect to the nozzle edge.
- The valve is moved so the shock point is set at TCC position. Any further relative valve movement desired is done from this reference position.
- Acquisition of a reference shot for the ultrafast interferometry (leaving only the probe going through and blocking the driver laser).
- Ultra-intense laser shot is performed and interaction occurs, including gas, driver laser and probe.
- The laser damage effect is evaluated (via bottom view system and with another gas acquisition) and the active diagnostics data are reviewed.

This process was repeated for each shot.

In addition, two corrections on the gas analysis were carried out after the experiment (which could not be done on-line because of time constrains). Both corrections are applied for the gas data shown in figure 6.17 and similar.

- **Fringe removal**: Undesirable vertical interference fringes appear at the He-Ne beam as a consequence of the multiple reflections on the beam-splitters set on the different diagnostics line. These can be observed as horizontal modulations (in phase and intensity) at figure 6.18 as the plots of the Phasics software are rotated 90° clock-wise with respect to the sensor geometry. Such fringes arrive as periodical intensity and phase perturbations at the detectors and are wrongly interpreted as density variations by the phase reconstruction algorithm. Such fringes could be cleaned while post-processing the data by Fourier methods. A FFT of the original data set is made and a zeros mask is applied to the artifact spatial frequency. Then the inverse FFT is made and the resulting phase map is inserted back into the SID4 density software for subsequent analysis.
- **Gas mixture**: when the dopant concentration in a gas mixture is low, most of the analysis assumed the density value measured with the larger concentration gas type as being equal to the mix [130]. In the case of the IonGasJet project, the valve operation required operation with dopant (Helium) concentrations over 10%. In this case a more accurate approximation is needed. The characterization was directly performed with the jet backed with the proper gas mixture, and considering in the analysis an effective polarizability of the form

$$\alpha_{\text{eff}} = \sum_i \left(\frac{N_i \alpha_i}{\sum_i N_i} \right), \tag{6.1}$$

where subscript i stands for each gas component [78]. In the case of the jets analysed by the Phasics software, the proper correction factor could be applied only afterwards.

The proper timing between gas jet opening, diagnostics and the laser shot is achieved thanks to an Schlieren imaging system measured by a fast photo-diode (see Chapter 3). As shown in figures 6.12 and 6.13, the strioscopy system shares the view angle and first optical components with the streak camera system and wavefront sensor. Simultaneous optical diagnostics in the same line are achieved thanks to beam-splitters. During the gas characterization before each high-power laser shot, the strioscopy signal was compared to the TTL signal triggering the Phasics sensor. In this way, the qualitative evolution of the jet could be related to a quantitative single snapshot of the gas density. The timing between the gas valve opening voltage and Phasics trigger signal was subsequently applied to the delay

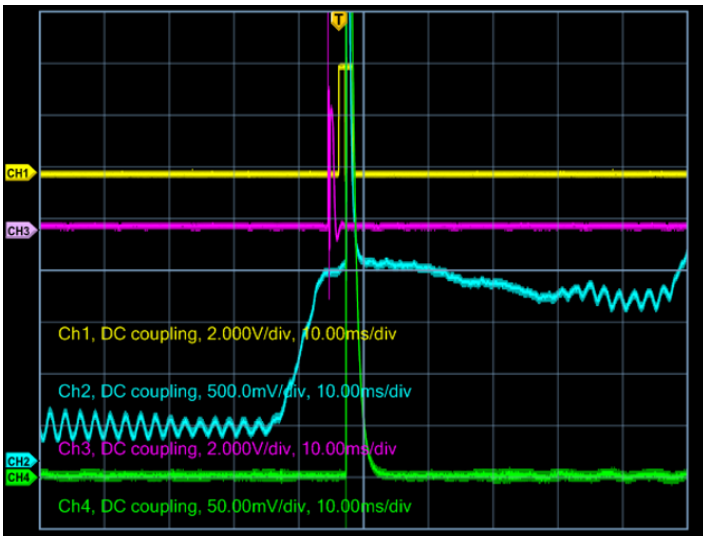

FIGURE 6.20: Oscilloscope signal presenting the typical VEGA 2 high-density gas jet experiment timing. Yellow: TTL trigger signal for wavefront sensor. Purple: General diagnostic trigger signal (for CMOS cameras, streak cameras and other active detectors). Green: signal of photodiode viewing leakage of the VEGA 2 beam through a beam transport mirror (before TCC). Blue: Gas jet strioscopy signal measured with photodiode (scattering from the driver laser is also seen).

between VEGA and gas valve voltage, replicating the same gas target conditions in the high-power laser shots. Furthermore, verification of the laser-target timing was possible after the shots by means of the Schlieren system photo-diode, which could acquire both inputs simultaneously. An example of the timing oscilloscope signal for the typical VEGA shot in this experiment is shown at figure 6.20.

The performance of the valve in the ultra-intense laser experimental environment was not satisfactory. The same closing malfunction happening when working with pure Helium was found systematically at every laser shot performed close enough to the valve ($\sim$ 500 µm), independently of the species composing the gas, probably caused by EMP-related (or neutralization current) effects [250]. Actually, the malfunction could be easily observed in the strioscopy signal if the time division is set accordingly. This behaviour of the valve meant the systematic filled the chamber with gas, overloading the vacuum equipment (vacuum gauges and pumps) and slowed down enormously the potential repetition rate of the experiment.

Experimental results

Two studies focused on ion acceleration dependence on the target properties but without variation of driver laser parameters, despite day-to-day changes. In the fist data set, different gas jet density profiles were employed with the driver laser aiming at the shock point. For the second set of data the interaction region changes from the density maximum into the wings of the jet.

First study: a variation in the gas density profile is obtained by changing the gate opening times of the gas valve and progressive laser damage on the same nozzle (HT2) in successive laser shots (#62, #63 and #64) with pure Helium. The different gas jet density profiles are shown in figure 6.21. One observes a rising feature right before the density peak on its left hand side. Its location and the location of the self emission peak roughly coincide

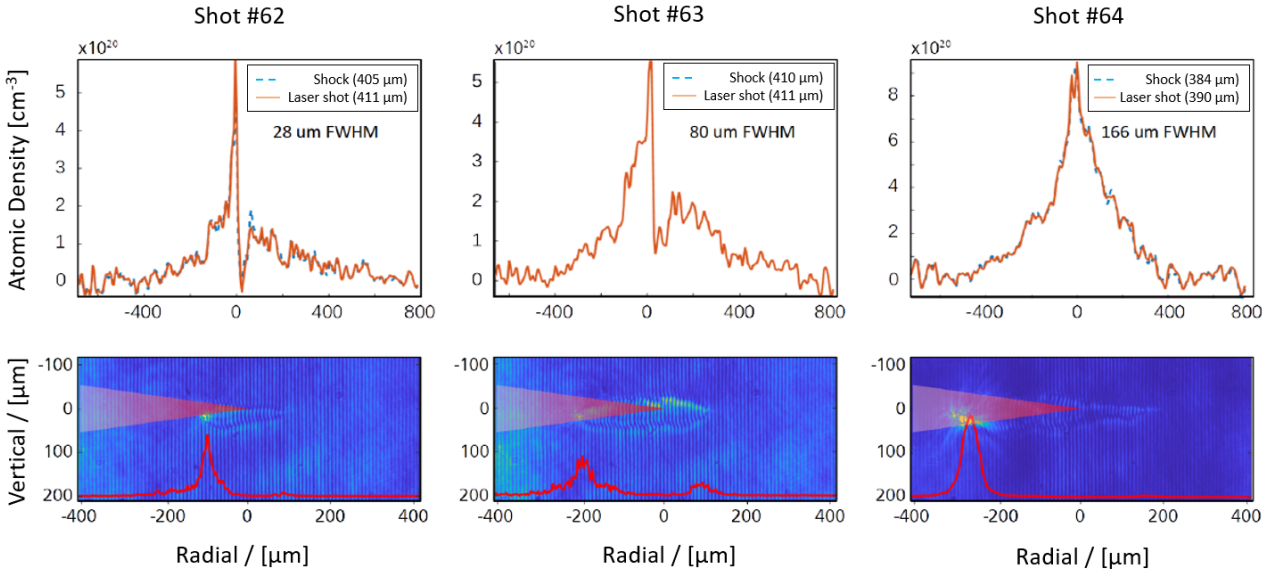

FIGURE 6.21: For three consecutive shots varying the pure Helium gas jet density profile: (top row) longitudinal un-driven gas jet density profile with indication of the respective distance to the nozzle for the shock and the shot position, (bottom row) ultrafast interferometric image (captured 1 ns after the interaction starts) superposed to aligned scaled laser beam and plasma streaked emission in arbitrary units as red line. The laser travels from left to right and is focused to x = 0; y = 0, the coordinates of the jet maximum density point.

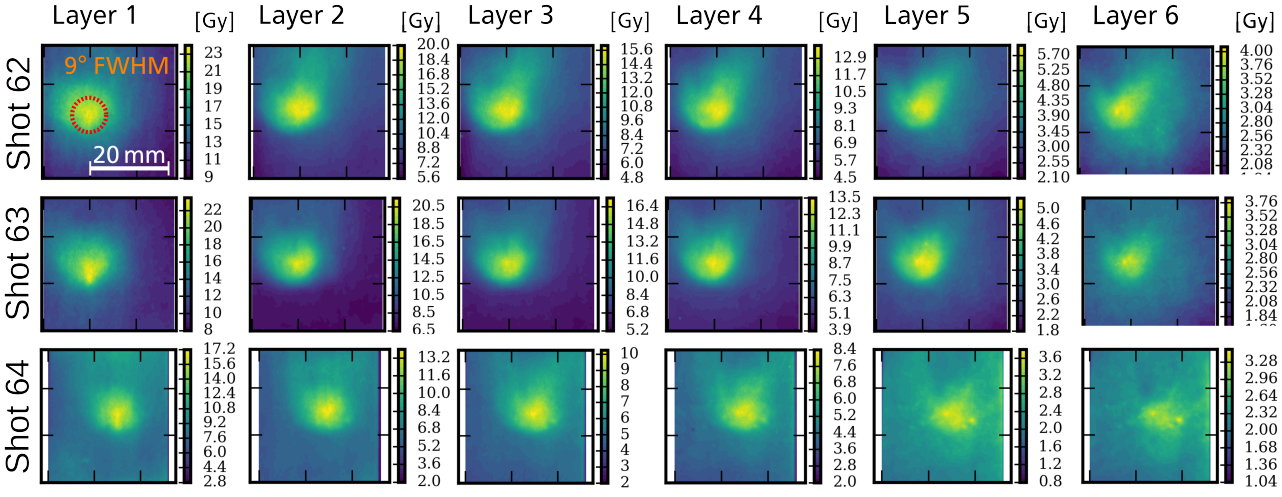

FIGURE 6.22: RCF imprints are converted to dose for three consecutive shots varying the gas jet density profile. The typical FWHM divergence angle of the beam imprint is 9°, all images have the same spatial scale. The driver laser and detected particles propagate towards the reader. For shots #62 and #63, the presumed pre-aligned laser axis corresponds to the centre of the illustrated frames. For shot #64 this does not apply due to a alignment error. Layers are numbered in ascending order in direction of particle propagation. Image taken from [75].

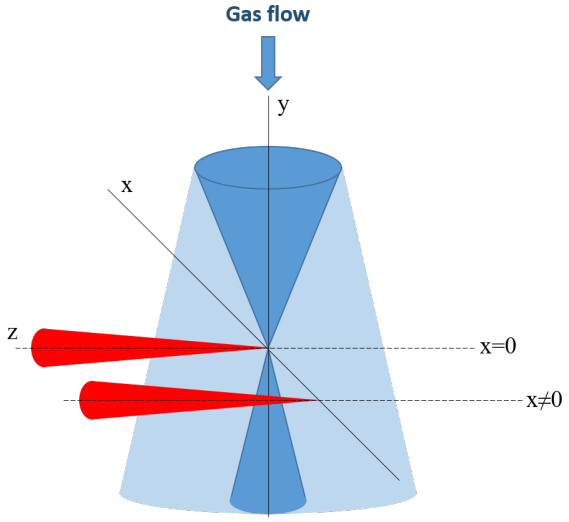

FIGURE 6.23: Sketch of the irradiation geometry at VEGA 2 experiment in high-density gas jet while performing transversal scans.

for shot #62 (which in fact can be also observed as scattered light in the interferometry image). Overall, for this series of shots, the laser has to traverse a rising areal density of gas before reaching the peak. Beyond the peak, a second self emission zone appears in vicinity of the end of the plasma channel only for shot #63. Comparing figure 6.21 (top row) and 6.21 (bottom row) the first self emission peak corresponds to a initial atomic density of $1.2 \times 10^{20}\text{cm}^{-3}$ to $1.6 \times 10^{20}\text{cm}^{-3}$ in all three cases. The appearance of intense plasma prompt emission before the shock point was periodically measured, and occasionally in the density decreasing part.

Dose converted RCF data for the three shots is shown in figure 6.22. A beam-like feature is imprinted over the full RCF stack, with similar divergence and amplitude for all shots. The average FWHM divergence of the beam is 9°. The RCF stack is not thick enough to confidently determine the particle beam trajectory. The deposited dose decreases noticeably throughout the stack. The depth of the last active layer in the stack corresponds to the electron range of $\approx$ 410 keV projectiles and the α-particle range of $\approx$ 42 MeV projectiles. Both species might contribute partially to the dose deposition. Without a diagnostic able to discriminate charge to mass ratio or the sign of the charge, ions are evidenced by a comparison to ToF data.

ToF spectra were measured in these shots with both transversal and forward PiN diodes. The spectra are not plotted due to the compromised analysis. If the signal found after decay of the photo-peak was due to electrons, their kinetic energy for such recorded arrival times would be $\approx$ 10 keV and below. Note that the applied shielding in front of the diodes cuts off electrons below 10 keV. Thus, a proper operation of the ToF signal could have indicated the presence of Helium ions at MeV range.

Second study: the influence of the transversal laser focus position (with respect to the gas jet shock position) was studied by translation of the valve as represented in figure 6.23, in this case fed with mix of Helium and Nitrogen in 1:9 ratio. Also, progressive laser damage on the nozzle surface (in this case TUCAN) degrades the shot-to-shot jet quality. Figure 6.24 shows the gas density measured before the shots as well as the corresponding interferometric picture. Note the difference shape of the density profiles with respect to the previous study, mainly caused by the use of a different nozzle (presenting already severe laser-induced damage) and the use of a other gas composition. The effect of the laser damage on the jet can be observed between the density plots of shots

#77 and #79. The lineouts from #80 to #83 show the extrapolation of the density to the laser-gas intersection axis at $x \neq 0$. Such density profile is available as the entire gas radial shape is known. In shots with clear first prompt emission peak, the emission zone has an un-driven molecular density of $\sim 2 \times 10^{19}\,\mathrm{cm}^{-3}$. There, an electron density of $n_e = N(\eta_{N_2} Z^*_{N_2} + \eta_{He} Z^*_{He}) = 2 \times 10^{19}\mathrm{cm}^{-3}(0.9 \times 14 + 0.1 \times 2) \sim 2.5 \times 10^{20}\mathrm{cm}^{-3}$, where η_i is the concentration of the i gas specie. This value is comparable to the values found in the first study for the emission regions. This first prompt emission peak moves towards the focus plane for larger transverse displacements, likely to the increase of the density value in the lobes of the density profile. Even though the density peak is not reached when performing the transversal scan, the bulk gas shows only small shot-to-shot differences. The overall electron density, imposing full ionization, ranges from $0.1 n_c$ to $2 n_c$. The fast interferograms in figure 6.24 shows particularly long ionization regions for this set of shots. However, it is not straightforward to interpret this interferometric data with respect to the laser-plasma process as the probing at early times of the interaction was not possible.

RCF dose measurements were acquired for shots #79, #85 and #87, with lateral displacements of 0, -50 µm and $+50$ µm respectively. The scans of the different radiochromic layers is presented in figure 6.25. Three features are repetitive and clearly pronounced on RCF in all shots.

- Most prominently, a small spot like peak with 3° FWHM half-opening angle is located 5 mm right of the expected laser axis and about 1 mm underneath. The beam is elliptical and the major axis of the ellipse is perpendicular to the laser polarization direction. The feature faints steeply from first to second layer and is barely visible in the third layer. The fourth layer does not allow to distinguish the feature. A longer plasma channel and a higher first prompt emission peak coincide with lower doses in the peak feature.

- Secondly, a wide Gaussian peak with FWHM half-opening angle of 11° is visible throughout the RCF stack, with its centre position superposing the laser axis. The Gaussian feature has a similar divergence as observed in the first study (9°), but is at much less dose. Also, a dip in its centre can be found in proximity of the laser axis for the last two layers, highlighted on the last layer of shot #87 with a white arrow.

- Third, four lobes appear on the last layers, highlighted with a cyan circle, two maxima and two minima. Both maxima are horizontally aligned next to each other, the minima are aligned vertically above them. This horizontal separation is coinciding with the laser polarization.

Finally, CR39 was exposed during shots #78, #84 and #86 with respective lateral displacements 0 µm, -50 µm and $+50$ µm (similar conditions as the shots with exposed RCFs). CR39 are post-processed by an chemical etching process which reveals pits as an indication for presence of ions. Projectiles with a low longitudinal energy transfer as electrons do not lead to the formation of track in these detectors. The analysed tracks (in the laser forward direction) would correspond to α-particles from 4 MeV to 40 MeV or Nitrogen ions with energies from 1 MeV to 2 MeV. Nevertheless, the track density map in the vicinity of the laser axis shows an uniform etch pit distribution over all pit sizes. The very low density of tracks found ($16800\,\mathrm{cm}^{-3}$) would correspond to mGy for α-particles. This indicates that all repetitive features on RCF do not correspond to ions, but more probably to electrons. An example of the raw data of the CR39 can be found in figure 6.26.

As result of the second study one notes a clear change of the dominating acceleration mechanism in the bulk of gas density profiles without pronounced density peak, which leads to reproducible characteristic features visible on RCF.

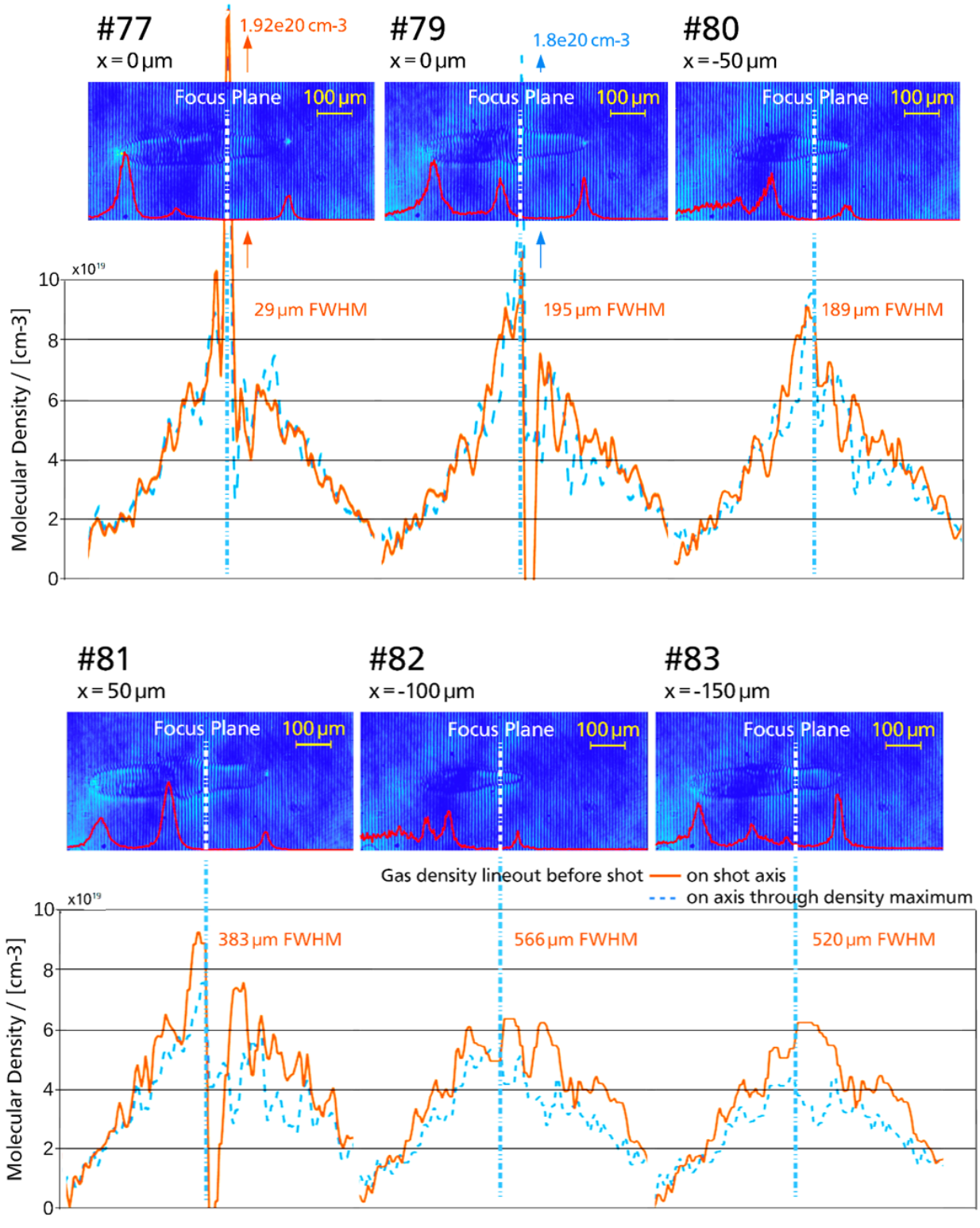

FIGURE 6.24: Upper rows: ultrafast interferometric images (captured 1 ns after the interaction starts) overlaid by prompt emission line-outs (measured with the streak camera) in arbitrary units (red line) for consecutive shots with variation of the transversal position of the laser-gas interaction. Bottom rows: longitudinal un-driven gas density profiles acquired prior to the corresponding high intensity shots.

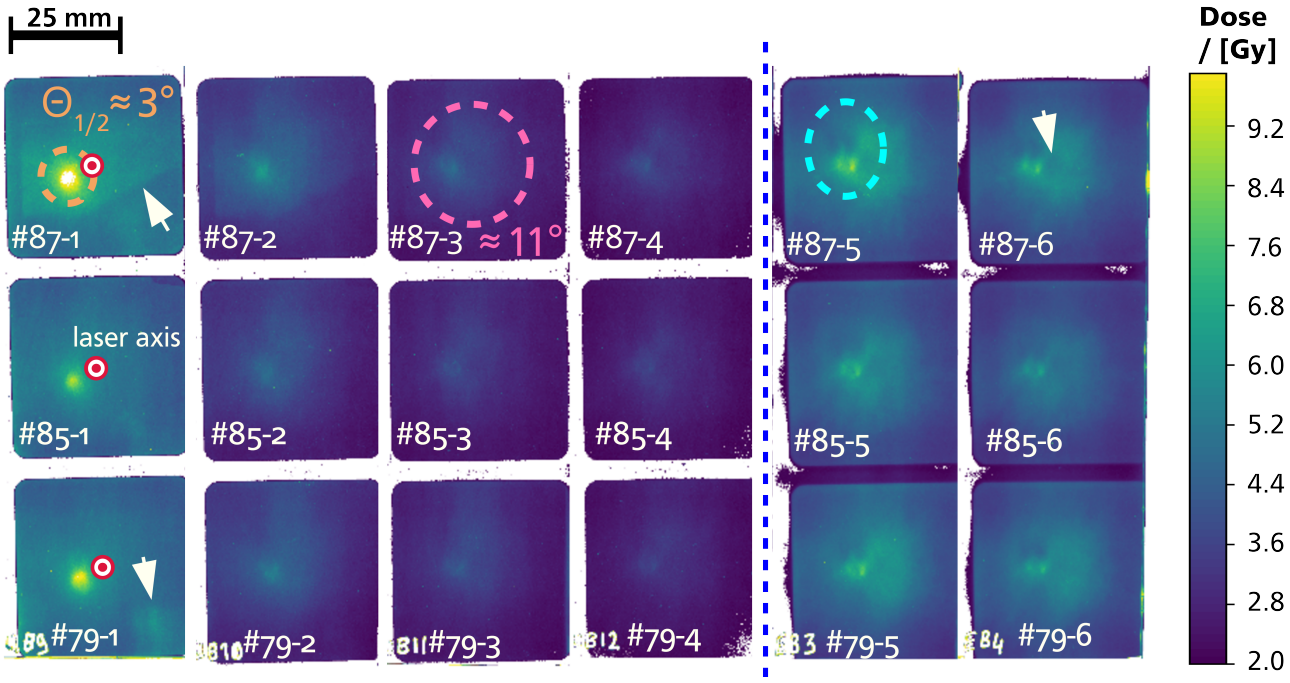

FIGURE 6.25: Overview on RCF results for shots #79, #85 and #87 with a respective transverse nozzle displacement of 0 µm, −50 µm and +50 µm as 2D dose maps. For display purpose, data is averaged over the three colour channels. RCF layers are numbered in ascending order in direction of particle propagation. The laser axis is indicated with a white dotted marker, its size represents the alignment uncertainty to the laser axis in air pressure. The unlaminated EBT-3 films used for both last layers were likely exposed to conditions, after their calibration and prior to the experiment, that changed their response to dose-deposition with respect to the calibrated response. This is clear from their detection of dose in the area blinded by the detector casing, which is blank on the first layers. Image taken from [75].

Conclusions and perspectives

The gas characterization performed before the experiment was necessary for understanding the valve operation and evaluating the different kind of jet profiles generated by different nozzles, its dependence with parameters, possible defects, etc. Nevertheless, the shot-to-shot target characterization implemented on the experiment turned out to be critical, both as an alignment tool and on-line target characterization diagnostic. Due to the progressive worsening of the quality of the jet due to the laser-induced damage, the prior characterization is not enough, as it is in the case of moderate-pressure conical nozzles for wakefield acceleration. The bottom view system was also essential for reproducible alignment of the target.

The ultrafast interferometry showed a single ionization region well after the interaction, which can be interpreted as an indication that the laser energy traverses and it is partially absorbed after the shock point. On the other hand, the streak imaging of the plasma showed regularly between one and three prompt emission points, which in most of the cases were related to a particular range of electronic densities.

RCF stacks dose deposition demonstrated forward acceleration of particles in both studies (with pure Helium and gas mix). Different spatial features are measured, as a beam-like deposition over a Gaussian background and local minima and maxima. Nevertheless, interpretation of this data along with the results from CR39 and ToF PiN diodes is not clear

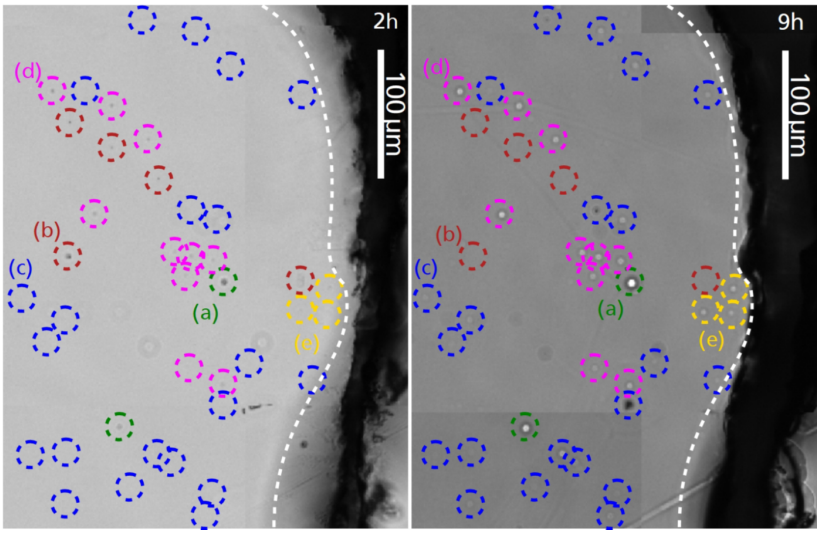

FIGURE 6.26: Diameter evolution for similar groups of etch pits on a CR39 with snapshots at 2 h and 9 h of etching in a NaOH solution of 6.25 N etchant at 70°. Highlighted are groups of circles concentric to each pit position. Group (a) shows growing pits with the etching time, (b) are surface artifacts, (c) pits underneath the detection spatial limit at 2 h of etching but measurable after 9 h, (d) are pits at the detection limit at 2 h and (e) are pits matching the energy of the alpha particle from the natural decay of Radon. The dashed line delimits a scratched area. The size and grow rate of pits (c) would fit with Helium or Nitrogen ions with $\sim$ 10 MeV. Image taken from [75].

enough to identify the composition of such radiation beam to be ions. Wakefield electron acceleration could be responsible of such dose deposition; it has been proven in the literature that such mechanism could produce *forked* beams [130, 171], related to direct laser acceleration. Both PiN diodes showed similar responses in the high intensity shots, meaning that the radiation triggering their reaction was generated both forward and transversally to the laser axis.

Despite not having conclusive ion acceleration results (and therefore no demonstration of collisionless shock triggering), the commissioning of the system in an ultra-intense laser experimental conditions highlighted a number of technical issues and taught important lessons for the following campaigns.

- The potential use of the high pressure gas as a target for high-repetition rate laser-driven ion acceleration requires the fast, reliable and repetitive operation of the gas system. In order to achieve this milestones the following changes should be accomplished
  - Minimizing the laser-induced damage on the nozzle structure is a necessary condition for HHR operation. The use of a different material for the nozzle is considered, as well as different nozzle design which could generate the shock point further away from the nozzle surface.
  - The valve malfunction due to EMP effects needs to be addressed. Sudden fill of the chamber with gas is not only a risk for the vacuum equipment but also slows down the experiment. A normally closed valve was acquired after the VEGA 2 experiment for this purpose.
  - An automatized vacuum system could be developed, which isolates the interaction chamber between shots (closing the gate valves between chambers right

after the laser shot) and starts assisted vacuum pumping in a short time. This system should be programmed also so an emergency protocol is triggered when reaching a certain pressure set point in the chamber (as a signal of valve leakage), so the equipment is kept safe and the gas evacuation is faster. Such actions would boost the experiment shot rate considerably.

- Optical investigation of the relevant plasma conditions needs a fine synchronization between pump and probe. The information of the plasma 1 ns after the interaction in a femtosecond-long interaction yields information about the residual background electronic density, but does not give any direct information about the potential acceleration mechanisms as most of the spatial and temporal plasma features have vanished at long times. Pump-probe synchronization at picosecond level around the interaction is desired for future experiments.

- Taking into account that the direction of the particle acceleration mechanism at play in near-critical plasmas is extremely dependent on the driver laser axis, a fine angular alignment is planned for future experiments. This adjustment is not so important in TNSA (solid target-overdense) experiments, where the privileged direction of acceleration is the target normal (in TNSA the angle of incidence is mainly relevant for the laser energy coupling to the target).

- A general improvement of the particle detectors is necessary to clearly identify and characterize ion acceleration. Thomson Parabolas with more sensitive detectors should be used, as imaging plates, which would however affect the shot rate. Longer time of flight distances for increasing resolution and the use of calibrated (diamond and semiconductor) detectors would be required to separate the reference photo-peaks from the ion signals. The deployment of electron spectrometers is also recommended as it can show indication of proper energy coupling [71].

6.3 Experiment at VEGA 3

A second competitive-access experimental campaign was granted to the research group at CLPU, this time in VEGA 3 PW laser facility. This follow-up of the previous experiment was proposed for testing the interaction of the high density gas target with a PW-level ultrashort laser. The Ph.D. candidate was in this case the local coordinator of the experiment. The main goals of this campaigns were:

- Demonstration of ion acceleration (in transversal but preferentially in the forward direction) and study of the acceleration mechanism. According to the theoretical models, the intensity enhancement due to the energy increase from VEGA 2 to VEGA 3 is in principle favourable for the triggering of collisionless shock and hence for potential ion acceleration. Implementation of fast electron spectra characterization as part of the acceleration mechanism investigation.

- Ultra-fast plasma inspection by different optical diagnostics.

- Standardization of the gas jet operation at high-power laser facilities.

From the experience at VEGA 2, several modifications and improvements with respect to the previous experiment were considered for this experiment.

- The repetition rate operation issues found at VEGA 2 experiment were improved.

  - A new design of nozzle (the so-called S900) was developed by the CENBG researchers. This type of shock nozzle generated the shock point twice as far from the nozzle surface compared to the previous models ($\sim$ 1 mm). Furthermore, a systematic decrease of the target density was targeted as, according to the research group simulations (see V. Ospina Ph.D. manuscript [249]) this would benefit laser penetration into the target and improve energy transfer. The new jets were characterized prior to the laser beam time.
  - A new -normally closed- valve was acquired from the gas system supplier. Despite being much slower than the valve used at VEGA 2, it was leakage-safe.
  - Nitrogen and Helium (and mixtures) were the gases chosen as target. Taking into account that CSA is a mass-dependent acceleration mechanism, the energy spectra of the accelerated ions of a mixture target could be an indication of the existence of this mechanism. The ideal target composition (for higher expected energies) would be Hydrogen, but due to its explosive nature it was not allowed by the facility at that time.
  - A fully-automatized vacuum control system was developed by the facility engineering division (work led by A. Martín-López, R. Hernández-Martín and J. Hernández-Toro), whose goal was to keep the vacuum equipment safe in case of emergency and to enhance gas pumping rate [251].

- Improved control of the laser parameters was arranged for this experiment, including:
  - Shot-to-shot measurement of the laser pulse duration was carried out right before TCC. This was possible by the construction of an auxiliary beamline from the reflection of VEGA 3 (after the OAP) on the pellicle used for debris protection. The time duration of the pulses was characterized by means of a commercially available second order autocorrelator. This diagnostics was specially important as scans in pulse duration were performed in this campaign.
  - The driver laser focal spot quality and pointing were accurately controlled daily.
  - A pick-up probe was built able to overlap in time and space with the driver laser.

The relevant contributions of the Ph.D. candidate for this experiment (besides the general coordination and support) are elaborated in the following sections. Finally, a fast summary of the main results obtained at VEGA 3 are outlined.

6.3.1 Gas characterization with Shack-Hartmann detector

As the gaseous target characterization became a routine activity at CLPU, a permanent gas characterization station was constructed. The setup design is detailed in figure 6.27. This design is capable of measurement of the phase (i.e. density) maps of the target in two perpendicular directions and with different spatial resolution with the help of a single-axis wavefront sensor, and simultaneously obtain an qualitative idea of the gas jet evolution with a strioscopy system.

The excellent-quality He-Ne laser HNLS008L-EC ($\lambda = 633$ nm) from Thorlasbs Inc. is expanded and it can be inserted into the vacuum chamber via two orthogonal paths. The path election can be decided with the help of a flip mirror mounted in a precision magnetic mount. The two perpendicular probing directions allows for more detailed assessment of the cylindrical symmetry of the target. In addition, with the help of a beam-splitter, both images can be sent simultaneously to a wavefront sensor (which yields the 3D density map at a certain time-stamp, if imposing cylindrical symmetry) and to a strioscopy system coupled to a photodiode accurately aligned in the region of interest of the jet (in the case of

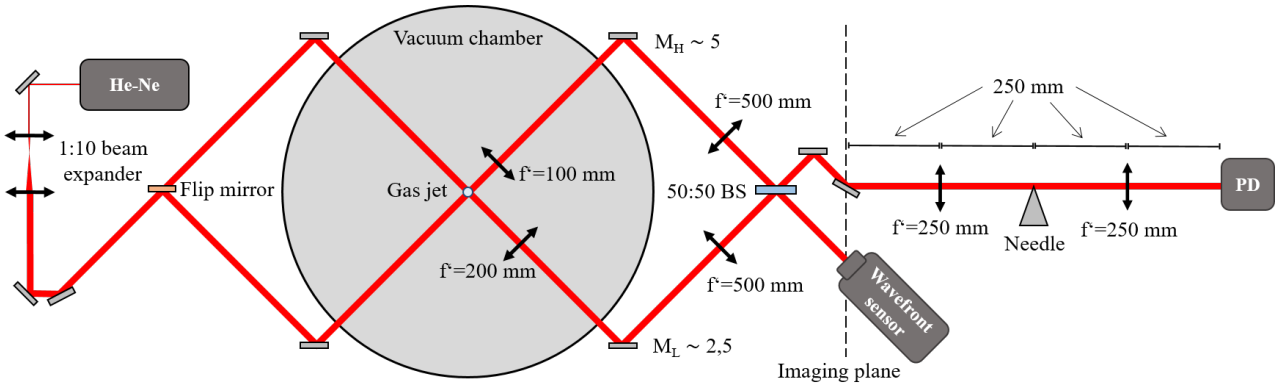

FIGURE 6.27: Permanent gas jet characterization station built at CLPU.

the shock nozzles, the shock point). This diagnostics gives the qualitative jet evolution in a single take.

A subsequent characterization campaign was dedicated to measure the specifics of the nozzle J2020, which was acquired for its employment at the VEGA 3 experiment (before the acquisition of the S900 models and the new normally-closed valve). This piece was supposed to imitate the geometry of the TUCAN nozzle design used at VEGA 2 experiment. A deep study (still using the normally-open valve) similar to the one done before the VEGA 2 experiment was performed for different parameters, including in this case scan in valve opening times. The backing pressure was fixed close to the maximum value accepted by the system ($\sim$ 410 bar) as a recommendation from the manufacturer for stable valve operation.

The wavefront sensor SID4 from Phasics was not available at the time slot booked for this characterization experiment. This is the reason why a commercial Shack-Hartmann (SH) detector was used instead, already presented in Chapter 3. This sensor has a main drawback; each micro-lens is linked to a phase point of the 2D phase map measured. The used SH detector has an array of 40×32 micro-lenses. Depending on the optical system magnification and the characteristic gradient length of the studied object, this might be not enough to resolve fine structures. The imaging systems designed yielded measured dimensionless magnification parameters of $M_H = 5.09$ and $M_L = 2.48$, which corresponded to spatial calibration of 22 µm/pix and 46 µm/pix and diffraction-limited spatial resolution of ≈ 3 µm and ≈ 4 µm respectively. Two typical phase maps taken by both systems are shown in figure 6.28.

Two distinctive features are observed in the phase maps. There is a visible asymmetry with respect to the central jet axis; applying therefore the Abel inversion in these data is a very strong approximation. Secondly, it can be observed that the asymmetric jet shock is generated around 300 µm away from the nozzle end. This is much closer to the nozzle than expected (and desired) and severe laser-induced damage would be expected after a few shots of the PW system.

Nevertheless, a parametric study of the instantaneous density map and time-resolved of the jet was performed with different gases at maximum possible pressure for increasing valve voltage pulse durations (until leakage of the valve was found for longer opening times). Figure 6.29 illustrates an example of the full characterization of the J2020 jet with Nitrogen and opening time 4.7 ms. From the density charts it is noticeable that the spatial resolution of the SH detector is poorer than the SID4 or interferometry shown in the previous sections, mostly caused by the pixel size.

The results of the parameter scan are summarized in figure 6.30. The main results is that there is a general trend towards better (narrower and higher) shock density points with increasing valve opening time (until valve malfunction is found). The spatial characteristics

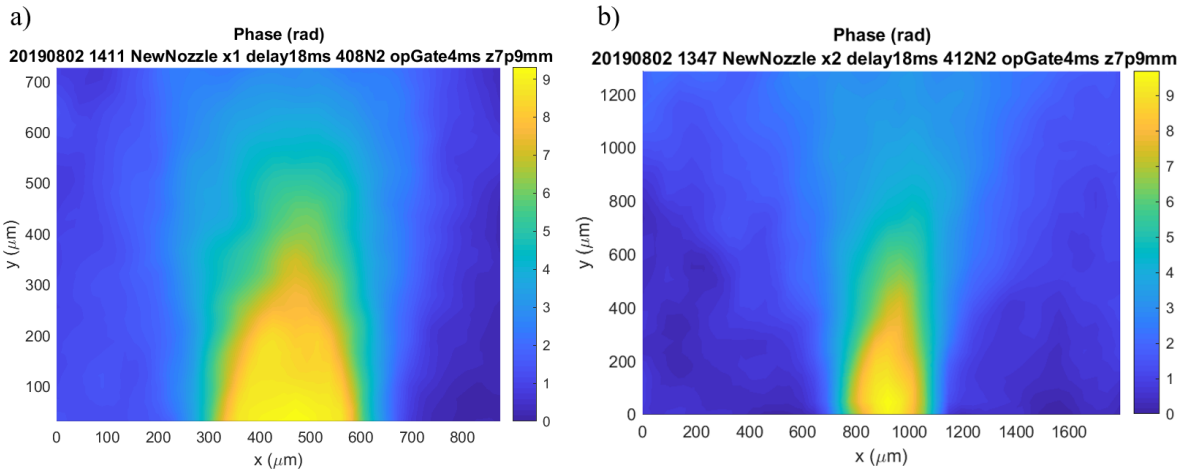

FIGURE 6.28: Typical phase maps measured by the SH wavefront sensor of the fully developed jets generated by the nozzle J2020 backed with $\sim$ 410 bars of Nitrogen. Measurements in orthogonal directions with the (a) high magnification and (b) low magnification imaging systems.

in the case of Helium are not shown, as the poor resolution here adds to the low signal-to-noise ratio met when measuring gases with very small refractive index. In any case, for Helium there is a clear density enhancement that appears when the valve leaks. Such behaviour was already observed in the first interferometric characterization campaign before VEGA 2 experiment. It was observed that the average vertical position of the shock point does not vary appreciably with the opening times but it rather depends on the gas composition; it is fixed at $\sim$ 320 μm for pure N_2 and the partial He mixture and is found at $\sim$ 530 μm in pure Helium.

Finally, the duration of the gas jet rise time (understood as the time spent since valve aperture until the maximum density shock achievement) is plotted for the different cases as a function of the duration of the valve voltage in figure 6.31. From the figure one notes that the longer the valve voltage pulse, the later the jet is developed. Also, the concentration of Helium seems to be detrimental for the valve operation. Larger concentration of Helium results in premature valve leak, in agreement with results from the characterization campaign before the VEGA 2 experiment.

It is worth to mention that the results obtained agree with the manufacturer specifications and a second characterization performed at CENBG (with a different valve and gas compressor). The defects appreciated in this jet in this characterization experiment (asymmetry, insufficient distance nozzle to shock point) in addition to the valve operation problems were the reasons why it was finally decided not to used the nozzle J2020 in VEGA 3 experiment, being as well crucial for the decision of purchasing a new normally-closed valve.

Gas jet rise time study

As part of the VEGA 3 experiment goals, despite the poor spatial resolution of the SH, an advantage was taken from this dataset for evaluating a possible decrease of the target density. The PIC simulations performed by the research group (see V. Ospina Ph.D. manuscript [249]) yielded an optimal peak molecular density for laser penetration and collisionless shock triggering of $2.5 \times 10^{19} \mathrm{cm}^{-3}$ for Nitrogen. This is a 10-fold decrease from typical maximum density values reached in normal jet operation conditions. The first strategy in

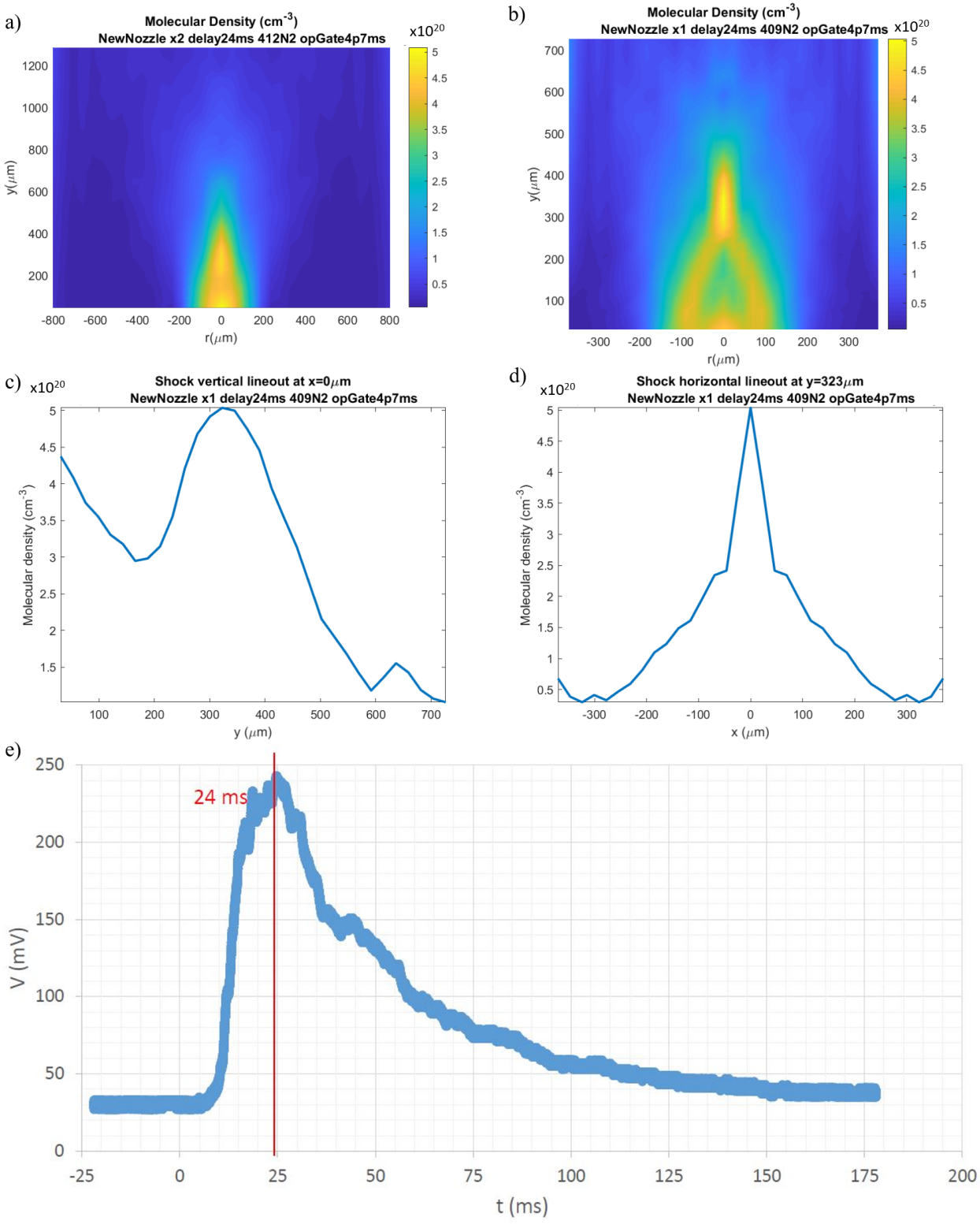

FIGURE 6.29: Results of the characterization of J2020 nozzle for $\sim$ 410 bars of Nitrogen with applied valve voltage during 4.7 ms. (a) Density map measured with low magnification imaging system and (b) with high magnification system, both at 24 ms after valve opening, when the peak density is found, see (e). (c) Vertical and (d) horizontal density lineouts at the jet shock point, taken from (b). (e) Strioscopy signal (photodiode voltage) showing the jet evolution; the maximum density is found at 24 ms.

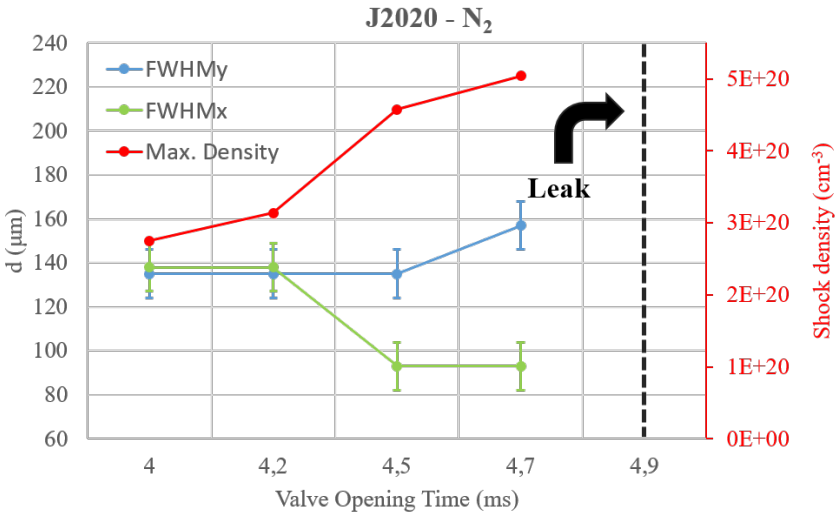

(A) Results for Nitrogen.

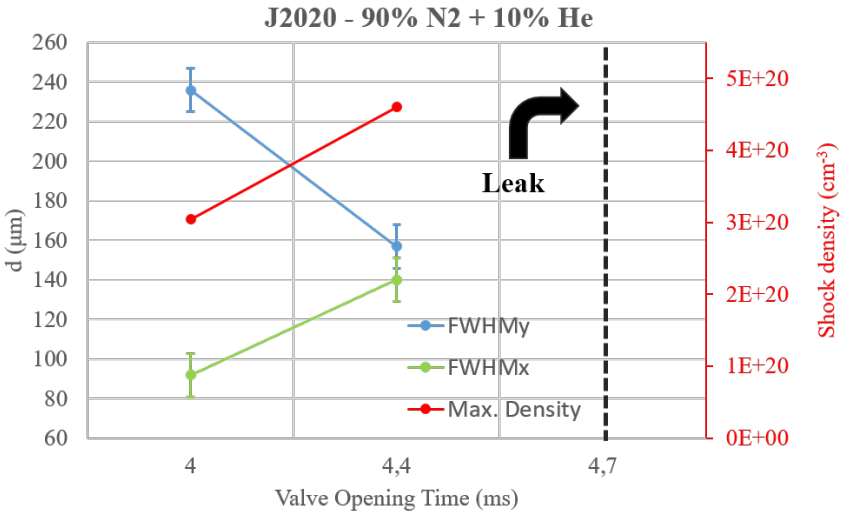

(B) Results for mixture of Nitrogen and Helium at 9:1 ratio.

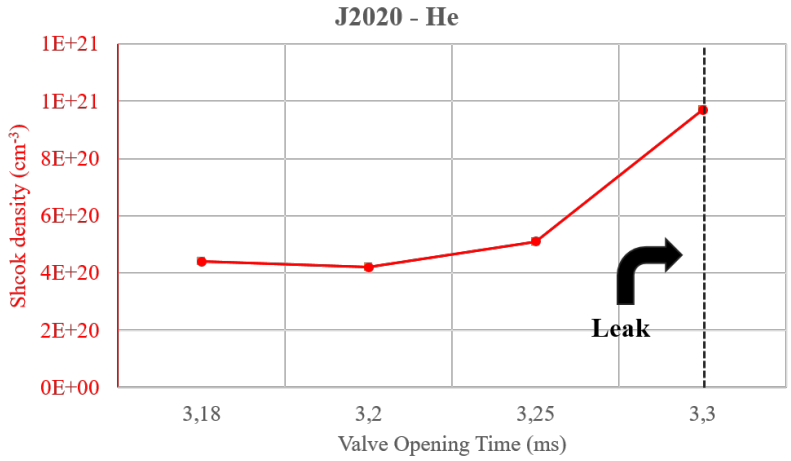

(C) Results for pure Helium.

FIGURE 6.30: Characterization summary of J2020 jet at 410 bar for (a) Nitrogen, (b) mix and (c) Helium. In red, maximum density measured at the shock position (at best delay) versus valve opening pulse width. Vertical (blue) and horizontal (green) density FHWM at the shock point are shown. Dashed lines represent the opening time which entails systematic valve leakage.

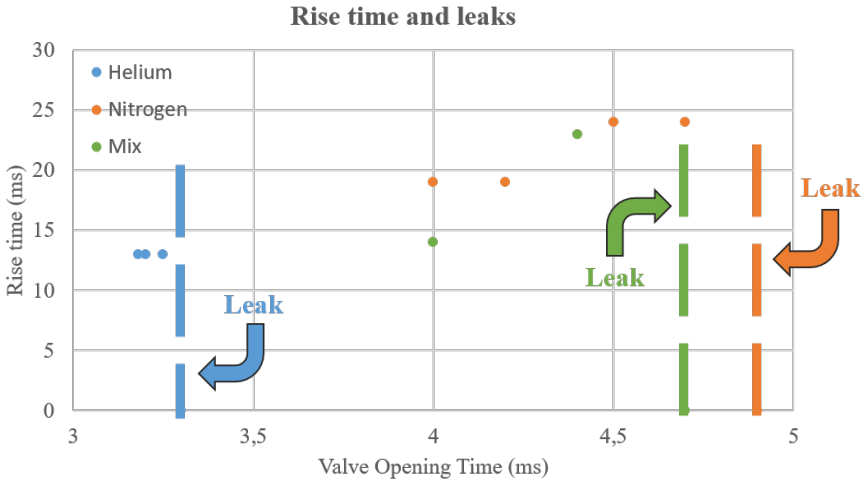

FIGURE 6.31: Duration of the rise time until maximum density is found with the strioscopy system (double-checked with the wavefront measurement) for different gases, at maximum pressure with J2020 nozzle. Dashed lines represent the opening times which lead to repetitive valve malfunction.

mind was to lower the backing pressure, but the valve seemed to show more unstable operation at lower pressure values. Reducing the valve opening time was also considered and studied (inside factory specifications), but the best results (see figure 6.30a) were still far away the target value. A third option evaluated was shooting onto the target during the jet formation stage (i.e. at the rise time). Figure 6.32 compares the shape and density of fully-developed jet with itself at early times. The shock is present since early stages of the jet formation, it shows a similar shape as in later times and its position is roughly conserved during the evolution (within the instrument spatial resolution). On the other hand, it is clear that the value of the density point is several times smaller. This behaviour was also demonstrated at different valve opening times. As a side effect, the gas between shock height (presumably the laser shot height) and the nozzle edge is much less dense, which could reduce the laser-induced damage.

Figure 6.33 summarizes the potential density decrease of the nozzle J2020 when shooting at early times. Density maps were measured at different delays between valve and sensor trigger with steps of $\Delta t = 2$ ms. Indeed, figure 6.33 shows that the evolution of the jets measured with the SH agrees with the characteristic rise time measured via strioscopy. It is clear that a density plateau is reached after $\sim$ 20 ms, whose density value depends on the operation parameters (pressure, valve opening time, gas composition and so on). In any case, the values of density converge at early times towards the value 1×10^{20} cm^{-3} at 6 ms. Density maps measured 4 ms after the valve opening do not show evidence of gas. A finer scan between 4 and 6 ms could be performed in order to try to reach the target density predicted as optimal in the PIC simulations.

This data was analysed in collaboration with A. Huerta, student of the University of Salamanca in a internship at CLPU at that time. The same characterization station was utilized afterwards by Dr. Ospina for the complete characterization of the S900 nozzles fabricated, with the only difference that the SID4 of Phasics was used as wavefront sensor (instead of the SH). An extensive explanation of the setup and test carried out can be found in her Ph.D. manuscript [249].

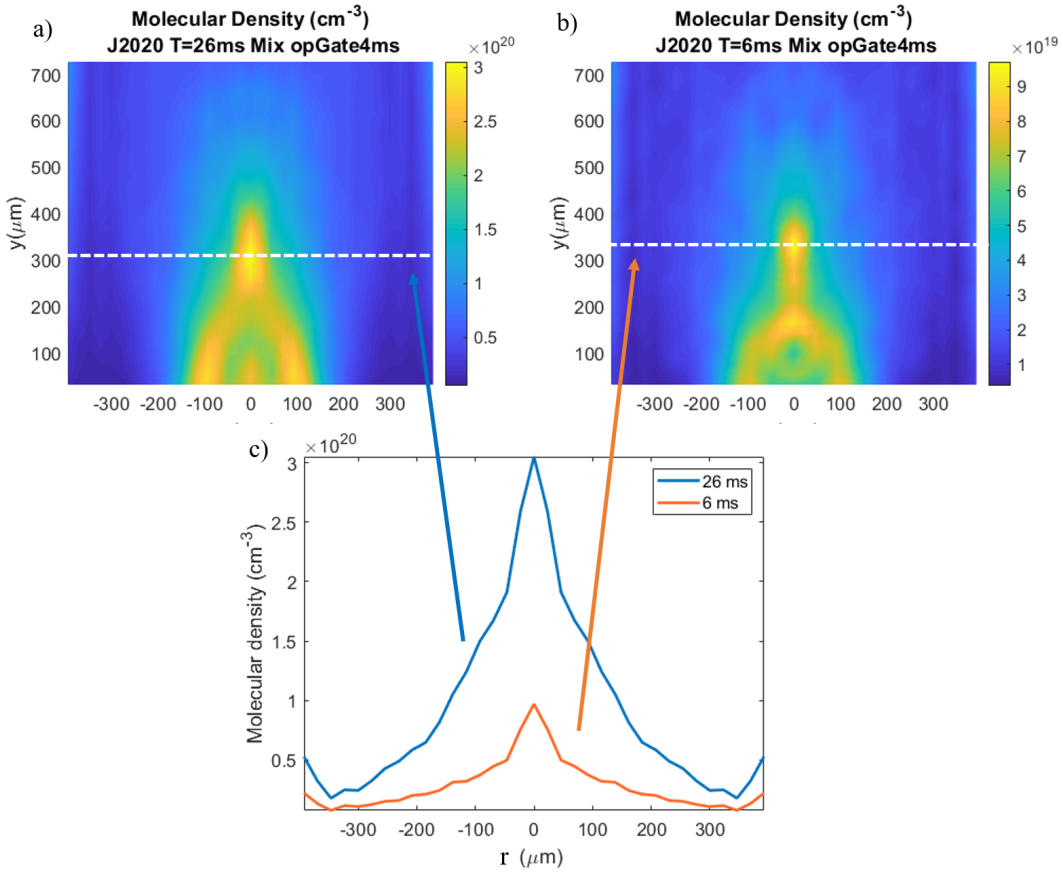

FIGURE 6.32: Density maps comparison of (a) a fully-developed J2020 jet (∼ 410 bar of 9:1 N_2:He mix, valve opening time 4 ms), measured 26 ms after valve trigger and (b) the same jet at early formation stages (6 ms after valve opening). (c) compares both radial density lineouts from (a) and (b).

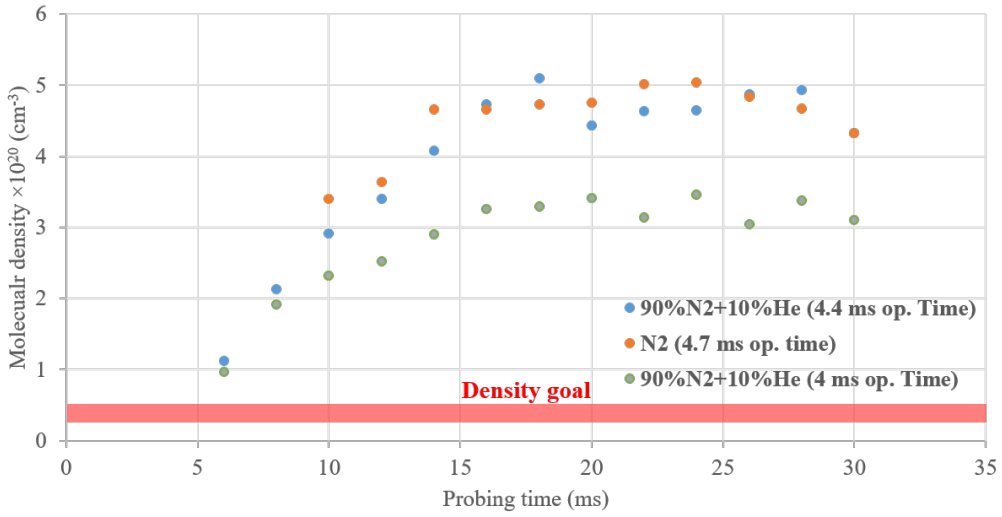

FIGURE 6.33: Shock density value measured at different times after the valve opening for three different operation conditions at shock height, in all cases for 410 bars of backing pressure. The density goal predicted by simulations is shown as a red stripe.

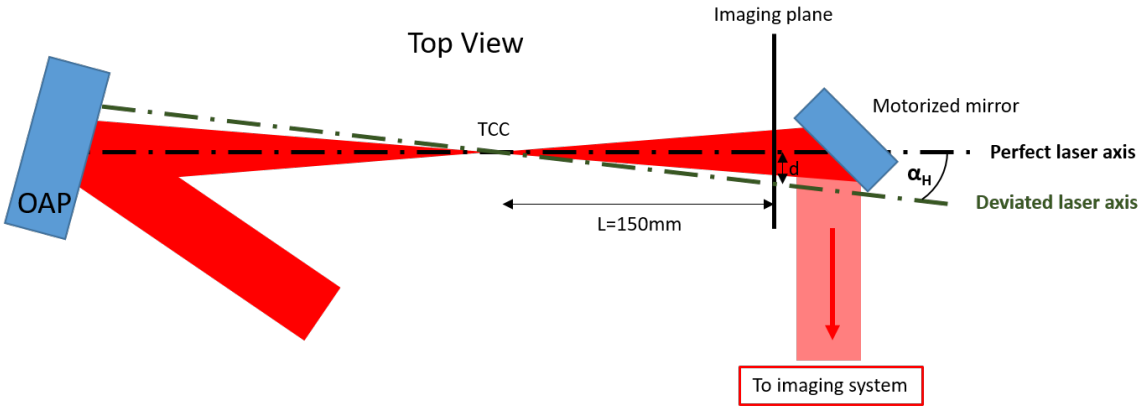

FIGURE 6.34: Top view sketch of the pointing control setup of VEGA 3 Ion-GasJet experiment.

6.3.2 VEGA 3 experiment description

A competitive access experiment at the VEGA 3 laser facility was carried out by the research group. The experimental interaction of the petawatt-level laser pulses with the high-density gas jet was studied, implementing every possible improvement with respect to the previous experiment. The Ph.D. candidate, besides being the host facility coordinator and member of the scientific collaboration, was in charge as well of the laser pointing control and probe beam construction.

Laser control

VEGA 3 pulses -with an energy on target of 18,5 J- were focused by an 2.5 meter long focal OAP mirror resulting in $f^{\#} \sim 11$. The focal spot size was routinely checked by a high magnification imaging system and showed a stable FWHM of $14 \pm 1\,\mu m$, yielding a maximum intensity of $\sim 10^{20}\,W/cm^2$ ($a_0 \sim 6$) at best compression. A shot-to-shot pulse length characterization line was built taking profit from the reflection of VEGA 3 on the debris protection pellicle set after the OAP (containing 6% of the total laser energy). The pulses are characterized by a commercial second order autocorrelator (from Avesta, ASF-15M) placed in this beamline, yielding pulse duration ranging from 30 fs to 100 fs. The laser energy is measured shot-to-shot in the laser bay by analysing a near-field picture of a calibrated leakage beam through one of the reflecting mirrors.

In order to control the forward axis of the potentially accelerated particles (i.e. the laser focalization axis) a dedicated pointing control system was developed by the candidate specifically for this experiment. Figure 6.34 illustrates the pointing control system. The physical line that the axis of VEGA should follow in the interaction chamber during focalization was pre-defined before the experiment, and it was fixed in the chamber by means of an alignment laser and two physical references (irises). This line is afterwards transferred to two points in the vacuum chamber that can be measured in vacuum. The first reference is the TCC point (or interaction point), which is exactly the position where the focal spot (and target) is brought to. Relative positioning of the laser, target and all diagnostics is achieved at this point thanks to two narrow tips that can be imaged from all possible angles and can be inserted and removed from TCC with motorized stages. The second point which defines the pointing of the laser after TCC (i.e. the laser axis) is located at a distance of $L = 150$ mm downstream from the interaction point. A motorized mirror can be inserted in vacuum in the path of the laser -during low energy alignment phase- and brings the beam into a demagnification imaging system which records the beam position at

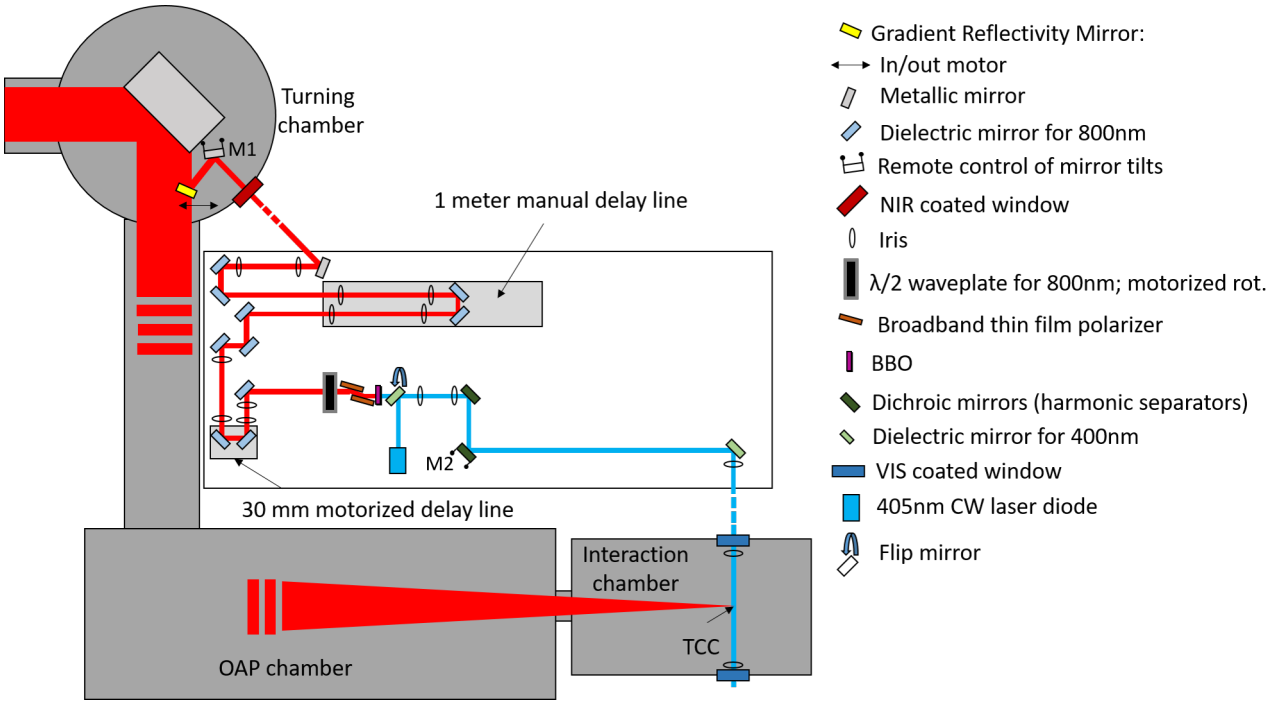

FIGURE 6.35: Detailed setup sketch (and components description) of the probe beam built for the VEGA 3 experiment.

position L. Measuring vertical d_V and horizontal d_H deviations of the VEGA beams with respect to the reference point, it is possible to evaluate (and correct) the angular deviation of the beam as $\alpha_i = \tan^{-1}(d_i/L)$, where the subscript i stands for horiziontal (H) or vertical (V) directions.

The laser pointing was determined daily with this methodology and the largest deviation found below was 1.5 mrad, well below the angular acceptance of the particle diagnostics set in the forward direction.

Probe beam

An unique probe beam was designed and built for this experimental campaign by the candidate. This beam was utilized as a ultrafast probe for shot-to-shot plasma interferometry, diagnostic which was during the VEGA 3 experiment under supervision of the IPPLM collaborators (led by Prof. Tadeusz Pisarczyk). Figure 6.35 depicts the probe design until TCC.

The probe is taken from the original VEGA 3 beam at an accessible point of its beam transport, well before the focalization. In order to minimize the diffraction fringes in reflection generated by a hard-edge cut of the beam, a 1' dielectric GRM was used instead of a regular one. By a special coating deposition process, the GRM presents a gaussian reflectivity profile (6 mm wide) in the center of the one of its surfaces, so the reflected beam has a gaussian-like profile. There is still a diffraction pattern in the transmitted beam due to the laser intersection with the mirror substrate rim. The pattern was characterized at low energy in front of the large diameter beam transport optics downstream; the local fluence enhancement generated by the fringe pattern was estimated to be well below the damage threshold of such optics for full power shots.

The reflection and size of the beam was calculated to extract $\approx$ 6 mJ of energy (for VEGA 3 full energy shot). The beam intensity was big enough to perform efficiently its frequency doubling via second harmonic generation with a BBO crystal and use this for plasma interferometry, but small enough to keep its B-integral at a reasonable value (< 10)

when travelling through several meters of atmosphere and a few centimetres of transmissive optics, avoiding severe non-linear effects. The B-integral was calculated to be (at center of the gaussian profile) ≈ 0.05 after 8 meters of travel in air and ≈ 0.4 after 1 mm of fused silica. This is the reason why the use of transmission optics was avoided when possible and, if needed, as thin as possible. For instance, the air-vacuum interface windows were 5 mm thick. The beam fluence was calculated to reach a maximum value of ≈ 20 mJ/cm^2 at the center of the beam (well below the optics damage threshold). The probe beam design also included two delay lines. The manual one was designed for coarse synchronization and it can move the probe several nanoseconds with respect to the pump. On the other hand, a motorized delay line, spanning a range of ~ 200 ps, was built for a fine temporal scan between pump and probe, with a step resolution of 3.3 fs.

An energy control device ($\lambda/2$ waveplate and a pair of reflection Brewster linear polarizers) were used for controlling the probe energy in case it needs to be reduced, being the maximum pulse energy (in the second harmonic) 0.1 mJ. Motorization of the tilts of one the mirrors before TCC was prepared for probe alignment in the chamber (M2 in figure 6.35), available from the experiment control room. Furthermore, tilt remote motorization was also available for the mirror after the pick-up (M1 in figure 6.35), so its angle can be controlled in vacuum. An auxiliary CW laser ($\lambda = 405$ nm) could be inserted in the path of the probe for alignment purposes.

Coarse pump-probe synchronization was performed similarly as in the case of VEGA 2 experiment by means of streak measurement of scattered photons of both beams. In this case a 500 µm diameter plastic sphere was set at TCC, whose purpose was photon scattering (from both pump and probe beams) in the angle of sight of the streak camera. The scattered optical radiation was collected by a bottom-view imaging system (and brought to the streak camera), system built in the VEGA 3 setup for both nozzle alignment and plasma emission streaked measurement. The temporal resolution of this method could not be better than 750 ps as it was limited by the jitter between the streak camera electric trigger signal and laser arrival. This limitation arose when simultaneous measurement of both pulses was attempted and could not be done, as the intensity ratio between pump and probe was larger than the streak camera dynamic range. The fine synchronization (with an estimated accuracy below $\Delta t = 1$ ps) was determined by observing in the interferogram the prompt gas ionization on the entrance of the gas jet profile, assuming that the ionization is almost *instantaneous* (or at least much shorter Δt) and assuming that it could be caused only by the most intense part of the pulse (and not the prepulse), which is a good assumption for the very good contrast of VEGA 3.

Other diagnostics

The target during the experiment were the near-critical dense jets generated by the SL-GT-10 system, delivered by the normally-closed valve. The target composition was either pure Nitrogen or Helium or 9:1 Nitrogen/Helium mixture. The nozzles shaping the gas density lineouts were J2021 (with same geometry as TUCAN) and 5 different replicas of the S900 geometries.

A sketch of the experimental setup can be found in 6.36. Several diagnostics were deployed for target and plasma inspection. Similarly as in VEGA 2 experiment, a strioscopy line and an in-line wavefront measurement (the SID4 from Phasics) were built for shot-to-shot gas inspection, evaluation of the potential laser-induced damage on the nozzle and jet degradation and valve positioning. A bottom-view imaging system was constructed for alignment purposes. In this case, this system was exploited as well for streaked imaging of the prompt plasma emission (by means of a streak camera, same model as in VEGA 2

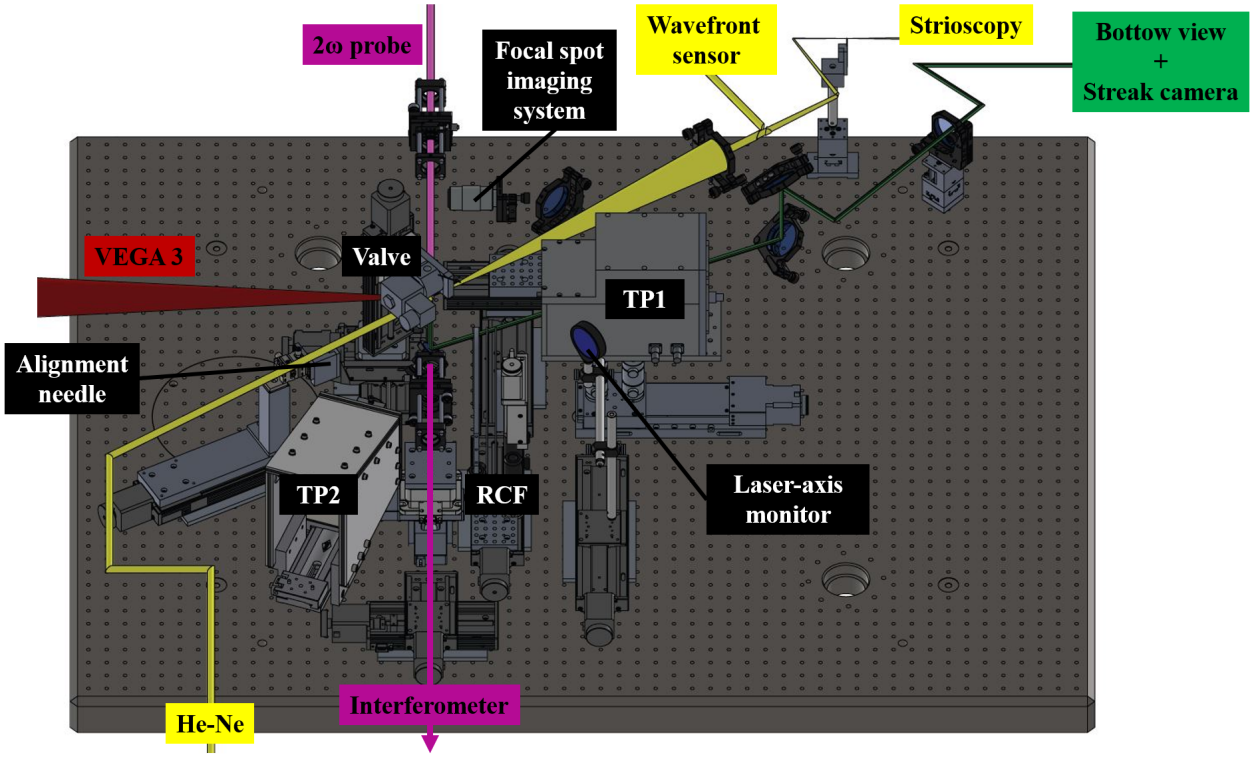

FIGURE 6.36: Detailed 3D drawing of the experimental setup of IonGasJet experiment at VEGA3.

campaign). Additionally, the synchronized frequency-doubled ultrafast probe beam back-illuminated the target in every shot; its phase was measured by a Nomarksy interferometer, which yielded information about the laser propagation through the target and about the local plasma density values at specific times after the interaction.

In addition, a complete set of particle diagnostic were used to evaluate energies and angular distribution of the emitted charged particles. Five different active crystalline semiconductor detectors [252] fully calibrated for Helium and Nitrogen ions (with decay characteristic time of $\tau \sim 1$ ns) were used as in ToF configuration and placed at $\alpha_V = 9°$ above the laser axis and inside a cone (centered in the laser forward direction) of $\alpha_H = \pm 17°$ at distances ranging from 0.8 m to 1.5 m from TCC. These detectors were built by the group of Dr. F. Consoli and Dr. M. Salvadori, from ENEA and CNR and Dr. Claudio verona and Dr. Giuseppe Prestopino from the University of Tor Vergata, Italy.

Two Thomson Parabolas were set at 0° and 100° with respect to the laser axis (in the equatorial plane). In contrast to VEGA 2 experiments, imaging plates of type TR (the most sensitive type available) covered with 2 layers of thin aluminized Mylar were used as detectors for both TPs. Stacks of RCFs were used as passive detectors of charged particles in the forward direction for several shots. Finally, it is worth mentioning that magnetic deviation electron spectrometers were used in order to characterize the temperature of the electron expelled from the plasma at different angles.

Summary of results

The detailed description of the experimental results is beyond the scope is this work. Scans in nozzle model, gas composition and pulse duration were accomplished. Despite keeping the rest of parameters fixed in a scan, successive shot-to-shot degradation of the nozzle

modified the target density shape. Nonetheless this change was monitored by the wavefront sensor before every shot. A complete study and interpretation of the results (benchmarked with PIC simulations) can be found in the Ph.D. manuscript of Dr. Ospina [249]. Nevertheless, a condensed summary of the results in given below.

- Electron temperatures were measured up to $T_e \approx 10$ MeV at 2° from the laser axis, which is five times larger than the expected ponderomotive scaling predicted by 3.141, meanwhile weaker electrons ($T_e \approx 4$ MeV) were characterized further away from the laser axis (21°). The enhanced electron energy scaling is one of the expected results according to energy coupling PIC simulations [71].
- ToFs detectors yielded energetic ion acceleration (with 5 detectors in a forward cone of 17° horizontal angle and inclination of 9° with respect to the horiziontal plane) for Helium ions up to 2.5 MeV, with a particle flux of 10^9 particles/sr for shots in pure He.
- No evidence of ion signal was detected on the TPs. It was estimated that the number of particles arriving to the detector (at the energy range available for the TPs) was below the sensitivity of the IPs, taking into account the effect of the Mylar shielding and the angular acceptance of the TP entrance pinhole. The possibility that there is not emission in the TP small solid angle is not discarded. PIC simulations have predicted significant magnetic field generation in the plasma-vacuum border driven by electron currents with potential to deviate the accelerated ion ions up to 10°, which might be the reason for the observation of oblique ion emission.
- Repeatable proof of deep laser penetration into the target (through the density shock point) was found by the different plasma diagnostics. Ultrafast probing of the plasma very close after the interaction time (between 10 and 100 ps) was successfully accomplished with the new probe beam setup. By means of interferometry, early ionization regions and ponderomotive channel structures (see figure 6.37) traversing the gas shock position were resolved both spatially and temporally.
- Asymmetric doughnut-shaped dose deposition was systematically measured in the forward direction with RCFs stacks, attributed mostly to electrons.

6.4 Conclusions and perspectives

In this Chapter the experimental effort to develop a high-repetition rate compatible laser-driven ion source has been presented. Practically it consisted of the irradiation of a ultra-intense femtosecond-duration laser pulses ($a_0 > 1$, 30-100 fs) onto high density gas jets, with ionized plasma dense peaks close to the critical density of the driver laser. The research line was divided in two separate experimental campaigns, both at CLPU, in VEGA 2 and VEGA 3 laser facilities. The first campaign at VEGA 2 worked as a first commissioning of the newly developed target in realistic experimental conditions (debris, laser damage, vacuum, EMP...), including an extended target characterization labour. The second campaign using the VEGA 3 laser allowed an enhancement of energy on target, but also several operational improvements were implemented with respect to the VEGA 2 experiment for its success. These include the use of new nozzle type and gas valve, control of the laser focalization axis, improvement of the probe design and particle detectors, among others.

The main results of this last experiment include the acceleration of Helium ions up to 2.5 MeV from pure He targets. According to the 2D PIC simulations performed by the research group [249], these accelerated particles would be originated from both the TNSA

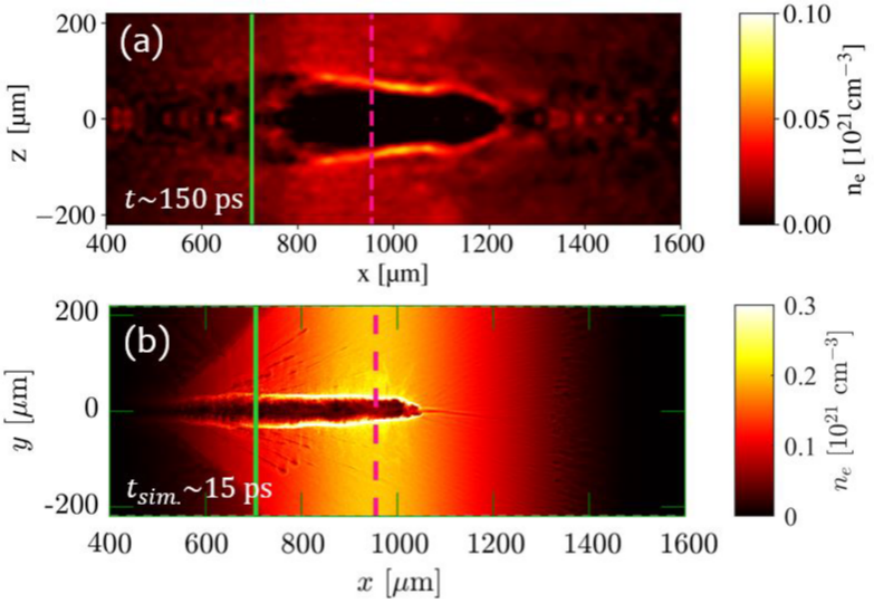

FIGURE 6.37: (a) Electron density chart from the ultrafast interferometry taken $\sim$ 150 ps after the interaction. (b) Electron density chart extracted from the 2D PIC simulations at an earlier time ($\sim$ 15 ps). In both figures, the green vertical line shows the laser focal plane, meanwhile the purple dashed line represents the plane where the gas shock position is located in this particular laser shot. Interferometric data analysed by the IPPLM, simulations carried out by Dr. Ospina-Bohórquez.

mechanism in the steep plasma downramp and from the fast-expanding ponderomotive channel walls created by the laser inside the plasma [164], structure which was characterized with the ultrafast interferometry. Angular-dependent electron temperature measurement were carried out and compared to the laser energy coupling of the experiment. Laser channelling and energy deposition through the plasma, as predicted by 2D PIC simulations, was confirmed by means of ultrafast interferometry and the prompt plasma emission streak imaging. Shot repetition-rate of a shot every 20 minutes was achieved, being the main bottleneck for a faster shot rate the need of shot-to-shot target assessment and alignment into TCC.

A number of issues were identified which subsequently were addressed leading to a following successful shock-driven ion acceleration experiment.

- Increasing of the laser intensity on target. According to simulations, the trigger of CSA is more probable for larger a_0 [71]. Such values could be reached if OAP with smaller f-number are used (for a smaller resulting focal volume) or via more energetic pulses.

- Using Hydrogen (pure or mix) in the target composition. Due to its larger charge-to-mass ratio, protons are more sensitive to the accelerating fields; the electrostatic potential needed for ion reflection via collisionless shocks is lower for hydrogen ions than for any other species.

- Improving the operation towards high-repetition-rate: more durable nozzles (other materials, new geometries with more distant shock points) and efficient vacuum pumping are just a few points that should be addressed.

- Well-suited particle detectors. Thomson Parabola spectrometers working with MCPs as active detectors could enhance the sensitivity the diagnostic.

- Include measurement of the induced magnetic field inside the plasma (by means of ultrafast probe beam polarimetry [253]) would be useful for identifying potential acceleration mechanisms.

A major part of the candidate's work was the detailed characterization of the high density gas jet targets. The detailed density profiles are critical for the proper modelling and interpretation of the resultant laser plasma interactions in the experiments. Different wavefront sensors were compared for determination of the density profiles of the gas targets. Commercial shear-lateral interferometers (SID4 from Phasics), Shack-Hartmann detectors and home-made Mach-Zehnder interferometers were compared. Because of its setup simplicity (single arm interferometer) and good spatial resolution (phase pixel size 24 μm), high dynamic range and low noise, Phasics sensors are good candidates for this kind of measurement. Retrieval of the density from phase is normally done by a built-in piece of software, which can be a good tool for fast online analysis between shots but limits the flexibility of a potential deeper analysis. Thus, it is important to compare to others standard interferometers to assess the accuracy and reliability. In addition, the candidate's contributions in target and laser alignment protocols and in plasma diagnostics (ultrafast probing interferometers) and have proven essential for control of the laser-plasma interaction parameters and identification of the potential particle acceleration mechanism respectively.

Chapter 7

Multi-pinhole Thomson Parabola for Characterizing Laser-driven Ion Beams

Investigation of the laser-driven ion beams is fundamental for both better understanding of the acceleration mechanisms and post-acceleration control of the beam. Extensive studies with different methodologies have been dedicated for investigating the source size, divergence, transversal emittance, trace-space and the spatial and energy resolved proton distribution [21, 22, 34].

In this Chapter the design and specifications of a high-repetition-rate compatible Thomson Parabola with multiple entrance pinholes is shown. This device is capable of measuring simultaneously the ion-type, energy and angular projection of an ion beam, therefore correlating spectral information with the spatial beam coordinates. By implementing a different operation mode with higher trace magnification, the transversal spectrally-resolved trace-space of the beam is investigated and beam properties such as the transversal emittance can be studied.

The design, construction and test of the diagnostic was lead by C. Salgado and the main contributions of its design were carried out in collaboration with D. de Luis and Dr. J. Apiñaniz. Its design was supervised by Prof. L. Volpe and Dr. G. Gatti. The corresponding data analysis was performed both by C. Salgado and Dr. J. Apiñaniz and supervised by Dr. A. Curcio and Dr. G. Gatti. The optical inspection of the pinholes was performed by Dr. M. Rico. All the aforementioned researchers were members of the scientific division of CLPU at that time.

7.1 Multi-pinhole Thomson Parabola spectrometer

A commissioning experiment was carried out by the CLPU scientific area at the VEGA 3 petawat laser facility at the CLPU. The experiment was focused on the interaction of the VEGA 3 pulses with solid target and accelerating ion beams through the TNSA mechanism. The multi-pinhole Thomson Parabola presented in Chapter 3 was the main diagnostic for ion beam characterization, both for energy spectrum measurement and ion type identification.

In this experiment a 3 µm-thick Al planar foil, was irradiated at 10° form the target normal in the horizontal plane by the VEGA 3 laser. For the case shown, a single 0.8 µm wavelength linearly p-polarized pulse of 10.9 J (on target) and 180 fs full width at half-maximum (FWHM) duration was focused by an F/11 off-axis parabolic mirror (OAP) into a 9.7 µm FWHM spot, containing 20% of the pulse energy, yielding an average intensity of 1.7×10^{19} W/cm^2 inside the FWHM and resulting in the acceleration of ions from the

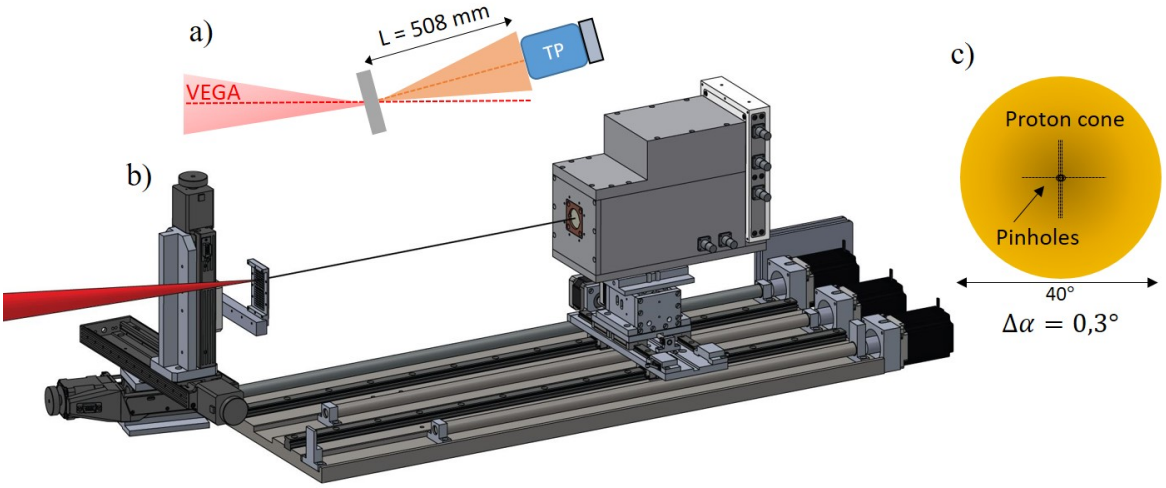

FIGURE 7.1: Sketch of the VEGA 3 ion acceleration commissioning experiment. a) Top-view of the setup. b) General layout. c) At scale comparison between expected ion beam size at pinhole plane and pinhole separation. Dashed lines are a guide for the reader of the pinholes positions. $\Delta\alpha$ is the corresponding angular spacing between the pinholes.

contamination layer on the target rear surface by the TNSA mechanism. The analysis of the focal spot quality was performed with an automated script written by the Ph.D. candidate.

The TP spectrometer was carefully aligned so the central pinhole was exactly facing the interaction point in the normal direction of the target surface at a distance $L = 508\,\text{mm}$ from target to the entrance pinhole. The distance from the pinhole to the MCP detector was, $L' = 223.5\,\text{mm}$ and $L'/L = 0.44$ The electric field electrode plates were fed with a voltage difference of $U = 10000\,\text{V}$. A simple sketch of the setup is shown in figure 7.1.

The photons from the MCP phosphor screen were collected by an imaging system consisting of an objective (Nikon AF-S NIKKOR 18-105mm 1:3.5-5.6G ED) with adaptable focal length range of $18 - 105\,\text{mm}$ and a Blackfly PGE-23S6M-C CMOS optical camera of 1920×1200 pixels of $5.86\,\mu\text{m}$ lateral size. The system was set up to an ultimate magnification of 0.0854 at the detector plane ($14.57\,\text{pixels/mm}$), which was calibrated thanks to a laser machined pattern in the object plane, next to the MCP. Figure 7.2 shows the raw traces acquired in a single laser shot.

It is important to note that the source-to-detector distance L in the setup prepared is much larger than the source size s (typically few hundred of micrometers in diameter). The magnification of the pinhole-camera effect on the detector plane is barely enough to distinguish spatial effects of the source, therefore considering a point-like source for analysis means. The examined angles in this case are 0 and $\pm\alpha$, being $\alpha = \tan^{-1}(a/L) = 0.3°$, much smaller than the typical TNSA beam divergence angle ($\approx 40°$). The chosen distance source-detector L was the minimum that the given experimental configuration permitted.

In this geometrical configuration the crossing of traces from different pinholes are abundant and need to be processed (see fig. 7.2). Crossings produce peak artifacts in the spectrum readout due to intersections. To avoid the artifacts we have proceeded by identifying the species involved on each crossing event. If one works in pixel position vs pixel value space, the peaks produced by intersections are aligned in position for all the involved species and can be treated in the same basis. The intersection peaks were identified, located and eliminated from the raw data to later perform a linear interpolation between both edges of the gap left by extraction. All the intersections were identified but only the ones producing significant distortion were eliminated. Peak removal criterion was based

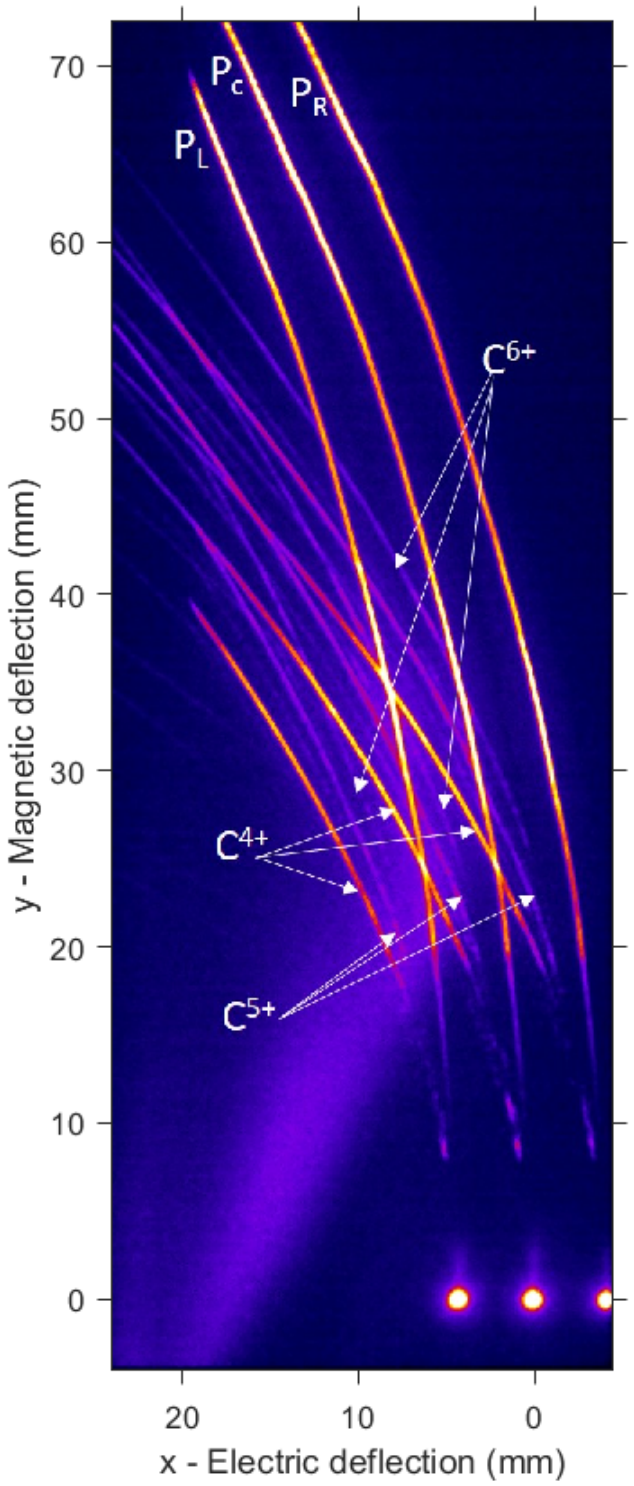

FIGURE 7.2: Multi-pinhole Thomson parabola traces obtained from a single laser shot at VEGA 3. The origin of the coordinate system corresponds to the zero-deflection point of the central beamlet. P_L, P_C and P_R point to the left, central and right proton traces respectively. C^{n+} indicate the three n-charged ion traces.

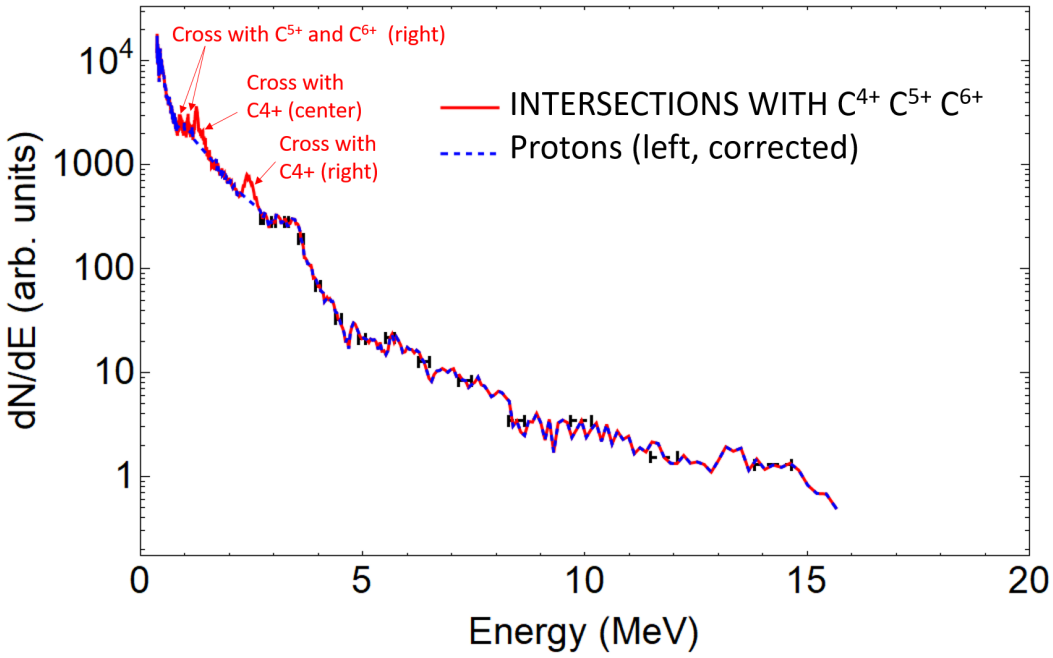

FIGURE 7.3: Left trace of proton spectrum in logarithmic scale. Blue: corrected spectrum. Red: same spectrum showing the peaks subtracted, corresponding to trace crosses. Several representative error bars (in black) are plotted picturing the estimated energy resolution.

on the persistence of the artifact after performing a gaussian smoothing over the data in pixel space. The convolved gaussian radius was set to 10 points as Fourier analysis of raw data revealed peaks of structures of sizes from 5 to 20 points. In this way both statistical variations and small structures up to 20 points are considered as noise and contribute to root mean square deviation (RMSD) value. The interpolated segments can be considered to follow the trend within variations according to this RMSD.

With the help of the particle tracker, expected impact positions onto the MCP as a function of the energy and ion q/m can be calculated. Therefore, spectrum retrieval is possible for each trace. A single beamlet proton spectrum is plotted in figure 7.3, together with the traces intersections signal peaks, which are considered measurement artifacts and removed. It shows the typical quasi-Maxwellian TNSA proton spectrum, with a cut-off energy close to 15 MeV. Figure 7.4 shows the three spectra retrieved from the three analysed proton traces. Figure 7.5 represents the three beamlets spectra of the C^{4+}. Finally, for sake of comparison, different ion species from the same pinhole are plotted in figure 7.6. The spectrum plots of figures 7.3, 7.4, 7.5 and 7.6 share the same (arbitrary) units, with a common noise level (i.e. cutoff detection limit) around 0.1 arb. units. The fluctuations in the determination of the cutoff (specially pronounced in figure 7.3) are related to the systematic measurement error. As expected, due to the small difference of the angles probed when compared to the typical TNSA beam divergence (around 40°), ion spectra of the same kind from different pinholes are similar to each other.

Future improvements of the detector are considered to overcome the actual limitations. An absolute charge calibration can be useful as a next step for detector refinement, by combining the use of the MCP with CR39 or RCF stacks [214], or possibly by testing the TP in a charge-controlled electrostatic particle accelerator. Such calibration would permit to estimate absolute spectra for each trace (i.e. retrieving charge/number of particles for each differential of energy, not in arbitrary units). From the results presented, it has also become clear that other limitation of the system is the parallel configuration of the electric dipole

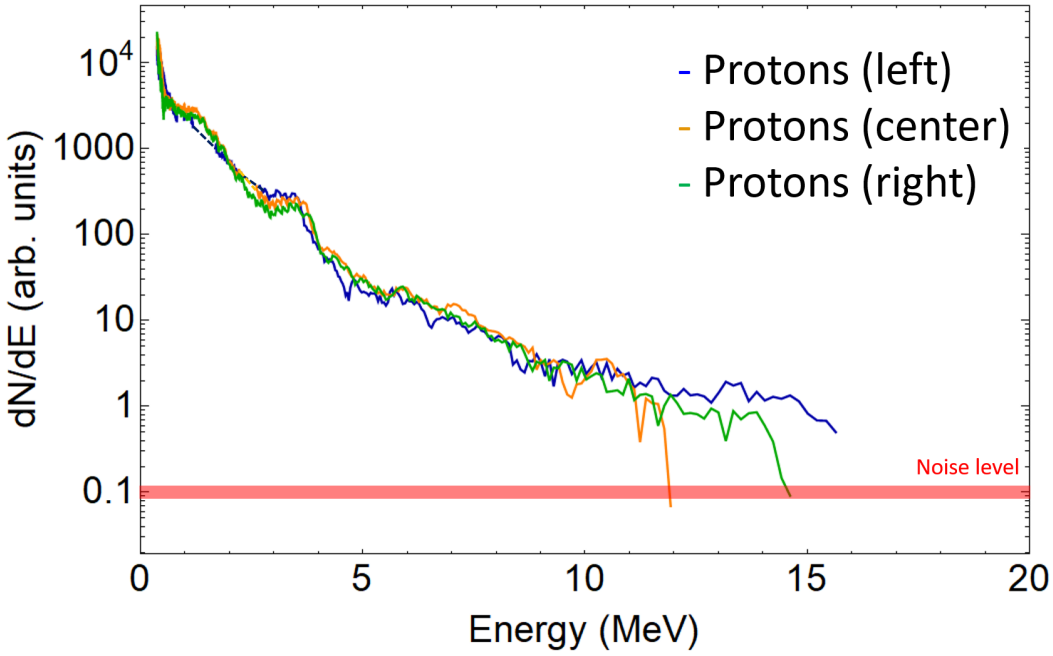

FIGURE 7.4: Left, center and right proton beamlets spectra in logarithmic scale. Dashed lines show the reconstructed spectrum range.

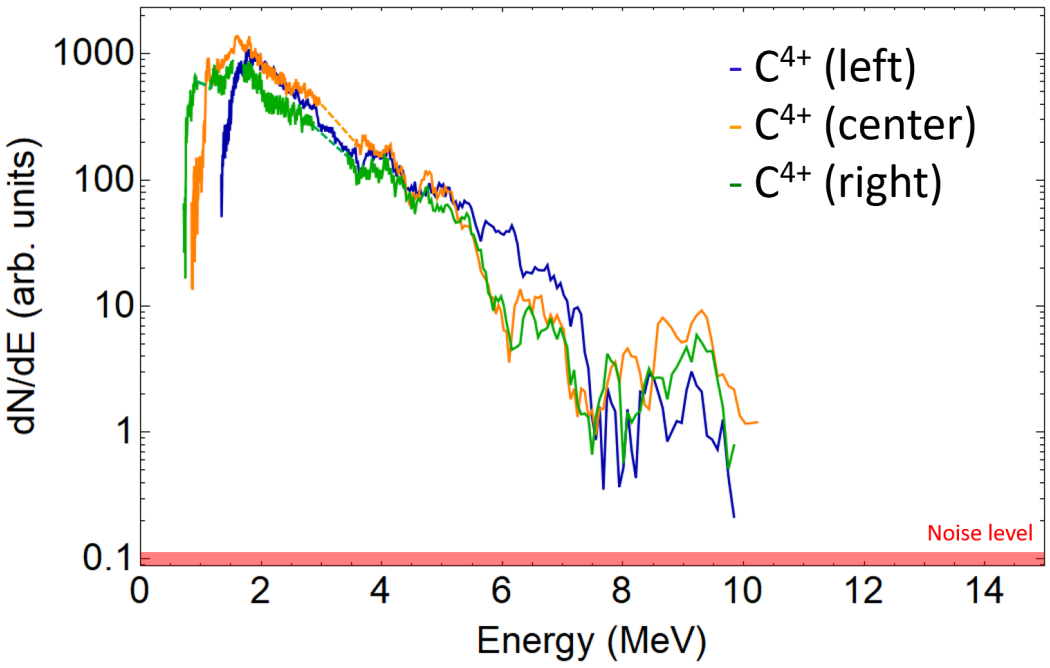

FIGURE 7.5: Left, center and right C^{4+} beamlets spectra in logarithmic scale. Dashed lines show the reconstructed spectrum range.

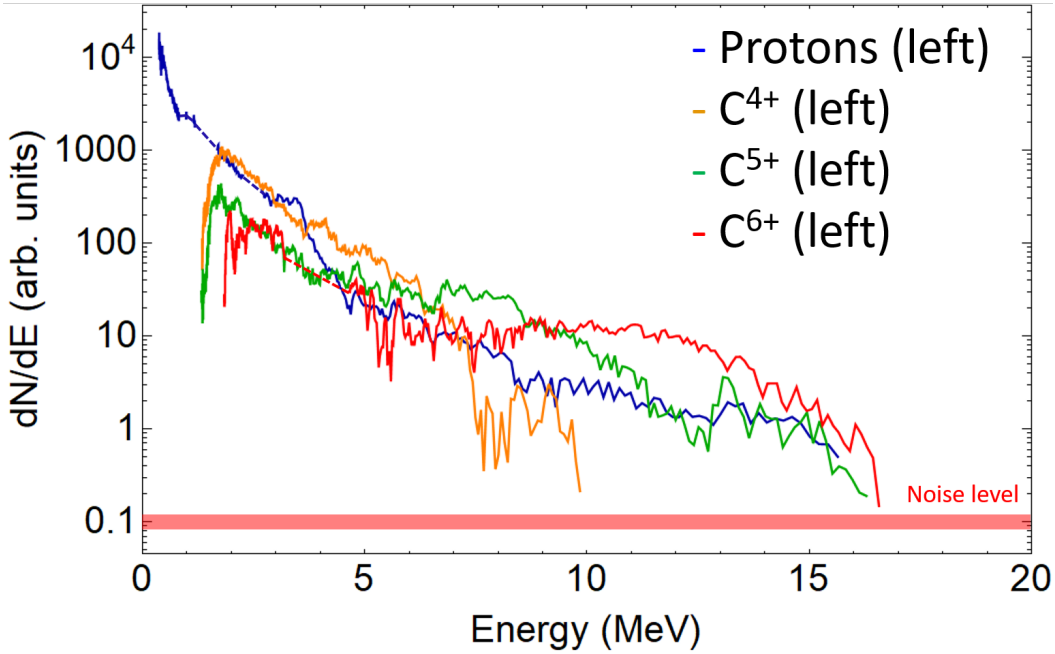

FIGURE 7.6: Left beamlets spectra for protons and C^{4+}, C^{5+} and C^{6+} ions in logarithmic scale. Dashed lines show the reconstructed spectrum range.

plates. The detector can be improved by adapting it into a wedged geometry (separation between the electrodes increases with ion path [216–218]), thus preventing low energy ions from colliding with the plates, especially pronounced for the ions of the less favourable (left) beamlet (for instance, see the lower energy part of the carbon spectra in figures 7.5 and 7.6.

On the other hand, the transformation of this device into an ion wide angle spectrometer (iWASP) [233] is easily achievable by switching off the plates electric potential (maintaining only the magnetic deflection) and replacing the pinhole array by an horizontal micrometer-wide slit.

Summarizing, a multi-pinhole TP which is able to retrieve ion spectra at different beam coordinates has been developed and tested. This device is backed by an analysis routine which is able to avoid measurement artifacts coming from the traces intersections at the detector. This fact brings great geometrical flexibility (and allows for inspection of a larger set of ion species, as they imply a greater number of traces on detector) when compared to previous similar works. Nevertheless, the analysis algorithm could be improved in a future work, not just by *removing* the cross event, but also trying to reconstruct the individual contribution of each trace and forcing their sum to be equal to the retrieved signal. This development is not trivial when the difference of signal levels between traces is as big as several orders of magnitude.

7.2 Emittance measurement

As mentioned in the chapter 3, the multi-pinhole TP can be converted to a energy-resolved emittance measurement device by just increasing the ratio L'/L . In the analogy with a pinhole camera it would correspond to increase its magnification. In the experimental configuration presented in the previous section, this can be simply achieved by bringing the TP closer to the interaction point.

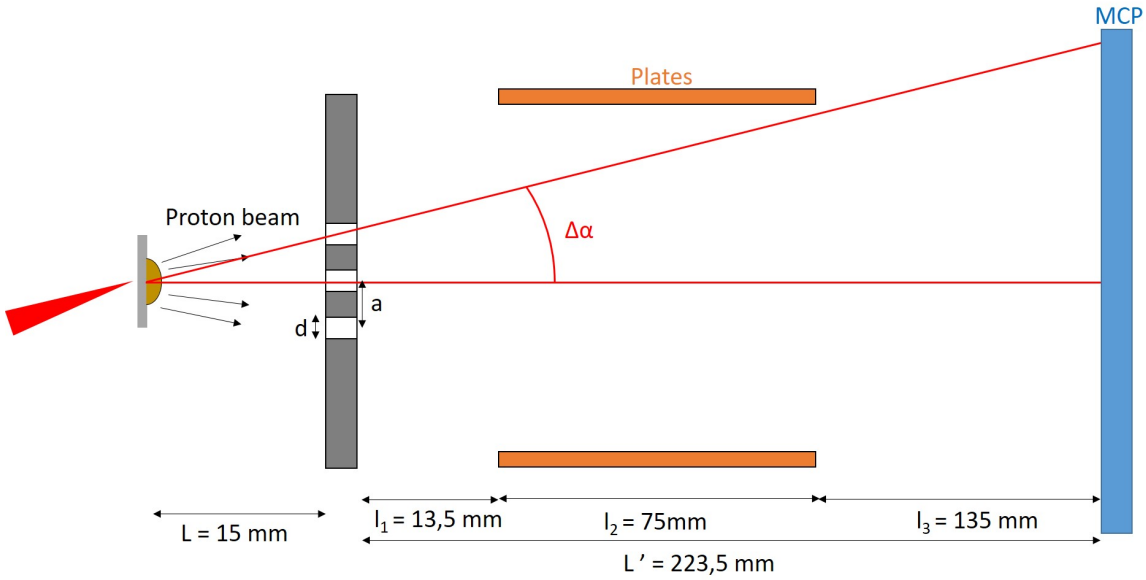

FIGURE 7.7: Detailed top-view sketch of the geometry of the beamlets trajectories in the Multi-Pinhole Thomson Parabola for emittance measurement.

7.2.1 $L'/L \sim 15$ and MCP as active detector

In the first attempt presented, the detector was brought as close as $L = 15$ mm to the interaction point, so $L'/L \approx 15$. The pinhole mask was accordingly modified to fit the new geometrical constrains, as the angular acceptance of the detector is defined by the pinhole mask, the electrical plates separation and the MCP width, as shown in figure 7.7. The tungsten mask of 500 µm thickness presented a 3-pinhole ($d = 100$ µm diameter) horizontal line with separation $a = 500$ µm. In such configuration, the difference between angles probed is $\Delta\alpha = 2°$, for a total horizontal angle spanned of $(3-1) \times 2° = 4°$. In this case, the ion beam was achieved by irradiation of a 3 µm-thick Al film by the VEGA 3 laser pulses (7.4 J on target, 206 fs) focused by the same F/11 OAP into a spot of 11 µm FWHM containing 23% of its energy, leading to an average intensity of 8×10^{18} W/cm^2 inside such a diameter. The angle of incidence was kept to 10°.

The new experimental configuration (L much shorter) had consequences on the rest of the setup. The imaging system of the laser focal spot (which is also used for aligning the targets at the interaction point prior to the experiment) had to be modified accordingly so it could leave enough room for the TP to be as close as needed. The first optic elements of such imaging system (an x10 microscope objective and a mirror) were displayed on a remote-controlled motorized stage (with two degrees of freedom in vertical and longitudinal axis) so when the detector is brought closer to TCC, it fits below the stage. On the other hand, the TP was mounted on a motorized platform with 3 degrees of freedom ($x - y - z$), so the distance TCC to detector L could be changed during the experiment to leave space to the imaging system when alignment is required. As will be explained below, the movement freedom allowed measuring the beam at different angles. A simplified sketch of the experimental setup can be found in figure 7.8. The basic operation components of the experiments are shown in the photograph of the figure 7.9. As can be seen in the photography, a flexible light shielding tube was added between the MCP and the view-port of the imaging system of the traces, whose goal was to reduce stray light arriving into the recording scientific camera.

The electric field plate voltage was set at $U = 5000$ V for the case shown. The MCP imaging system focal distance was modified for matching the new distance between CMOS and

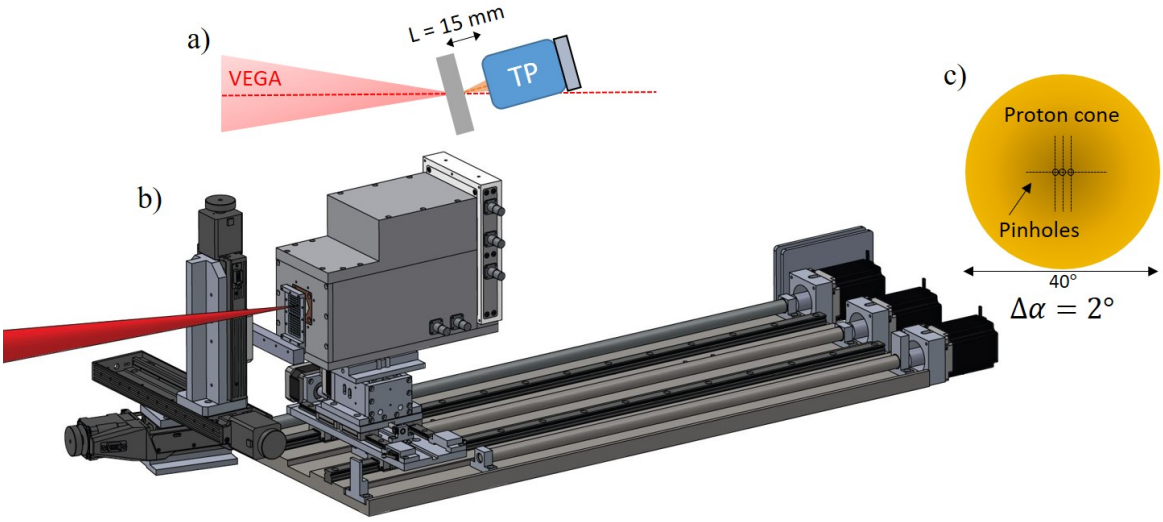

FIGURE 7.8: Sketch of the VEGA 3 laser-driven ion beam emittance measurement experiment with MCP as detector. a) Top-view of the setup. b) General layout. c) Comparison between expected ion beam size at pinhole plane and pinhole separation. Dashed lines are a guide for the reader of the pinholes positions. $\Delta\alpha$ is the corresponding angular spacing between the pinholes.

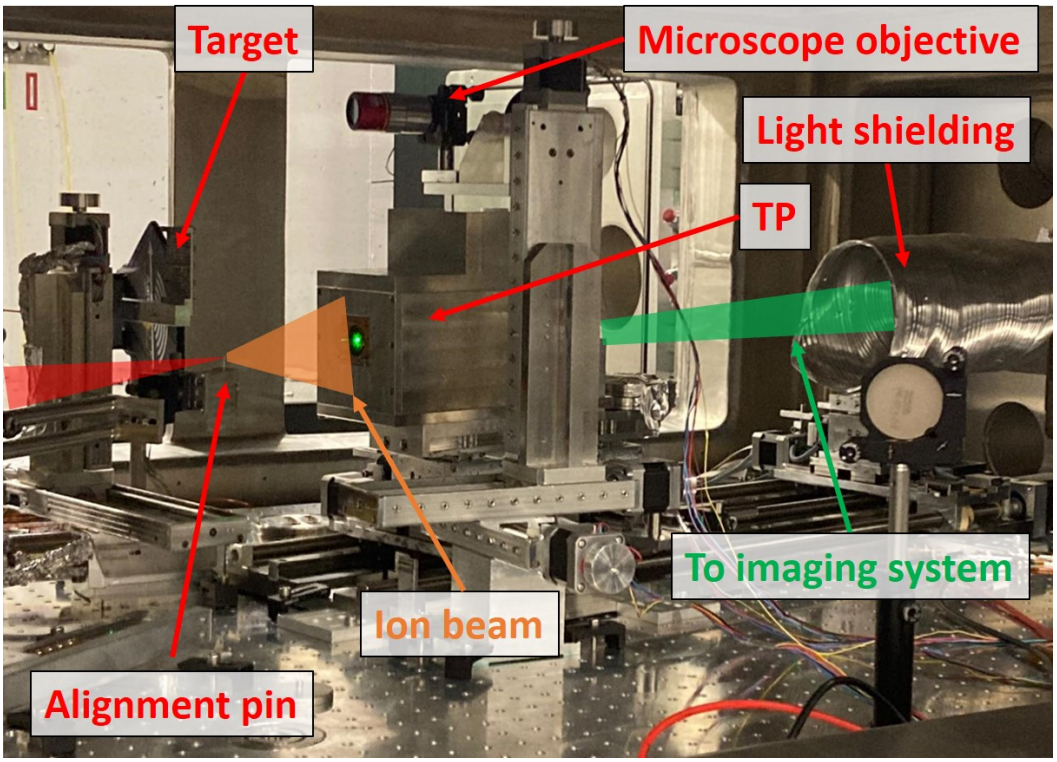

FIGURE 7.9: Picture of the experimental setup during alignment phase.

measured object, leading to a spatial calibration of 116 μm/pixel. When performing a high-power laser and solid interaction experiment so close to the instrumentation precautions should be taken. An aluminized Mylar foil (400 nm Al + 2 μm Mylar) was used to cover and protect the MCP from optical light and debris. An extra 3 μm Al filter was placed in the bottom of the MCP to cover the no-deflection point, were presumably the damage could be more severe. The resulting ion traces are shown in figure 7.10.

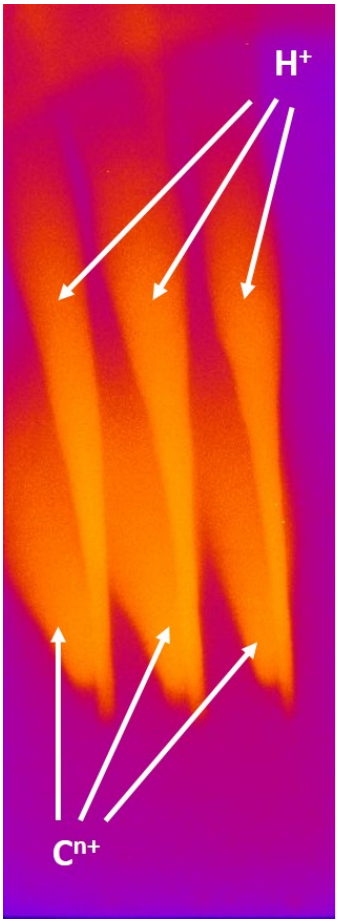

FIGURE 7.10: Multi-pinhole TP traces for $L'/L = 15$ and MCP as detector. Parabolas reference points were not observable due to the extra filters placed in front of the detector.

As expected, thanks to the magnification enhancement, the traces are thicker than in the previous case, which can be interpreted as an increase of the measurement accuracy of the beamlets divergence. This can be also understood because the beam is measured at a plane where the beam is much smaller than in the previous case. When comparing beam and pinhole sizes, it is possible to realize that many more particle trajectories are allowed to cross the mask and arrive to the detector. Indeed, an energy-dependent trace thickness variation is observed for all traces. The immediate drawback of the new setup is the increase of the point spread function (PSF) of the trace signals. The PSF describes the minimum size that the system can measure. For instance, in optics the PSF defines how a single point object is spread on the image after an imaging system). In the case considered, by analogy with a pinhole camera, the PSF can be given as the angle subtended under the pinhole diameter from the target position. The projection at the detector plane gives a minimum signal size of $\delta_{min} = (1 + L'/L)d$. This is also translated into a worsening of the spectral resolution of the instrument, as the energy resolution is directly related to the spatial one.

L (mm)	L′ (mm)	L′/L	δ_{min} (mm)	ΔE^+ (MeV)	ΔE^- (MeV)	$\Delta\theta \approx$ d/L (mrad)
508	223.5	0.44	0.144	0.12	0.12	0.2
45	223.5	5	0.6	0.50	0.47	2.2
15	223.5	15	1.6	1.43	1.18	6.7
15	375.5	25	2.6	1.20	1.01	6.7

TABLE 7.1: For different geometrical configurations of the multi-pinhole TP operation, minimum trace thickness possible (δ_{min}), error in energy measurement due to vertical energies mixing due to vertical size of pinholes (ΔE) at 10 MeV and minimum beamlet angle possible ($\Delta\theta$, i.e. angle subtended under pinhole diameter). Note that ΔE is asymmetric due to non-linear relation between vertical position and energy at the detector plane.

See Table 7.1 for specific values of PSF and energy measurement error for some specific (relevant) setup geometries (third row shows the parameters for this setup).

Furthermore, another non-desired effect appears which is clearly visible in figure 7.10. The traces are thick enough that the overlap with each other. The carbon species are impossible to distinguish and overlap in space with the proton ones; this fact makes the analysis of both protons and carbon traces virtually unfeasible. This problem could be addressed in several different ways. One possible solution is to increase the separation between the pinholes. Nevertheless, this should be followed by an increase of the gap between the electrical plates and increase of the MCP width, which is not straightforward.

7.2.2 $L'/L \sim 5$ and MCP as active detector

The signal overlapping problem can be solved if a part of the instrument spatial resolution is sacrificed, increasing L to a compromise value. In the second attempt shown here, L was increased to 45 mm yielding a magnification around $L'/L \approx 5$. The mask was replaced for a more flexible choice: a line of 7 pinholes of diameter of $d = 100$ µm separated by $a = 1$ mm. The separation between the pinholes was calculated so the traces are separated enough at the detector plane. On the other hand, the beamlets of the extreme pinholes will be outside the detector acceptance, as they collide with the electrical plates or simply outside the MCP, as it can be clearly seen in figure 7.11. Geometrical details are given in the table 7.1 (second row). In this case, the extra filter in the bottom of the MCP was removed so the parabola reference points could be detected. The signal detected evidence 5 different traces (two of them partially blocked or outside the detector area). The experimental conditions of this shot were similar to the previous case: VEGA 3 focal laser pulse of energy 3.5 J and duration of 140 fs were focalized on a spot of 12 µm FWHM, with averaged intensity of 4.6×10^{18} W/cm^2 on a Al foil of 6 µm of thickness. The TP voltage was 5000 V. The signal shows proton and carbon traces being clearly differentiated now, but the carbon ions still overlap with each other.

7.2.3 BC-400 scintillator as active detector

The search for a larger particle imaging magnification, wider angle spanned and better resolution (besides the fact that the MCP was not available at this point of the experimental campaign anymore) were the reasons after changing the active detector of the device. It was decided to use a 85 × 60 mm 1.5 mm-thick BC-400 plastic scintillator [211]. Plastic scintillators are cheap compared to MCPs and can be cut in pieces as large as desired, which eliminate the acceptance limitation of the MCP; the only restriction is then the electric field

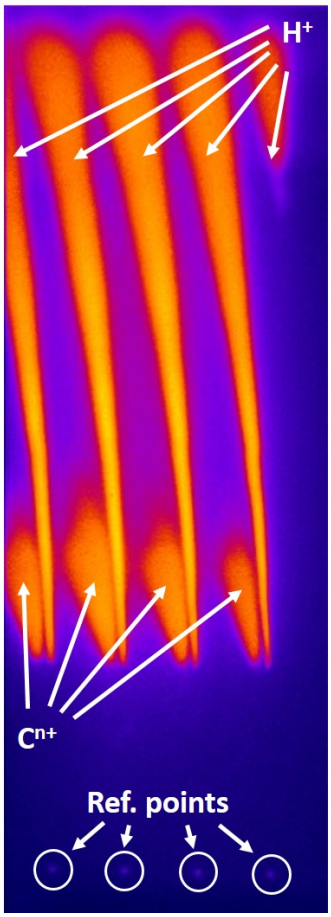

FIGURE 7.11: Multi-pinhole TP traces for $L'/L = 5$ and MCP as detector.

plate separation. Nevertheless, the main drawback about plastic scintillators are their photon response. The photon yield of the scintillator (which were collected afterwards by the same imaging system used for the MCP) is much lower than the MCP one, and it cannot be enhanced electronically as it is possible with the MCP via its bias voltage. As for the MCP, in order to calculate the energy spectrum from a trace, the scintillator response should be calibrated. The relation between number of ions that impact in the scintillator and the corresponding photon conversion is not straightforward, as it depends on the energy deposition function, which is as well a function of the ion energy.

In this test, the TP was brought back closer to TCC with $L = 15\,\text{mm}$. In order to have maximum flexibility but still enough separation between traces, a new mask of 13 pinholes in line of diameter $d = 100\,\mu\text{m}$ and separation $a = 500\,\mu\text{m}$ was used. As in the previous case, the central beamlets will impact on the detector, meanwhile the ones in the borders are stopped at the electrical plates. In this geometry, the difference between the beamlets angles probed is $\Delta\alpha = 2°$, with 4 visible traces, therefore a total horizontal angle spanned of $(4-1)\times 2° = 6°$.

On the other hand, the scintillator was mounted on a motorized stage independent of the TP motion control. This fact gives the possibility of in-vacuum lateral and vertical alignment of the detector with respect to the pinholes, and more importantly, capability to change the distance l_3 (i.e changing L') by an amount $\Delta L'$; this means changing the free flight distance of the particles and therefore change the PSF, magnification and instrument resolution. The two configurations shown in this section are $L' = 223.5\,\text{mm}$ (same as in other cases, yielding $L'/L \approx 15$) and $L' = 379.5\,\text{mm}$, which gives $L'/L \approx 25$. All the

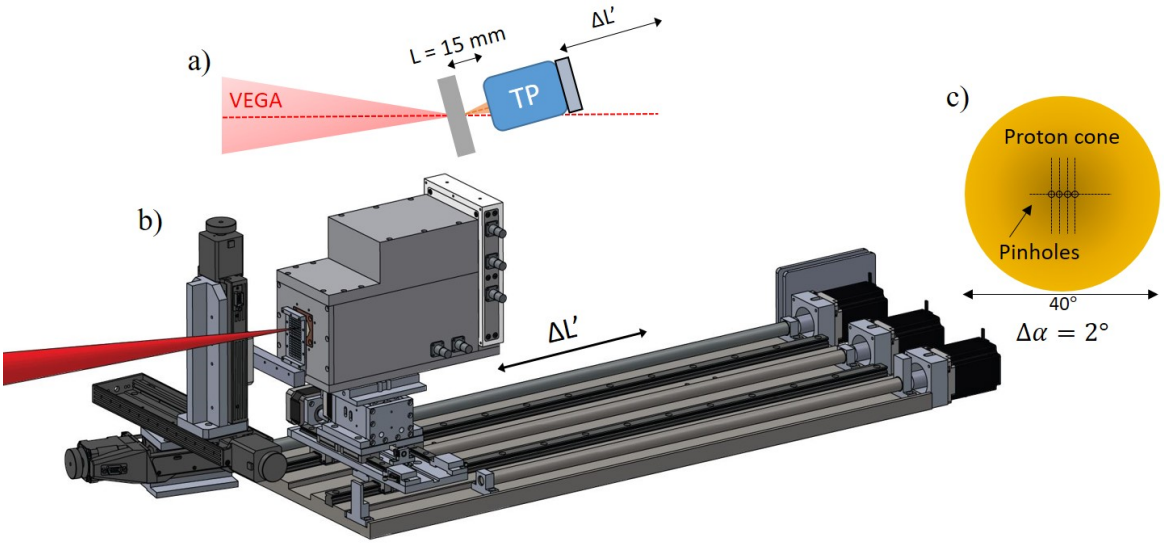

FIGURE 7.12: Sketch of the VEGA 3 laser-driven ion beam emittance measurement experiment using a scintillator foil as active detector. a) Top-view of the setup. b) Simplified layout (the MCP was substituted by a sctintillating screen). c) Comparison between expected ion beam size at pinhole plane and pinhole separation. Dashed lines are a guide for the reader of the pinholes positions. $\Delta\alpha$ is the corresponding angular spacing between the pinholes.

geometrical conditions and related resolutions are summarized in the table 7.1 (third and fourth rows). The experimental setup is depicted in figure 7.12.

More precautions were needed for the proper operation of the BC-400. These scintillators are transparent to optical light, requiring therefore some kind of optical protection on the side facing the laser. A 12 µm-thick black-dyed polycarbonate (Pokalon®) opaque foil was chosen for light shielding. Monte-Carlo simulation with the help of the code MCNP6 [254] were carried out in order to estimate the ion transmission through such filter and the expected deposition in the plastic scintillator. Details of the simulations are given in Appendix B. The main conclusion after these calculations are that the expected proton spectrum is fully detectable with this configuration, meanwhile only high energy Carbon ions ($>$ 10MeV) will be detected. This fact was experimentally confirmed; performing the TNSA experiment with this configuration and the electric field of the TP active, only proton traces were measured. Pure proton detection simplifies enormously the data analysis: no trace overlapping occurs and ion species discrimination is no longer necessary, so the electric field can be turned off. For the rest of the experiment only magnetic deviation was applied. In order to maximize the signal response of the parabolas reference point, a scintillating Lanex screen [243], which is highly sensitive to X-rays, was placed in the bottom part of the detector plane, right below the BC-400 layer.

The resulting signals are shown in figure 7.13. For both cases shown (with two different magnifications), the laser-plasma conditions were identical, the 21.6 J, 240-fs long laser pulses were focused onto the front surface of a 6 µm-thick Al foil in a spot of 16.7 µm FWHM, resulting in an average intensity of 1.8×10^{19} W/cm^2 inside the FWHM. The angle of incidence of VEGA onto the target was 10° as well. The imaging system collecting the scintillator photons was rearranged for both detector positions.

The signal show vertical traces (the magnetic deviation direction) with very sharp edges. There is a clear difference in the shape of the trace at different vertical coordinates (i.e.

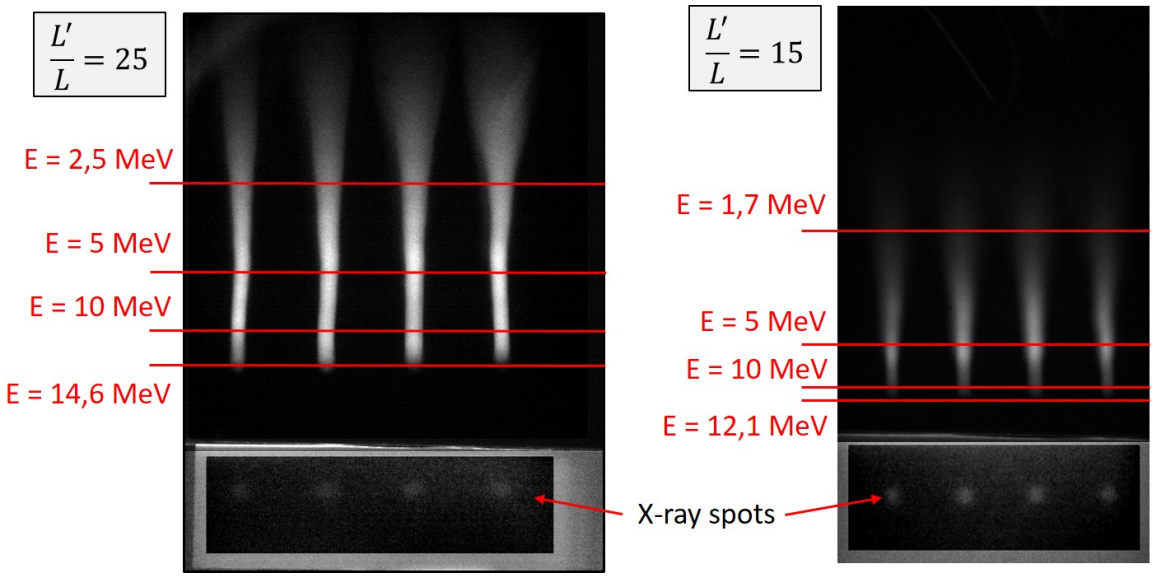

FIGURE 7.13: Proton traces obtained with scintillator as active detector. The contrast of the reference points (X-ray spots), detected in a Lanex screen, is enhanced for visualization purposes. Four representative energies for each shot are outlined with red lines: the cut-off energy of each shot, 10 MeV, 5 MeV and the signal's mean energy.

energies), which encodes energy-resolved beam quality information. A horizontal lineout at a fixed energy is a direct measurement of the divergence of the four beamlets at this energy. This information, because of its constant energy, is independent of the scintillator energy-dependent response, so the calibration is not needed for the moment. When plotting a horizontal lineout (in divergence units) in the coordinate system (x, x') the result is a measurement of the beam trace space at that energy, as it was shown in Chapter 3. The resulting trace spaces for each shot and for four specific energies are shown in figures 7.14 ($L'/L \approx 25$) and 7.15 ($L'/L \approx 15$). The spatial coordinate where each lineout is plotted corresponds to the pinhole locations. The divergence lineouts shown are not the raw data but they are the deconvolution of the raw functions with a square function of thickness δ_{min} (the corresponding pinhole projection or PSF), therefore accounting for the effect of the non-infinitely small pinhole size at the data reconstruction. The deconvolution was carried out using an algorithm integrated in Wolfram Mathematica code based on the Richardson-Lucy method [255, 256]. Note that for all cases, it was checked that the signal thickness is larger than the $\delta_{\min}$. The RMS beamlet divergence values σ'_i given at the insets of figures 7.14 and 7.15 are calculated from the deconvoluted function.

Trace-space plots are powerful beam dynamics diagrams and plenty of information about the transversal beam quality can be retrieved. Specifically, each term of the equation for the RMS lateral emittance 4.26 can be obtained from the trace-space. The resulting geometrical emittance values are shown in figure 7.16. A more detailed interpretation of the estimation can be done if the terms of the equation are consider separately, following the formulae given in Chapter 3. First of all, the first statistical moments of the distribution $\langle x \rangle$ and $\langle x' \rangle$ (i.e. the main beam position and pointing) are shown in figures 7.17a and 7.17b. From the first figure it is possible to conclude that the beam is relatively well aligned in the middle position of the 4 pinholes; particle counts contribute symmetrically in both sides (negative and positive space numbers) for all energies and it is possible to interpret that the beam is centred in the detector mask. On the other hand, a very interesting conclusion can be seen when observing the pointing. A clear trend towards the laser axis direction is

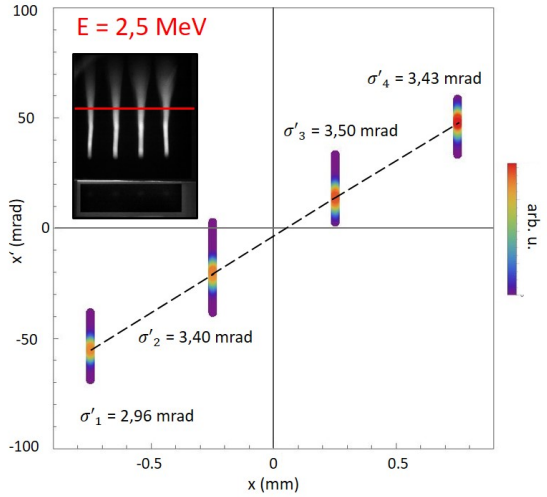

(A) Trace space for the mean energy 2.5 MeV.

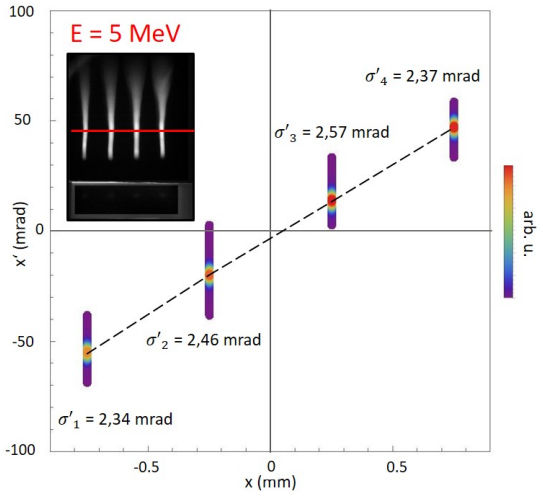

(B) Trace space at 5 MeV.

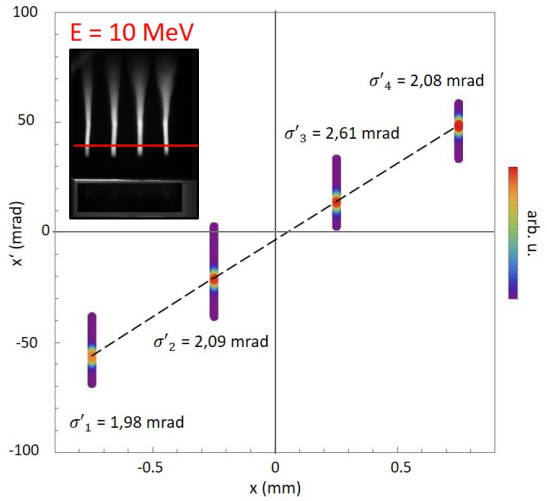

(C) Trace space at 10 MeV.

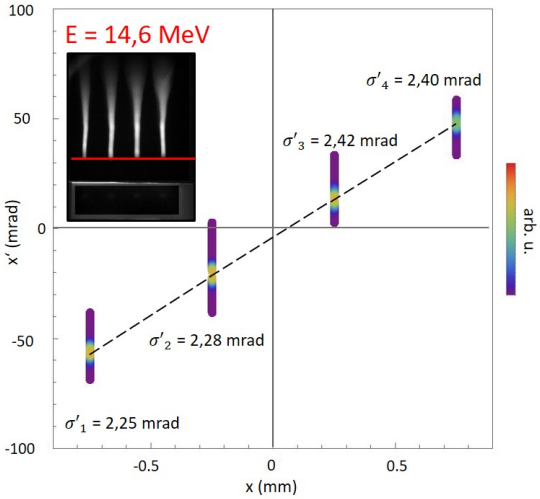

(D) Trace space for cutoff energy 14.6 MeV.

FIGURE 7.14: Trace space for 4 different energies for the shot with $L'/L \approx 25$. Insets point the corresponding lineout of each energy directly overlaid over the raw data pictures. Text close to each lineout represent the RMS size (in mrad) of each beamlet. Dashed lines connect the centres of the lineouts.

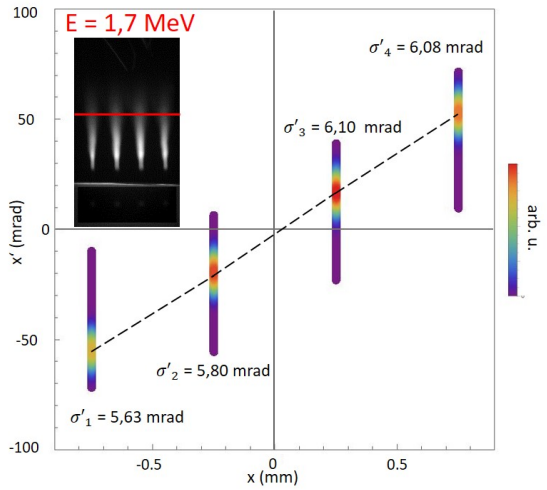

(A) Trace space for the mean energy 1.7 MeV.

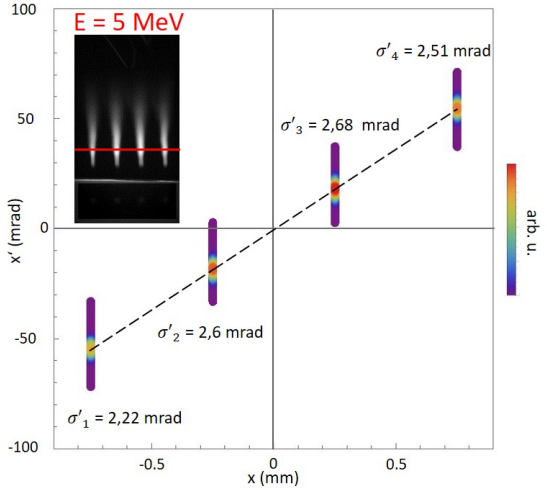

(B) Trace space at 5 MeV.

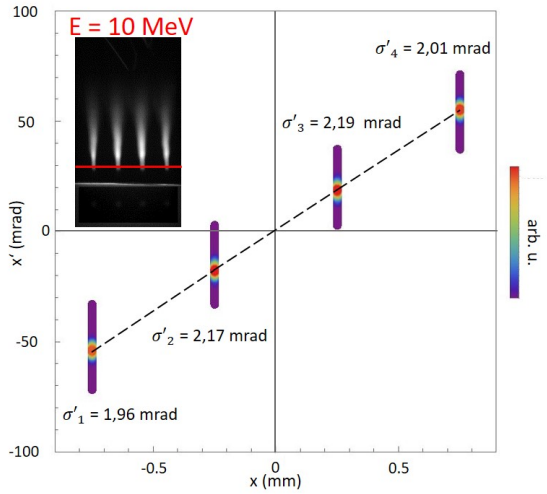

(C) Trace space at 10 MeV.

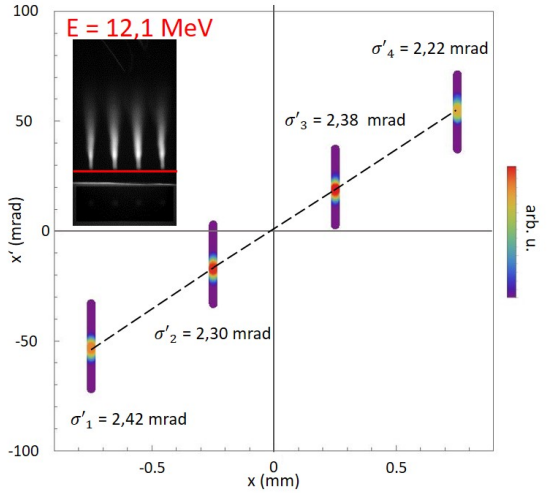

(D) Trace space for cutoff energy 12.1 MeV.

FIGURE 7.15: Trace space for 4 different energies for the shot with $L'/L \approx 15$. Insets point the corresponding lineout of each energy directly overlaid over the raw data pictures. Text close to each lineout represent the RMS size (in mrad) of each beamlet. Dashed lines connect the centres of the lineouts.

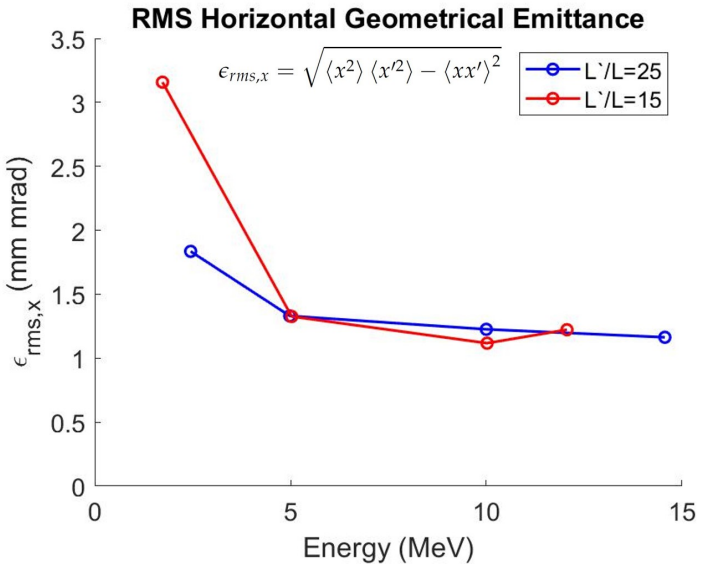

FIGURE 7.16: Horizontal RMS geometrical emittance $\epsilon_{rms,x}$ for both shots ($L'/L = 25$ in blue and $L'/L = 15$ in red) analysed at some illustrative energies. Inset shows the formulae for the emittance. Its definition is detailed in equation 4.26.

seen for larger energies. This is actually an expected effect as it is reported in the literature. The deviation towards the laser axis of the more energetic part of laser-driven proton beam has been demonstrated and its has been attributed to laser-phase shaping or prepulse effects [257–259]. The maximum deviation measured (10 mrad $\sim 0.6°$) is $\sim$ 5% of the angle between target normal and laser axis.

The second order moments of the particle distribution $\sigma_x = \sqrt{\langle x^2 \rangle}$ and $\sigma_{x'} = \sqrt{\langle x'^2 \rangle}$ (this is from the 4 beamlets combined) are shown in figure 7.18. With a significant number of pinholes (beamlets) spanning the full diameter of the beam, these quantities would stand for the energy-resolved RMS horizontal beam size and divergence. In any case, despite taking into account only four probing beamlets, from both figures a trend is observable: higher energies are concentrated in the center of the beam. In the divergence plot 7.17b beam pinching is also observed at 5 MeV.

Further analysis can be carried out in order to find out which term contributes the most to the total emittance of the beam. Figure 7.19 shows the mean values of the beamlets pointing $\langle x'_i \rangle$ (the mean value of the divergence lineouts) at different energies for both analysed shots. It is clear that the trace space shows an almost perfect linear correlation for all the energies and therefore it is expected that most of the contribution to the emittance comes from the trace space particle distribution area.

Moreover, the variance and covariance terms can be compared. In figure 7.20, $\sqrt{\langle x^2 \rangle \langle x'^2 \rangle}$ and $\langle xx' \rangle$ are shown for both cases.

After a detailed analysis of the contribution of each term to the emittance from the previous graphs, one can deduce that the larger contribution comes from the intrinsic divergence of the beamlets. This means that the emittance of the beam is driven by the non-zero area of the particle distribution at the trace space (which is related to the beamlet divergence) rather than a non-linear relation of the trace-space coordinates. This fact is straightforwardly confirmed when comparing the emittance and mean beamlet divergence ($\langle \sigma' \rangle = (1/N) \sum_i^p n_i \sigma'_i$) plots (see figures 7.21a and 7.21b). Indeed, both graphs share a common trend. This can be more accurately demonstrated if comparing the exact emittance

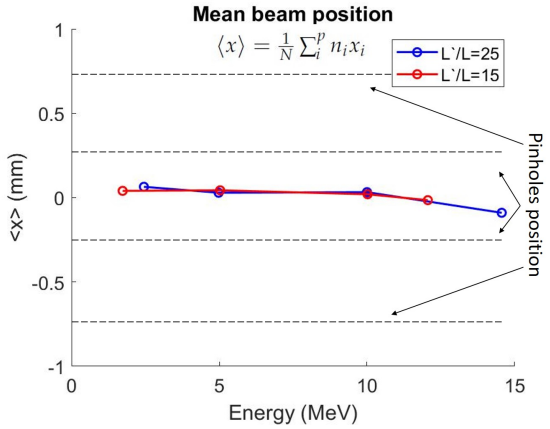

(A) Mean beam position. Dashed lines show the pinholes locations.

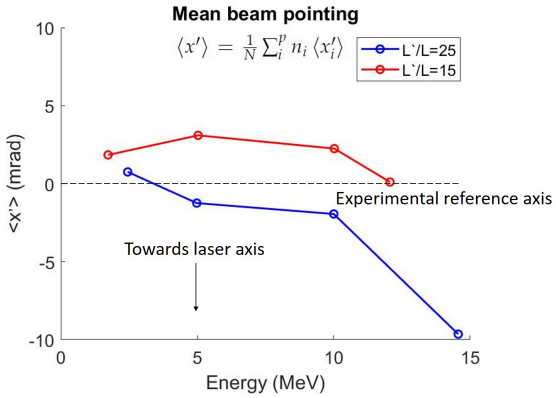

(B) Mean laser pointing. Dashed line show the predefined alignment axis of the TP.

FIGURE 7.17: Energy resolved mean beam position and pointing estimated from trace-space measurement. Insets show the formulae of each term. Their definition is explained in equation 4.26. Blue lines: dataset with $L'/L = 25$. Red lines: dataset with $L'/L = 15$.

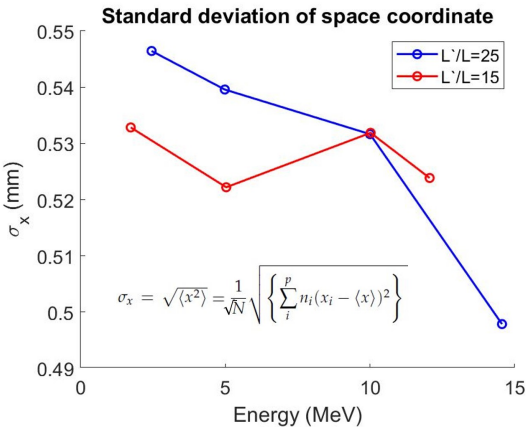

(A) Energy resolved standard deviation of x. Representation of the RMS size of the beam at the pinhole mask plane.

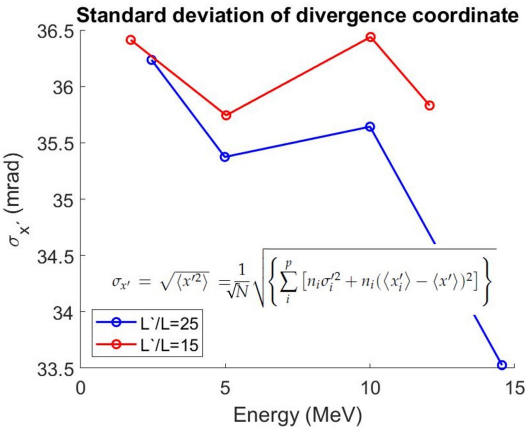

(B) Energy resolved standard deviation of x'. Representation of the RMS beam divergence at the pinhole mask plane.

FIGURE 7.18: Measured second order moments of the particle distribution measured with the multi-pinhole TP. Insets show the formulae of each term. Their definition is explained in equation 4.26. Blue lines: dataset with $L'/L = 25$. Red lines: dataset with $L'/L = 15$.

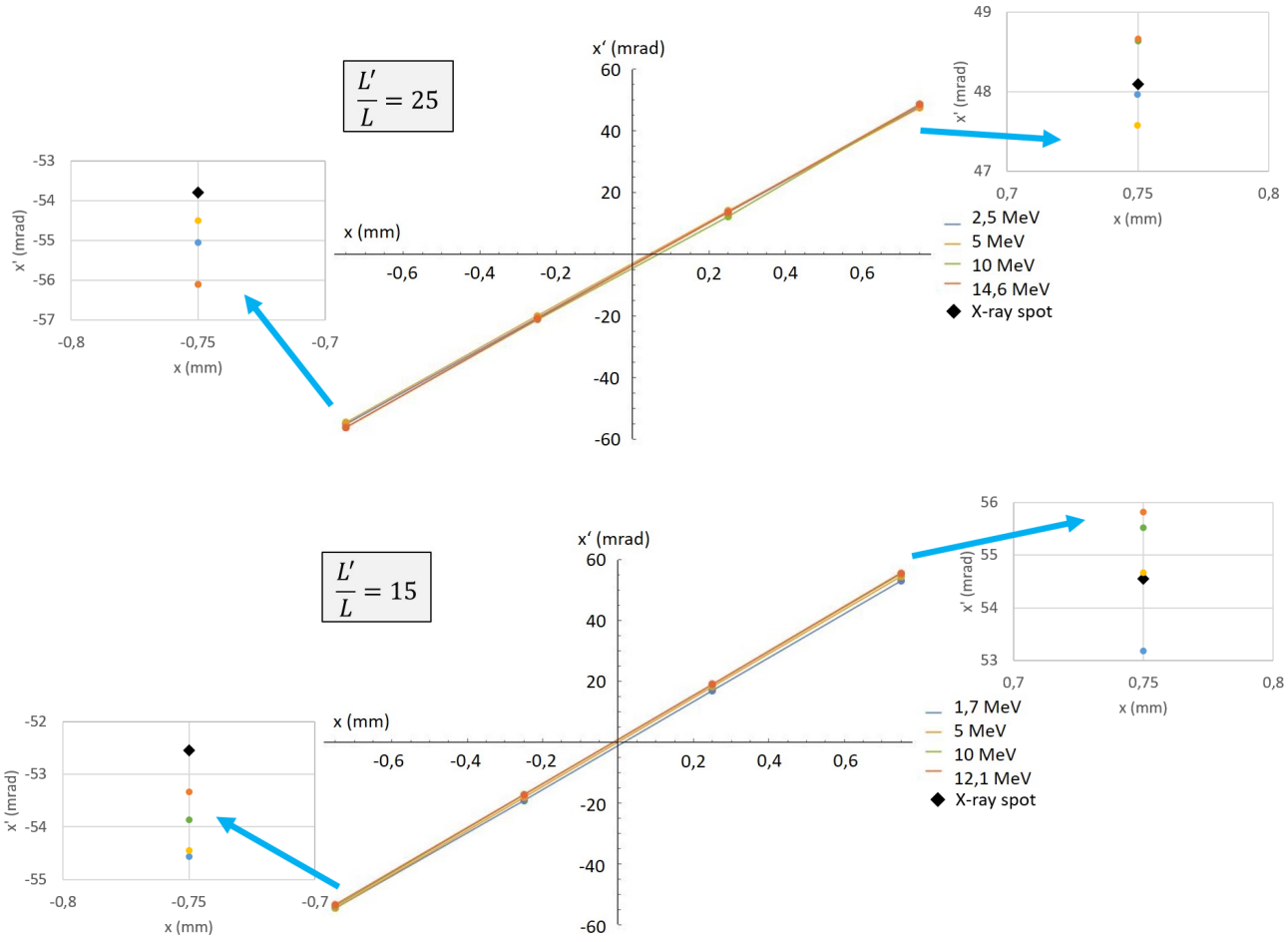

FIGURE 7.19: Representation of the mean divergence values of each beamlet lineout $\langle x'_i \rangle$ (i.e. the trace centroids) in the trace space for both experimental configurations (upper plot: dataset with $L'/L = 25$, bottom plot: dataset with $L'/L = 15$). Insets detail the centroids value for the extreme beamlets.

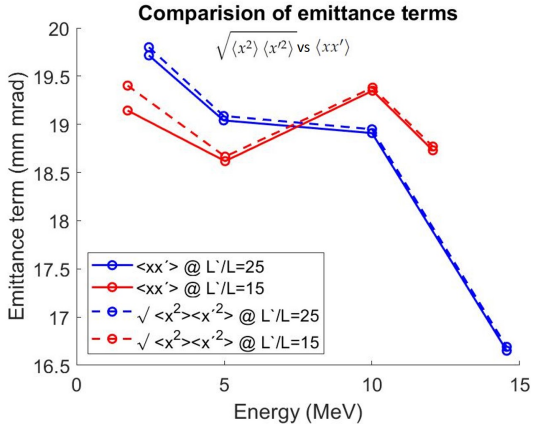

(A) Plot of the covariance term of the emittance $\langle xx' \rangle$ (solid lines) and the variance term $\sigma_x \sigma'_x = \sqrt{\langle x^2 \rangle \langle x'^2 \rangle}$ (dashed lines).

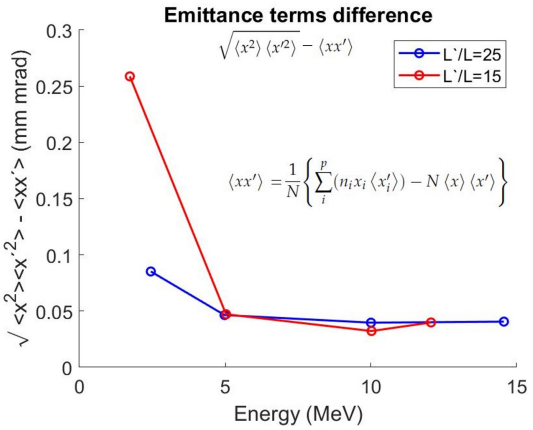

(B) Plot of the difference between the variance ($\sigma_x \sigma'_x$) and covariance ($\langle xx' \rangle$) terms contributing to the beam emittance.

FIGURE 7.20: Plots of the terms contributing to the emittance (A) and their difference (B) versus the energy for both datasets (blue lines: dataset with $L'/L = 25$, red lines: dataset with $L'/L = 15$). Inset of (B) shows the expression for the covariance term (whose parameters can be found in equation 4.26). The variance term is the product of the plots in figures 7.18a and 7.18b.

values and the emittance calculated with approximated form

$$\epsilon_{approx} = \sqrt{\langle x^2 \rangle \langle x'^2 \rangle_{approx}} = \frac{1}{N} \sqrt{\left\{ \sum_i^p n_i (x_i - \langle x \rangle)^2 \right\} \left\{ \sum_i^p n_i \sigma_i'^2 \right\}}, \tag{7.1}$$

which only takes into account the beamlet divergence contribution (see 7.21b). As expected, the values do not differ much from the exact formula. On the other hand, in figure 7.21a for the first time in this analysis error bars considered. Horizontal error bars correspond to the energy resolution given by the magnetic deflection and the minimum trace size δ_{min} due to the pinhole size. Vertical error bars represent the systematic angular error of the system (0.2 mrad for $L'/L = 25$ and 0.34 mrad for $L'/L = 15$). Considering that the emittance values for the approximated formula are similar to the exact one, it is a good approximation to propagate the error of the emittance following the formula 7.1. In such way, the complete plot of energy resolved emittance values is achieved, including error bars, which is shown in figure 7.22.

The main conclusion coming from figure 7.22 is that there is a pronounced trend towards lower geometrical emittance at higher energies. A finer graph could be obtained if further energies are analysed. In order to compare with previous results in the literature, the normalized emittance should be calculated (using equation 3.196). For non-relativistic particles as the laser-driven protons ($\gamma \sim 1$), it is enough to multiply the geometrical emittance valued by $\beta = v/c$. Results are shown in figure 7.23. The graph of the normalized emittance for different energies flattens compared with the geometrical emittance values.

A summary of the results obtained is shown in the table 7.2. Comparison with previous results found in the literature is also given. All values are represented in figure 7.24. Firstly, note that the normalized emittance values obtained are comparable with the results found in the literature, although the decreasing trend with increasing energy is not so pronounced for this work. Secondly, an outstanding emittance measurement precision is achieved with this method, with relative errors below 10 %. Finally, the coarse energy resolution of the previous works is limited due to the kind of detector used (stacks of RCF), meanwhile the

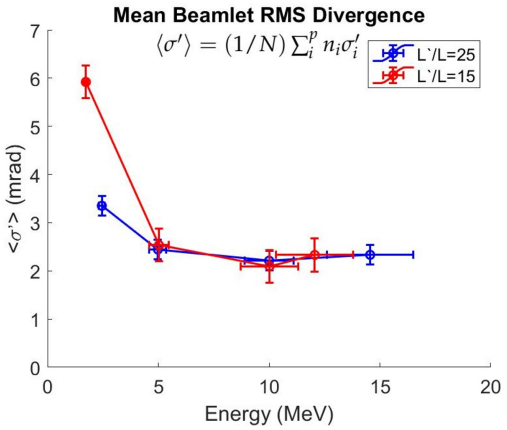

(A) Energy-resolved plot of the mean value of the RMS divergence of the beamlets. Inset shows the formula for the mean divergence, where σ_i' is the rms trace divergence of the i-th beamlet.

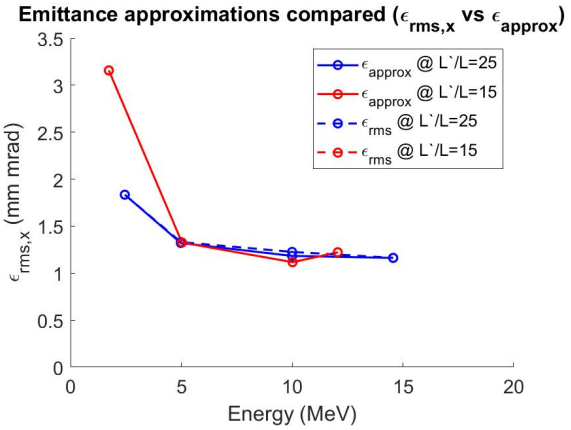

(B) Plot of the emittance values calculated with the approximation formula 7.1 (solid line) and with the exact formula 4.26 (dashed line) versus proton energy.

FIGURE 7.21: Plots of beamlet divergence and emittance values. Blue lines: dataset with $L'/L = 25$. Red lines: dataset with $L'/L = 15$. From the similarity of both graphs, it follows that the main contribution to the emittance is the intrinsic beamlet divergence.

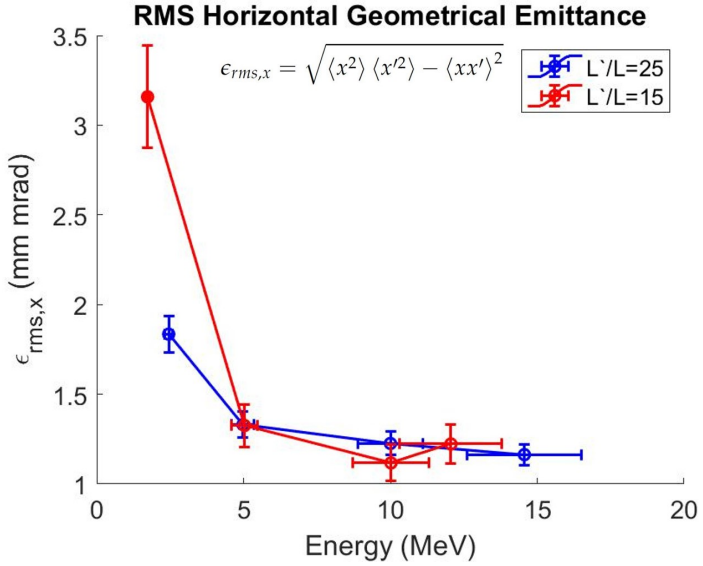

FIGURE 7.22: Horizontal RMS geometrical emittance $\epsilon_{rms,x}$ for both shots ($L'/L = 25$ in blue and $L'/L = 15$ in red) versus proton energy, including vertical error bars, derived from the emittance approximate form of 7.1, and horizontal error bars representing the spectrometer energy resolution. Inset shows the formula for the geometrical emittance.

This work ($\tau = 240$ fs)					
$L'/L = 25$			$L'/L = 15$		
E (MeV)	ϵ (mm mrad)	ϵ_N (mm mrad)	E (MeV)	ϵ (mm mrad)	ϵ_N (mm mrad)
2.5±0.1	1.8±0.1	0.13±0.01	$1.73^{+0.09}_{-0.08}$	3.1±0.3	0.19±0.02
5.0±0.4	1.33±0.07	0.14±0.01	$5^{+0.5}_{-0.4}$	1.3±0.1	0.14±0.02
10±1	1.23±0.07	0.18±0.02	10±1	1.1±0.1	0.16±0.03
15±2	1.16±0.06	0.20±0.02	12±2	1.2±0.1	0.20± 0.03
Borghesi et. al. [35] ($\tau = 100$ fs)			**Cowan et. al.** [29] ($\tau = 850$ fs)		
E (MeV)	ϵ_N (mm mrad)		E (MeV)	ϵ_N (mm mrad)	
-	-		7	<0.015	
-	-		9	<0.008	
15	0.3		10	<0.004	
Ter-Avestiyan et. al. [238] ($\tau = 30$ fs)			**Wu et. al.** [239] ($\tau = 30$ fs)		
E (MeV)	ϵ_N (mm mrad)		E (MeV)	ϵ_N (mm mrad)	
Nürnberg et. al. [34]					
E (MeV)	ϵ_N (mm mrad)		Facility		
1.2	0.063		PHELIX ($\tau = 580$ fs)		
6.4	0.136		TRIDENT ($\tau = 600$ fs)		
9.9	0.054				
13.5	0.028				
4.7	0.245		100TW-LULI ($\tau = 350$ fs)		
9.8	0.120				
13.3	0.022				
6.2	1.598		VULCAN ($\tau = 1000$ fs)		
17.4	0.858				
Roth et. al. [185]					
E (MeV)	ϵ_N (mm mrad)		Facility		
-	<0.314		RAL ($\tau = 500$ fs)		
-	<0.031		100TW-LULI ($\tau = 300$ fs)		
-	<0.031		TRIDENT ($\tau = 850$ fs)		

TABLE 7.2: Different emittance values (geometrical and normalized) obtained in this work and results found in the bibliography. τ stands for the corresponding pulse duration.

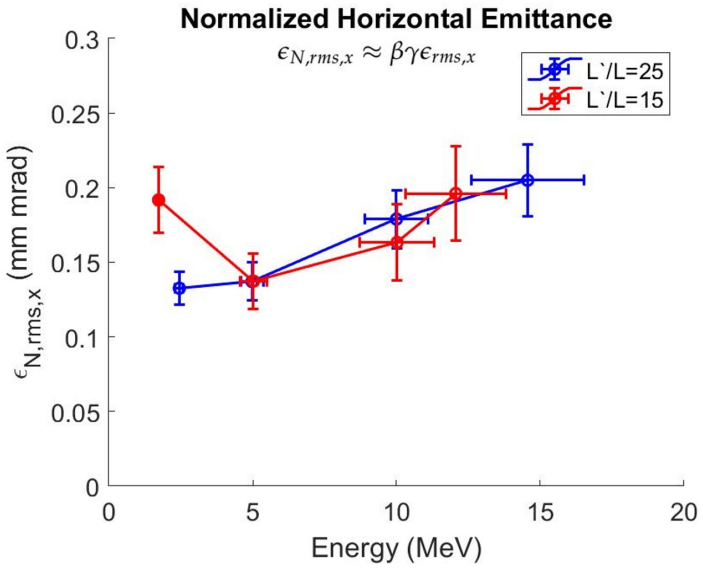

FIGURE 7.23: Horizontal RMS normalized emittance $\epsilon_{N,rms,x}$ versus proton energy for both shots analysed, including error bars. Blue line: dataset with $L'/L = 25$, red line: dataset with $L'/L = 15$. Inset shows the formula for the normalized emittance.

presented method can actually have a continuous assessment of the emittance for all the spectrum (within the TP energy resolution). On the other hand, the work of Ter-Avestiyan *et. al.* [186, 227] had a similar instrumentation approach (a multi-channel TP) for a tomographic reconstruction of a laser-driven proton beam. Nevertheless, they restricted their analysis to the first-order momenta of the particle distribution in the trace-space (i.e. $\langle x \rangle$ and $\langle x' \rangle$). This would be equivalent to the study in this manuscript of the trace centroids which gives the mean correlation between spatial coordinate and emission angle (figure 7.19).

It is also worth to compare between both results for different pinhole effect magnification $L'/L \sim 25$ and $L'/L \sim 15$. Being that the experimental laser-solid conditions are very similar in both shots, similar results are expected. Indeed, emittance values for both situations are coincident within the error bars where the same energy is measured. Following the table 7.1, note that the increase of magnification between both cases has been achieved by increasing L' and not by decreasing L. This has implications in the measurement accuracy, as a longer free path for proton vertical deviation is translated into a better energy resolution but keeping the same pinhole angular acceptance.

It is important to understand and improve the source of errors and limitations that the measurement system has. Besides the working hypotheses of the pepper-pot method already presented in the Chapter 3, some of the experimental systematic errors present in the presented calculations are outlined in the following list.

- The most restrictive condition is the fact that the emittance is actually calculated from a limited discretized version of the trace-space in that only four horizontally-aligned beamlets spanning 6° (approximately 15% of the full beam area) are measured.

- Due to the vertical magnetic deflection, the free flight distance of the particles is actually a function their energy, which could mean an apparent broadening of the traces. Nevertheless, the maximum relative particle path related to this matter ($\Delta L'(E)/L'$) was estimated to be below 1%. Therefore, this effect was not taken into account in the analysis. On the other hand, the energy resolution of the detector is also affected

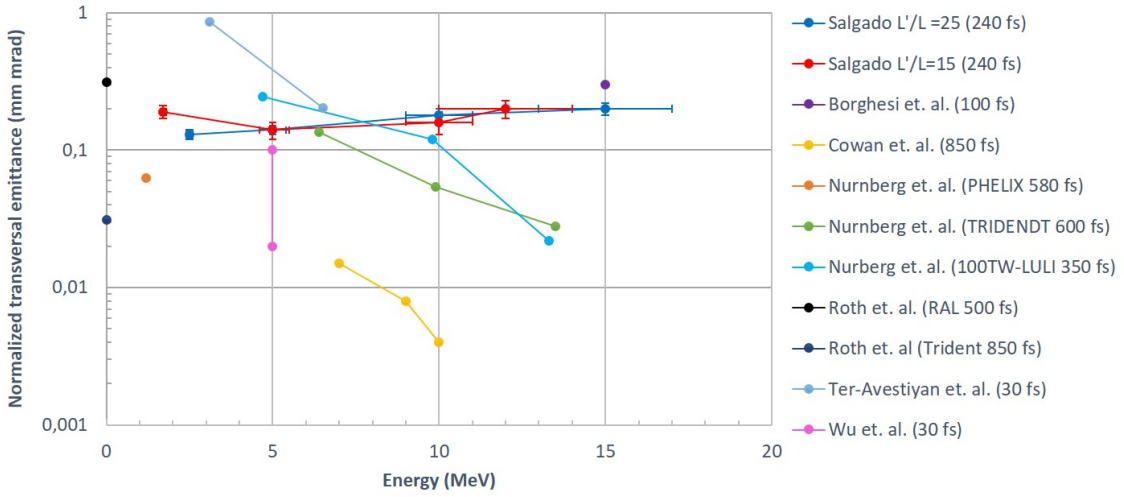

FIGURE 7.24: Comparison (in logarithmic scale) of the results for normalized emittance estimated in this work and previous work in the bibliography, including driver pulse duration.

by the angle of incidence of the particles on the scintillator, which is higher for lower energy ions. The particles will travel some distance within the scintillator vertical direction until they exit the volume or stop -plus an potential scattering effect- which deteriorates the vertical (i.e. spectral) resolution. In any case, the resulting systematic error is still smaller than the pinhole-dominated resolution for the case shown.

- The fact that the pinholes have a non-negligible vertical size implies not only a certain energy resolution but also a *vertical trace mixing*, which could result in an artificial shaping of the traces. Nevertheless, being the diameter of the pinholes much smaller that all the characteristic lengths of the measurement technique, the effect is not taken into account. Note from Chapter 3 that the requirement of small pinholes is one of the conditions for the pepper-pot analysis.

- Because of the intrinsic beam divergence, the incidence on the pinhole mask is not perfectly perpendicular. Therefore, the protons cross the pinholes with a very small angle of incidence and some vignetting effect could appear. Ideally, pepper-pot pinholes should admit all particles over their width, independent of their angle. Vignetting effect is considered negligible if $l_{\text{pin}}\alpha \gg d$, where l_{pin} is the pinhole plate thickness, d the pinhole diameter and α the incidence angle [77]. For the case studied in this work, $l_{\text{pin}}\alpha_{\text{max}} = 0.5\,\text{mm} \times 0.0524\,\text{rad} \approx 0.026\,\text{mm}$ and $d = 0.1\,\text{mm}$, therefore the condition is fulfilled to some extent. It would be interesting to take into account such effect when exploring the wings of the beam where angle of incidence is larger.

- The deposition of proton energy in the scintillator is in the bulk of the plastic (the chosen scintillator was 1.5 mm thick), leading to some lateral scattering. Moreover, as the depth of the deposition is a function of the particle energy itself, then the possible effect on the trace thickness might depend as well on the particle energy. The estimated lateral spreading of the traces has been experimentally obtained by comparison with the ones measured with the MCP under the same conditions (considering those as no-scattered traces). Lateral trace enhancement was estimated to reach values below $9\% \pm 8\%$ of the typical rms sizes measured, therefore considering this effect to be a second order correction to be made in a future work, characterizing properly

the response of the scintillators either by Monte Carlo simulations or by means of an experimental calibration.

Thanks to the fact that both TP and active detector were mounted in 3-axis motorized stages and profiting from the high repetition rate of the laser VEGA and the diagnostic itself, systematic (and redundant) lateral and vertical scans of the beam were performed with the high magnification mode ($L \approx$ mm). The scan encompassed hundreds of shots with a limited vertical range from $-1.8°$ to $3°$ and the horizontal from $-18°$ to $+18°$, until the horizontal edge of the beam was reached. Beam statistics were also taken with repetitive measurements at the same location, whose results will determine the beam quality repeatability. The systematic evaluation of the larger section of the beam (in a continuous-like fashion for the energy resolution) requires a fully automatized analysis script and it is beyond the scope of this thesis. It will be presented in a future work.

The use of the device in a real experimental environment has shown some limitations that should be addressed, as noted here.

- The angular acceptance of the tool is for the moment the most important limitation found. Ideally, a large two-dimensional pinhole mask is required for the single-shot characterization of the full beam. Enough separation of the plates, free-flight distance and a much larger active detector is required for such purpose. A new design for a second version of the multi-pinhole Thomson Parabola should be carried out. In addition, it would be valuable to make the trace separation to be larger in order to use the electric field to differentiate ion species. The new design would need a fully new geometrical design, new dipoles with larger separation (even wedged geometry) and a larger area MCP/scintillator.

- An absolute calibration of the MCP/scintillator response to ions of energy in the range of interest is mandatory for calculating the absolute spectrum of each beamlet. The calibration is specially interesting for the scintillators, whose response is far from linear and depends on the scintillator thickness and particle energy and species. Including this information in the analysis would yield a complete (but still discretized) divergence-spectrum relation. Such information is critical for the design of the post-acceleration beamline optics required for applications. A work on calibration of TP coupled to scintillators for relative spectrum retrieval has been recently published [260].

- The photonic signal level of each of the traces has been proven to be enough for a acceptable signal level within the dynamic range of the scientific cameras used. Therefore, a possible narrowing of the diameter of the pinholes (aiming for a reduction of the PSF and minimum trace size) can be obtained but still keeping a good signal-to-noise ratio.

- Placing the detector so close to the interaction point has consequences after hundreds of laser shots on solid targets. Each shot deposits a layer of Aluminium debris (originally part of the target) on the front face of the mask. Figure 7.25 show some detailed pictures of the mask after being exposed to the experimental conditions. After ~ 100 shots, evidence of blocking of pinholes appeared. Nevertheless, the debris was easily cleaned (and the pinholes cleared) with ultrasonic cleaning technique. The state of the exposed mask after the cleaning is acceptable for another experimental campaign. Potential distortion of the parabolic ion traces -related to EMP effect- may arise and should be taken into account when working at kJ laser facilities [261, 262]

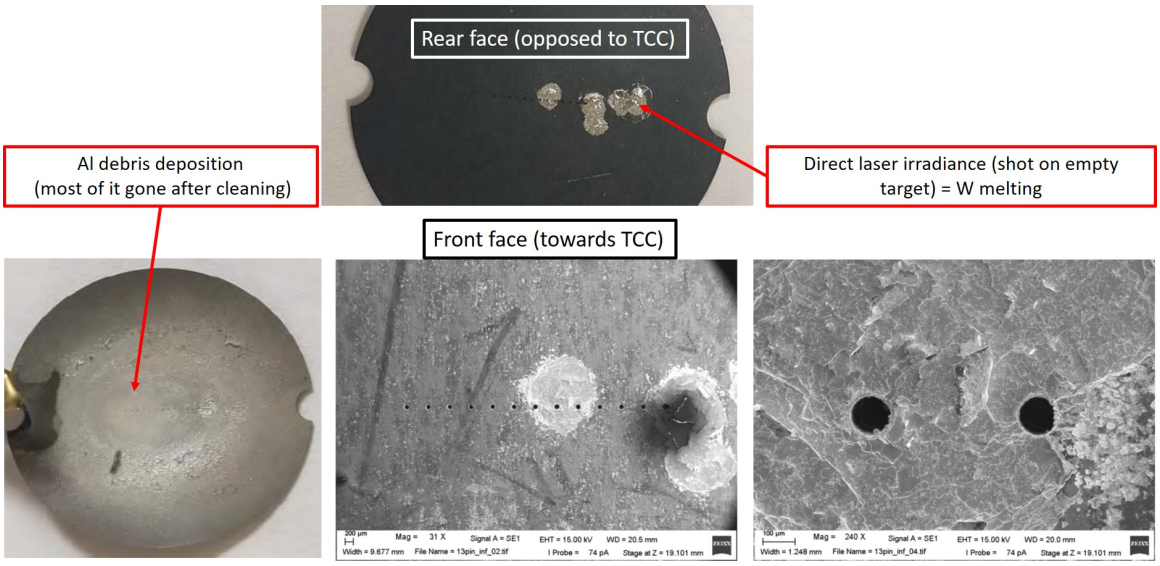

FIGURE 7.25: Pictures of the pinhole mask after experimental exposition. Top: rear (inner) surface; evidence of tungsten melting and resolidification. Bottom left: front (outer) surface before cleaning (debris is appreciable). Bottom center: front (outer) surface; Scanning Electron Microscope (SEM) picture of the cleaned pinholes. Bottom right: front (outer) surface; detailed SEM picture of the most damaged pinhole.

7.3 Conclusions and perspectives

The design, construction and test of a flexible ion detector has been shown in this Chapter. Two different operation modes for the device, depending on its geometrical configuration, have been experimentally demonstrated.

- **Multi-pinhole Thomson Parabola**: simultaneous measurements of spectra and ion species for discretized beamlets with different emission angles from a laser-plasma ion acceleration experiment, compatible with high repetition rate operation, has been tested. A novel analysis method, which can examine the crossing parabolic traces on the detector plane, grants access to several variables with large flexibility.
- **Spectrally-resolved emittance monitor**: by means of the same device, using a mixed methodology between pepper-pot and a Thomson Parabola, spectrally-resolved trace-space and emittance determination has been proven for laser-driven proton sources. Due to their applications in conventional accelerators, most of the emittance estimation techniques up to now have been designed for dealing with mono-energetic, single-species ion beams. The particular characteristic of the laser-driven ion beams (especially the ones accelerated via TNSA) require angular, spectral and species-wise resolutions that were not considered before. The most interesting feature of the presented method is not only the fact that it has the potential for separating ion species, but also that it can yield for each energy a measurement of the quality of the beam. The development of this diagnostic technique is especially important at the current development phase of the laser-plasma acceleration technology, where applications requiring ultra-high beam quality within specific bandwidths are attaining lot of attention. Further integration of the energy-resolved emittance values could give the total emittance of the beam.

  Comparison with other methods found in the literature show a substantial improvement in energy resolution, with relative errors for the emittance below 10%- with the

limitations and approximations pointed above- but still agreeing with the expected values. Furthermore, the method presented does not require micro-structuring of the target surface (which may lead to undesired beam inhomogeneities and could yield different emittance values with respect to a flat target due to electron filamentation or sheath field modification [34]). In addition, the method presented, unlike most of the techniques found in the literature, is fully HHR-compatible and is capable of measuring simultaneously the trace-space information for all the proton spectrum.

Both configuration of this detector have been proven useful for ions accelerated via TNSA mechanism, where a strong correlation between particle energy and position/divergence has been demonstrated. Such a detector would be of interest for novel acceleration mechanism under research in the laser-plasma field, such as CSA or RPA, as well as for beam quality measurements of transported/focused ion beamlines for applications, which should be monitored as they are susceptible to emittance deterioration due to chromatic effects or/and non-linearity of the applied fields [263]. On the other hand, the disparity of results in the bibliography for the beam laminarity (approximately 2 orders of magnitude of difference between greater and smaller values) for rather similar initial conditions (see figure 7.24 and table 7.2) makes clear that the beam dynamics of laser-driven ion sources are not fully controlled and understood yet. There is room for further research in this field and the development of more precise instrumentation is required. Future work is suggested for an improved version of the multi-pinhole TP. This includes introducing more pinholes and increasing to overall width and acceptance angle, potentially smaller pinholes and a more accurate calibration of the scintillator response.

Chapter 8

Summary and conclusions

Laser-driven particle beams cannot compete yet with conventional accelerators in terms of stability, charge and average flux, which is needed for most of foreseen applications. In order to overcome a low average particle flux, the high repetition rate of the new generation of PW-level, fs-duration lasers have turned out as one of the critical recent developments in the laser technology for LPA. However, the challenge still remains in obtaining targetry able to follow the operation rate of these lasers (in terms of alignment, refreshing, stability...) but also in the creation of a new generation of plasma and beam diagnostics able to work efficiently at HRR with the required temporal and spatial precision to detail the very fine beam and plasma features.

The work depicted in this manuscript addresses the former demand. A series of specially designed diagnostics have been developed for gaseous targetry inspection, ultrafast plasma measurements and particle beam quality monitoring. Special effort was made during the instrument conception for compatibility with HRR operation. The purpose, methodology, experimental implementation into the laboratory and analysis of the results of each of these tools has been elaborated.

8.1 Gas targetry measurements

A series of characterization campaigns of gaseous targets for ultra-intense laser-matter interaction experiments has been performed. Underdense moderate-pressure conical and rectangular gas jets (with densities $\sim 10^{19}\,\mathrm{cm}^{-3}$), and near-critical high-pressure conical and shock gas jets (corresponding densities $\sim 10^{21}\,\mathrm{cm}^{-3}$) have been successfully measured, identifying their longitudinal and radial profiles, their time-evolution and their dependences with gas backing pressure, nozzle geometry, gas composition and valve operation parameters. Benchmark of the results with fluid analytical models have been carried out for the cylindrical nozzle geometry. Four different measurement techniques (all of them based on wavefront reconstruction of a probing laser, namely Mach-Zehnder interferometry, strioscopy, a commercial Shack-Hartmann detector and commercial 4-wave lateral shearing interferometer) have been implemented in different experimental setups and compared in the manuscript. These diagnostics have been assembled both in a parallel working bench previous to the experiment and on-site in the experimental area during the laser beam time.

The successful implementation of the gas jets as targets in several experiments with ultra-intense lasers has been presented and the corresponding results outlined. In particular results have been presented from two experimental campaigns:

- An experiment at the VEGA 2 facility (200 TW) for laser wakefield electron acceleration was performed, where the betatron yield around 1.5 keV was optimized. The purpose of such campaign was both to commission the VEGA 2 laser system and

to prove its operation as a driver laser primary source to generate an ultrafast X-ray spectroscopy station for laser-generated warm dense matter.

- An experiment at the VEGA 3 facility (1 PW) of high harmonic generation in a novel focal cone geometry was carried out, which allowed to generate a large amount of XUV coherent radiation despite the low efficiency of the process. These result may pave the way for usage of PW-level femtosecond lasers as high harmonic drivers in gas targets.

8.2 Diagnostics development for laser-driven ion accelerators in near-critical plasma regime

A collaborative research line on ultra-intense laser interaction with high-density gas target for HRR-compatible ion acceleration has been presented. Two consecutive experiments at VEGA 2 and VEGA 3 laser facilities at CLPU have been introduced, including setup, diagnostics and main results.

- An experiment with the VEGA 2 (200 TW, 30 fs) laser was accomplished for the commissioning of the high-density gas jet system used as target in realistic ultra-intense experimental conditions. In this manner, a preliminary study of the corresponding laser-plasma interaction regime was achieved. This included the development of a platform for ultrafast interferometry, which is a well-know technique in underdense plasmas but it has been rarely used in near-critical dense plasmas. The corresponding elaboration of a frequency-doubled ultra-fast probe beam from a pick-up of the driver laser and the pump-probe synchronization techniques have been explained. Successfully measurement of the residual plasma density (reaching values above $0.1n_c$), as well as proof of repetitive laser penetration and energy deposition through the target has been obtained, which were relevant findings for the experimental optimization. The effect of laser damage on the nozzles and EMP on the valve was studied and strategies for their mitigation were conceived, including the construction of specific diagnostics for HRR shot-to-shot assessment of the gas jet quality. In addition, different characterization campaigns of the gaseous targets were performed before and after this experiment. Several parametric studies of the gas performance and its evolution as a function of the pressure, valve voltage and gas composition were carried out, meanwhile refined methodology was applied for the analysis of such data, including a Fourier-based phase cleaning algorithm and a generalization of the analysis of the density for gaseous mixtures.

- A consecutive experiment with the VEGA 3 (1 PW, 30 fs) laser was successfully performed focused on the extensive study of the near-critical plasma laser interaction regime and resulting particle yield. Knowledge acquired during the first experiment was implemented in almost every aspect of the subsequent campaign, including gas and vacuum operation, alignment protocol and plasma and particle detectors improvement. The main result of this campaign was the ToF evidence of acceleration of Helium ions up to 2.5 MeV inside a small cone of 17° horizontal angle centered on the laser forward direction with an inclination of 9° with respect to the horizontal plane, which is, to the best of our knowledge, one of the first experimental measurements of this kind achieved with fs-class driver laser and gaseous targets. Electron temperatures of 13 MeV were also measured, 6-fold larger than the expected ponderomotive scaling, which is a feature of laser and near-critical plasma interaction. Ultra-fast plasma interferometry was also achieved with picosecond resolution, being able to characterize early ionization regions of the interaction and the formation

of ponderomotive channel structures. Despite being far from the goal of the modern Ti:Sa laser systems, this campaign presents one of the highest repetition rates reported in experiments of PW lasers interacting with near-critical-plasmas ($20\,\mathrm{min}^{-1}$).

8.3 Angular and energy resolved ion beam tomography and emittance measurement

Angular-resolved tomography of a laser-driven ion source, with fine resolution in both energy and angle and capability of ion charge-to-mass ratio differentiation has been achieved in a TNSA experiment. The tool for such measurement was a modified version of a Thomson Parabola spectrometer, by means of an adapted entrance pinhole array. HRR-compatible measurements have been demonstrated using a highly sensitive MCP attached to a phosphor screen as an active detector for the TP traces. A refined method for TP trace analysis allowed the traces to cross on the detector, resulting in enhanced practical experimental flexibility. Laser-driven protons and carbon ions were measured during the commissioning experiment of such device (a TNSA ion acceleration experiment consisting of the irradiation of a 3 micron thick Aluminium foil with VEGA 3 petawatt pulses), reaching cutoff energies for protons above 15 ± 1 MeV.

On the other hand, when working in a high magnification mode (i.e. much closer to the ion source), this device proved its operation as an energy-resolved pepper-pot proton beam diagnostic. With this technique, a HRR-compatible complete study proton transversal trace-space has been elaborated, presenting very small error bars for the energy-resolved beam emittance and spanning the full proton spectrum in a single shot. Different beam laminarity regimes have been identified when comparing the lower and higher energy part of the spectrum. More valuable information of the beam could be retrieved from the trace-space, such as the tendency of the mean beam pointing and divergence with the proton energy. Agreement with previous laser-driven proton beam emittance results is found ($\epsilon_N \sim 0.2$ mm mrad) and the connection with former methodologies is done. The usage of plastic BC-400 scintillators as trace active detectors of TP has been tested, showing its their potential for HRR particle detectors.

The manuscript demonstrates this methodology as a powerful tool for complete transversal beam quality measurement for broadband and low-emittance laser-driven ion beams with very fine energy resolution. Particle beam lateral emittance is a parameter rather difficult to access and it has been ignored in most of the literature about laser-driven particle beams. Nevertheless, it is a key value to be monitored, as it defines the capability of such beams to be transported, selected and focused, which is fundamental for applications. Comparison with previous measurement techniques showed very small relative errors for the emittance values, a measurable improvement in energy resolution in most of the cases and several operation advantages (e.g. compatibility with high-repetition rate, no requirements of structuring the target and single-shot full spectrum retrieval, among others). The huge dispersion found in the literature for the beam emittance in very similar conditions is an indication that deeper applied research for the understanding of the proton beam dynamics close to the source is fundamental.

8.4 Future work

8.4.1 Gas targetry measurements

This manuscript made clear the necessity for experimental gaseous target characterization (when its usage is planned for laser-plasma experiments) beyond fluid simulations. Gas

jet density measurements have become a routine practice at CLPU, where each new gas jet is tested before its implementation in experiments in VEGA, thanks to the characterization bench constructed and depicted in this manuscript. Future related work will encompass the viability of 3D-printed de Laval nozzles [264] for creating repetitive density profile and the investigation and comparison of different Abel Inversion scripts.

8.4.2 Near critical plasmas for ion acceleration

Further conceptual and technical improvements are foreseen for a third campaign in a fs-class high-power laser in pursuit of efficient ion CSA in high-density gaseous targets. These include the use of Hydrogen as part of the target, the development of more durable nozzles (either by the use of more resistant materials or different nozzle geometries), improved particle detectors, and efficient vacuum pumping and target alignment, towards HRR operation. Magnetic field measurements in the plasma via ultrafast Faraday rotation [253] and improved ion diagnostics would be of major importance for certain identification the potential ion acceleration mechanism. Furthermore, PIC simulations indicate that larger laser a_0 would be beneficial for the triggering of collisionless shocks. Therefore the utilization of more energetic driver laser or shorter f-number OAP will be required. For now, an experimental proposal at BELLA petawatt laser at the Lawrence Berkeley National Laboratory (40 J, 40 fs, expected intensity on focus 10^{21} W/cm^{-2}) was submitted by our research team in 2022 and a decision on the application is expected soon.

8.4.3 Emittance measurements

The necessary improvements for a more complete ion emittance measurement with the proposed methodology have been identified. A new design of the multi-pinhole TP should be accomplished, with a different geometrical design, larger dipole separation and larger active detector area in order to enhance its angular accepetance and be able to characterize the complete (but discretized) trace space of the beam in a single shot. This new design should also allow for trace separation by electric field effect to recover the capability to discriminate the ion species. An absolute calibration of the BC-400 plastic scintillator should be implemented for additional retrieval of the absolute ion spectrum. On the other hand, the usage of this multi-pinhole TP for evaluation of beam quality during selection, transport and focalization in magnetic beamlines is foreseen. In this case, comparison with other measurements methods (as the quadrupole scan technique [239]) is possible.

Chapter 9

Resumen y conclusiones en castellano

Los haces de partículas acelerados por láser no pueden competir por ahora con los aceleradores convencionales en términos de estabilidad, carga y flujo medio, los cuales son requeridos para la mayoría de las aplicaciones previstas. Para poder superar la limitación de flujo, la alta tasa de repetición de los nuevos sistemas de láseres de PW y duración de femtosegundo se ha tornado como uno de los desarrollos cruciales en la tecnología relativa en la aceleración laser. Sin embargo, el desafío todavía permanece en la obtención de blancos capaces de seguir dicha tasa de repetición, así como en la creación de una nueva generación de diagnósticos de partículas y de plasmas capaces de trabajar eficientemente a altas tasas de repetición con las precisiones espaciales y temporales requeridas para resolver los finos detalles de dichos experimentos.

El trabajo mostrado en esta tesis se centra en esta última demanda. Una serie de diagnósticos han sido diseñados y desarrollados para la inspección de blancos gaseosos, medidas ultra-rápidas de plasmas y monitorización de de calidad de haces de partículas. Se ha mostrado especial dedicación durante la concepción de dichas técnicas para su compatibilidad con la operación a alta tasa de repetición. El objetivo, metodología, implementación experimental y análisis de resultados de dichas herramientas de medida han sido elaborado en la tesis.

9.1 Medidas de blancos gaseosos

Una serie de campañas de caracterización de blancos gaseosos para experimentos de interacción de láseres intensos y materia han sido llevadas a cabo. Jets de gas sub-densos de goemetría cónica y rectangular (con densidades moleculares $\sim 10^{19}\,\mathrm{cm}^{-3}$) y jets de choque y cónicos de alta presión (con densidades moleculares $\sim 10^{21}\,\mathrm{cm}^{-3}$) han sido satisfactoriamente medidos, indentificando sus perfiles longitudinales y radiales, su evolución temporal durante su formación y sus dependencias con la presión, geometría de la boquilla, composición del gas y parámetros de operación de su válvula. Los resultados para las boquillas cónicas han sido comparados con modelos analíticos de Física de fluidos. Cuatro técnicas de medida distintias han sido implementadas y comparadas, todas ellas basadas en la reconstrucción del frente de onda de un láser sonda: interferometría, estrioscopía y el uso de sensores de frente de onda tipo Shack-Hartmann y tipo *interferómetro de cizalladura lateral de ondas*. Estos diagnósticos han sido utilizados en campañas de caracterización especificas así como de manera on-line en los propios experimentos.

La implementación de los blancos gaseosos en varios experimentos con láser de alta intensidad han sido presentados y los resultados correspondientes mostrados. En particular, se destacan dos campañas:

- Un experimento en el láser VEGA 2 (200 TW) para la aceleración de electrones en estela láser fue llevado a cabo, donde el flujo de radiación de Betatron en 1.5 keV fue optimizado. El objetivo de dicho experimento fue la puesta a punto del láser, así como

la creación de una estación de espectroscopía ultra-rápida de rayos X para "materia densa cálida" generada por láser.

- Un experimento en el láser VEGA 3 (1 PW) para la generación de altos armónicos en la goemetría de cono focal fue llevado a cabo, el cuál permitió generar grandes cantidades de radiación coherente en el rango del ultra-violeta extremo a pesar de la baja eficiencia del proceso. Estos resultados podrían allanar el camino para el uso de sistemas láser de petavatio y femtosegundo para generación de altos armónicos en gas.

9.2 Desarrollo de diagnósticos para la aceleración de iones basada en láser en plasmas de densidad crítica

Se ha presentado una línea de investigación colaborativa centrada en el estudio de la interacción de láseres intensos con blancos gaseosos de alta densidad para la aceleración de iones a alta tasa de repetición. Se muestran dos experimentos en los láseres VEGA 2 y VEGA 3 en el CLPU, incluyendo configuración, diagnósticos y principales resultados.

- El experimento con el láser VEGA 2 (200 TW, 30 fs) se centró en la puesta a punto del sistema de blanco gaseoso de alta presión, así como su uso en condiciones experimentales extremas realistas. De este modo, un estudio preliminar del correspondiente régimen de interacción láser-plasma fue llevado a cabo. Dicho estudio ha requerido el desarrollo de una plataforma para interferometría de plasmas ultra-rápida, la cual es una técnica de uso común en plasmas sub-densos pero raramente utilizada en plasmas de densidad crítica. En el manuscrito se ha detallado la correspondiente elaboración de un haz láser "sonda" ultra-corto y doblado en frecuencia tomado del láser principal con el objetivo de realizar la interferometría, así como las técnicas usadas para la sincronización entre ambos láseres. Se han obtenido medidas de la densidad de plasma residual tras el experimento (alcanzando valores por encima de $0.1n_c$) y evidencias de la penetración del láser y su deposición de energía a través del blanco gaseoso de manera sistemática, información que ha resultado relevante para la optimización experimental. El daño causado por el láser en las boquillas, asi como el efecto del pulso electromagnético en la válvula de gas han sido caracterizados y estrategias para la mitigación de ambos han sido concebidas, incluyendo la construcción de diagnósticos específicos para la evaluación de la calidad del jet de gas tiro a tiro. Por otra parte, diferentes campañas de caracterización del blanco gaseoso fueron llevadas a cabo previamente y simuláneamente al experimento. Se realizaron distintos estudios paramétricos del operación del blanco y su evolución en función de la presión, voltaje suministrado a la válvula y la composición del gas. Además, una nueva y refinada metodología fue aplicada para el análisis de estos datos, incluyendo un algoritmo de limpiado de la fase del láser basado en un filtro de Fourier y la generalización de la conversión de fase del láser a densidad molecular para mezclas de gases.

- Un experimento posterior en VEGA 3 (1 PW, 30 fs) fue llevado a cabo, centrado en el estudio detallado del régimen de interacción de láseres intensos con plasmas de densidad crítica y la producción de partículas relacionada. La experiencia adquirida tras el experimento en VEGA 2 fue aplicada en todos los aspectos de la nueva campaña, incluyendo mejoras en la operación del blanco de gas y de su evacuación, el protocolo de alineado y los detectores de plasmas y partículas. El principal resultado fue la evidencia (con la técnica de tiempo de vuelo) de la aceleración de iones de Helio hasta 2.5 MeV detectados en un cono estrecho de 17° de ángulo horizontal centrado

la dirección de avance del láser, con una inclinación respecto al plano horizontal de 9°. Este resultado es una de las primeras evidencias experimentales reportadas de dicha aceleración con láseres de fetmosegundo y blancos gaseosos de densidad crítica. Temperaturas de electrones eyectados de 13 MeV han sido también medidas, seis veces por encima del valor esperado de acuerdo con el escalado "ponderomotivo", siendo esta una de las características típicas de la interacción laser y plasmas de densidad crítica. La interferometría ultra-rápida fue en este caso conseguida con resolución de picosegundo, siendo capaz de caracterizar regiones de ionización tempranas en el gas y la formación de canales ponderomotivos. A pesar de estar lejos del objetivo de los modernos sistemas láser de Ti:Zafiro, esta campaña presenta una de las tasas de repetición más altas reportadas en experimentos de interacción de láseres de petavatio con plasmas de densidad crítica ($20\,\mathrm{min}^{-1}$).

9.3 Tomografía de iones resuelta en energía y medida de emitancia

En un experimento de tipo TNSA se ha logrado la tomografía resuelta en ángulo y energía de una fuente de iones generada por láser, con alta resolución en energía y ángulo y capacidad de discriminación entre especies iónicas de distinta relación carga-masa. La herramienta usada para dicho cometido ha sido una versión modificada de un espectrómetro tipo Thomson Parabola, gracias al uso de una matriz de orificios de entrada. Se ha demostrado su compatibilidad con la operación a alta tasa de repetición usando una MCP como detector activo de las trazas de partículas. Un método refinado para el análisis de dichas trazas ha permitido que las mismas puedan cruzarse en el detector, resultando en una mayor practicidad y flexibilidad del aparato. Protones e iones de carbono acelerados por láser han sido caracterizados en un experimento de TNSA basado en la irradiación de una lámina de 3 micrómetros de Aluminio con los pulsos focalizados del láser de petavatio VEGA 3, midiendo energías para los protones por encima de 15 ± 1 MeV.

Por otra parte, trabajando en un modo de alta magnificación (es decir, situando la TP muy cerca de la fuente de iones), dicha herramienta ha sido utilizada como diagnóstico tipo "pepper-pot" de protones resuelto en energía. Un estudio completo del espacio de fases transveral de los protones (a alta tasa de repetición) ha sido logradao con esta técnica, demostrando alta sensibilidad para la medida de la emitancia del haz a lo largo de todo el espectro en un solo disparo. Se han indentificado distintos regímenes de laminaridad de los protones acelerados entre las partes de altas y de bajas energías del espectro. Además, otra información relacionada ha podido ser obtenida a través de la medida del espacio de fases, como la tendencia de la dirección y divergencia del haz de protones con su energía. Los resultados obtenidos son consistentes con las medidas de emitancias encontradas en la literatura ($\epsilon_N \sim 0.2$ mm mrad). El uso de centelleadores plásticos (BC-400) como detectores activos de las trazas de partículas ha sido probado, demostrando su potencial uso como detectores de alta tasa de repetición.

La tesis demuestra esta metodología como una potente herramienta para la medida completa y de precisión de la calidad transversal de los haces de protones generados por laser, normalmente de gran ancho de banda y baja emitancia. La emitancia lateral de los haces de partículas es uno de los parámetros más difcíciles de caracterizar experimentalmente y ha sido ignorado en gran parte de la literatura de aceleración basada en láser. Sin embargo, es un parámetro vital ya que define la capacidad de dichos haces de ser transportados y focalizados, lo cual es crítico para aplicaciones. Una mayor precisión en la determinación de la emitancia y en la resolución espectral ha sido demostrada comparando la técnica desarrollada con la metodologías previas, además de presentar mejoras operacionales (como la compatibilidad con alta tasa de repetición y los menores requerimientos

experimentales). La gran dispersión de resultados para la emitancia para condiciones iniciales similares encontrada en la literatura es una indicación de que una investigación más profunda es requerida en este caso para la compresión de la dinámica de los iones acelerados.

9.4 Futuro trabajo

9.4.1 Medidas de jets gaseosos

La tesis ha mostrado la necesidad de la caracterización experimental de los blancos gaseosos destinados para su uso en experimentos de interacción laser plasma, más allá de simulaciones de Física de fluidos. Las medidas de densidad de jets de gas se han convertido en una tarea rutinaria en el CLPU, donde cada nuevo blanco gaseoso es medido y probado antes de su implementación experimental gracias al banco de medida construido y descrito en este trabajo. El próximo trabajo relaciodado será el uso de la misma estación para probar la viabilidad de boquillas impresas en 3D [264] para la generación de perfiles de densidad de gas repetitivos, así como la comparación de distintos algoritmos para la Inversión de Abel para su análisis.

9.4.2 Aceleración de iones en plasmas de densidad crítica

Mejoras técnicas y de concepto serán aplicadas en una tercera campaña experimental en una instalación laser de alta potencia para la aceleración eficiente de iones a través de ondas de choque de electrostáticas en el plasma usando blancos gaseosos. Éstas incluyen el uso de Hidrógeno como compuesto del blanco, el desarrollo de boquillas más resistentes al daño láser (con el uso de mejores materiales o diferentes geometrías), mejora de detectores de partículas y una evacuación del gas mejorada y alineamiento rápido, en un intento de coseguir alta tasa de repetición. La identificación del mecanismo de aceleración de partículas será facilitado con mejores detectores de iones, así como con la medida de campos magnéticos en el plasma a través de medida ultra-rápida de rotación de Faraday [253]. Por otra parte, las simulaciones PIC parecen indicar que una mayor intensidad láser en foco (es decir, a_0 mayor) sería beneficioso para desencadenar las ondas de choque. Por lo tanto, el uso de un láser mas potente o de una óptica de focalización mas corta sería necesario. En este momento, un experimento en el láser de petavatio BELLA en LBNL, EE.UU. (40 J, 40 fs, $10^{21}\,\mathrm{W/cm^{-2}}$) ha sido propuesto por el grupo de investigación en 2022 y su resolución es esperada pronto.

9.4.3 Medida de emitancia

Se han identificado las mejoras necesarias para una medida completa de la emitancia de haces de iones acelerados por láser. Un nuevo diseño con una geometría distinta debe ser realizado, con mayor separación del dipolo y un detector activo de mayor área para así aumentar la aceptación angular del diagnóstico y poder caracterizar el espacio de fases de toda la superficie del haz en un solo disparo. Este nuevo diseño debe a su vez ser capaz de separar las trazas a través del campo eléctrico y recuperar discriminación de las dintintas especies de iones. La calibración absoluta de los centelleadores BC-400 debe ser realizada para poder obtener de manera simultánea la medida absoluta del espectro de las partículas. Por otra parte, se ha previsto el uso del detector para la monitorización de la calidad de un haz de protones transportado por un sistema de lentes magnéticas. En este caso la comparación con otras técnicas de medida de emtancia es posible, como por ejemplo la técnica de escaneo de cuadrupolo [239].

Appendix A

Diagnostic basics

This chapter presents a brief description of two commercially available detectors relevant for this thesis. First, the basic operation and specifications of the microchannel plate used for trace detection of the Thomson Parabola is shown. The working principle of a streak camera is elaborated in the second part of the appendix.

A.1 Microchannel plate

A microchannel plate (MCP) is a high-resolution spatially-resolved electron multiplier [65]. As shown in figure A.1, MCPs are composed by an array of thin glass capillaries, each of them working as an independent electron multiplier, fused together into a large plate. Ionizing radiation impacting the walls of the channels (which are titled with respect to the detectors' normal) generates secondary electrons, which are drifted by a bias voltage supplied between the front and back sides of the detector. During this drift, electrons hit the walls of the channels, subsequently amplifying the electron bunch charge (up to 10^4 in a single amplification stage can be obtained). Several microchannel arrays can be stacked for multi-staged signal amplification. The resulting electrons are then electrically carried towards a fluorescent phosphor screen (typical fluorescence time $\sim$ 1 ns) and converted in optical photons that can be collected by an imaging system. For a single stage MCP, the final spatial resolution is approximately equal to the capillary diameter.

As shown in Chapter 6, an MCP was used for detection of ion traces and their conversion into a optical signals in the Thomson Parabola Spectrometer. The model chosen was the F2813-12P from Hamamatsu Photonics. This model, with an effective sensing area of 78 $\times$ 29 mm, presents a single electron multiplication stage, with microchannels of 15 µm of internal diameter and inter-channel wall thickness of 4 µm and a center-to-center separation of 19 µm. The angle of the channels with respect to the sensor surface normal is 8°.

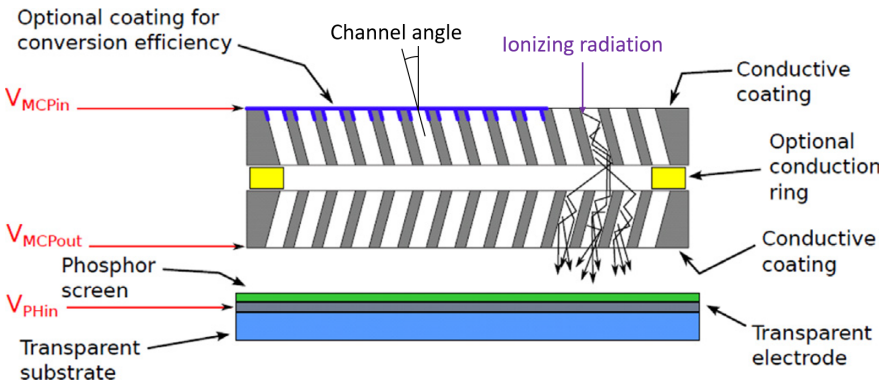

FIGURE A.1: Sketch of the lateral section of a two-stage MCP. Red arrows show the bias voltage application layers. Image adapted from [65].

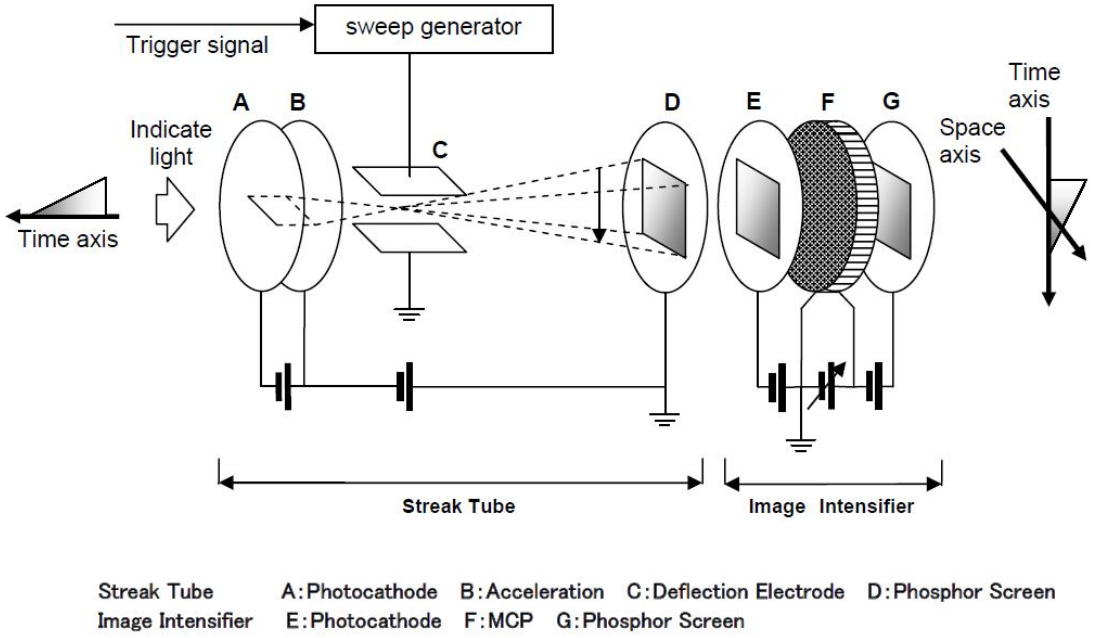

FIGURE A.2: Sketch of the Streak Camera operation principle. Image taken from [265].

A.2 Streak Camera

Streak Cameras are opto-electronic devices able to take fine time-resolved one-dimensional images. The operation principle is straightforward and it is summarized in figure A.2. The incident photons are converted into electrons usign a photocathode and are sent through a fast deflection sweep circuit which resolves in time the initial light distribution

The original photon signal to be measured passes through a thin (10s to 100s of micrometers wide) slit, which means that only information in one spatial axis can be analysed. Normally, laser-plasma experimental setups are designed so the signal is imaged onto the slit plane with the required magnification. The slit can be afterwards imaged onto the photocathode of the streak tube, where photons are converted into electrons which are therefore accelerated with the help of electrodes. In the streak tube a high-speed voltage ramp signal is applied orthogonally to the slit direction. In this way electrons are swept in the so called *time-axis* as a function of their arrival time. The electrons are then stopped by a phosphor screen, which converts electrons into photons. The result is a two-dimensional image, but where the axis perpendicular to the slit symbolizes the the time coordinate of the original radiation. An image intensifier can be included behind the phosphor screen by incorporating an MCP, which allows for single photo-electron detectability and increased dynamic range. In order to record the processed signal, a third imaging lens re-images the phosphor screen photons onto a scientific camera. Furthermore, the sweep generator, streak tube electrodes and camera trigger should be properly synchronized with the signal for proper operation. In the case of ultrashort laser experiments, synchronization with the laser itself (by means of a photodiode) is needed for low-jitter acquisition. The trigger configuration scheme is shown in figure A.3. The time resolution is given by the maximum speed of the sweep voltage. In the case of the streak cameras used in the work of this thesis, the total sweep ranges can vary from 1 ms to 500 ps, yielding a time resolution better than 5 ps.

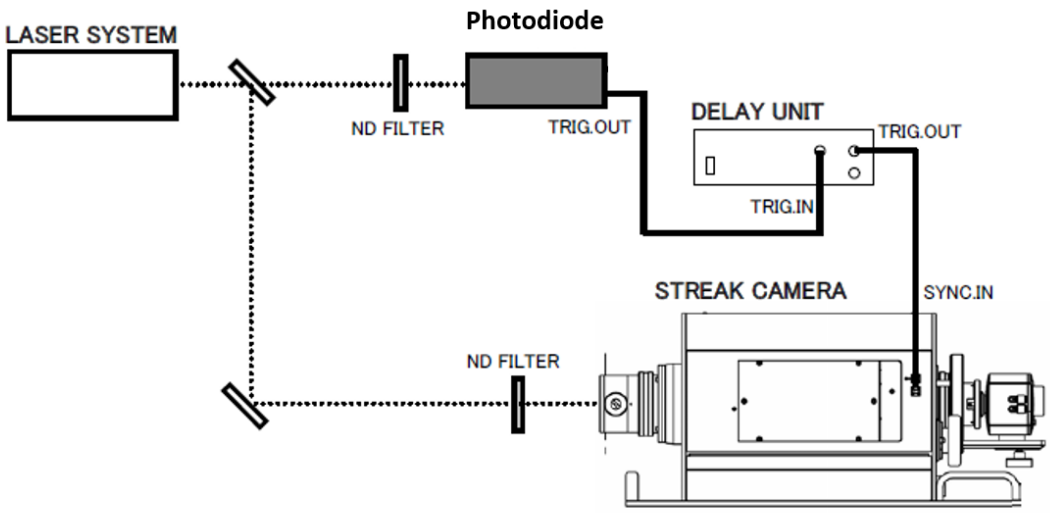

FIGURE A.3: Wiring diagram of the trigger signal for the Streak Camera C10647-01, from Hamamatsu Photonics [265].

Appendix B

Monte Carlo simulations for ion energy deposition

T. Cebriano was in charge of Monte-Carlo simulations for the experiment of ion beam emittance measurement. The code used at that time was MCNP (version 6) [254]. Monte-Carlo codes are a group of computational algorithms which rely on using random sampling in order to obtain numeral solutions to physical or mathematical problems. In the case of MCNP, this method is used to create a general particle transport code.

As explained in Chapter 6, the code was use to predict the expected deposition of energy in the BC-400 plastic scintillator of the ions accelerated via TNSA with the VEGA 3 laser system.

Based on the spectra retrieved with the TP when using MCP as detector, the parameters for the input beam of the simulations were defined. Collimated and monoenergetic protons and carbon ions beams with charge states +4, +5 and +6 with some representative energies (0.5, 1, 5, 10, 15 and 20 MeV) were simulated. Meanwhile, the target was initially set to be a 13 μm-thick polycarbonate foil. The results of the simulations are summarized in the figure B.1. The second column of each ion table shows the percentage of particles that crossed the target in the simulation, meanwhile the third column represents the average energy of the ions after going trough the sample. BPR stands for Bragg Peak Range and it is the average material thickness that a specific ion of certain energy has to travel in order to deposit all its energy.

The main conclusion after the simulations are:

- the lower energies Carbon ions (< 10 MeV) will not reach the scintillator,
- if they exist in the beam, higher energy Carbon ions (> 10 MeV) will reach the scintillator
- almost all the energy range of protons will cross Pokalon filter and reach the scintillating plate.

A second set of simulations were carried out by adding a 2mm-thick BC-400 layer after the Pokalon. The result are shown in figure B.2. The main conclusion after these calculations is that lower energy protons (< 10 MeV) will be fully stopped at the scintillator and will deposit their full energy inside. Nevertheless, the higher energy protons (> 10 MeV) deposit a non negligible part of their energy inside the plastic and in principle it should generate visible light through the scintillating process.

13 um Pokalon

H^+ Energy (MeV)	Transmission efficiency (%)	Transmitted Energy (MeV)
5	100	4,88
10	100	9,93
15	100	14,95
20	100	19,96

C^{4+} Energy (MeV)	Transmission efficiency (%)	Transmission efficiency (MeV)	BPR (µm)
0.5	0	0	1,7
1	0	0	2,6
5	0	0	9,5
10	99,998	3,37	20
15	99,9998	9,87	33
20	100	15,8	47

C^{5+} Energy (MeV)	Transmission efficiency (%)	Transmission efficiency (MeV)	BPR (µm)
0.5	0	0	1,3
1	0	0	2,3
5	0	0	7,5
10	99,997	0,64	15
15	99,996	7,27	24
20	99,996	13,62	35

C^{6+} Energy (MeV)	Transmission efficiency (%)	Transmission efficiency (MeV)	BPR (µm)
0.5	0	0	1,1
1	0	0	1,8
5	0	0	6
10	0	0	12
15	100	4,3139	19
20	100	11,0693	26

FIGURE B.1: Tables with the simulated transmission efficiency values through the 13 µm-thick pokalon and BPR for the different ions and energies considered.

13 um Pokalon + 2 mm BC400

H^+ Energy (MeV)	Transmission efficiency (%)	Transmitted Energy (MeV)
20	99,3938	13.7505
15	98.9618	5.76142
10	0	0

FIGURE B.2: Table with the simulated transmission efficiency through the pokalon film and 2 mm of plastic scintillator.

Bibliography

[1]T. H. Maiman, "Stimulated optical radiation in ruby", Nature **6**, 493–494 (1960).

[2]V. Tornari, "On development of portable digital holographic speckle pattern interferometry system for remote-access monitoring and documentation in art conservation", Strain **55**, e12288 STRAIN-1378.R1, e12288 (2019).

[3]F. Fankhauser and S. Kwasniewska, *Lasers in ophthalmology: basics, diagnostics and surgical aspects. a review.* (Kugler Publications, 2003).

[4]L. Nuckolls J. H., "Early steps toward inertial fusion energy (ife) (1952 to 1962)", 10.2172/658936.

[5]D. Strickland and G. Mourou, "Compression of amplified chirped optical pulses", Optics Communications **56**, 219–221 (1985).

[6]A. Macchi, F. Cattani, T. V. Liseykina, and F. Cornolti, "Laser acceleration of ion bunches at the front surface of overdense plasmas", Phys. Rev. Lett. **94**, 165003 (2005).

[7]E. Esarey, C. B. Schroeder, and W. P. Leemans, "Physics of laser-driven plasma-based electron accelerators", Rev. Mod. Phys. **81**, 1229–1285 (2009).

[8]E. Esarey, B. A. Shadwick, P. Catravas, and W. P. Leemans, "Synchrotron radiation from electron beams in plasma-focusing channels", Phys. Rev. E **65**, 056505 (2002).

[9]Y. Fu, K. Nishimura, R. Shao, K. Midorikawa, P. Lan, and E. Takahashi, "High efficiency ultrafast water-window harmonic generation for single-shot soft x-ray spectroscopy", Communications Physics **3**, 92 (2020).

[10]F. Albert, M. E. Couprie, A. Debus, M. C. Downer, J. Faure, A. Flacco, L. A. Gizzi, T. Grismayer, A. Huebl, C. Joshi, M Labat, W. P. Leemans, A. R. Maier, S. P. D. Mangles, P. Mason, F. Mathieu, P. Muggli, M. Nishiuchi, J. Osterhoff, P. P. Rajeev, U. Schramm, J. Schreiber, A. G. R. Thomas, J.-L. Vay, M. Vranic, and K. Zeil, "2020 roadmap on plasma accelerators", New Journal of Physics **23**, 031101 (2021).

[11]Z.-H. He, B. Beaurepaire, J. A. Nees, G. Gallé, S. A. Scott, J. R. S. Pérez, M. G. Lagally, K. Krushelnick, A. G. R. Thomas, and J. Faure, "Capturing structural dynamics in crystalline silicon using chirped electrons from a laser wakefield accelerator", Scientific Reports **6**, 36224 (2016).

[12]M. Barberio, M. Sciscio, S. Vallieres, F. Cardelli, S. N. Chen, G. Famulari, T. Gangolf, G. Revet, A. Schiavi, M. Senzacqua, and P. Antici, "Laser-accelerated particle beams for stress testing of materials", Nature Communications **9**, 372 (2018).

[13]P. K. Patel, A. J. Mackinnon, M. H. Key, T. E. Cowan, M. E. Foord, M. Allen, D. F. Price, H. Ruhl, P. T. Springer, and R. Stephens, "Isochoric heating of solid-density matter with an ultrafast proton beam", Phys. Rev. Lett. **91**, 125004 (2003).

[14]M. Roth, T. E. Cowan, M. H. Key, S. P. Hatchett, C. Brown, W. Fountain, J. Johnson, D. M. Pennington, R. A. Snavely, S. C. Wilks, K. Yasuike, H. Ruhl, F. Pegoraro, S. V. Bulanov, E. M. Campbell, M. D. Perry, and H. Powell, "Fast ignition by intense laser-accelerated proton beams", Phys. Rev. Lett. **86**, 436–439 (2001).

[15]K. W. D. Ledingham et al., "Towards laser driven hadron cancer radiotherapy: a review of progress", Appl. Sci. **4**, 402–443 (2014).

[16]C. N. Danson, C. Haefner, J. Bromage, T. Butcher, J.-C. F. Chanteloup, E. A. Chowdhury, A. Galvanauskas, L. A. Gizzi, J. Hein, D. I. Hillier, and et al., "Petawatt and exawatt class lasers worldwide", High Power Laser Science and Engineering **7**, e54 (2019).

[17]P. Gibbon, "Introduction to plasma physics", in Proceedings of the cas-cern accelerator school: plasma wake acceleration (2016).

[18]W. Hogan, E. Moses, B. Warner, M. Sorem, and J. Soures, "The national ignition facility", Nuclear Fusion **41**, 567 (2001).

[19]V. Malka, "Laser plasma accelerators", Physics of Plasmas **19**, 055501 (2012).

[20]T. Tajima and J. M. Dawson, "Laser electron accelerator", Phys. Rev. Lett. **43**, 267–270 (1979).

[21]H. Daido, M. Nishiuchi, and A. S. Pirozhkov, "Review of laser-driven ion sources and their applications", Rep. Prog. Phys. **75**, 056401 (2012).

[22]A. Macchi, M. Borghesi, and M. Passoni, "Ion acceleration by superintense laser-plasma interaction", Rev. Mod. Phys. **85**, 751–793 (2013).

[23]`https://www.icuil.org/pdf/icuil-world-map-2020.pdf`, accessed: 2022-05-25.

[24]S. Corde, K. Ta Phuoc, G. Lambert, R. Fitour, V. Malka, A. Rousse, A. Beck, and E. Lefebvre, "Femtosecond x rays from laser-plasma accelerators", Rev. Mod. Phys. **85**, 1–48 (2013).

[25]G. Sarri, D. J. Corvan, W. Schumaker, J. M. Cole, A. Di Piazza, H. Ahmed, C. Harvey, C. H. Keitel, K. Krushelnick, S. P. D. Mangles, Z. Najmudin, D. Symes, A. G. R. Thomas, M. Yeung, Z. Zhao, and M. Zepf, "Ultrahigh brilliance multi-mev γ-ray beams from nonlinear relativistic thomson scattering", Phys. Rev. Lett. **113**, 224801 (2014).

[26]M. Roth, D. Jung, K. Falk, N. Guler, O. Deppert, M. Devlin, A. Favalli, J. Fernandez, D. Gautier, M. Geissel, R. Haight, C. E. Hamilton, B. M. Hegelich, R. P. Johnson, F. Merrill, G. Schaumann, K. Schoenberg, M. Schollmeier, T. Shimada, T. Taddeucci, J. L. Tybo, F. Wagner, S. A. Wender, C. H. Wilde, and G. A. Wurden, "Bright laser-driven neutron source based on the relativistic transparency of solids", Phys. Rev. Lett. **110**, 044802 (2013).

[27]H. Chen, S. C. Wilks, D. D. Meyerhofer, J. Bonlie, C. D. Chen, S. N. Chen, C. Courtois, L. Elberson, G. Gregori, W. Kruer, O. Landoas, J. Mithen, J. Myatt, C. D. Murphy, P. Nilson, D. Price, M. Schneider, R. Shepherd, C. Stoeckl, M. Tabak, R. Tommasini, and P. Beiersdorfer, "Relativistic quasimonoenergetic positron jets from intense laser-solid interactions", Phys. Rev. Lett. **105**, 015003 (2010).

[28]G. Sarri, W. Schumaker, A. Di Piazza, M. Vargas, B. Dromey, M. E. Dieckmann, V. Chvykov, A. Maksimchuk, V. Yanovsky, Z. H. He, B. X. Hou, J. A. Nees, A. G. R. Thomas, C. H. Keitel, M. Zepf, and K. Krushelnick, "Table-top laser-based source of femtosecond, collimated, ultrarelativistic positron beams", Phys. Rev. Lett. **110**, 255002 (2013).

[29]T. E. Cowan, J. Fuchs, H. Ruhl, A. Kemp, P. Audebert, M. Roth, R. Stephens, I. Barton, A. Blazevic, E. Brambrink, J. Cobble, J. Fernández, J.-C. Gauthier, M. Geissel, M. Hegelich, J. Kaae, S. Karsch, G. P. Le Sage, S. Letzring, M. Manclossi, S. Meyroneinc, A. Newkirk, H. Pépin, and N. Renard-LeGalloudec, "Ultralow emittance, multi-mev proton beams from a laser virtual-cathode plasma accelerator", Phys. Rev. Lett. **92**, 204801 (2004).

[30]B. Dromey, M. Coughlan, L. Senje, M. Taylor, S. Kuschel, B. Villagomez-Bernabe, R. Stefanuik, G. Nersisyan, L. Stella, J. Kohanoff, M. Borghesi, F. Currell, D. Riley, D. Jung, C.-G. Whalstrom, C. Lewis, and M. Zepf, "Picosecond metrology of laser-driven proton bursts", Nature Communications **7**, 10642 (2016).

[31]O. Lundh, J. Lim, C. Rechatin, L. Ammoura, B.-I. A., X. Davoine, G. Gallot, J.-P. Goddet, E. Lefebvre, V. Malka, and J. Faure, "Few femtosecond, few kiloampere electron bunch produced by a laser–plasma accelerator", Nature Phys. **7**, 219–222 (2011).

[32]S. Ter-Avetisyan, M. Schnürer, R. Polster, P. Nickles, and W. Sandner, "First demonstration of collimation and monochromatisation of a laser accelerated proton burst", Laser and Particle Beams **26**, 637–642 (2008).

[33]T. Toncian, M. Borghesi, J. Fuchs, E. d'Humières, P. Antici, P. Audebert, E. Brambrink, C. A. Cecchetti, A. Pipahl, L. Romagnani, and O. Willi, "Ultrafast laser-driven microlens to focus and energy-select mega-electron volt protons", Science **312**, 410–413 (2006).

[34]F. Nürnberg, M. Schollmeier, E. Brambrink, A. Blažević, D. C. Carroll, K. Flippo, D. C. Gautier, M. Geißel, K. Harres, B. M. Hegelich, O. Lundh, K. Markey, P. McKenna, D. Neely, J. Schreiber, and M. Roth, "Radiochromic film imaging spectroscopy of laser-accelerated proton beams", Review of Scientific Instruments **80**, 033301 (2009).

[35]M. Borghesi, A. J. Mackinnon, D. H. Campbell, D. G. Hicks, S. Kar, P. K. Patel, D. Price, L. Romagnani, A. Schiavi, and O. Willi, "Multi-mev proton source investigations in ultraintense laser-foil interactions", Phys. Rev. Lett. **92**, 055003 (2004).

[36]J. J. Santos, M Bailly-Grandvaux, L Giuffrida, P Forestier-Colleoni, S Fujioka, Z Zhang, P Korneev, R Bouillaud, S Dorard, D Batani, M Chevrot, J. E. Cross, R Crowston, J.-L. Dubois, J Gazave, G Gregori, E d'Humières, S Hulin, K Ishihara, S Kojima, E Loyez, J.-R. Marquès, A Morace, P Nicolaï, O Peyrusse, A Poyé, D Raffestin, J Ribolzi, M Roth, G Schaumann, F Serres, V. T. Tikhonchuk, P Vacar, and N Woolsey, "Laser-driven platform for generation and characterization of strong quasi-static magnetic fields", New Journal of Physics **17**, 083051 (2015).

[37]J. Apinaniz, S. Malko, R. Fedosejevs, and et al., "A quasi-monoenergetic short time duration compact proton source for probing high energy density states of matter", Sci. Rep. **11**, 6881 (2021).

[38]F. Mirani, A. Maffini, F. Casamichiela, A. Pazzaglia, A. Formenti, D. Dellasega, V. Russo, D. Vavassori, D. Bortot, M. Huault, G. Zeraouli, V. Ospina, S. Malko, J. I. Apinaniz, J. A. Pérez-Hernández, D. D. Luis, G. Gatti, L. Volpe, A. Pola, and M. Passoni, "Integrated quantitative pixe analysis and edx spectroscopy using a laser-driven particle source", Science Advances **7**, eabc8660 (2021).

[39]P. Puyuelo-Valdés, S. Vallières, M. Salvadori, S. Fourmaux, S. Payeur, J.-C. Kieffer, F. Hannachi, and P. Antici, "Combined laser-based x-ray fluorescence and particle-induced x-ray emission for versatile multi-element analysis", Scientific Reports **11**, 9998 (2021).

[40]M. Barberio, S. Veltri, M. Scisciò, and P. Antici, "Laser-accelerated proton beams as diagnostics for cultural heritage", Scientific Reports **7**, 40415 (2017).

[41]I. Spencer, K. Ledingham, R. Singhal, T. McCanny, P. McKenna, E. Clark, K. Krushelnick, M. Zepf, F. Beg, M. Tatarakis, A. Dangor, P. Norreys, R. Clarke, R. Allott, and I. Ross, "Laser generation of proton beams for the production of short-lived positron emitting radioisotopes", Nucl. Instrum. Methods Phys. Res., Sect. B **183**, 449–458 (2001).

[42]F. Kroll, F.-E. Brack, C. Bernert, S. Bock, E. Bondenstein, K. Büchner, T. E. Cowan, L. Gaus, R. Gebhardt, U. Helbig, L. Karsch, T. Kluge, S. Kraft, M. Krause, E. Lessmann, U. Masood, S. Meister, J. Metzkes-Ng, A. Nossula, J. Pawelke, J. Pietzsch, T. Püschel, M. Reimold, M. Rehwald, C. Richter, H.-P. Schlenvoigt, U. Schramm, M. E. P. Umlandt, T. Ziegler, K. Zeil, and E. Beyreuther, "Tumour irradiation in mice with a laser-accelerated proton beam", Nature Physics **18**, 1745–2481 (2022).

[43]W. P. Leemans, B. Nagler, A. J. Gonsalves, C. Tóth, K. Nakamura, C. G. R. Geddes, E. Esarey, C. B. Schroeder, and S. M. Hooker, "Gev electron beams from a centimetre-scale accelerator", Nature Phys. **2**, 696–699 (2006).

[44]J Faure, D Gustas, D Guénot, A Vernier, F Böhle, M Ouillé, S Haessler, R Lopez-Martens, and A Lifschitz, "A review of recent progress on laser-plasma acceleration at kHz repetition rate", Plasma Physics and Controlled Fusion **61**, 014012 (2018).

[45]W. Schumaker, N. Nakanii, C. McGuffey, C. Zulick, V. Chyvkov, F. Dollar, H. Habara, G. Kalintchenko, A. Maksimchuk, K. A. Tanaka, A. G. R. Thomas, V. Yanovsky, and K. Krushelnick, "Ultrafast electron radiography of magnetic fields in high-intensity laser-solid interactions", Phys. Rev. Lett. **110**, 015003 (2013).

[46]C. J. Zhang, J. F. Hua, Y. Wan, C.-H. Pai, B. Guo, J. Zhang, Y. Ma, F. Li, Y. P. Wu, H.-H. Chu, Y. Q. Gu, X. L. Xu, W. B. Mori, C. Joshi, J. Wang, and W. Lu, "Femtosecond probing of plasma wakefields and observation of the plasma wake reversal using a relativistic electron bunch", Phys. Rev. Lett. **119**, 064801 (2017).

[47]O. Lundh, C. Rechatin, J. Faure, A. Ben-Ismaïl, J. Lim, C. De Wagter, W. De Neve, and V. Malka, "Comparison of measured with calculated dose distribution from a 120-mev electron beam from a laser-plasma accelerator", Medical Physics **39**, 3501 (2012).

[48]C. A. Lindstrøm, "Staging of plasma-wakefield accelerators", Phys. Rev. Accel. Beams **24**, 014801 (2021).

[49]W. Wang, K. Feng, C. Yu, Y. Xu, R. Qi, Y. Chen, Z. Qin, Z. Zhang, M. Fang, J. Liu, K. Jiang, H. Wang, C. Wang, X. Yang, F. Wu, Y. Leng, J. Liu, R. Li, and Z. Xu, "Free-electron lasing at 27 nanometres based on a laser wakefield accelerator", Nature **595**, 516–520 (2021).

[50]F Albert, A. G. R. Thomas, S. P. D. Mangles, S Banerjee, S Corde, A Flacco, M Litos, D Neely, J Vieira, Z Najmudin, R Bingham, C Joshi, and T Katsouleas, "Laser wakefield accelerator based light sources: potential applications and requirements", Plasma Physics and Controlled Fusion **56**, 084015 (2014).

[51]M. Z. Mo, Z. Chen, S. Fourmaux, A. Saraf, K. Otani, J. C. Kieffer, Y. Y. Tsui, A. Ng, and R. Fedosejevs, "Laser wakefield generated x-ray probe for femtosecond time-resolved measurements of ionization states of warm dense aluminum", Review of Scientific Instruments **84**, 123106 (2013).

[52]S. Kneip, C. McGuffey, F. Dollar, M. S. Bloom, V. Chvykov, G. Kalintchenko, K. Krushelnick, A. Maksimchuk, S. P. D. Mangles, T. Matsuoka, Z. Najmudin, C. A. J. Palmer, J. Schreiber, W. Schumaker, A. G. R. Thomas, and V. Yanovsky, "X-ray phase contrast imaging of biological specimens with femtosecond pulses of betatron radiation from a compact laser plasma wakefield accelerator", Applied Physics Letters **99**, 093701 (2011).

[53]J. Wenz, S. Schleede, K. Khrennikov, M. Bech, P. Thibault, M. Heigoldt, F. Pfeiffer, and S. Karsch, "Quantitative x-ray phase-contrast microtomography from a compact laser-driven betatron source", Nature Communications **6**, 7568 (2015).

[54]I. P. Christov, M. M. Murnane, and H. C. Kapteyn, "High-harmonic generation of attosecond pulses in the "single-cycle" regime", Phys. Rev. Lett. **78**, 1251–1254 (1997).

[55]F. Krausz and M. Ivanov, "Attosecond physics", Rev. Mod. Phys. **81**, 163–234 (2009).

[56]M. Z. Mo, A. Ali, S. Fourmaux, P. Lassonde, J. C. Kieffer, and R. Fedosejevs, "Quasimonoenergetic electron beams from laser wakefield acceleration in pure nitrogen", Applied Physics Letters **100**, 074101 (2012).

[57]A. Zewail, "Femtochemistry: atomic-scale dynamics of the chemical bond", The Journal of Physical Chemistry A **104**, 5660–5694 (2000).

[58]K. Ta Phuoc, R. Fitour, A. Tafzi, T. Garl, N. Artemiev, R. Shah, F. Albert, D. Boschetto, A. Rousse, D.-E. Kim, A. Pukhov, V. Seredov, and I. Kostyukov, "Demonstration of the ultrafast nature of laser produced betatron radiation", Physics of Plasmas **14**, 080701 (2007).

[59]S. Malko, W. Cayzac, V. Ospina-Bohórquez, K. Bhutwala, M. Bailly-Granvaux, C. McGuffey, R. Fedosejevs, X. Vaisseau, A. Tauschwitz, J. Apinaniz, D. de Luis, G. Gatti, M. Huault, J. A. Pérez-Herández, S. X. Hu, A. J. White, L. A. Collins, K. Nichols, P. Neumayer, J. Verberger, G. Perstopin, C. Verona, J. J. Santos, D. Batani, F. N. Beg, L. Roso, and L. Volpe, "Proton stopping measurements at low velocity in warm dense carbon", Nature Communications **13**, 2893 (2020).

[60]L. Volpe, R. Fedosejevs, G. Gatti, J. A. Pérez-Hernández, C. Méndez, J. Apinaniz, X. Vaisseau, C. Salgado, M. Huault, S. Malko, and et al., "Generation of high energy laser-driven electron and proton sources with the 200 tw system vega 2 at the centro de laseres pulsados", High Power Laser Science and Engineering **7**, e25 (2019).

[61]M. C. Downer, R. Zgadzaj, A. Debus, U. Schramm, and M. C. Kaluza, "Diagnostics for plasma-based electron accelerators", Rev. Mod. Phys. **90**, 035002 (2018).

[62]R. Trevino, *Ultrafast optics course*, 2018.

[63]I. H. Hutchinson, *Principles of plasma diagnostics* (Cambridge University Press, 2005).

[64]M. Borghesi, D. H. Campbell, A. Schiavi, M. G. Haines, O. Willi, A. J. MacKinnon, P. Patel, L. A. Gizzi, M. Galimberti, R. J. Clarke, F. Pegoraro, H. Ruhl, and S. Bulanov, "Electric field detection in laser-plasma interaction experiments via the proton imaging technique", Physics of Plasmas **9**, 2214–2220 (2002).

[65]P. Bolton et al., "Instrumentation for diagnostics and control of laser-accelerated proton (ion) beams", Physica Medica **30**, 255–270 (2014).

[66]S. Semushin and V. Malka, "High density gas jet nozzle design for laser target production", Review of Scientific Instruments **72**, 2961–2965 (2001).

[67]J. Couperus, A. Köhler, T. Wolterink, A. Jochmann, O. Zarini, H. Bastiaens, K. Boller, A. Irman, and U. Schramm, "Tomographic characterisation of gas-jet targets for laser wakefield acceleration", Nuclear Instruments and Methods in Physics Research Section A: Accelerators, Spectrometers, Detectors and Associated Equipment **830**, 504–509 (2016).

[68]I. Prencipe, J. Fuchs, S. Pascarelli, D. W. Schumacher, R. B. Stephens, N. B. Alexander, R. Briggs, M. Büscher, M. O. Cernaianu, A. Choukourov, and et al., "Targets for high repetition rate laser facilities: needs, challenges and perspectives", High Power Laser Science and Engineering **5**, e17 (2017).

[69]P. Gibbon, *Short pulse laser interactions with matter: an introduction* (Imperial College Press, 2005).

[70]K. Schmid and L. Veisz, "Supersonic gas jets for laser-plasma experiments", Review of Scientific Instruments **83**, 053304 (2012).

[71]A Debayle, F Mollica, B Vauzour, Y Wan, A Flacco, V Malka, X Davoine, and L Gremillet, "Electron heating by intense short-pulse lasers propagating through near-critical plasmas", New Journal of Physics **19**, 123013 (2017).

[72]D. Haberberger, S. Tochitsky, F. Fiuza, C. Gong, R. A. Fonseca, L. O. Silva, W. B. Mori, and C. Joshi, "Collisionless shocks in laser-produced plasma generate monoenergetic high-energy proton beams", Nature Phys. **8**, 95–99 (2012).

[73]F. Fiuza, A. Stockem, E. Boella, R. A. Fonseca, L. O. Silva, D. Haberberger, S. Tochitsky, W. B. Mori, and C. Joshi, "Ion acceleration from laser-driven electrostatic shocks", Physics of Plasmas **20**, 056304 (2013).

[74]F. Sylla, M. Veltcheva, S. Kahaly, A. Flacco, and V. Malka, "Development and characterization of very dense submillimetric gas jets for laser-plasma interaction", Review of Scientific Instruments **83**, 033507 (2012).

[75]M. Ehret, C. Salgado-Lopez, V. Ospina-Bohorquez, J. A. Perez-Hernandez, M. Huault, M. de Marco, J. I. Apinaniz, F. Hannachi, D. De Luis, J. H. Toro, D. Arana, C. Mendez, O. Varela, A. Debayle, L. Gremillet, T. H. Nguyen-Bui, E. Olivier, G. Revet, N. D. Bukharskii, H. Larreur, J. Caron, C. Vlachos, T. Ceccotti, D. Raffestin, P. Nicolai, J. L. Feugeas, M. Roth, X. Vaisseau, G. Gatti, L. Volpe, and J. J. Santos, "Ion acceleration by an ultrashort laser pulse interacting with a near-critical-density gas jet", 10.48550/ARXIV.2012.09455 (2020).

[76]M. Migliorati, A. Bacci, C. Benedetti, E. Chiadroni, M. Ferrario, A. Mostacci, L. Palumbo, A. R. Rossi, L. Serafini, and P. Antici, "Intrinsic normalized emittance growth in laser-driven electron accelerators", Phys. Rev. ST Accel. Beams **16**, 011302 (2013).

[77]S. Humphries, *Charged particle beams* (Wiley, New York, 2002).

[78]M. Born and E. Wolf, *Principles of optics: electromagnetic theory of propagation, interference, and diffraction of light* (Oxford, Pergamon Press, 1964).

[79]A. E. Siegman, *Lasers* (University Science Books, 1986).

[80]K. F. Renk, *Basics of laser physics* (Springer, 2017).

[81]B. E. A. Saleh and M. C. Teich, *Fundamentals of photonics* (Wiley-Interscience, 2007).

[82]H. Kogelnik and T. Li, "Laser beams and resonators", Appl. Opt. **5**, 1550–1567 (1966).

[83]*Lasers and laser-related equipment — Test methods for laser beam widths, divergence angles and beam propagation ratios — Part 1: Stigmatic and simple astigmatic beams*, Standard (International Organization for Standardization, Jan. 2005).

[84]*Lasers and laser-related equipment — Test methods for laser beam widths, divergence angles and beam propagation ratios — Part 2: General astigmatic beams*, Standard (International Organization for Standardization, July 2021).

[85]R. Borghi and M. Santarsiero, "M2 factor of bessel–gauss beams", Opt. Lett. **22**, 262–264 (1997).

[86]R. M. Herman and T. A. Wiggins, "Rayleigh range and the m2 factor for bessel–gauss beams", Appl. Opt. **37**, 3398–3400 (1998).

[87]*The nobel prize in physics 2018*, (2022) https://www.nobelprize.org/prizes/physics/2018/summary/ (visited on 03/13/2022).

[88]J. W. Yoon, Y. G. Kim, I. W. Choi, J. H. Sung, H. W. Lee, S. K. Lee, and C. H. Nam, "Realization of laser intensity over 10^{23}W/cm^2", Optica **8**, 630–635 (2021).

[89]C. Thaury, F. Quéré, J.-P. Geindre, A. Levy, P. Monot, M. Bougeard, F. Réau, P. d'Oliveira, P. Audebert, R. Marjoribanks, and P. Martin, "Plasma mirrors for ultrahigh-intensity optics", Nature Phys. **3**, 424—429 (2007).

[90]J. Itatani, J. Faure, M. Nantel, G. Mourou, and S. Watanabe, "Suppression of the amplified spontaneous emission in chirped-pulse-amplification lasers by clean high-energy seed-pulse injection", Optics Communications **148**, 70–74 (1998).

[91]A. Jullien, O. Albert, F. Burgy, G. Hamoniaux, J.-P. Rousseau, J.-P. Chambaret, F. Augé-Rochereau, G. Chériaux, J. Etchepare, N. Minkovski, and S. M. Saltiel, "10?10 temporal contrast for femtosecond ultraintense lasers by cross-polarized wave generation", Opt. Lett. **30**, 920–922 (2005).

[92]K.-H. Hong, B. Hou, J. A. Nees, E. Power, and G. A. Mourou, "Generation and measurement of $> 10^8$ intensity contrast ratio in a relativistic khz chirped-pulse amplified laser", Applied Physics B **81**, 447—457 (2005).

[93]J. D. Jackson, *Classical electrodynamics* (John Wiley and Sons, 1962).

[94]M. J. Weber, *Handbook of optical materials* (CRC Press, 2002).

[95]H. A. Lorentz, "Ueber die beziehung zwischen der fortpflanzungsgeschwindigkeit des lichtes und der körperdichte", Annalen der Physik **245**, 641–665 (1880).

[96]L. Lorenz, "Ueber die refractionsconstante", Annalen der Physik **247**, 70–103 (1880).

[97]R. W. Boyd, *Nonlinear optics* (Academic Press, 2008).

[98]P. L. Kelley, "Self-focusing of optical beams", Phys. Rev. Lett. **15**, 1005–1008 (1965).

[99]R. R. Alfano and S. L. Shapiro, "Observation of self-phase modulation and small-scale filaments in crystals and glasses", Phys. Rev. Lett. **24**, 592–594 (1970).

[100]G. Yang and Y. R. Shen, "Spectral broadening of ultrashort pulses in a nonlinear medium", Opt. Lett. **9**, 510–512 (1984).

[101]L. Roso-Franco, "Self-reflected wave inside a very dense saturable absorber", Phys. Rev. Lett. **55**, 2149–2151 (1985).

[102]A. Einstein, "Über einen die erzeugung und verwandlung des lichtes bettreffenden gesichtspunkt", Annalen der Physik **17**, 132–148 (1905).

[103]R. A. Millikan, "Einstein's photoelectric equation and contact electromotive force", Phys. Rev. **7**, 18–32 (1916).

[104]M. Göppert-Mayer, "Über elementarakte mit zwei quantensprüngen", Annalen der Physik **401**, 273–294 (1931).

[105]W. Kaiser and C. G. B. Garrett, "Two-photon excitation in CaF_2: Eu^{2+}", Phys. Rev. Lett. **7**, 229–231 (1961).

[106]L. V. Keldysh, "Ionization in the field of a strong electromagnetic wave", Soviet Physics JETP **20**, 1307 (1965).

[107]A. McPherson, G. Gibson, H. Jara, U. Johann, T. S. Luk, I. A. McIntyre, K. Boyer, and C. K. Rhodes, "Studies of multiphoton production of vacuum-ultraviolet radiation in the rare gases", J. Opt. Soc. Am. B **4**, 595–601 (1987).

[108]M Ferray, A L'Huillier, X. F. Li, L. A. Lompre, G Mainfray, and C Manus, "Multiple-harmonic conversion of 1064 nm radiation in rare gases", Journal of Physics B: Atomic, Molecular and Optical Physics **21**, L31–L35 (1988).

[109]J. L. Krause, K. J. Schafer, and K. C. Kulander, "High-order harmonic generation from atoms and ions in the high intensity regime", Phys. Rev. Lett. **68**, 3535–3538 (1992).

[110]A. Macchi, *A superintense laser-plasma interaction theory primer* (Springer, 2013).

[111]S. C. Wilks, W. L. Kruer, M. Tabak, and A. B. Langdon, "Absorption of ultra-intense laser pulses", Phys. Rev. Lett. **69**, 1383–1386 (1992).

[112]J. D. Callen, "Fundamentals of plasma physics", in (2004).

[113]F. Chen, *Introduction to plasma physics and controlled fusion* (Springer, 2016).

[114]T. Kroker, M. Grossmann, K. Sengstock, M. Drescher, P. Wessels-Staarmann, and J. Simonet, "Ultrafast electron cooling in an expanding ultracold plasma", Nature Communications **12**, 10.1038/s41467-020-20815-8 (2021).

[115]R. Fedosejevs, X. F. Wang, and G. D. Tsakiris, "Onset of relativistic self-focusing in high density gas jet targets", Phys. Rev. E **56**, 4615–4639 (1997).

[116]V. Malka, "Plasma wake accelerators: introduction and historical overview", in Proceedings of the cas-cern accelerator school: plasma wake acceleration (2016).

[117]M. Everett, A. Lal, D. Gordon, C. E. Calyton, K. A. Marsh, and C. Joshi, "Trapped electron acceleration by a laser-driven relativistic plasma wave", Nature **368**, 527–529 (1994).

[118]V. Malka, J. Faure, J. R. Marquès, F. Amiranoff, J. P. Rousseau, S. Ranc, J. P. Chambaret, Z. Najmudin, B. Walton, P. Mora, and A. Solodov, "Characterization of electron beams produced by ultrashort (30 fs) laser pulses", Physics of Plasmas **8**, 2605–2608 (2001).

[119]V. Malka, S. Fritzler, E. Lefebvre, M.-M. Aleonard, F. Burgy, J.-P. Chambaret, J.-F. Chemin, K. Krushelnick, G. Malka, S. P. D. Mangles, Z. Najmudin, M. Pittman, J.-P. Rousseau, J.-N. Scheurer, B. Walton, and A. E. Dangor, "Electron acceleration by a wake field forced by an intense ultrashort laser pulse", Science **298**, 1596–1600 (2002).

[120]C. Gahn, G. D. Tsakiris, A. Pukhov, J. Meyer-ter Vehn, G. Pretzler, P. Thirolf, D. Habs, and K. J. Witte, "Multi-mev electron beam generation by direct laser acceleration in high-density plasma channels", Phys. Rev. Lett. **83**, 4772–4775 (1999).

[121]A. Modena, Z. Najmudin, A. E. Dangor, C. E. Clayton, K. A. Marsh, C. Joshi, V. Malka, C. B. Darrow, C. Dansons, D. Neely, and F. N. Walsh, "Electron acceleration from the breaking of relativistic plasma waves", Nature **377**, 606–608 (1995).

[122]P. E. Masson-Laborde, M. Z. Mo, A. Ali, S. Fourmaux, P. Lassonde, J. C. Kieffer, W. Rozmus, D. Teychenné, and R. Fedosejevs, "Giga-electronvolt electrons due to a transition from laser wakefield acceleration to plasma wakefield acceleration", Physics of Plasmas **21**, 123113 (2014).

[123]A. Pukhov and J. Meyer-ter Vehn, "Laser wake field acceleration: the highly non-linear broken-wave regime", Applied Physics B **74**, 355–361 (2002).

[124]J. Faure, Y. Glinec, A. Pukhov, S. Kiselev, S. Gordienko, E. Lefebvre, J.-P. Rousseau, F. Burgy, and V. Malka, "A laser–plasma accelerator producing monoenergetic electron beams", Nature **431**, 541–544 (2004).

[125]C. G. R. Geddes, C. Toth, J. van Tilbord, E. Esarey, C. B. Schroeder, D. Bruhwiler, C. Nieter, J. Cary, and W. P. Leemans, "High-quality electron beams from a laser wakefield accelerator using plasma-channel guiding", Nature **431**, 538–541 (2004).

[126]S. P. D. Mangles, C. D. Murphy, Z. Najmudin, A. G. R. Thomas, J. L. Collier, A. E. Dangor, E. J. Divall, P. S. Foster, J. G. Gallacher, C. J. Hooker, D. A. Jaroszynski, A. J. Langley, W. B. Mori, P. A. Norreys, F. S. Tsung, R. Viskup, B. R. Walton, and K. Krushelnick, "Monoenergetic beams of relativistic electrons from intense laser–plasma interactions", Nature **431**, 535–538 (2004).

[127]W. Lu, M. Tzoufras, C. Joshi, F. S. Tsung, W. B. Mori, J. Vieira, R. A. Fonseca, and L. O. Silva, "Generating multi-gev electron bunches using single stage laser wakefield acceleration in a 3d nonlinear regime", Phys. Rev. ST Accel. Beams **10**, 061301 (2007).

[128]A. Couairon and A. Mysyrowicz, "Femtosecond filamentation in transparent media", Physics Reports **441**, 47–189 (2007).

[129]A. Pak, K. A. Marsh, S. F. Martins, W. Lu, W. B. Mori, and C. Joshi, "Injection and trapping of tunnel-ionized electrons into laser-produced wakes", Phys. Rev. Lett. **104**, 025003 (2010).

[130]I. G. González, H Ekerfelt, M Hansson, T. L. Audet, B Aurand, F. G. Desforges, S. D. Dufrénoy, A Persson, X Davoine, C.-G. Wahlström, B Cros, and O Lundh, "Effects of the dopant concentration in laser wakefield and direct laser acceleration of electrons", New Journal of Physics **20**, 053011 (2018).

[131]B. B. Pollock, C. E. Clayton, J. E. Ralph, F. Albert, A. Davidson, L. Divol, C. Filip, S. H. Glenzer, K. Herpoldt, W. Lu, K. A. Marsh, J. Meinecke, W. B. Mori, A. Pak, T. C. Rensink, J. S. Ross, J. Shaw, G. R. Tynan, C. Joshi, and D. H. Froula, "Demonstration of a narrow energy spread, ~ 0.5 GeV electron beam from a two-stage laser wakefield accelerator", Phys. Rev. Lett. **107**, 045001 (2011).

[132]C. G. R. Geddes, K. Nakamura, G. R. Plateau, C. Toth, E. Cormier-Michel, E. Esarey, C. B. Schroeder, J. R. Cary, and W. P. Leemans, "Plasma-density-gradient injection of low absolute-momentum-spread electron bunches", Phys. Rev. Lett. **100**, 215004 (2008).

[133]K. Schmid, A. Buck, C. M. S. Sears, J. M. Mikhailova, R. Tautz, D. Herrmann, M. Geissler, F. Krausz, and L. Veisz, "Density-transition based electron injector for laser driven wakefield accelerators", Phys. Rev. ST Accel. Beams **13**, 091301 (2010).

[134]K. K. Swanson, H.-E. Tsai, S. K. Barber, R. Lehe, H.-S. Mao, S. Steinke, J. van Tilborg, K. Nakamura, C. G. R. Geddes, C. B. Schroeder, E. Esarey, and W. P. Leemans, "Control of tunable, monoenergetic laser-plasma-accelerated electron beams using a shock-induced density downramp injector", Phys. Rev. Accel. Beams **20**, 051301 (2017).

[135]H. T. Kim, K. H. Pae, H. J. Cha, I. J. Kim, T. J. Yu, J. H. Sung, S. K. Lee, T. M. Jeong, and J. Lee, "Enhancement of electron energy to the multi-gev regime by a dual-stage laser-wakefield accelerator pumped by petawatt laser pulses", Phys. Rev. Lett. **111**, 165002 (2013).

[136]J. Faure, C. Rechatin, A. Norlin, A. Lifschitz, Y. Glinec, and V. Malka, "Controlled injection and acceleration of electrons in plasma wakefields by colliding laser pulses", Nature **444**, 737—739 (2006).

[137]T. Kurz, T. Heinemann, M. F. Gilljohann, Y. Y. Chang, J. P. Couperus Cabadağ, A. Debus, O. Kononenko, R. Pausch, S. Schöbel, R. W. Assmann, R. W. Bussmann, H. Ding, J. Götzfried, A. Köhler, G. Raj, S. Schindler, K. Steiniger, O. Zarini, S. Corde, A. Döpp, B. Hidding, S. Karch, U. Schramm, A. Martinez de la Ossa, and A. Irman, "Demonstration of a compact plasma accelerator powered by laser-accelerated electron beams", Nature Communications **12**, 2895 (2021).

[138]A. Rousse, K. T. Phuoc, R. Shah, A. Pukhov, E. Lefebvre, V. Malka, S. Kiselev, F. Burgy, J.-P. Rousseau, D. Umstadter, and D. Hulin, "Production of a kev x-ray beam from synchrotron radiation in relativistic laser-plasma interaction", Phys. Rev. Lett. **93**, 135005 (2004).

[139]K. T. Phuoc, F. Burgy, J.-P. Rousseau, V. Malka, A. Rousse, R. Shah, D. Umstadter, A. Pukhov, and S. Kiselev, "Laser based synchrotron radiation", Physics of Plasmas **12**, 023101 (2005).

[140]S. Cipiccia, M. R. Islam, B. Ersfeld, R. P. Shanks, E. Brunetti, G. Vieux, X. Yang, R. C. Issac, S. M. Wiggins, G. H. Welsh, M.-P. Anania, D. Maneuski, R. Montgomery, G. Smith, M. Hoek, D. J. Hamilton, N. R. C. Lemos, D. Symes, P. P. Rajeev, V. O. Shea, J. M. Dias, and D. A. Jaroszynski, "Gamma-rays from harmonically resonant betatron oscillations in a plasma wake", Nat. Phys. **7**, 867–871 (2011).

[141]K. Ta Phuoc, A. Rousse, M. Pittman, J. P. Rousseau, V. Malka, S. Fritzler, D. Umstadter, and D. Hulin, "X-ray radiation from nonlinear thomson scattering of an intense femtosecond laser on relativistic electrons in a helium plasma", Phys. Rev. Lett. **91**, 195001 (2003).

[142]K. Ta Phuoc, S. Corde, C. Thaury, V. Malka, A. Tafzi, J. P. Goddet, S. Shah R. C. Sebban, and A. Rousse, "All-optical compton gamma-ray source", Nature Photonics **6**, 1749–4893 (2012).

[143]G. R. Plateau, N. H. Matlis, C. G. R. Geddes, A. J. Gonsalves, S. Shiraishi, C. Lin, R. A. van Mourik, and W. P. Leemans, "Wavefront-sensor-based electron density measurements for laser-plasma accelerators", Review of Scientific Instruments **81**, 033108 (2010).

[144]W. L. Kruer, *The physics of laser plasma interactions*, eng, Frontiers in physics ; 73 (Westview Press, Boulder, 2003).

[145]S. Atzeni and J. Meyer-ter Vehn, *The physics of inertial fusion: beam plasma interaction, hydrodynamics, hot dense matter* (Oxford University Press, 2004).

[146]S. J. Gitomer, R. D. Jones, F. Begay, A. W. Ehler, J. F. Kephart, and R. Kristal, "Fast ions and hot electrons in the laser–plasma interaction", The Physics of Fluids **29**, 2679–2688 (1986).

[147]F. N. Beg, A. R. Bell, A. E. Dangor, C. N. Danson, A. P. Fews, M. E. Glinsky, B. A. Hammel, P. Lee, P. A. Norreys, and M. Tatarakis, "A study of picosecond laser–solid interactions up to 10^{19}W/cm^2", Physics of Plasmas **4**, 447–457 (1997).

[148]E. L. Clark, K. Krushelnick, M. Zepf, F. N. Beg, M. Tatarakis, A. Machacek, M. I. K. Santala, I. Watts, P. A. Norreys, and A. E. Dangor, "Energetic heavy-ion and proton generation from ultraintense laser-plasma interactions with solids", Phys. Rev. Lett. **85**, 1654–1657 (2000).

[149]E. L. Clark, K. Krushelnick, J. R. Davies, M. Zepf, M. Tatarakis, F. N. Beg, A. Machacek, P. A. Norreys, M. I. K. Santala, I. Watts, and A. E. Dangor, "Measurements of energetic proton transport through magnetized plasma from intense laser interactions with solids", Phys. Rev. Lett. **84**, 670–673 (2000).

[150]A. Maksimchuk, S. Gu, K. Flippo, D. Umstadter, and V. Y. Bychenkov, "Forward ion acceleration in thin films driven by a high-intensity laser", Phys. Rev. Lett. **84**, 4108–4111 (2000).

[151]R. A. Snavely, M. H. Key, S. P. Hatchett, T. E. Cowan, M. Roth, T. W. Phillips, M. A. Stoyer, E. A. Henry, T. C. Sangster, M. S. Singh, S. C. Wilks, A. MacKinnon, A. Offenberger, D. M. Pennington, K. Yasuike, A. B. Langdon, B. F. Lasinski, J. Johnson, M. D. Perry, and E. M. Campbell, "Intense high-energy proton beams from petawatt-laser irradiation of solids", Phys. Rev. Lett. **85**, 2945–2948 (2000).

[152]S. C. Wilks, A. B. Langdon, T. E. Cowan, M. Roth, M. Singh, S. Hatchett, M. H. Key, D. Pennington, A. MacKinnon, and R. A. Snavely, "Energetic proton generation in ultra-intense laser–solid interactions", Physics of Plasmas **8**, 542–549 (2001).

[153]B. M. Hegelich, B. Albright, P. Audebert, A. Blazevic, E. Brambrink, J. Cobble, T. Cowan, J. Fuchs, J. C. Gauthier, C. Gautier, M. Geissel, D. Habs, R. Johnson, S. Karsch, A. Kemp, S. Letzring, M. Roth, U. Schramm, J. Schreiber, K. J. Witte, and J. C. Fernández, "Spectral properties of laser-accelerated mid-z mev/u ion beams", Physics of Plasmas **12**, 056314 (2005).

[154]L. Romagnani, J. Fuchs, M. Borghesi, P. Antici, P. Audebert, F. Ceccherini, T. Cowan, T. Grismayer, S. Kar, A. Macchi, P. Mora, G. Pretzler, A. Schiavi, T. Toncian, and O. Willi, "Dynamics of electric fields driving the laser acceleration of multi-mev protons", Phys. Rev. Lett. **95**, 195001 (2005).

[155]M. Kaluza, J. Schreiber, M. I. K. Santala, G. D. Tsakiris, K. Eidmann, J. Meyer-ter Vehn, and K. J. Witte, "Influence of the laser prepulse on proton acceleration in thin-foil experiments", Phys. Rev. Lett. **93**, 045003 (2004).

[156]L. Yin, B. J. Albright, K. J. Bowers, D. Jung, J. C. Fernández, and B. M. Hegelich, "Three-dimensional dynamics of breakout afterburner ion acceleration using high-contrast short-pulse laser and nanoscale targets", Phys. Rev. Lett. **107**, 045003 (2011).

[157]L. Willingale, S. R. Nagel, A. G. R. Thomas, C. Bellei, R. J. Clarke, A. E. Dangor, R. Heathcote, M. C. Kaluza, C. Kamperidis, S. Kneip, K. Krushelnick, N. Lopes, S. P. D. Mangles, W. Nazarov, P. M. Nilson, and Z. Najmudin, "Characterization of high-intensity laser propagation in the relativistic transparent regime through measurements of energetic proton beams", Phys. Rev. Lett. **102**, 125002 (2009).

[158]F. Fiuza, A. Stockem, E. Boella, R. A. Fonseca, L. O. Silva, D. Haberberger, S. Tochitsky, C. Gong, W. B. Mori, and C. Joshi, "Laser-driven shock acceleration of monoenergetic ion beams", Phys. Rev. Lett. **109**, 215001 (2012).

[159]J. Denavit, "Absorption of high-intensity subpicosecond lasers on solid density targets", Phys. Rev. Lett. **69**, 3052–3055 (1992).

[160]L. O. Silva, M. Marti, J. R. Davies, R. A. Fonseca, C. Ren, F. S. Tsung, and W. B. Mori, "Proton shock acceleration in laser-plasma interactions", Phys. Rev. Lett. **92**, 015002 (2004).

[161]A. Pak, S. Kerr, N. Lemos, A. Link, P. Patel, F. Albert, L. Divol, B. B. Pollock, D. Haberberger, D. Froula, M. Gauthier, S. H. Glenzer, A. Longman, L. Manzoor, R. Fedosejevs, S. Tochitsky, C. Joshi, and F. Fiuza, "Collisionless shock acceleration of narrow energy spread ion beams from mixed species plasmas using 1 μm lasers", Phys. Rev. Accel. Beams **21**, 103401 (2018).

[162]P. Puyuelo-Valdes, J. L. Henares, F. Hannachi, T. Ceccotti, J. Domange, M. Ehret, E. d'Humieres, L. Lancia, J.-R. Marquès, X. Ribeyre, J. J. Santos, V. Tikhonchuk, and M. Tarisien, "Proton acceleration by collisionless shocks using a supersonic h2 gas-jet target and high-power infrared laser pulses", Physics of Plasmas **26**, 123109 (2019).

[163]S. N. Chen, M. Vranic, T. Gangolf, E. Boella, P. Antici, M. Bailly-Grandvaux, P. Loiseau, H. Pépin, G. Revet, J. J. Santos, A. M. Schroer, M. Starodubtsev, O. Willi, L. O. Silva, E. d'Humières, and J. Fuchs, "Collimated protons accelerated from an overdense gas jet irradiated by a 1 µm wavelength high-intensity short-pulse laser", Scientific Reports **7**, 2045–2322 (2017).

[164]P. K. Singh, V. B. Pathak, J. H. Shin, I. W. Choi, K. Nakajima, S. K. Lee, J. H. Sung, H. W. Lee, Y. J. Rhee, C. Aniculaesei, C. M. Kim, K. H. Pae, M. H. Cho, C. Hojbota, S. G. Lee, F. Mollica, V. Malka, C.-M. Ryu, H. T. Kim, and C. H. Nam, "Electrostatic shock acceleration of ions in near-critical-density plasma driven by a femtosecond petawatt laser", Scientific Reports **10**, 18452 (2020).

[165]A. Pukhov and J. Meyer-ter Vehn, "Relativistic magnetic self-channeling of light in near-critical plasma: three-dimensional particle-in-cell simulation", Phys. Rev. Lett. **76**, 3975–3978 (1996).

[166]S. S. Bulanov, V. Y. Bychenkov, V. Chvykov, G. Kalinchenko, D. W. Litzenberg, T. Matsuoka, A. G. R. Thomas, L. Willingale, V. Yanovsky, K. Krushelnick, and A. Maksimchuk, "Generation of gev protons from 1 pw laser interaction with near critical density targets", Physics of Plasmas **17**, 043105 (2010).

[167]T. Nakamura, S. V. Bulanov, T. Z. Esirkepov, and M. Kando, "High-energy ions from near-critical density plasmas via magnetic vortex acceleration", Phys. Rev. Lett. **105**, 135002 (2010).

[168]F. Sylla, A. Flacco, S. Kahaly, M. Veltcheva, A. Lifschitz, G. Sanchez-Arriaga, E. Lefebvre, and V. Malka, "Anticorrelation between ion acceleration and nonlinear coherent structures from laser-underdense plasma interaction", Phys. Rev. Lett. **108**, 115003 (2012).

[169]M. H. Helle, D. F. Gordon, D. Kaganovich, Y. Chen, J. P. Palastro, and A. Ting, "Laser-accelerated ions from a shock-compressed gas foil", Phys. Rev. Lett. **117**, 165001 (2016).

[170]A. J. Goers, G. A. Hine, L. Feder, B. Miao, F. Salehi, J. K. Wahlstrand, and H. M. Milchberg, "Multi-mev electron acceleration by subterawatt laser pulses", Phys. Rev. Lett. **115**, 194802 (2015).

[171]O. N. Rosmej, N. E. Andreev, S Zaehter, N Zahn, P Christ, B Borm, T Radon, A Sokolov, L. P. Pugachev, D Khaghani, F Horst, N. G. Borisenko, G Sklizkov, and V. G. Pimenov, "Interaction of relativistically intense laser pulses with long-scale near critical plasmas for optimization of laser based sources of MeV electrons and gamma-rays", New Journal of Physics **21**, 043044 (2019).

[172]A Lifschitz, F Sylla, S Kahaly, A Flacco, M Veltcheva, G Sanchez-Arriaga, E Lefebvre, and V Malka, "Ion acceleration in underdense plasmas by ultra-short laser pulses", New Journal of Physics **16**, 033031 (2014).

[173]L. Willingale, S. P. D. Mangles, P. M. Nilson, R. J. Clarke, A. E. Dangor, M. C. Kaluza, S. Karsch, K. L. Lancaster, W. B. Mori, Z. Najmudin, J. Schreiber, A. G. R. Thomas, M. S. Wei, and K. Krushelnick, "Collimated multi-mev ion beams from high-intensity laser interactions with underdense plasma", Phys. Rev. Lett. **96**, 245002 (2006).

[174]E d'Humières, P Antici, M Glesser, J Boeker, F Cardelli, S Chen, J. L. Feugeas, F Filippi, M Gauthier, A Levy, P Nicolaï, H Pépin, L Romagnani, M Scisciò, V. T. Tikhonchuk, O Willi, J. C. Kieffer, and J Fuchs, "Investigation of laser ion acceleration in low-density targets using exploded foils", Plasma Physics and Controlled Fusion **55**, 124025 (2013).

[175]M. Gauthier, A. Lévy, E. d'Humières, M. Glesser, B. Albertazzi, C. Beaucourt, J. Breil, S. N. Chen, V. Dervieux, J. L. Feugeas, P. Nicolaï, V. Tikhonchuk, H. Pépin, P. Antici, and J. Fuchs, "Investigation of longitudinal proton acceleration in exploded targets irradiated by intense short-pulse laser", Physics of Plasmas **21**, 013102 (2014).

[176]P. Antici, E. Boella, S. N. Chen, D. S. Andrewws, M. Barberio, J. Böker, F. Cardelli, J. L. Feugeas, M. Glesser, P. Nicolaï, L. Romagnani, M. Scisciò, M. Starodubtsev, O. Willi, J. C. Kieffer, V. Tikhonchuk, H. Pépin, L. O. Silva, E. d'Humières, and J. Fuchs, "Acceleration of collimated 45 MeV protons by collisionless shocks driven in low-density, large-scale gradient plasmas by a 10^{20} W/cm^2, 1 μm laser", Scientific Reports **7**, 2045–2322 (2017).

[177]J. H. Bin, M. Yeung, Z. Gong, H. Y. Wang, C. Kreuzer, M. L. Zhou, M. J. V. Streeter, P. S. Foster, S. Cousens, B. Dromey, J. Meyer-ter Vehn, M. Zepf, and J. Schreiber, "Enhanced laser-driven ion acceleration by superponderomotive electrons generated from near-critical-density plasma", Phys. Rev. Lett. **120**, 074801 (2018).

[178]I Prencipe, A Sgattoni, D Dellasega, L Fedeli, L Cialfi, I. W. Choi, I. J. Kim, K. A. Janulewicz, K. F. Kakolee, H. W. Lee, J. H. Sung, S. K. Lee, C. H. Nam, and M Passoni, "Development of foam-based layered targets for laser-driven ion beam production", **58**, 034019 (2016).

[179]J. L. Henares, P. Puyuelo-Valdes, F. Hannachi, T. Ceccotti, M. Ehret, F. Gobet, L. Lancia, J.-R. Marquès, J. J. Santos, M. Versteegen, and M. Tarisien, "Development of gas jet targets for laser-plasma experiments at near-critical density", Review of Scientific Instruments **90**, 063302 (2019).

[180]M. Reiser, *Theory and design of charged particle beams* (Wiely, New York, 1994).

[181]X. L. Xu, J. F. Hua, F. Li, C. J. Zhang, L. X. Yan, Y. C. Du, W. H. Huang, H. B. Chen, C. X. Tang, W. Lu, P. Yu, W. An, C. Joshi, and W. B. Mori, "Phase-space dynamics of ionization injection in plasma-based accelerators", Phys. Rev. Lett. **112**, 035003 (2014).

[182]A. Curcio, M. Anania, F. Bisesto, E. Chiadroni, A. Cianchi, M. Ferrario, F. Filippi, D. Giulietti, A. Marocchino, M. Petrarca, V. Shpakov, and A. Zigler, "Trace-space reconstruction of low-emittance electron beams through betatron radiation in laser-plasma accelerators", Phys. Rev. Accel. Beams **20**, 012801 (2017).

[183]T. Ceccotti, A. Lévy, H. Popescu, F. Réau, P. D'Oliveira, P. Monot, J. P. Geindre, E. Lefebvre, and P. Martin, "Proton acceleration with high-intensity ultrahigh-contrast laser pulses", Phys. Rev. Lett. **99**, 185002 (2007).

[184]M. Nishiuchi, H. Daido, A. Yogo, S. Orimo, K. Ogura, J. Ma, A. Sagisaka, M. Mori, A. S. Pirozhkov, H. Kiriyama, S. V. Bulanov, T. Z. Esirkepov, I. W. Choi, C. M. Kim, T. M. Jeong, T. J. Yu, J. H. Sung, S. K. Lee, N. Hafz, K. H. Pae, Y.-C. Noh, D.-K. Ko, J. Lee, Y. Oishi, K. Nemoto, H. Nagatomo, K. Nagai, and H. Azuma, "Efficient production of a collimated mev proton beam from a polyimide target driven by an intense femtosecond laser pulse", Physics of Plasmas **15**, 053104 (2008).

[185]M. ROTH, E. BRAMBRINK, P. AUDEBERT, A. BLAZEVIC, R. CLARKE, J. COBBLE, T. COWAN, J. FERNANDEZ, J. FUCHS, M. GEISSEL, and et al., "Laser accelerated ions and electron transport in ultra-intense laser matter interaction", Laser and Particle Beams **23**, 95–100 (2005).

[186]S. Ter-Avetisyan, M. Schnürer, P. V. Nickles, W. Sandner, M. Borghesi, T. Nakamura, and K. Mima, "Tomography of an ultrafast laser driven proton source", Physics of Plasmas **17**, 063101 (2010).

[187]B. Green, S. Kovalev, V. Asgekar, and et al., "High-field high-repetition-rate sources for the coherent thz control of matter", Scientific Reports **6**, 22256 (2016).

[188]"A vuv free electron laser at the tesla test facility at desy, conceptual design report", Desy Print, 10.3204/PUBDB-2018-04126 (1995).

[189]F.-E. Brack, F. Kroll, L. Gaus, C. Bernet, E. Beyreuther, T. E. Cowan, L. Karsch, S. Kraft, L. A. Kunz-Schughart, E. Lessmann, J. Metzkes-Ng, L. Obst-Huebl, J. Pawelke, M. Rehwald, H.-P. Schlenvoigt, U. Schramm, M. Sobiella, E. R. Szabó, T. Ziegler, and K. Zeil, "Spectral and spatial shaping of laser-driven proton beams using a pulsed high-field magnet beamlin", Scientific Reports **10**, 9118 (2020).

[190]P. Tournois, "Acousto-optic programmable dispersive filter for adaptive compensation of group delay time dispersion in laser systems", Optics Communications **140**, 245–249 (1997).

[191]E. M. Kosik, A. S. Radunsky, I. A. Walmsley, and C. Dorrer, "Interferometric technique for measuring broadband ultrashort pulses at the sampling limit", Opt. Lett. **30**, 326–328 (2005).

[192]A. Nayak, I. Orfanos, I. Makos, M. Dumergue, S. Kühn, E. Skantzakis, B. Bodi, K. Varju, C. Kalpouzos, H. I. B. Banks, A. Emmanouilidou, D. Charalambidis, and P. Tzallas, "Multiple ionization of argon via multi-xuv-photon absorption induced by 20-gw high-order harmonic laser pulses", Phys. Rev. A **98**, 023426 (2018).

[193]Y. M. Li and R Fedosejevs, "Density measurements of a high-density pulsed gas jet for laser-plasma interaction studies", Measurement Science and Technology **5**, 1197–1201 (1994).

[194]K. Svensson, M. Hansson, F. Wojda, L. Senje, M. Burza, B. Aurand, G. Genoud, A. Persson, C.-G. Wahlström, and O. Lundh, "Supersonic jets of hydrogen and helium for laser wakefield acceleration", Phys. Rev. Accel. Beams **19**, 051301 (2016).

[195]P Hariharan, *Basics of interferometry* (Academic Press, 2007).

[196]S. Lorenz, G. Grittani, E. Chacon-Golcher, C. M. Lazzarini, J. Limpouch, F. Nawaz, M. Nevrkla, L. Vilanova, and T. Levato, "Characterization of supersonic and subsonic gas targets for laser wakefield electron acceleration experiments", Matter and Radiation at Extremes **4**, 015401 (2019).

[197]W. H. Press, S. A. Teukolsky, W. T. Vetterling, and B. P. Flannery, *Numerical recipes: the art of scientific computing* (Cambridge University Press, 2007).

[198]G. Pretzier, "A new method for numerical abel-inversion", Zeitschrift für Naturforschung A **46**, 639–641 (1991).

[199]C. Killer, *Abel inversion algorithm*, 2022.

[200]M. F. Kasim, J. Holloway, L. Ceurvorst, M. C. Levy, N. Ratan, J. Sadler, R. Bingham, P. N. Burrows, R. Trines, M. Wing, and P. Norreys, "Quantitative single shot and spatially resolved plasma wakefield diagnostics", Phys. Rev. ST Accel. Beams **18**, 081302 (2015).

[201]J.-C. Chanteloup, F. Druon, M. Nantel, A. Maksimchuk, and G. Mourou, "Single-shot wave-front measurements of high-intensity ultrashort laser pulses with a three-wave interferometer", Opt. Lett. **23**, 621–623 (1998).

[202]S. Velghe, J. Primot, N. Guérineau, M. Cohen, and B. Wattellier, "Wave-front reconstruction from multidirectional phase derivatives generated by multilateral shearing interferometers", Opt. Lett. **30**, 245–247 (2005).

[203]J. Primot and L. Sogno, "Achromatic three-wave (or more) lateral shearing interferometer", J. Opt. Soc. Am. A **12**, 2679–2685 (1995).

[204]B. Schäfer, M. Lübbecke, and K. Mann, "Hartmann-shack wave front measurements for real time determination of laser beam propagation parameters", Review of Scientific Instruments **77**, 053103 (2006).

[205]C. Peth, S. Kranzusch, K. Mann, and W. Viöl, "Characterization of gas targets for laser produced extreme ultraviolet plasmas with a hartmann-shack sensor", Review of Scientific Instruments **75**, 3288–3293 (2004).

[206]K. L. Baker, J. Brase, M. Kartz, S. S. Olivier, B. Sawvel, and J. Tucker, "The use of a shack–hartmann wave front sensor for electron density characterization of high density plasmas", Review of Scientific Instruments **73**, 3784–3788 (2002).

[207]Y. Inada, S. Matsuoka, A. Kumada, H. Ikeda, and K. Hidaka, "Shack–hartmann type laser wavefront sensor for measuring two-dimensional electron density distribution over extinguishing arc discharge", Journal of Physics D: Applied Physics **45**, 435202 (2012).

[208]A. Sävert, S. P. D. Mangles, M. Schnell, E. Siminos, J. M. Cole, M. Leier, M. Reuter, M. B. Schwab, M. Möller, K. Poder, O. Jäckel, G. G. Paulus, C. Spielmann, S. Skupin, Z. Najmudin, and M. C. Kaluza, "Direct observation of the injection dynamics of a laser wakefield accelerator using few-femtosecond shadowgraphy", Phys. Rev. Lett. **115**, 055002 (2015).

[209]A. Flacco, J. Vieira, A. Lifschitz, F. Sylla, S. Kahaly, M. Veltcheva, L. O. Silva, and V. Malka, "Persistence of magnetic field driven by relativistic electrons in a plasma", Nat. Phys. **11**, 409–413 (2015).

[210]A. Buck, M. Nicolai, K. Schmid, C. M. S. Sears, A. Sävert, J. M. Mikhailova, F. Krausz, M. C. Kaluza, and L. Veisz, "Real-time observation of laser-driven electron acceleration", Nat. Phys. **7**, 543–548 (2011).

[211]M. Huault, D. De Luis, J. I. Apinaniz, M. De Marco, C. Salgado, N. Gordillo, C. Gutiérrez Neira, J. A. Pérez-Hernández, R. Fedosejevs, G. Gatti, and et al., "A 2d scintillator-based proton detector for high repetition rate experiments", High Power Laser Science and Engineering **7**, e60 (2019).

[212]J. Thomson, "Xlvii. on rays of positive electricity", The London, Edinburgh, and Dublin Philosophical Magazine and Journal of Science **13**, 561–575 (1907).

[213]J. A. Cobble, K. A. Flippo, D. T. Offermann, F. E. Lopez, J. A. Oertel, D. Mastrosimone, S. A. Letzring, and N. Sinenian, "High-resolution thomson parabola for ion analysis", Review of Scientific Instruments **82**, 113504 (2011).

[214]K. Harres, M. Schollmeier, E. Brambrink, P. Audebert, A. Blažević, K. Flippo, D. C. Gautier, M. Geißel, B. M. Hegelich, F. Nürnberg, J. Schreiber, H. Wahl, and M. Roth, "Development and calibration of a thomson parabola with microchannel plate for the detection of laser-accelerated mev ions", Review of Scientific Instruments **79**, 093306 (2008).

[215]R. Rajeev, K. P. M. Rishad, T. M. Trivikram, V. Narayanan, and M. Krishnamurthy, "A thomson parabola ion imaging spectrometer designed to probe relativistic intensity ionization dynamics of nanoclusters", Review of Scientific Instruments **82**, 083303 (2011).

[216]S. Kojima, S. Inoue, T. H. Dinh, N. Hasegawa, M. Mori, H. Sakaki, Y. Yamamoto, T. Sasaki, K. Shiokawa, K. Kondo, T. Yamanaka, M. Hashida, S. Sakabe, M. Nishikino, and K. Kondo, "Compact thomson parabola spectrometer with variability of energy range and measurability of angular distribution for low-energy laser-driven accelerated ions", Review of Scientific Instruments **91**, 053305 (2020).

[217]D. Carroll, P. Brummitt, D. Neely, F. Lindau, O. Lundh, C.-G. Wahlström, and P. McKenna, "A modified thomson parabola spectrometer for high resolution multi-mev ion measurements—application to laser-driven ion acceleration", Nuclear Instruments and Methods in Physics Research Section A: Accelerators, Spectrometers, Detectors and Associated Equipment **620**, COULOMB09, 23–27 (2010).

[218]D. Gwynne, S. Kar, D. Doria, H. Ahmed, M. Cerchez, J. Fernandez, R. J. Gray, J. S. Green, F. Hanton, D. A. MacLellan, P. McKenna, Z. Najmudin, D. Neely, J. A. Ruiz, A. Schiavi, M. Streeter, M. Swantusch, O. Willi, M. Zepf, and M. Borghesi, "Modified thomson spectrometer design for high energy, multi-species ion sources", Review of Scientific Instruments **85**, 033304 (2014).

[219]S. Ter-Avetisyan, M. Schnürer, and P. V. Nickles, "Time resolved corpuscular diagnostics of plasmas produced with high-intensity femtosecond laser pulses", **38**, 863–867 (2005).

[220]S. Ter-Avetisyan, L. Romagnani, M. Borghesi, M. Schnürer, and P. Nickles, "Ion diagnostics for laser plasma experiments", Nuclear Instruments and Methods in Physics Research Section A: Accelerators, Spectrometers, Detectors and Associated Equipment **623**, 1rs International Conference on Frontiers in Diagnostics Technologies, 709–711 (2010).

[221]S. Ter-Avetisyan, M. Schnürer, S. Busch, E. Risse, P. V. Nickles, and W. Sandner, "Spectral dips in ion emission emerging from ultrashort laser-driven plasmas", Phys. Rev. Lett. **93**, 155006 (2004).

[222]S. Ter-Avetisyan, B. Ramakrishna, D. Doria, G. Sarri, M. Zepf, M. Borghesi, L. Ehrentraut, H. Stiel, S. Steinke, G. Priebe, M. Schnürer, P. V. Nickles, and W. Sandner, "Complementary ion and extreme ultra-violet spectrometer for laser-plasma diagnosis", Review of Scientific Instruments **80**, 103302 (2009).

[223]K. Flippo, B. Hegelich, B. Albright, L. Yin, D. Gautier, S. Letzring, M. Schollmeier, J. Schreiber, R. Schulze, J. Fernandez, and et al., "Laser-driven ion accelerators: spectral control, monoenergetic ions and new acceleration mechanisms", Laser and Particle Beams **25**, 3–8 (2007).

[224]C. Salgado-López, J. I. Apinaniz, J. L. Henares, J. A. Pérez-Hernández, D. de Luis, L. Volpe, and G. Gatti, "Angular-resolved thomson parabola spectrometer for laser-driven ion accelerators", Sensors **22**, 10.3390/s22093239 (2022).

[225]R. Prasad, F. Abicht, M. Borghesi, J. Braenzel, P. V. Nickles, G. Priebe, M. Schnürer, and S. Ter-Avetisyan, "Thomson spectrometer–microchannel plate assembly calibration for mev-range positive and negative ions, and neutral atoms", Review of Scientific Instruments **84**, 053302 (2013).

[226]H. Chen, A. U. Hazi, R. van Maren, S. N. Chen, J. Fuchs, M. Gauthier, S. Le Pape, J. R. Rygg, and R. Shepherd, "An imaging proton spectrometer for short-pulse laser plasma experiments", Review of Scientific Instruments **81**, 10D314 (2010).

[227]S. Ter-Avetisyan, M. Schnürer, P. V. Nickles, W. Sandner, T. Nakamura, and K. Mima, "Correlation of spectral, spatial, and angular characteristics of an ultrashort laser driven proton source", Physics of Plasmas **16**, 043108 (2009).

[228]S Ter-Avetisyan, M Borghesi, M Schnürer, P. V. Nickles, W Sandner, A. A. Andreev, T Nakamura, and K Mima, "Characterization and control of ion sources from ultra-short high-intensity laser–foil interaction", Plasma Physics and Controlled Fusion **51**, 124046 (2009).

[229]T. Sokollik, M. Schnürer, S. Ter-Avetisyan, P. V. Nickles, E. Risse, M. Kalashnikov, W. Sandner, G. Priebe, M. Amin, T. Toncian, O. Willi, and A. A. Andreev, "Transient electric fields in laser plasmas observed by proton streak deflectometry", Applied Physics Letters **92**, 091503 (2008).

[230]S. Ter–Avetisyan, M. Schnürer, P. V. Nickles, T. Sokollik, E. Risse, M. Kalashnikov, W. Sandner, and G. Priebe, "The thomson deflectometer: a novel use of the thomson spectrometer as a transient field and plasma diagnostic", Review of Scientific Instruments **79**, 033303 (2008).

[231]Y. Zheng, L. N. Su, M. Liu, B. C. Liu, Z. W. Shen, H. T. Fan, Y. T. Li, L. M. Chen, X. Lu, J. L. Ma, W. M. Wang, Z. H. Wang, Z. Y. Wei, and J. Zhang, "Note: a new angle-resolved proton energy spectrometer", Review of Scientific Instruments **84**, 096103 (2013).

[232]S. Yang, X. Yuan, Y. Fang, X. Ge, Y. Deng, W. Wei, J. Gao, F. Fu, T. Jiang, G. Liao, F. Liu, M. Chen, Y. Li, L. Zhao, Y. Ma, Z. Sheng, and J. Zhang, "A two-dimensional angular-resolved proton spectrometer", Review of Scientific Instruments **87**, 103301 (2016).

[233]D. Jung, R. Hörlein, D. C. Gautier, S. Letzring, D. Kiefer, K. Allinger, B. J. Albright, R. Shah, S. Palaniyappan, L. Yin, J. C. Fernández, D. Habs, and B. M. Hegelich, "A novel high resolution ion wide angle spectrometer", Review of Scientific Instruments **82**, 043301 (2011).

[234]L. Senje, M. Yeung, B. Aurand, S. Kuschel, C. Rödel, F. Wagner, K. Li, B. Dromey, V. Bagnoud, P. Neumayer, M. Roth, C.-G. Wahlström, M. Zepf, T. Kuehl, and D. Jung, "Diagnostics for studies of novel laser ion acceleration mechanisms", Review of Scientific Instruments **85**, 113302 (2014).

[235]Y. Zhang, Z. Zhang, B. Zhu, W. Jiang, L. Cheng, L. Zhao, X. Zhang, X. Zhao, X. Yuan, B. Tong, J. Zhong, S. He, F. Lu, Y. Wu, W. Zhou, F. Zhang, K. Zhou, N. Xie, Z. Huang, Y. Gu, S. Weng, M. Xu, Y. Li, and Y. Li, "An angular-resolved multi-channel thomson parabola spectrometer for laser-driven ion measurement", Review of Scientific Instruments **89**, 093302 (2018).

[236]P. Elleaume, C. Fortgang, C. Penel, and E. Tarazona, "Measuring Beam Sizes and Ultra-Small Electron Emittances Using an X-ray Pinhole Camera", Journal of Synchrotron Radiation **2**, 209–214 (1995).

[237]M Zhang, "Emittance formula for slits and pepper-pot measurement", 10.2172/395453.

[238]S. Ter-Avetisyan, P. K. Singh, M. H. Cho, A. Andreev, K. F. Kakolee, H. Ahmed, C. Scullion, S. Sharif, P. Hadjisolomou, and M. Borghesi, "Proton acceleration through a charged cavity created by ultraintense laser pulse", Physics of Plasmas **26**, 103106 (2019).

[239]M. J. Wu, D. Y. Li, J. G. Zhu, T. Yang, X. Y. Hu, Y. X. Geng, K. Zhu, M. J. Easton, Y. Y. Zhao, A. L. Zhang, H. Y. Lu, W. J. Ma, C. Lin, and X. Q. Yan, "Emittance measurement along transport beam line for laser driven protons", Phys. Rev. Accel. Beams **23**, 031302 (2020).

[240]S. K. Barber, J. van Tilborg, C. B. Schroeder, R. Lehe, H.-E. Tsai, K. K. Swanson, S. Steinke, K. Nakamura, C. G. R. Geddes, C. Benedetti, E. Esarey, and W. P. Leemans, "Measured emittance dependence on the injection method in laser plasma accelerators", Phys. Rev. Lett. **119**, 104801 (2017).

[241]C. Nordling and J. Österman, *Physics handbook for science and engineering* (Professional Publishing House, 2006).

[242]J. Woisetschläger, M. Hipp, T. Neger, and P. Reiterer, "Digital evaluation of interferograms", Measurement **36**, 53–66 (2004).

[243]A. Buck, K. Zeil, A. Popp, K. Schmid, A. Jochmann, S. D. Kraft, B. Hidding, T. Kudyakov, C. M. S. Sears, L. Veisz, S. Karsch, J. Pawelke, R. Sauerbrey, T. Cowan, F. Krausz, and U. Schramm, "Absolute charge calibration of scintillating screens for relativistic electron detection", Review of Scientific Instruments **81**, 033301 (2010).

[244]G Zeraouli, "Experimental studies for generation, transport and applications of ultra-fast laser driven x-ray sources", PhD thesis (Universidad de Salamanca, 2020).

[245]Y. Kobayashi, T. Ohno, T. Sekikawa, Y. Nabekawa, and S. Watanabe, "Pulse width measurement of high-order harmonics by autocorrelation", Applied Physics B **70**, 389–394 (2000).

[246]L. B. E. Bom, Y. Pertot, V. R. Bhardwaj, and T. Ozaki, "Multi-μj coherent extreme ultraviolet source generated from carbon using the plasma harmonic method", Opt. Express **19**, 3077–3085 (2011).

[247]F. A. Jenkins and H. E. White, *Fundamentals of optics / by francis a. jenkins and harvey e. white*, English, 4th ed. (McGraw-Hill New York, 1950).

[248]M Ehret, "Charged particle beam acceleration and strong discharge currents' fields generation by laser - a study on laser-driven ion sources and beam transport suited for application in high-energy-density physics experiments", PhD thesis (Université de Bordeaux and Technische Universitat Darmstadt, 2021).

[249]V Ospina-Bohórquez, "Experimental and numerical investigations on ion acceleration from near-critical gas targets", PhD thesis (Université de Bordeaux and Universidad de Salamanca, 2022).

[250]K. Nelissen, M. Liszi, M. De Marco, V. Ospina, I. Drotár, G. Gatti, C. Kamperidis, and L. Volpe, "Characterisation and modelling of ultrashort laser-driven electromagnetic pulses", Sci. Rep. **10**, 3108 (2020).

[251]A Martín-López, "Safety system automatization for gaseous targets experiments and real-time leak detection in the vacuum system", MA thesis (Universidad de Salamanca, 2021).

[252]M. Salvadori, F. Consoli, C. Verona, M. Cipriani, M. P. Anania, P. L. Andreoli, P. Antici, F. Bisesto, G. Costa, G. Cristofari, R. De Angelis, G. Di Giorgio, M. Ferrario, D. Giulietti, M. Migliorati, R. Pompili, and A. Zigler, "Accurate spectra for high energy ions by advanced time-of-flight diamond-detector schemes in experiments with high energy and intensity lasers", Sci. Reports **11**, 3071 (2021).

[253]I. Kochetkov, T. Pisarczyk, M. Kalal, T. Chodukowski, A. Zaraś-Szydłowska, Z. Rusiniak, R. Dudzak, J. Dostal, M. Krupka, L. Juha, and P. Korneev, "Complex interferometry of magnetized plasma: Accuracy and limitations", Physics of Plasmas **28**, 102110, 10.1063/5.0063162 (2021).

[254]J. A. Kulesza, T. R. Adams, J. C. Armstrong, S. R. Bolding, F. B. Brown, J. S. Bull, T. P. Burke, A. R. Clark, R. A. Forster III, J. F. Giron, A. S. Grieve, C. J. Josey, R. L. Martz, G. W. McKinney, E. J. Pearson, M. E. Rising, C. J. Solomon Jr., S. Swaminarayan, T. J. Trahan, S. C. Wilson, and A. J. Zukaitis, *MCNP® Code Version 6.3.0 Theory & User Manual*, tech. rep. LA-UR-22-30006, Rev. 1 (Los Alamos National Laboratory, Los Alamos, NM, USA, 2022).

[255]W. H. Richardson, "Bayesian-based iterative method of image restoration∗", J. Opt. Soc. Am. **62**, 55–59 (1972).

[256]L. Lucy, "An iterative technique for the rectification of observed distributions", Astronomical Journal **79**, 745 (1974).

[257]F. Lindau, O. Lundh, A. Persson, P. McKenna, K. Osvay, D. Batani, and C.-G. Wahlström, "Laser-accelerated protons with energy-dependent beam direction", Phys. Rev. Lett. **95**, 175002 (2005).

[258]D Batani, R Jafer, M Veltcheva, R Dezulian, O Lundh, F Lindau, A Persson, K Osvay, C.-G. Wahlström, D. C. Carroll, P McKenna, A Flacco, and V Malka, "Effects of laser prepulses on laser-induced proton generation", New Journal of Physics **12**, 045018 (2010).

[259]K. Zeil, J. Metzkes, T. Kluge, and et al., "Direct observation of prompt pre-thermal laser ion sheath acceleration", Nat. Commun. **3**, 874 (2012).

[260]R. Nedbailo, J. Park, R. Hollinger, S. Wang, D. Mariscal, J. Morrison, H. Song, G. Zeraouli, G. G. Scott, T. Ma, and J. J. Rocca, "Compact high repetition rate thomson parabola ion spectrometer", Review of Scientific Instruments **94**, 023505 (2023).

[261]F. Grepl, J. Krása, A. Velyhan, M. De Marco, J. Dostál, M. Pfeifer, and D. Margarone, "Distortion of thomson parabolic-like proton patterns due to electromagnetic interference", Applied Sciences **11**, 10.3390/app11104484 (2021).

[262]M. Sciscio, G. Di Giorgio, P. L. Andreoli, M. Cipriani, G. Cristofari, R. De Angelis, M. Salvadori, G. A. P. Cirrone, L. Giuffrida, D. Margarone, G. Milluzzo, G. Petringa, and F. Consoli, "High-sensitivity thomson spectrometry in experiments of laser-driven low-rate neutronless fusion reactions", Laser and Particle Beams **2023**, 3531875 (2023).

[263]M. Wu, J. Zhu, D. Li, T. Yang, Q. Liao, Y. Geng, X. Xu, C. Li, Y. Shou, Y. Zhao, Y. Lu, H. Lu, W. Ma, C. Lin, K. Zhu, and X. Yan, "Collection and focusing of laser accelerated proton beam by an electromagnetic quadrupole triplet lens", Nuclear Instruments and Methods in Physics Research Section A: Accelerators, Spectrometers, Detectors and Associated Equipment **955**, 163249 (2020).

[264]A. Döpp, E. Guillaume, C. Thaury, J. Gautier, K. Ta Phuoc, and V. Malka, "3D printing of gas jet nozzles for laser-plasma accelerators", Review of Scientific Instruments **87**, 073505, 10.1063/1.4958649 (2016).

[265]*High dynamic range streak camera c13410 instruction manual*, version 1.01E, Hamamatsu Photonics K.K. ().